

# **Optical Remote Sensing of properties and concentrations of atmospheric trace constituents**

by

DANIELA VIVIANA VLADUTESCU

A dissertation submitted to the graduate faculty in Engineering in partial fulfillment of  
the requirements for the degree of Doctor of Philosophy,

The City University of New York

2008

This manuscript has been read and accepted for the Graduate Faculty in Engineering in satisfaction of the dissertation requirement for the degree of Doctor of Philosophy

Fred Moshary\_\_\_\_\_

\_\_\_\_\_  
Date Chair of Examining Committee

Mumtaz K. Kassir\_\_\_\_\_

\_\_\_\_\_  
Date Executive Officer

Barry Gross\_\_\_\_\_

Samir Ahmed\_\_\_\_\_

Michael R. Hardesty\_\_\_\_\_

Yonghua Wu\_\_\_\_\_

Supervision Committee

THE CITY UNIVERSITY OF NEW YORK

Abstract

**Optical Remote Sensing of properties and concentrations of atmospheric trace constituents**

by

Daniela Viviana Vladutescu

Advisor: Professors Fred Moshary and Barry Gross

The effect of human activities on the global climate may lead to large disturbances of the economic, social and political circumstances in the middle and long term. Understanding the dynamics of the Earth's climate is therefore of high importance and one of the major scientific challenges of our time.

The estimation of the contribution of the Earth's climate system components needs observation and continuous monitoring of various atmospheric physical and chemical parameters. Temperature, water vapor and greenhouse gases concentration, aerosol and clouds loads, and atmospheric dynamics are parameters of particular importance in this respect. The quantification of the anthropogenic influence on the dynamics of these above-mentioned parameters is of crucial importance nowadays but still affected by significant uncertainties.

In the present context of these huge uncertainties in our understanding of how these different atmospheric compounds contribute to the radiative forcing, a significant part of my research interest is related to the following topics:

- Development of lidar (Light Detection and Ranging)-based remote sensing techniques for monitoring atmospheric compounds and processes

- Aerosols hygroscopic properties and atmospheric modeling
- Water vapor mixing ratio and relative humidity estimation in the troposphere
- Characterization of the long-range transported aerosols
- Ambient gases detection using Fourier Transform Interferometers (FTIR)
- Design of inexpensive Fabry Perot Interferometer for visible and near infrared for land and ocean surface remote sensing applications.

The lidar-based remote sensing measurement techniques for the monitoring of climate change parameters were implemented at the City College of the City University of New York (CCNY/CUNY) LIDAR station and are presented in the second section of the paper. The geographical location of the CCNY lidar station is 40.86N, -73.86W.

Among the lidar retrievals one important application is the detection of water vapor in the atmosphere. Water vapor is an important greenhouse gas due to its high concentration in the atmosphere (parts per thousand), among the trace constituents, and its interaction with tropospheric aerosols particles. The upward convection of water vapor and aerosols due to intense heating of the ground lead to aggregation of water particles or ice on aerosols in the air forming different types of clouds at various altitudes. In this regard a reliable method of retrieving atmospheric water vapor profiles is presented in the third part of the paper. The proposed technique here is the Raman lidar procedure that is calibrated afterwards. The accuracy of the water vapor measurements is obtained by calibration techniques based on different techniques that were compared and validated. The calibration method is based on data fusion from different sources like: GPS (global positioning system) sunphotometer, radiosonde.

The condensation of water vapor on aerosols is affecting their size, shape, refractive index and chemical composition. The warming or cooling effect of the clouds hence formed are both possible depending on the cloud location, cover, composition and structure. The effect of these clouds on radiative global forcing and therefore on the short and long term global climate is of high interest in the scientific world. In an effort to understand the hygroscopic properties of aerosols, a major interest is manifested in obtaining accurate vertical water vapor profiles simultaneously with aerosol extinction and backscatter profiles. A reliable method of retrieving atmospheric water vapor profiles and aerosols backscatter and extinction in the same atmospheric volume is presented in the fourth chapter of the paper.

As mentioned above the determination of greenhouse gases and other molecular pollutants is important in process control as well as environmental monitoring. Since many molecular vibrational modes are in the infrared, molecules can absorb light from an infrared source (such as the sun or an artificial source such as a glow rod) and therefore, if the source spectrum is known, the absorption spectra of the sample can be measured. Therefore, any spectroscopy method needs a well characterized infrared source as well as an accurate high resolution spectrometer.

In the fifth chapter of the paper is presented a standard technique for open-path detection of greenhouse gases which is based on Fourier Transform Infrared Spectroscopy (FTIR). A MIDAC open path FTIR instrument is presented along with measurements and analyses.

In the group of spectrometers with a high spatial spectral resolution is found as well the Fabry Perot Interferometer that is presented in chapter 6. A visible-near infrared (VIS-

NIR) scanning Fabry Perot Imager design is proposed based on combinations of Fabry Perot etalons and/or broadband interference filters that can in principle be used as a hyperspectral sensors from geostationary spaceborne platforms.

**KEYWORDS:**

Lidar, Raman, Mie, water vapor mixing ratio, backscatter, extinction, relative humidity, aerosol hygroscopic properties, atmospheric model, FTIR, FPI, green house gases

## Aknowledgements

I want to express my grateful thanks to Prof. Fred Moshary and Prof. Barry Gross who made possible this work. I want to thank them for their patience and constant guidance over the years (Spring 2002 - Spring 2008) spent within the Optics and Remote Sensing Laboratory at CCNY.

I also want to thank the committee members Prof. Samir Ahmed, Dr. Yonghua Wu, and Dr. Michael R. Hardesty for their helpful suggestions and review of my work.

The research presented here, and in a general way the results obtained during my CCNY lifetime were not possible without a strong collaboration, joint help, critical discussions, scientific confrontations, participation to many measurement field campaigns and data interpretation with the Environmental Research Station team at CCNY and Princeton. I am confident that all the roofist and the fieldist will always remember those hot summer hours on the CCNY roof or the Princeton measurement field (the winters were not less memorable). Therefore I want to thank Yonghua Wu, Ben Herman, Tom Legbandt, Shuki Chaw, Jing Zhou, Albin Zhang, Min Min Oo, Leona Charles, Miquel Bustamante, Paul (Australia), Cheun Meei Gan, Diomaris Padilla, Richard Peterson; and Princeton : Mary Lynn, Jim Smith, June Yeung, Yan Zhang for all the hours spent together and the stimulating discussions.

I thank my husband Marius Constantin for supporting, understanding and helping all the way.

I want to thank my parents and grandparents for raising me in the love of science. I will always cherish the evenings spent with my dad solving math and physics problems, unraveling the mystery beyond the real life phenomena. I express my gratitude to my mother who gave me strength and power through all the hard times in my life and literally stood there by my side and took over all my responsibilities as a mother during the 6 years of research. A big thank you to my sister, Petronela, entire family and friends who understood my dedication to this work during all these years.

*“I express my humble gratitude to God for the force, the courage and the necessary health to start, to continue and to finish this work”*

## TABLE OF CONTENTS

<b>Chapter I Introduction</b>	1
<b>Chapter II Lidar methodology and the CCNY multiwavelength lidar system design</b>	11
1. Introduction	12
1.1 Atmospheric research at the CCNY station	12
1.2 Basics of the lidar techniques	16
2. LIDAR related light atmosphere interaction processes	20
2.1 Elastic-Rayleigh scattering	22
2.2 Elastic-Mie scattering	25
2.3 Raman (inelastic scattering)	29
2.4 Optical parameters of atmospheric particles	37
3. CCNY multiwavelength lidar system	
3.1 Instrumentation diagram	42
3.2 Typical profiles	51
4. Conclusions and References	53
<b>Chapter III Water vapor retrieval based on Raman lidar technique</b>	56
1. Introduction	57
1.1 Climate impacts of atmospheric water vapor	58
1.2 Water vapor measurement techniques	62
2. Raman lidar water vapor measurement methodology	66
3. Calibration and validation	70
3.1 Data fusion	70

3.2 GPS/ sunhpotometer and radiosonde based calibration technique	70
3.3 Validation of measurements	75
3.3.1 Daytime water vapor measurements	75
3.3.2 Nighttime water vapor measurements	77
4. Conclusions and references	84
<b>Chapter IV Aerosol hygroscopic properties</b>	<b>88</b>
1. Introduction	89
1.1 Basics of the aerosol hygroscopic properties	90
2. Mathematical modeling relating optical scattering coefficients to the hygroscopic properties of aerosols	101
2.1 Analyses and results	105
2.2 Comparison of lidar measurements to existing models	110
3. Sensitivity of optical scattering coefficients to the hygroscopic properties of aerosols	111
3.1 Multiwavelength inversion of hygroscopic models and dry state radii	113
4. Conclusions and References	117
<b>Chapter V Atmospheric gases concentrations using Fourier Transform Interferometer measurements</b>	<b>120</b>
1. Introduction	122
1.1 Spectroscopic properties of atmospheric gases	122
2. Basics of the FTIR technique	134
2.1 Interference and Autocorrelation	134
2.2 Michelson interferometer	139
2.3 Open path FTIR	144

2.4 MIDAC M2401FTIR characteristics	146
3 Results and discussions	152
3.1 Retrieval algorithm	152
3.2 Results	156
4. Conclusions and References	160
<b>Chapter VI High Spatial Spectral Resolution VIS-NIR Scanning Fabry Perot Imager for Geostationary spaceborne applications</b>	162
1. Introduction	163
1.1 Theoretical considerations of Fabry Perot etalons	163
2. System components	169
2.1 Optical design	170
3 Spatial-spectral response and beam misalignment of Fabry Perot Etalons	177
4. Fabry Perot System Configuration	187
4.1 Single cavity Fabry Perot Interferometer in series with a passband filter	187
4.2 Multucavity Fabry Perot Interferometer Design	190
5. Signal Processing	195
5.1 Signal Processing	195
5.2 Temporal behavior of the system	197
5.3 Spectral Response budget	197
6. Conclusions and References	198

## List of Tables

Table 2.1	Usual lidar ratios in visible	38
Table 2.2	Technical specifications of the transmitter	44
Table 2.3	Lidar measured powers	45
Table 2.4	Specifications of the Mie-Raman lidar system at CCNY	51
Table 3.1	Comparison of surface relative humidity as retrieved by hygrometer and lidar	84
Table 4.1	Individual channels uncertainties	114
Table 5.1	Technical data of the FTIR system	149
Table 5.2	Retrieved atmospheric gases concentrations	160
Table 6.1	Preliminary Instrument/ System Specification	174

## List of Figures

Fig 1.1	Air pollutants affect climate by absorbing or scattering radiation	3
Fig 1.2	Global mean radiative forcing of the climate system	4
Fig 2.1	City College weather station located on the roof of the Marshak Science Building	13
Fig 2.2	Size parameter $\zeta$ as a function of wavelength of the incident radiation and particle radius $r$	21
Fig 2.3	Schematic of the incident and scattered light waves	23
Fig 2.4	Induced dipole moment	29
Fig 2.5	Three normal vibrational modes of the water vapor molecule	33
Fig 2.6	Energy levels diagrams and the correspondent Raman spectra for diatomic molecule	34
Fig 2.7	Raman frequency shifts of Q branch of the atmospheric molecules	36
Fig 2.8	a) Schematic of the multi-wavelength Raman lidar installed at the CCNY station. b) Image of the lidar beam launched from the optics and remote sensing lab at CCNY	43
Fig 2.9	Glan Prism design	45
Fig 2.10	a) Schematic of the optical set-up of the receiver, b) Optical set up of the detectors	47
Fig 2.11	Transmission of interference filters	47
Fig 2.12	Receiver components	48
Fig 2.13	Input (power supply) and Output (LICEL) of the receiver optical detectors	50
Fig 2.14	Vertical profiles of 4 different channels measured above CCNY station using a 60 min average at 12:21pm on 12 <sup>th</sup> of August 2006	52
Fig 2.15	Lidar image and vertical profile measured at CCNY station over the day of Sept 7th, 2006	53
Fig 3.1	Illustration of the central role of OH radical in the oxidation of tropospheric trace gases	60
Fig 3.2	Measured water vapor mixing ratio and fraction of it below 2km, 3km	71

	and 4km, above Brookhaven National Laboratory (BNL), during 2007	
Fig 3.3	a)Water vapor as fraction from the total column integrated water vapor in the atmosphere , b)Fractional error(standard deviation/mean) by month, c) Water vapor mixing ratio fraction versus total column d) Error of water vapor amount between CCNY at 12pm and BNL at 8pm (radiosonde evening launching time) stations at below 2km e) Error of water vapor amount between CCNY at 8pm and BNL at 8pm (radiosonde evening launching time) stations at below 2km	73
Fig 3.4	GPS-Aeronet intercomparison with 10 percent error bars	74
Fig 3.5	Frequency distribution of the aeronet percentage error with respect to GPS measurements	74
Fig 3.6	Water vapor mixing ratio profile measured by the CCNY lidar and radiosondes at the BNL station at 11:48am, 09/07/06	75
Fig. 3.7	Relative humidity retrieved on different days at morning time around 11:30am	76
Fig 3.8	Lidar, radiosonde and WRF (weather research and forecasting model )	77
Fig 3.9	.Lidar image on a)October 31 <sup>st</sup> 2006 between 12pm and 6 pm and on b) May23 between 6:15pm until 12:50am on May24,2007	78
Fig 3.10	Backward trajectories plotted for October 31 <sup>st</sup> , 2006 at 8pm	79
Fig 3.11	a) Night time vertical profiles of the five lidar returns in the Analog to digital mode and Photon Counting mode respectively (October 31, 2006), b) A/D and PC Raman lidar returns at 8:46pm on May 23 <sup>rd</sup> , 2007	80
Fig. 3.12	Water vapor mixing ratio measured in the photon counting mode and calibrated by the above detailed methodWater vapor mixing ratio vertical profile obtained from an average of 60 lidar files collected before 8:46pm on May 23 <sup>rd</sup> , 2007	81
Fig 3.13	Lidar images and relative humidity profiles retrieved on a) September 25 <sup>th</sup> , 2006 and b) April 25 <sup>th</sup> , 2007	82
Fig 3.14	Temperature and dew point temperature profiles measured above CCNY and BNL on a)09/25/06 at 1pm at CCNY and 8am at BNL;	83

	b)04/25/07 at 4pm at CCNY and 8am at BNL	
Fig 4.1	Radiation forcing of atmospheric aerosols and their impact on precipitation	91
Fig 4.2	Lidar images on a) September 26 <sup>th</sup> , 2006 and b) May 25 <sup>th</sup> , 2007 indicating a clear residual layer from the anterior day	99
Fig. 4.3	Growth factor for the 6 atmospheric models with a dry radii of 0.2 $\mu$ m	103
Fig 4.4	Normalized (wet to dry) ratios a) backscatter (355) /extinction (355) b) backscatter (355) / backscatter (1064)	105
Fig 4.5	a)Lidar image at the 1064nm and b). Relative humidity vs. altitude on Sept 25 <sup>th</sup> , 2006 at 12:35pm	106
Fig 4.6	a) RH vs Pressure based on hypsometric eqn. b) Pressure vs Altitude scale	107
Fig 4.7	Lidar retrieved water vapor mixing ratio	107
Fig 4.8	Aerosol backscatter ratio 355nm/1064nm vs. RH	107
Fig. 4.9	Aeronet retrievals for hygroscopic aerosols a) PSD showing accumulation mode b) low albedo	108
Fig. 4.10	Normalized color ratio(355 nm to 1064 nm) for six atmospheric models (left) and normalized lidar ratio (right) for six atmospheric models and radii from 0.2 to 1 $\mu$ m	110
Fig. 4.11	Normalized aerosol backscatter ratio of the 355nm and 1064nm lidar returns on a) Sept 25 <sup>th</sup> ,2006, b) April 25 <sup>th</sup> ,2007	112
Fig. 4.12	a)Probability metric as a function of the ratio of normalized backscatter at 1064nm to normalized backscatter at 355nm for different atmospheric states (model and radii) at 80% and 95% RH, b) probability metric as a function of the ratio of normalized backscatter at 355 to normalized extinction at 355nm for different atmospheric states (model and radii) at 80% and 95% relative humidity.	115
Fig. 4.13	Probability metric as a function of lidar and color ratio at 80% and 95% relative humidity	116
Fig. 4.14	Fractional improvement using four constraints	116
Fig 5.1	Electromagnetic(EM)-spectrum and types of interactions with EM-	123

	radiation	
Fig 5.2	a)Electron cloud oscillations during optical transitions in an atom. The emitted radiation follows a very similar pattern, b) Electric field patterns of a classically oscillating dipole. Electromagnetic radiation is emitted. The atomic dipole shown above exhibits exactly the same pattern.	123
Fig. 5.3	The normal modes of vibration of the a) H <sub>2</sub> O and b) of CO <sub>2</sub> and the energy levels of each mode	125
Fig 5.4	Radiation transmitted by the atmosphere	127
Fig 5.5	Infrared spectrum of humid air.	128
Fig 5.6	Schematic illustration of infrared spectroscopy	132
Fig 5.7	Plane parallel atmosphere and the relationship between slant and vertical paths.	134
Fig 5.8	a) Michelson Interferometer, b)Linear equivalent of the optical path; c) moving mirror tilted at an angle $\theta$	141
Fig 5.9	Bistatic and monostatic FTIR configurations	146
Fig 5.10	FTIR instrument in Bistatic mode, the IR source is placed at the opposite end of the optical path	147
Fig 5.11	Plume concentration in the FTIR field of view	147
Fig 5.12	a)Spectroscopic field measurements with the open path bistatic MIDAC FTIR system. b) MIDAC M2401-C open-path FTIR instrument c)Illuminator (Spectrometer) without telescope	148
Fig 5.13	Two of the possible causes of misalignment a) source is tilted with respect to the detector,b) source is off the main field of view axis	149
Fig 5.14	Peak to peak volts on the left and data points on the right obtained during correct alignments displayed by the AutoQuant Pro (AQ) Software	150
Fig 5.15	Interferogram (bottom) measured with the MIDAC M2401-C FTIR system and Fourier transformed by the AQ software into the IR spectrum (top)	151
Fig 5.16	Baseline corrected absorption spectrum retrieved by the AQ software	151

Fig 5.17	Spectrum overlaid with background spectra. a) standard processing b) custom background	153
Fig. 5.18	Absorbance spectra calculated using the standard processing and the custom background processing	153
Fig 5.19	Convolved methane line to test instrument width. a) overlaid spectra with different widths b) residuals as function of width.	154
Fig. 5.20	Spectral microwindow with 2 ambient absorption features and all other features contribute < 0.1%	157
Fig 5.21	Comparison of mid IR spectrum measured at two different locations	158
Fig 5.22	Match-ups based on least square fitting (LSQ) of theoretical spectra and experimental spectra for 4 different micro-windows at CCNY station on April 22 <sup>nd</sup> , 2003	158
Fig 5.23	Match-ups based on least square fitting (LSQ) of theoretical spectra and experimental spectra for 4 different micro-windows at Princeton University on October 5 <sup>th</sup> , 2007	159
Fig 6.1	Reflection and transmission of a beam incident at an angle $\theta_i$ on a FP etalon of with a distance between plates of d	165
Fig 6.2	Schmidt Cassegrain telescope back focal length(bfl) and secondary mirror diameter for different focal lengths of primary and secondary mirrors	171
Fig 6.3	Schematic of the Schmidt Cassegrain Telescope design	172
Fig 6.4	Optical set up of the Fabry Perot Interferometer	173
Fig 6.5	Required exposure time across the spectrum for an SNR=100 assuming an optically thick aerosol layer covering a typical deep ocean signal	177
Fig 6.6	Imaging angles and light vector	179
Fig 6.7	Plane FP cavity transfer function	180
Fig 6.8	Fabry Perot Transfer Function contour representation	182
Fig 6.9	Spatial Spectral 99% power contours signifying response of a FP filter for different plate separation to beam radii ratios $1/2 \geq L/a \geq 1/20$	185

Fig 6.10	Beam misalignment	186
Fig 6.11	Frequency detuning versus x(or y) axis for angle misalignment varied from $0 \leq \theta \leq .1$ for a ratio $L/a=1/20$	186
Fig 6.12	Imperfect cavity design	187
Fig 6.13	a)Spectral response of a single FP etalon. The diagonals represent multiple resonances occuring with the same intensity b)Resonance Boundaries of FP	188
Fig 6.14	Schematic of the optical train containing single Fabry Perot Interferometer	190
Fig 6.15	a) Filter stage resonance order for each passband and b) Filter stage length range for each passband	190
Fig 6.16	Three-etalon series configuration. The transmission between consecutive cavities is denoted by $t$ , the etalons reflectivities are denoted by $R_j$ and the input spectrum by $E_{in}$ . The transmission of each cavity is represented by $T_j$	191
Fig 6.17	Single cavity etalon transmissions for three different spacings (uncoupled cavities) b) Transmissions of 2 respectively 3 cavities etalons.	193
Fig 6.20	a)Spectral response of a dual etalon system and b) Triple etalon system	194
Fig 6.22	Detected and retrieved water leaving radiance	196

## Chapter I

### Introduction

The atmosphere is a colloid where the gas is the dispersed medium and the particles are dispersed phase. The particles consist of solid and liquid phases and undergo multiple changes during their stay in atmosphere. The reasons of these changes are chemical reactions within the particles and of particles with gases, coagulation of particles and alterations of relative humidity is believed to have the smallest time constant in most cases. Following the basic classification in the literature, a distinction can be made between primary sources and secondary source and consequently between primary and secondary mechanisms.

Primary aerosols are solid or liquid particles that are ejected directly into the atmosphere. Primary aerosols are pre-formed by processes occurring on land or water. The processes may be natural or anthropogenic. The primary, or direct, sources of particulate matter are mostly of natural origin, including meteorites(extraterrestrial or interplanetary), the world oceans(sea-salt), arid and semiarid regions(soil dust), terrestrial material (volcanic debris), and terrestrial biota (biological material).

Secondary aerosols are solid or liquid particles that are created in the atmosphere after chemical or physical transformations of *precursor* gases. The precursor gases become particles by phase changes (condensation from gas to liquid), adsorption onto pre-existing particles, chemical reactions with other gases that produce particles, and absorption into water droplets. The secondary, or indirect, sources are the atmospheric layers, in which complex chemical reactions take place and convert the available natural and man-made atmospheric trace gases into solid and liquid particles. This phase

transition is called Gas to Particle Conversion (GPC) and the resulting particle size is generally below  $0.1\mu\text{m}$ .

Two types of GPC are recognized, *homogeneous nucleation* and *heterogeneous nucleation*. *Homogeneous* nucleation takes place when *brand new* particles are produced by condensation of precursor gases. This process generally requires that the involved gas vapors occur at a supersaturation of several hundred % in the air space. Hydrocarbons are an exception; they may change from the gas to liquid phase even in unsaturated conditions. *Heterogeneous* nucleation takes place when gas molecules condense onto pre-existing solid or liquid particles. Only minor supersaturation of gases required for this pathway to occur (a few % of supersaturation) [1].

In general, aerosols influence the climate via two ways: the direct effect by scattering and absorbing incoming solar radiation, and the indirect effect by acting as cloud condensation nuclei (CCN) and/or ice nuclei (IN), which modify the microphysics, radiative properties and lifetime of clouds. The direct effect from scattering by non absorbing aerosols such as particulate sulfate cools the Earth system (so-called the whitehouse effect, as opposed to the greenhouse effect by  $\text{CO}_2$ ,  $\text{CH}_4$ ,  $\text{N}_2\text{O}$ , etc) [2-4]. Absorption by aerosols such as black carbon and mineral dust, on the other hand, warm the earth by heating the atmosphere. This heating, in turn, can hinder the condensation and flatten the temperature gradient, which damps the convection and draws less water into the atmosphere, leading to a loss of cloud cover, a decrease in cloud albedo, and a further warming of the Earth system. This tendency to warm the Earth by “cloud burning” from aerosol absorption is called the "semi-direct effect" [5]. The aerosol indirect effect is also split into two components: the 1st type indirect effect, in which an

increase in aerosols leads to an increase in the cloud droplet concentration and a decrease in cloud droplet size, and, as a result, an increase in cloud albedo (also termed as “cloud albedo effect”) [6]; and the 2<sup>nd</sup> indirect effect, where the aforementioned reduction in cloud droplet size also tends to lower the precipitation efficiency, and increase the liquid water content, thereby the increasing cloud lifetime (also termed as “cloud lifetime effect”) [7] and cloud thickness [6].

A schematic representation of these effects is presented in figure 1.1

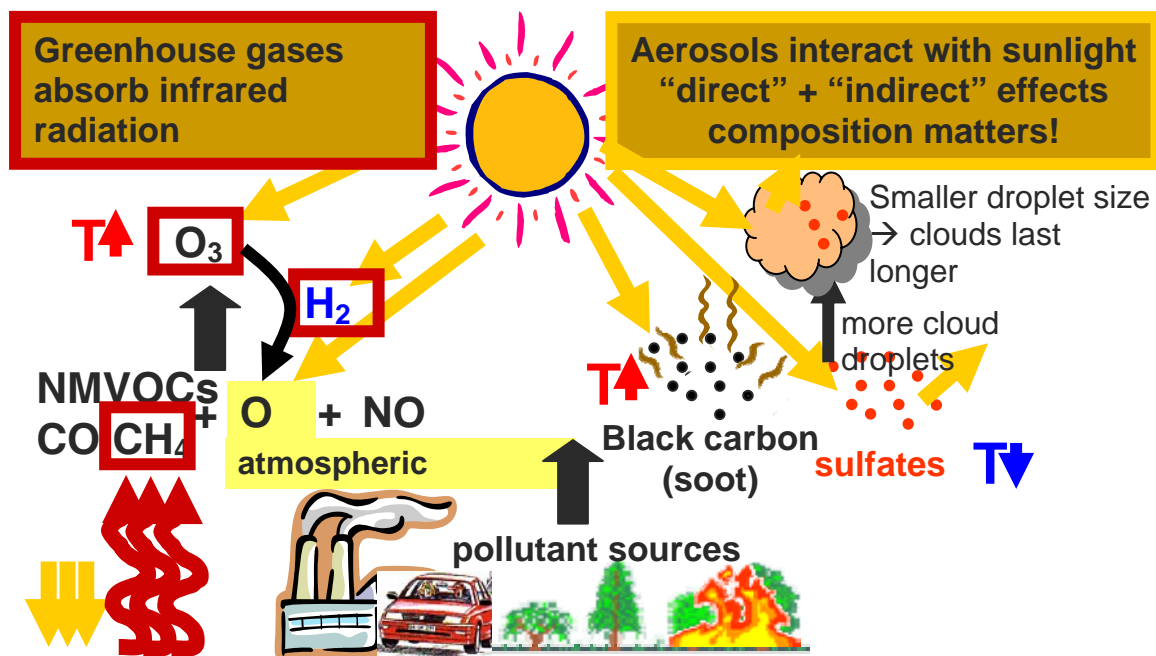


Fig 1.1 Air pollutants affect climate by absorbing or scattering radiation

Therefore, both direct and indirect effects tend to reduce the amount of solar radiation reaching to the Earth’s surface, while the semi-direct effect also increases solar heating in the atmospheric column. However, the magnitude of the indirect effect is far more uncertain than that of the direct effect [8]. In addition to aerosols’ impact on temperature, the direct and indirect effects can also affect the precipitation. This is more apparent in

the case of the indirect and semi-direct effects, which alter the cloud properties. These in turn can alter the atmospheric stability, possibly leading to modifications in precipitation patterns induced by convection and monsoonal circulations [9-12]. A global mean of the radiative forcing of the climate system by the different atmospheric constituents is presented in figure 1.2

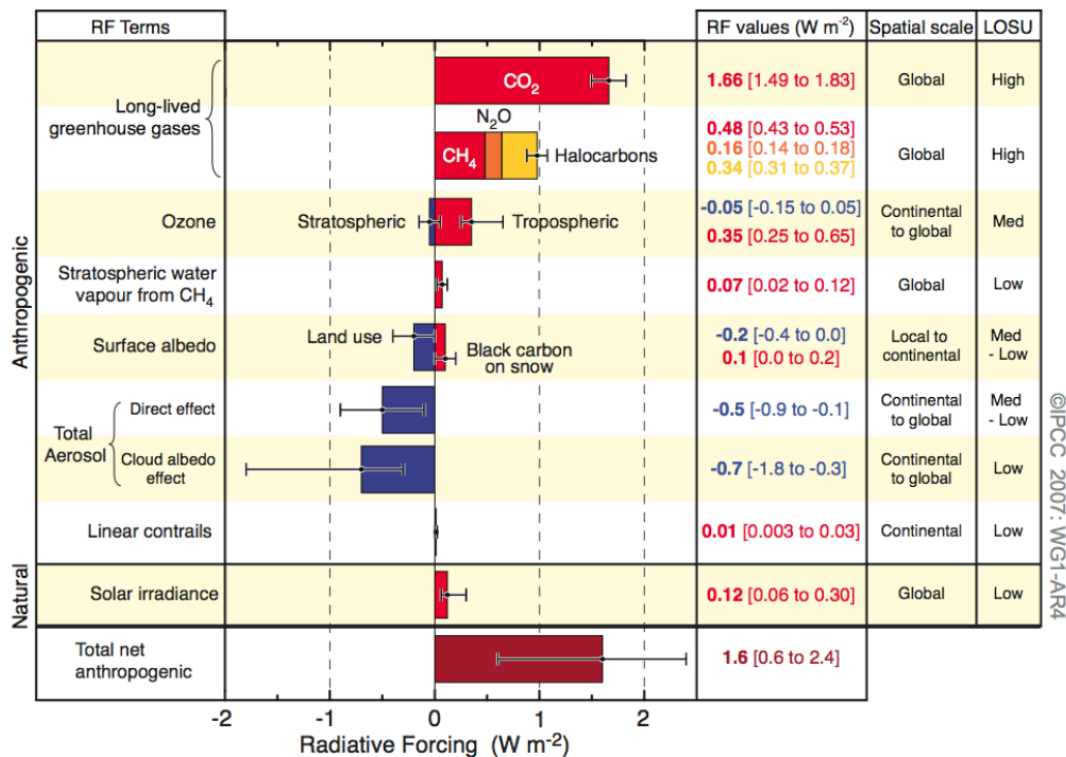


Figure 1.2 Global mean radiative forcing of the climate system

The reduction in surface solar radiation by aerosol direct and indirect effects also likely modify the hydrological cycle through the surface energy budget alteration and subsequent reduction in evaporation to the extent that it can spin down the water cycle [13]. Moreover, aerosols can affect the environment in a variety of different ways. Fine particles may adversely affect human health, especially in regard to cardio-vascular illnesses [14] and reduce visibility by their scattering and absorption of radiation [15-16].

Concerns about the impact on visibility and human health have led to proposals to reduce the concentration of fine particles through regulations and emission control in the United States (US EPA, 1996), and China (China SEPA, 2003), etc. (Due to the heavy air pollution in China, the regulatory standard for ambient air quality of PM<sub>10</sub> (the aerosol particles with diameter less than 10  $\mu\text{m}$ ) from China SEPA is higher - $250\mu\text{g}/\text{m}^3$ - than that from U.S. EPA.- $150\mu\text{g}/\text{m}^3$ ) [17]. Aerosols can also affect photosynthesis and Carbon-uptake rates of ecosystems subject to large aerosol loadings by perturbing leaf temperatures and the amount of photosynthetic active radiation (PAR) available to green plants [18]. In addition, sulfate and nitrate are the primary causes of acid rain, which affects large industrial regions over the world [19].

Considering the above and the importance of atmospheric constituents monitoring, the paper presents several measurement techniques of properties and concentrations of different atmospheric aerosols and gases. In this regard the second part of this paper is describing the CCNY multiwavelength lidar system. The lidar scheme is based on a laser emission at 355nm, 532nm and 1064nm and on the consequent detection of both elastic (Mie) and inelastic (Raman) atmospheric backscatter light. Thus the backscatter radiation is collected at the elastic radiation 355nm, 532nm, 1064nm and the rotational-vibrational Raman radiation for nitrogen (387nm) and water vapor (407nm).

In view of the water vapor significance for Earth's climate and the methods of measuring it, the third part of the paper presents water vapor measurement methodology based on Raman lidar retrievals and then discusses and compares a set of two calibration techniques of the multiwavelength Raman lidar at the 407nm. The calibration algorithms are using data fusion from three different sources: day and night Raman Lidar

measurements, CIMEL sunphotometer and radiosonde data from the OKX station (Brookhaven laboratory) in New York State (NYS), to estimate the correct calibration constant and the corresponding technique. The water vapor mixing ratio measured by the City College of New York (CCNY) Raman lidar is then validated with GPS-MET (global positioning meteorological system) sources collocated with the CCNY lidar system or located in the proximity of the CCNY station and NOAA meteorological predicted profiles. The results of our calibrations are then presented to illustrate both short term and long term stability capabilities.

Since the lidar returns offer high spatial resolution of the vertical profile of both water vapor and aerosols in the same atmospheric volume chapter four is proposing to investigate the aerosols hygroscopic properties and presents a hygroscopic model that returns the optical properties of hygroscopic aerosols along with the ability of identifying unknown atmospheric states that are being explored. It is shown here the relationship between aerosol backscattering and relative humidity and the possibility to identify the different types of aerosol sources based on their hygroscopic behavior.

In previous work, simultaneous measurements of relative humidity (RH) with backscatter measurements from a surface nephelometer were used to probe the hygroscopic properties of aerosols. However, most of these measurements were not able to probe the high RH domain since such high RH is difficult to control. For this reason, experiments using a 355nm Raman water vapor and aerosol lidar at the Atmospheric Radiation Measurements (ARM) site were used. The measurements were capable of providing simultaneous backscatter and RH profiles, and performing the experiments under low altitude cloud decks insured stable well mixed layers as well as probing RH

profiles to above 95%. The later is required for the differentiation of different aerosol hygroscopic models. The proposed research here is to use the water vapor and aerosol backscatter measurements to explore the nature and variability of urban aerosol hygroscopic properties using multi-wavelength Raman lidar measurements at 355nm, as well as backscatter measurements at 532nm and 1064nm. The addition of the longer wavelength channels allows us to more accurately validate the homogeneity of the aerosol layer as well as provide additional multi wavelength information that can be used to validate and modify the aerosol models underlying the hygroscopic trends observed in the Raman Channel. In particular, we show that aerosols backtracked to different sources (bio-mass, maritime due to sea breeze) have different hygroscopic behavior which are compared to theoretical models.

As shown above the atmospheric trace gases are another important contributor to the radiative forcing of climate. Therefore chapter 5 is presenting a FTIR system designed to measure different gases concentration in the atmosphere. Unlike a diffraction grating based spectrometer which directs different frequencies to different detectors (pixels), the interference spectrometer generates an interferogram that is then Fourier Transformed to obtain spectra. The finite sampling of the FFT results in an instrument resolution function which needs to be taken into account when resolving sharp absorption features. Thus, the absorption spectra seen by the instrument is a convolution of the spectral line shape and the instrument response.

In the sixth chapter of the paper a scanning Fabry Perot Imager is designed for geostationary spaceborne applications. The instrument is a high spectral resolution spectrometer designated to detect radiation in the VIS-NIR range. In a single stage etalon

design, a number of interference filters are required that can be rotated in front of the etalon to eliminate overlapping orders. A procedure is developed to optimize the number and bandwidth of filters for a given Fabry Perot cavity length and spectral coverage requirements. An alternate approach utilizing multiple etalons in a cascade geometry is also investigated as a means to achieve both high spectral resolution and large free spectral range required for the proposed application. It is shown that the S/N can be made sufficiently large with only moderate decoupling of the etalon cavities. In addition, preliminary studies of the affects of cavity misalignment for both single etalons and multiple etalons are carried.

*References*

- [1] G. A. d'Almeida, P. Koepke, E.P. Shettle, *Atmospheric Aerosols. Global Climatology and Radiative Characteristics*, A. Deepak Publishing, Virginia, United States 1991
- [2] Robert J. Charlson, Francisco P. J. Valero, John H. Seinfeld, *In Search of Balance*, Science, Vol. 308. no. 5723, pp. 806 – 8076, 6 May 2005:
- [3] Charlson, R.J., S.E. Schwartz, J.M. Hales, R.D. Cess, J.A. Coakley, Jr., J.E. Hansen, and D.J. Hoffman, *Climate forcing by anthropogenic aerosols*,. Science, 255, 423-430, 1992.
- [4] S. E. Schwartz, *Uncertainty in Climate Change caused by Aerosols*, Science, Vol. 272, 24 May 1996
- [5] Yan Huang, *Assessments of the Direct and Indirect Effects of Anthropogenic Aerosols on Regional Precipitation over East Asia Using a Coupled Regional Climate-Chemistry-Aerosol Model*, Georgia Institute of Technology, 2005
- [6] Twomey S., *The influence of pollution on the shortwave albedo of clouds*, Journal of the Atmospheric Sciences, Vol 34. Issue 7, 1149–1152, July 1997
- [7] Albrecht B.A., *Aerosols, cloud microphysics and fractional cloudiness*, Science, 245, 1227-1230
- [8] S. E. Schwartz, Andreae M.O, *Uncertainty in Climate Change caused by Aerosols*, Science, Vol. 272, 24 May 1996
- [9] V. Ramanathan, P. J. Crutzen, J. T. Kiehl, D. Rosenfeld, *Aerosols, Climate, and the Hydrological Cycle*, Science, 294, 2119, 7 December 2001

- [10] Graf H.F., *The complex interaction of aerosols and clouds*, *Atm Science*, Vol 303, February 2004
- [11] Boucher et.al, Intercomparison of models representing direct shortwave radiative forcing by sulfate aerosols, *Journal of Geophysical Research*, 103, 16979-16998, July 1998
- [12] S. E. Schwartz, *Intercomparison of Radiation Transfer Models Representing Direct Shortwave Forcing by Sulfate Aerosols*, *Atmospheric Radiation Measurement*,
- [13] Beate G. Liepert,<sup>1</sup> Johann Feichter,<sup>2</sup> Ulrike Lohmann,<sup>3</sup> and Erich Roeckner, *Can aerosols spin down the water cycle in a warmer and moister world?*, *Geophysical Research Letters*, Vol. 31, L06207, ( 2004)
- [14] Dockery D. W., Pope III C. A. , *Acute respiratory effects of particulate air pollution*, *Annu. Rev. Public. Health.* , 15, 107-132, 1994
- [15] Ball R.J., Robinson G. D., *The origin of haze in the central United States and its effect on solar irradiation*, *American Meteorological Society* , 1982
- [16] Husar R.B., Husar J.D., Martin Laurent, Distribution of continental surface aerosol extinction based on visual range data, *Atmospheric Environment*, 34, 5067-5078, 2000
- [17] David G. Streets-Air quality during the 2008 Beijing Olympic Games
- [19] Mauzerall D.L., Wang X., *Protecting Agricultural Crops from the effects of tropospheric ozone exposure: Reconciling Science and Standard Setting in the United States, Europe and Asia*, *Annu. Rev. Energy. Environ.* 26, 237-268, 2001
- [18] NAPAP, National Acid Precipitation Assessment Program Report to Congress, An Integrated Assessment, 2005

## Chapter II

### **Lidar methodology and the CCNY multiwavelength lidar system design**

In the last 6 years, environmental research at the CCNY has been focused on the atmosphere and ocean study. The reference global position of the atmospheric station instrument arrays is North Latitude  $40.81920857^\circ$ , West Longitude  $73.94904472^\circ$  and 98.365 m (322.637 ft) above mean sea level. The CCNY station is an outstanding research facility that is capable of monitoring many atmospheric parameters, including trace gases and aerosols as well as solar radiation. These measurements are obtained using techniques such as infrared spectroscopy, instruments for *in situ* determination of aerosol properties, sun photometer, GPS receivers, meteorological sensors, and many others. Since 2002, a multi-wavelength LIDAR system developed at CCNY has been installed. The goal of a lidar implementation at JFJ was to provide atmospheric profiles of aerosol-cirrus optical properties, water vapor mixing ratio and planetary boundary layer (PBL) properties with high temporal and spatial resolution.

This chapter briefly introduces the measurement techniques that exist at the station and explains the basic principles of the lidar technique. The fundamentals concerning the lidar methodology are reviewed. The latest configuration of the CCNY lidar system is described in detail. Finally, examples of typical LIDAR signals are illustrated.

## **1. Introduction**

### **1.1 Auxiliary measurements at CCNY**

New York City is the largest city in the United States, with its metropolitan area ranking among the largest urban areas in the world. New Yorkers (more than 8mil. people live in the city) are collectively responsible for one percent of the nation's total greenhouse gas emissions though comprising 2.7% of the nation's population [1]. As a coastal city, New York is particularly susceptible to the effects of global climate change and the need for understanding the processes of climate change and formulating appropriate policy to address the scientific findings is more and more necessary. Therefore the development of appropriate instrumentation for such an interesting and complex environment is crucial for the testing and validation of atmospheric models. The main instrumentation is being built around CCNY through funding from a variety of agencies including NOAA, NASA, NSF, etc.

#### *Weather station*

A picture of the NOAA-CREST weather station located on the roof of the Marshak Science Building at CCNY is shown in figure 2.1. The geographical coordinates of the station are North Latitude  $40.81920857^\circ$ , West Longitude  $73.94904472^\circ$  and 98.365 m (322.637 ft) above mean sea level [2].

The station's sensor array collects data that includes wind speed, direction and their vectors; air, dew point, wet bulb, heat index and wind chill temperatures; relative humidity; air pressure; rain; plant trans-evaporation and solar flux.

### *Radiation measurements*

To process lidar measurements, total atmospheric column measurements are needed. There are two instruments that serve this purpose.

A) The multifilter rotating -MFR-7 Shadowband Radiometer measures total, diffuse, and direct irradiance at six wavelengths (415, 500, 615, 673, 870, and 940 nm, each 10 nm FWHM). Daytime aerosol optical depth [6] and water vapor column [7] are routinely estimated using a 7 wavelength-band (UV-VIS-NIR) sun track photometer. The instrument directly measures the incoming solar energy (sky radiance) at selected wavelengths of 340, 380, 440, 670, 870, 1020 nm (aerosols), and 936 nm (water vapor) .

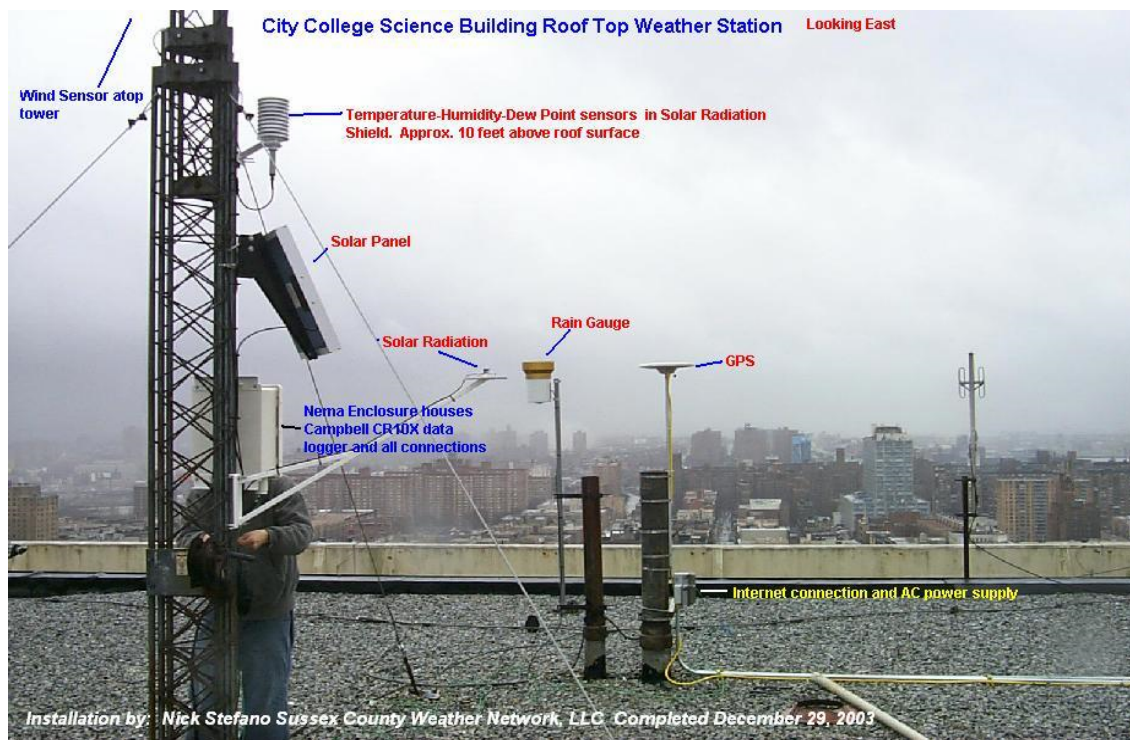


Figure 2.1 City College weather station located on the roof of the Marshak Science Building.

The direct spectral irradiance is measured, allowing a determination of the total column of several atmospheric constituents (like total column water vapor).

In addition, a new processing scheme is being implemented which makes combined use of the diffuse and direct beams to allow improved retrieval of aerosol properties.

B) The CIMEL Electronique 318A spectral radiometer is a solar-powered, weather-hardy, robotically-pointed sun and sky spectral sun photometer. A sensor head fitted with 25 cm collimators is attached to a 40 cm robot base which systematically points the sensor head at the sun according to a preprogrammed routine. The Cimel controller, batteries, and Vitel satellite transmission equipment are usually deployed in a weatherproof plastic case of 30 cm x 62 cm x 46 cm dimensions. The total weight of the Cimel sun photometer itself is approximately 15 kg, with an additional 22 kg contributed by the control box, battery, transmitter, the weatherproof case, and other materials. The radiometer makes two basic measurements, either direct sun or sky, both within several programmed sequences. The direct sun measurements are made in eight spectral bands requiring approximately 10 seconds. Eight interference filters at wavelengths of 340, 380, 440, 500, 670, 870, 940 and 1020 nm are located in a filter wheel which is rotated by a direct drive stepping motor. The 940 nm channel is used for column water abundance determination. A preprogrammed sequence of measurements is taken by these instruments starting at an air mass of 7 in the morning and ending at an air mass of 7 in the evening. Optical depth is calculated from spectral extinction of direct beam radiation at each wavelength based on the Beer-Bouguer Law. Attenuation due to Rayleigh scatter, and absorption by ozone, and gaseous pollutants is estimated and removed to isolate the aerosol optical depth (AOD). A sequence of three such measurements are taken 30 seconds apart creating a triplet observation per wavelength. During the large air mass periods direct sun measurements are made at 0.25 air mass intervals, while at smaller air

masses the interval between measurements is typically 15 minutes. The time variation of clouds is usually greater than that of aerosols causing an observable variation in the triplets that can be used to screen clouds in many cases. Additionally the 15-minute interval allows a longer temporal frequency check for cloud contamination.

In addition to the direct solar irradiance measurements that are made with a field of view of 1.2 degrees, these instruments measure the sky radiance in four spectral bands (440, 670, 870 and 1020 nm) along the solar principal plane (i.e., at constant azimuth angle, with varied scattering angles) up to nine times a day and along the solar almucantar (i.e., at constant elevation angle, with varied azimuth angles) up to six times a day. The approach is to acquire aureole and sky radiances observations through a large range of scattering angles from the sun through a constant aerosol profile to retrieve size distribution, phase function and aerosol optical depth. More than eight almucantar sequences are made daily at an optical air mass of 4, 3, 2 and 1.7 both morning and afternoon. Sky radiance measurements are inverted with the Dubovik and Nakajima inversions to provide aerosol properties of size distribution and phase function over the particle size range of 0.1 to 5  $\mu\text{m}$ .

*Precipitable water vapor (PWV):*

Again, two independent measurements of water vapor are available. A) The Trimble 5700 receiver and Trimble Zephyr GPS antenna located within the weather station instrument array continuously monitors the signal time delay from several geosynchronous satellites. These delay times are transmitted to NOAA and processed together with selected weather data from our site to derive a set of raw delay times. This

data set is then further interpreted in context of a larger time-managed spatial array of other sites' data to derive the moisture content in the air column over our site every 30 minutes. Time stamp is in UTC (GMT). B) The 935nm channel of the CIMEL allows us to obtain total water column. Comparisons of these two methods are shown in chapter 3 to agree within 10% and is more than suitable for calibration needs.

## **1.2 Basics of the lidar techniques**

It is within this larger measurement suite that the lidar system was installed and has operated since 2002 at the CCNY station. Data from this lidar system provides various atmospheric profiles with high spatial and temporal resolution. Profiles of the optical properties of aerosols, planetary boundary layer, clouds and troposphere water vapor mixing ratio are obtained on a regular basis. The combination of LIDAR observations with the existing measurements at the CCNY station provides a unique opportunity to conduct long-term inter-calibration and complementary or simultaneous monitoring of different atmospheric parameters over various space-time scales.

The LIDAR technique is based on the detection and analysis of backscatter light that results from the interaction of a laser beam with atmospheric constituents. Probing the atmosphere with a laser is similar to using radar, with the difference that the lidar uses electromagnetic radiation (light) from the optical domain instead of radio waves. The LIDAR technique is an active method because it uses an artificial light source for the retrieval of atmospheric parameters. This contrasts with passive methods, which use light emission from natural light sources (sun, moon) or thermal emission. A typical LIDAR system (see Figure 2.7) consists of a transmitter and a receiver. The transmitter emits

short-time laser pulses into the atmosphere. The laser emission is *specific* - it has a small spatial divergence light beam, and it is quasi-monochromatic and coherent - and it can emit very high power density, short time pulses (e.g. 475mJ at 532 nm, pulse width ~1-2 ns < 1064nm which is 8-12ns, laser repetition rate at 30 Hz). The laser beam interacts with the atmospheric constituents as it propagates through a multitude of phenomena such as elastic light scattering (molecular-Rayleigh, aerosols- Mie), and inelastic (molecular – Raman) light scattering, fluorescence and absorption. A receiving telescope collects a very small fraction of the backscattered light. In addition to the telescope, the receiver usually contains a polychromatic filter for the spectral separation, high sensitivity photodetectors, and fast sampling rate analog-to-digital converters. The magnitude of the received signal is proportional to the number density of the atmospheric scatterers (molecules or aerosols), their intrinsic properties (i.e. probability of interaction with the electromagnetic radiation at the laser wavelengths, called cross-section value) and with the laser incident energy. The detected light backscatter power  $P(z, \lambda)$  at the wavelength  $\lambda$  from a distance  $z$  can be expressed by the so-called lidar equation cf. Eq. (1) as follows:

$$P(\lambda_D, z) = P(\lambda_L, z_0) \cdot K_s(z) \cdot \frac{A_0}{z^2} \cdot \delta z \cdot \beta_{am}(\lambda_D, \lambda_L, z) \cdot T_{\rightarrow}(\lambda_L, z) \cdot T_{\leftarrow}(\lambda_D, z) \quad (1)$$

where  $P(\lambda_L, z_0)$  represents the mean power emitted by the laser source at wavelength  $\lambda_L$ .

Here,  $\lambda_D$  is the wavelength at which the backscattered radiation is detected by the lidar receiver. While radiation is usually detected at the laser wavelength ( $\lambda_L$ , elastic processes), it is also possible that a shift in wavelength will occur due to inelastic processes such as the Raman effect.  $K_s(z)$  is the instrument function that takes into account the transmitter and receiver efficiencies, the overlap function (the degree of

spatial recovering between the emitted beam and the receiver field of view).  $A_0$  is the effective receiver area (i.e. area of the telescope collector mirror) and  $\delta z$  is the spatial resolution expressed as:

$$\delta z = \frac{c(\tau_D + \tau_L + \tau_P)}{2} \quad (2)$$

where  $c$ [m/s] is the light speed,  $\tau_D$ [s] is the detection response time (i.e. digitizer and detector's response),  $\tau_L$ [s] is the laser pulse width, and  $\tau_P$  [s] is the optical interaction process lifetime. Generally the digitizer response time,  $\tau_D$ , (typically  $\sim 10^{-7}$ s) limits the spatial resolution (e.g.  $\sim$ tens of m or m). The CCNY lidar system uses Hamamatsu photomultiplier tubes R1527 with a response time of 25.4ns (anode pulse rise time 2.2ns, electron transit time 22ns, transit time spread 1.2ns). Both the laser pulse width,  $\tau_L$ [s] (typically  $\sim 8-12 \cdot 10^{-9}$  s), and the optical interaction lifetime  $\tau_P$  [s] (typically within  $\sim 10^{-9}-10^{-12}$  s) have negligible contributions. The altitude ( $z_i$ ) from which the light is scattered may be determined as:  $z_i = i \cdot \delta z$ , where  $i = 1$  to number of acquisition channels of the laser triggered analog to digital converter. For example with an acquisition sampling rate of 40MHz the pulse width is  $\tau = 1/40\text{MHz} = 2.5 \cdot 10^{-8}$  s which results in a spatial resolution of  $\delta z = c \cdot \tau / 2 = 3.75$  m resolution (per 1 bin). It is also crucial that the repetition rate be sufficiently slow to allow the echo to return without interference to the next pulse. In our case, a rep rate of 30 Hz is clearly more than sufficient to increase detection SNR. Suitable averaging of the shots is required in the CCNY lidar system the average is performed over 1800 files. This is particularly true for weak raman signals in daylight.

To complete the description of the lidar equation,  $T_{\rightarrow}$  is the atmospheric transmittance from the transmitter to the probed volume and  $T_{\leftarrow}$  is the atmospheric transmittance from the probed volume to the receiver, and they are calculated as follows:

$$T_{\rightarrow}(\lambda_L, z) = \exp\left(-\int_{z_0}^z \alpha_{atm}(\lambda_L, z) dz\right) \quad \text{and} \quad T_{\leftarrow}(\lambda_D, z) = \exp\left(-\int_z^{z_0} \alpha_{atm}(\lambda_D, z) dz\right)$$

where  $\alpha_{atm}(\lambda, z)$  is the atmospheric extinction coefficient and may be different on the two directions of the laser pulses, as is the case of the Raman backscatter radiation. The atmospheric backscattering coefficient,  $\beta_{atm}(\lambda, z)$ , is the key element of the lidar equation Eq. (1), and is proportional to the cross-section of the involved physical process  $\sigma_{atm}(\lambda_L, \lambda_D, z)$  and to the number density  $n(z)$  of the scatterers (i.e. atoms, molecules, particles, clouds) in the probed volume. The subscript “atm” encompasses all possible physical interactions within the atmosphere (like Mie scattering, molecular Rayleigh scattering, Raman scattering reflection, refraction, diffraction and fluorescence). In addition, since the scattering lengths of aerosols are sufficiently long, we are free to approximate the medium as single scattering. This is in contrast to lidar within clouds.

The  $(1/z^2)$  term in the lidar equation due to dependence of solid angle on range can be eliminated by a simple redefinition. This range corrected equation (i.e. Eq. (3)) reads as follows:

$$P_{RCS}(\lambda_D, z) = C_s(z) \cdot \beta_{atm}(\lambda_D, \lambda_L, z) \cdot T_{\rightarrow}(\lambda_L, z) \cdot T_{\leftarrow}(\lambda_D, z) \quad (3)$$

where  $P_{RCS}$  is the range corrected signal (i.e. detected signal multiplied by the square of the altitude) and  $C_s(z)$  is the instrument function.

Section 2 is devoted to a brief description of these light-atmosphere interaction processes upon which the lidar methodology used in this work is based. Section 3

includes a description of the latest configuration of the CCNY-LIDAR system (i.e. set-up and instrument specifications) and signal examples.

## **2. LIDAR related light-atmosphere interaction processes**

The description of the laser beam interaction with atmospheric constituents (i.e. molecules, particles, clouds) is based on the fundamental theory of electromagnetic wave propagation in various media. The atmosphere contains a wide range of constituents extending from atoms and molecules (Angstrom range  $d \sim 10^{-3}$ - $10^{-4}$   $\mu\text{m}$ ) to aerosols ( $d \sim 10^{-2}$ - $5$   $\mu\text{m}$ ), cloud water droplets and ice crystals ( $d \sim 1$ - $10^3$   $\mu\text{m}$  and even larger). The mixture of these different components results in a series of complex atmospheric interactions that take place with a laser beam. The intensity of the light resulting from these processes is proportional with the initial intensity  $I_0$ , the number density of the active diffusers  $n$  and the differential angular cross – section  $\sigma$ . If a quasi-parallel, monochromatic, coherent and linearly polarized light (i.e. a laser beam) is sent to the atmosphere, different processes may take place with different probabilities determined by their correspondent cross-sections,  $\sigma = f(\lambda, \text{process, atmospheric scatterer})$ . The interaction may lead to elastic (Rayleigh and Mie) and inelastic (Raman) scattering, absorption, reflection, and/or diffraction. Based on these processes, various spectroscopic and nonspectroscopic measurement techniques have been developed for monitoring the atmosphere [3]. The interactions may be “non-selective”, like Rayleigh, Mie or Raman scattering, and more or less important depending on the atmospheric composition (e.g. aerosol loading in the case of Mie scattering). Absorption, for example, is a selective process, and is dependent on the absorption cross section at the laser wavelength. The

resonant processes (Rayleigh or Raman) are also selective, meaning that the laser wavelength radiation matches specific electronic transitions of the molecule.

Two important microscopic scattering parameters, in addition to backscatter and extinction coefficients, are used to express aerosol-atmosphere interactions; the dimensionless size parameter ( $\zeta$ ), with  $\zeta = 2\pi r m / \lambda$  (where  $d$  is the geometric dimension of the diffuser), and the complex refractive index ( $m$ ) with  $m(\lambda) = n(\lambda) + i k(\lambda)$ . The real and the complex part of the refraction index provide information about non-absorbing and absorbing aerosol capacity. For  $\zeta \ll 1$ , Rayleigh or molecular scattering prevails; at  $\zeta \sim 1$ , Mie-aerosol scattering begins to increase in importance, and for  $\zeta \gg 1$ , scattering is purely geometric (e.g. reflection by clouds) as seen in fig 2.2.

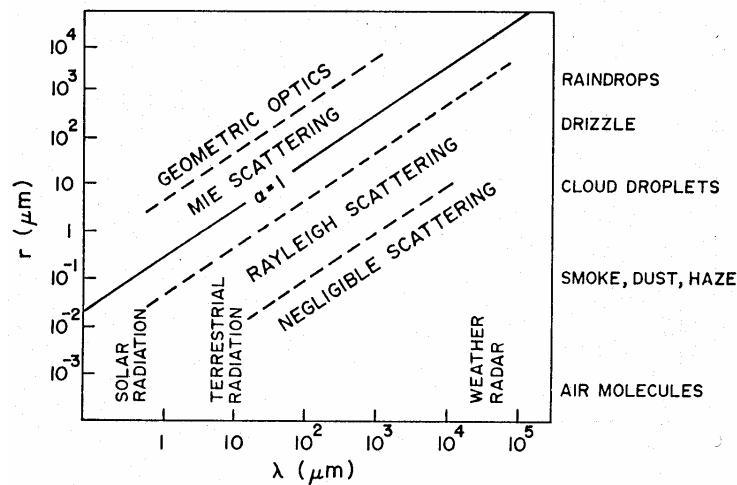


Figure 2.2. Size parameter  $\zeta$  as a function of wavelength of the incident radiation and particle radius  $r$

The molecular and aerosol elastic/inelastic processes involved in the use of the LIDAR methods presented in this paper are the retrieval of aerosol properties using elastic ( $\lambda_L = \lambda_R$ ) light scattering; i.e. Mie scattering ( $\lambda_L \sim d$ , where  $d$  is the diameter of the particle) and measurements of  $H_2O$  vapor in the atmosphere based on molecular

inelastic ( $\lambda_L$  different than  $\lambda_R$  light scattering; i.e. Raman scattering ( $\lambda_L \gg d$ , with  $d$  the molecular dimension))

## 2.1 Elastic-Rayleigh scattering

In the case of the elastic light scattering process, also called Rayleigh scattering, the atmospheric molecules scatter the incident radiation elastically (i.e.  $\lambda_D = \lambda_L$ ). The electromagnetic incident wave induces a dipolar moment  $P$  within the molecular system. The strength of the induced dipole moment is given by  $P = \alpha E$  where  $E$  is the intensity of the electric field of the incident electromagnetic wave and  $\alpha$  is the polarizability tensor of the molecule (explained in more detail in section 2.3 of this chapter). For the atmospheric diffusers, such as nitrogen and oxygen molecules,  $\alpha$  has a constant and isotropic component, which explains the re-emission of the radiation at the same frequency as the incident electromagnetic wave. For one incoming photon, one photon is re-emitted with the same energy. The elastic contribution always superposes itself on other non-elastic effects. If the excitation wavelength is much higher than the dimension of the atoms and molecules, the Rayleigh scattering condition is fulfilled. The Rayleigh backscatter is proportional to the diffusers' number density and to the Rayleigh differential cross section. The air differential (angular) Rayleigh cross-section,  $\frac{d\sigma_m}{d\Omega}$  [ $\text{cm}^2 \text{ molecule}^{-1} \text{sr}^{-1}$ ],

may be expressed as given by [4] and expressed by Eq. (4):

$$\frac{d\sigma_m(\phi, \theta, \lambda)}{d\Omega} = \frac{9\pi^2(m_{air}^2 - 2)}{\lambda^4 n_{air}^2 (m_{air}^2 + 2)^2} \left( \frac{6 + 3\rho}{6 - 7\rho} \right) \{ \cos^2 \phi \cdot \cos^2 \theta + \sin^2 \phi \} \quad (4)$$

where

- $\lambda$  [cm] is the wavelength,  $n_{\text{air}}$  is the air molecule number density and is equal to  $2.54743 \cdot 10^{19} \text{ cm}^{-3}$  [molecules  $\text{cm}^{-3}$ ],
- $m_{\text{air}}$  is the air complex refractive index. However, we may ignore in general any absorption resonances so the refractive index is real. In particular, the real part of the refractive index  $n(\lambda)$  is an empirical formula for the real refractive index for dry air at standard temperature and pressure (STP) at wavelengths greater than 230nm and given in [5] as:

$$n(\lambda) = 10^{-8} \left[ \frac{5791817}{238.0185 - (1/\lambda)^2} + \frac{167909}{57362 - (1/\lambda)^2} \right] + 1 \quad (5)$$

- $\phi$  [rad] is the polarization angle and  $\theta$  [rad] is the scattering angle (see Figure 2.3).

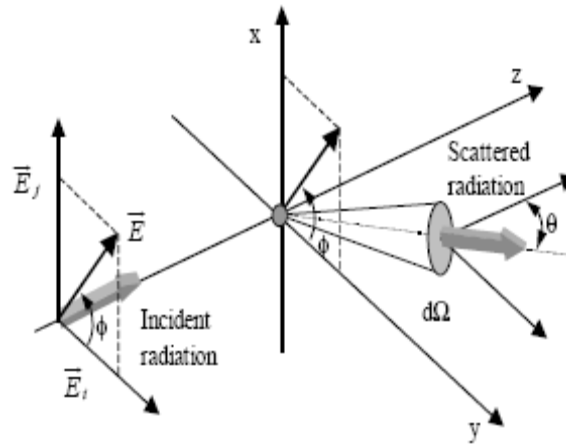


Figure 2.3 Schematic of the incident and scattered light waves

- The second term on the left side is the King factor given by equation (6) below

$$F_k(\lambda) = \frac{6 + 3\rho(\lambda)}{6 - 7\rho(\lambda)} \quad (6)$$

where  $\rho(\lambda)$  is the total (Raman plus Rayleigh) depolarization from a natural light source, the value of which ranges between 0.0357 and 0.0273 over the

wavelength interval 250-1000nm and is determined by the magnitudes of the parallel and perpendicular components of the dynamic polarizability,  $\alpha^{parallel}(\lambda)$  and  $\alpha^{perpendicular}(\lambda)$  as follows

$$\rho_0^t(\lambda) = \frac{6\varepsilon(\lambda)}{45 + 7\varepsilon(\lambda)} \quad (7)$$

$$\varepsilon(\lambda) = 3 \frac{\alpha^{parallel}(\lambda) - \alpha^{perpendicular}(\lambda)}{\alpha^{parallel}(\lambda) + 2\alpha^{perpendicular}(\lambda)} \quad (8)$$

The Rayleigh scattering phase function is isotropic (i.e. ratio of one direction/all directions backscatter powers) and is  $3/8\pi$  leading to:

$$\sigma_m(\lambda) = \frac{8\pi}{3} \pi \sigma_m(\lambda) = \frac{24\pi^3 (n^2(\lambda) - 1)^2}{\lambda^4 n_{air}^2 (n^2(\lambda) + 2)^2} F_k(\lambda) \quad (9)$$

where  $\pi \sigma_m$  is the backscatter (at  $180^\circ$ ) molecular (correspondent to the sum of  $N_2$  and  $O_2$ ) cross-sections. The scattered light intensity pattern is symmetric in the forward and backward directions, and totally polarized at  $90^\circ$  [6]. Calculations of molecular cross-sections as expressed by Eq. (4) were amply addressed in [3-6].

For this work, a simpler but realistic semi-empirical formula for the estimation of the differential backscattering cross section given by [4,7] was proposed as given cf. Eq. (10) below:

$$\frac{\pi d\sigma_m}{d\Omega} = 5.45 \cdot 10^{-32} \left( \frac{550}{\lambda} \right)^{4.09} \quad (10)$$

where  $d\sigma/d\Omega$  is expressed in  $m^2 \text{ molec}^{-1}$  and  $\lambda$  in nm. Therefore the backscatter coefficient,  $\beta_m$ , is obtained by multiplying Eq. above with the air number density  $n_{air}(z)$ .

$$\beta_\pi^{simpler}(n_{air}(z), \lambda) = n_{air}(z) * \frac{\pi d\sigma_m}{d\Omega} = n_{air}(z) * \left[ 5.45 \left( \frac{550}{\lambda(nm)} \right)^4 * 10^{-28} \right] (cm^{-1} sr^{-1}) \quad (11)$$

Then by multiplication with the inverse of Rayleigh phase function, the molecular extinction coefficient  $\alpha_m(z)$  is obtained:

$$\alpha_m(z) = \frac{8\pi}{3} * \beta_m(z) = \frac{8\pi}{3} * n_{air}(z) * \frac{\pi d\sigma_m}{d\Omega} \quad (12)$$

with  $\alpha_m$  expressed in  $m^{-1}$  and  $\beta_m$  in  $m^{-1}sr$ . The air number density  $n_{air}(z)$  is determined from the air pressure and temperature profiles as measured by radiosondes. The formula above indicates a Rayleigh cross-section that follows a  $\sim \lambda^{-4}$  wavelength dependency, and for this reason, the shorter the wavelength, the more scattered the corresponding radiations. The scattering cross-section is relatively small, on the order of  $\sim 10^{-28} cm^2.molec^{-1}$ , but the air concentration number i.e.  $\sim 10^{19} molec.cm^{-3}$  partially compensates for the inefficiency of this process. Once the different scattering coefficients are derived, The LIDAR equation [8] for the molecular–Rayleigh backscattering is:

$$P_{RCS_m}(\lambda_L, z) = C_s(z) \cdot \beta_m(\lambda_L, z) \cdot \exp\left[-2 \int_{z_0}^z \alpha_m(\lambda, z) dz\right] \quad (13)$$

## 2.2 Elastic-Mie scattering

In the presence of particles of size comparable to the excitation wavelength ( $> 0.1 \mu m$ ), Mie scattering processes becomes important. Thus the laser radiation is elastically scattered ( $\lambda_D = \lambda_L$ ) by small atmospheric particles (i.e. aerosols) of size comparable to the radiation wavelength. The Mie backscatter usually dominates the Rayleigh scattering, exhibiting high cross-section values ranging from  $10^{-26}$  to  $10^{-8} cm^2.molec^{-1}$  (e.g.  $10^{-10} cm^2.molec^{-1}$  in the visible spectra at  $\sim 500 nm$  for particles with size around  $0.1 \mu m$ ) [7].

The angular characteristics of Mie scattering (i.e. cross-section) for all particle sizes and wavelengths are expressed by two intensity distribution functions. These functions

are fundamental for all the subsequent definitions of the scattering cross sections and volume coefficients [4,6]. Light scattered by a particle that is observed at angle  $\theta$  may be treated as consisting of two components of intensities  $i_c$  and  $i_p$ , i.e. perpendicular (polarized) and parallel to the plane of observation, respectively:

$$\begin{aligned} i_c(\zeta, m, \theta) &= \left[ \sum_{n=1}^{\infty} \frac{2n+1}{n(n+1)} (a_n \pi_n + b_n \tau_n) \right]^2 \\ i_p(\zeta, m, \theta) &= \left[ \sum_{n=1}^{\infty} \frac{2n+1}{n(n+1)} (a_n \tau_n + b_n \pi_n) \right]^2 \end{aligned} \quad (14)$$

where  $n$  are positive integers. The values of  $a_n$  and  $b_n$  result from Ricatti-Bessel functions, the arguments of which are the size parameter  $\zeta$ , and the complex refractive index,  $m$ . The functions  $\pi_n$  and  $\tau_n$  depend only on the angle  $\theta$  and involve the first and second derivatives of the Legendre polynomials of order  $n$  and argument  $\cos\theta$ . The intensity of the light scattered by the particles is:

$$I(\theta, \phi) = E_\phi \frac{\lambda^2}{4\pi^2} (i_c \sin^2 \phi + i_p \cos^2 \phi) \quad (15)$$

where  $E_\phi$  is the irradiance of the incident light. The differential cross-section  $d\sigma/d\Omega$  [ $\text{cm}^2\text{sr}^{-1} \text{molec}^{-1}$ ] is given by:

$$\frac{d\sigma_a(\theta, \phi)}{d\Omega} = \frac{I(\theta, \phi)}{E_\phi} = \frac{\lambda^2}{4\pi^2} (i_c \sin^2 \phi + i_p \cos^2 \phi) \quad (16)$$

Based on cross-section values the asymmetry parameter,  $g$ , is defined as:

$$g = \frac{\int_0^\pi \sigma_a(\theta) \cos(\theta) \sin(\theta) d\theta}{\int_0^\pi \sigma_a(\theta) \sin(\theta) d\theta} \quad (17)$$

For isotropic or symmetric scattering (e.g. Rayleigh or spherical particle scattering), the asymmetry parameter is zero, while for a purely forward scattering the parameter is 1. The asymmetry parameter of the cloudless atmosphere ranges from 0.1 (very clean) to 0.75 (polluted). For a cloudy atmosphere, asymmetry parameter values vary between 0.8 and 0.9 [3]. The total scattering cross section  $\sigma_a$  [ $\text{cm}^2\text{molec}^{-1}$ ] may be calculated using Eq. (18) by integrating over the  $4\pi$  sr

$$\sigma_a = \int_0^{4\pi} \frac{d\sigma_a(\theta, \phi)}{d\Omega} d\omega = 2\pi \int_0^\pi \sigma_a(\theta) \sin\theta d\theta \quad (18)$$

The total scattering cross section values cover a wide range and are larger than the diffusers' geometric cross sections. The ratio of the scattering to geometric cross sections is defined as the efficiency factors as follows:

$$Q_{scat} = \frac{\sigma_a}{\pi r^2} = \frac{2}{r^2} \int_0^\pi \sigma_a(\theta) d\theta \quad \text{and} \quad Q_\pi = \frac{\sigma_a(\theta = \pi)}{\pi r^2} \quad (19)$$

where  $r$  is the radius of the aerosol particle and the complex part of the refractive index is not taken into account. The link between the extinction  $\alpha$ , backscatter  $\beta$  coefficients and the efficiency factors  $Q_{scat}$  and  $Q_\pi$  is given by

$$\alpha_a = \pi \int_0^\infty r^2 Q_{ext} n(r) dr \quad \text{and} \quad \beta_a = \pi \int_0^\infty r^2 Q_\pi n(r) dr \quad (20)$$

where  $n(r)$  is the aerosol size distribution and in the calculation of  $Q_{ext}$  the complex part of the refractive index is taken into account (i.e.  $Q_{ext} = Q_{scat} + Q_{abs}$ ). The ratio of the scattering ( $Q_{scat}$ ) to extinction efficiency factors is called *single scattering albedo* ( $\omega_0$ ),

$$\omega_a = \frac{Q_{scat}}{Q_{scat} + Q_{ext}} \quad (21)$$

which represents the fraction of scattered light with respect to the total light. For a non-absorbing particle, the *single scattering albedo* is 1. The lidar equation for aerosol scattering (Mie) is based on the Rayleigh lidar equation (index m) at which the Mie terms (index a) are added as follows:

$$P_{RCS}(\lambda_L, z) = C_s(z) \cdot [\beta_m(\lambda, z) + \beta_a(\lambda, z)] \cdot \exp\left[-2 \int_{z_0}^z [\alpha_m(\lambda, z) + \alpha_a(\lambda, z)] dz\right] \quad (22)$$

where  $\beta_a$  and  $\alpha_a$  are the aerosol backscatter and extinction coefficients and may be determined by inverting Eq. (22) as it is explained in detail in chapter II section 2.4.

*Aerosol extinction wavelength dependency: Angstrom turbidity law*

Important parameters are also the *Angstrom coefficients*  $\gamma$  and  $b$  that describe the wavelength dependency of the extinction coefficient:

$$\alpha_a = b\lambda^{-\gamma} \quad (23)$$

The above power law wavelength dependency cf. Eq. (23) is known as the empirical Angstrom turbidity. This wavelength dependence (i.e. power law) of the aerosols' extinction  $\alpha_a$  is a valid approximation to the Mie theory [3].  $b$  is an index proportional to the aerosol concentration while the wavelength exponent  $\gamma$  varies from 0 to 4 and is related to the size distribution.

In the almost molecular Rayleigh regime (i.e., low aerosol loading), the extinction coefficient varies with wavelength according to a power law with an exponent  $\gamma$  ranging  $\sim 3 - 4$ , whereas in large-particle regime, this exponent ranges between 1 and 0. An optically thick and dense cloud will have  $\gamma=0$  (i.e. no wavelength dependency), and values smaller than 1 are typical for sea salt or mineral dust particles ( $\sim 1-3\mu\text{m}$ ) and

values larger than 1 are typical for smaller aerosol sizes ( $< 1\mu\text{m}$ ). The Angstrom coefficients are good indicators of particle size  $\gamma$  and number concentration  $\beta$  but do not provide precise information on the aerosol size distribution or the shape of the particles.

### 2.3 Raman (inelastic scattering)

As described before, the scattering of light may be thought of as the redirection of light that takes place when an electromagnetic (EM) wave (i.e. an incident light ray) encounters an obstacle or nonhomogeneity, in our case the scattering material (solid, liquid or gas). As the EM wave interacts with the matter, the electron orbits within the constituent molecules are perturbed periodically with the same frequency ( $\nu_0$ ) as the electric field of the incident wave. The oscillation or perturbation of the electron cloud results in a periodic separation of charge within the molecules, which is called an induced dipole moment. The oscillating induced dipole moment manifests as a source of EM radiation, thereby resulting in scattered light. The majority of light scattered is emitted at the identical frequency ( $\nu_0$ ) of the incident light, a process referred to as elastic scattering and presented in sections 2.1 and 2.2 of chapter 2. However, as explained below, additional light is scattered at different frequencies, a process referred to as inelastic scattering. Raman scattering is one such example of inelastic scattering.

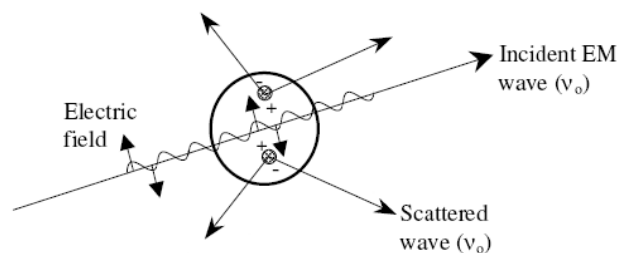


Figure 2.4. Induced dipole moment

As discussed above, an incident electromagnetic wave induces a dipole moment during the light-material interaction. As seen in section 2.1 of this chapter the two components of the dipole moment strength are the polarizability which is a material property that depends on the molecular structure and nature of the bonds (presented in more detail in section 2.3 of this chapter) and the electric field that may be expressed as

$$E = E_o \cos(2\pi\nu_o t), \quad (24)$$

where  $\nu_o$  is the frequency (Hz) of the incident EM ( $\nu_o = c/\lambda$ ). Substituting Eq. (24) into the dipole moment equation yields the time-dependent induced dipole moment,

$$P = \alpha E_o \cos(2\pi\nu_o t) \quad (25)$$

Because the ability to perturb the local electron cloud of a molecular structure depends on the relative location of the individual atoms, it follows that the polarizability is a function of the instantaneous position of constituent atoms. For any molecular bond, the individual atoms are confined to specific vibrational modes, in which the vibrational energy levels are quantized in a manner similar to electronic energies. The vibrational energy of a particular mode is given by

$$E_{vib} = \left( j + \frac{1}{2} \right) h \nu_{vib} \quad (26)$$

where  $j$  is the vibrational quantum number ( $j = 0, 1, 2, \dots$ ),  $\nu_{vib}$  is the frequency of the vibrational mode, and  $h$  is the Planck constant. The physical displacement  $dQ$  of the atoms about their equilibrium position due to the particular vibrational mode may be expressed as

$$dQ = Q_o \cos(2\pi\nu_{vib} t) \quad (27)$$

where  $Q_0$  is the maximum displacement about the equilibrium position. For a typical diatomic molecule (e.g.  $N_2$ ), the maximum displacement is about 10% of the bond length [12]. For such small displacements, the polarizability may be approximated by a Taylor series expansion, namely,

$$dQ = Q_0 \cos(2\pi\nu_{vib}t) \quad (28)$$

where  $\alpha_0$  is the polarizability of the molecular mode at equilibrium position. Based on the vibrational displacement of Eq. (27), the polarizability may be given as

$$\alpha = \alpha_0 + \frac{\partial\alpha}{\partial Q}dQ \Rightarrow \alpha = \alpha_0 + \frac{\partial\alpha}{\partial Q}Q_0 \cos(2\pi\nu_{vib}t) \quad (29)$$

Finally, Eq. (29) may be substituted into the dipole moment equation (25), which yields

$$P = \alpha_0 E_0 \cos(2\pi\nu_0 t) + \frac{\partial\alpha}{\partial Q} Q_0 E_0 \cos(2\pi\nu_0 t) \cos(2\pi\nu_{vib} t) \quad (30)$$

Using a trigonometric identity, the above relation may be recast as

$$P = \alpha_0 E_0 \cos(2\pi\nu_0 t) + \left( \frac{\partial\alpha}{\partial Q} \frac{Q_0 E_0}{2} \right) \{ \cos[2\pi(\nu_0 - \nu_{vib})t] + \cos[2\pi(\nu_0 + \nu_{vib})t] \} \quad (31)$$

Examination of the above equation reveals that induced dipole moments are created at three distinct frequencies, namely  $\nu_0$ ,  $(\nu_0 - \nu_{vib})$ , and  $(\nu_0 + \nu_{vib})$ , which results in scattered radiation at these same three frequencies. The first scattered frequency corresponds to the incident frequency, hence is elastic scattering (e.g. Mie or Rayleigh), while the latter two frequencies are shifted to lower or higher frequencies and are therefore inelastic processes. The scattered light in these latter two cases is referred to as Raman scattering, with the down-shifted frequency (longer wavelength) referred to as Stokes scattering (much stronger), and the up-shifted frequency (shorter wavelength) referred to as anti-

Stokes scattering. C.V. Raman was the first to describe this type of inelastic scattering, for which he was awarded the Noble prize in physics in 1930. [10]

The Raman frequency shift is completely independent of the incident light frequency,  $\nu_0$ . However, raman spectra are studied using light sources in the visible or ultraviolet due to the  $\lambda^{-4}$  dependency of the Raman cross-section. Raman and Infrared (IR) absorption spectra are often complementary, since vibrations and rotations of some molecules that are not observable in the IR may be active in Raman. As seen in above eq 31 the Raman scattering is linked to molecular polarizability ( $\alpha$ ). In order for a vibration or rotation to be Raman-active, the polarizability must change during the rotation or vibration causing the molecule to get an induced dipole moment. Any non-spherical molecule can change its polarizability and thus they are Raman active. Homeopolar molecules, such as  $O_2$ , and  $N_2$ , which are not infrared active in terms of absorption, are thus Raman active[3, 11]. The Raman spectra of  $N_2$  molecules (~78 % of atmosphere) and of water vapor ( $H_2O$ ) are addressed within this work via the Raman-based lidar applications.  $N_2$  (class of symmetry  $D_{\infty h}$ ) has a single symmetrical elongation vibration mode  $\leftarrow N-N \rightarrow$  and the selection rules for vibrational Raman transition are  $\Delta = 0, \pm 1, \pm 2, \dots$  (vibrational quantum number). For each vibrational band, the rotational Raman selection rules conduct to three spectral bands called O (for  $\Delta J = -2$ ), Q (for  $\Delta J = 0$ ) and S (for  $\Delta J = +2$ ), where J denotes the rotational quantum number. Water vapor (class of symmetry  $C_{2h}$ )[10] is a tri-atomic plane molecule (see Figure 2.5) with 3 degrees of freedom. The three corresponding normal vibrational modes are: symmetrical elongation ( $\nu_1=3657.05\text{cm}^{-1}$ ), deformation of bond angle ( $\nu_2=1594.75\text{cm}^{-1}$ ) and antisymmetrical elongation ( $\nu_3=3755.93\text{cm}^{-1}$ ).

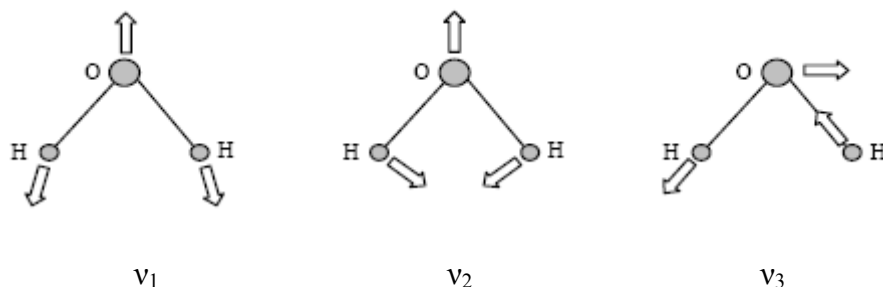


Figure 2.5. Three normal vibrational modes of the water vapor molecule.

The selection rules are  $\Delta v_j = 0, \pm 1, \pm 2, \dots$ , where  $v_i$  are the vibrational modes and  $j$  was defined above as the vibrational quantum number. The most probable and important mode (i.e. intense) is the oscillation  $v_2$ . For  $\Delta v = 0$  and  $\Delta J = 0$  the Cabanne scattering line is obtained. For  $\Delta v = 0$  and  $\Delta J = \pm 2$ , the pure rotational O and S Raman spectral bands are obtained. At normal atmospheric temperatures most molecules are in their vibrational ground state  $v = 0$ . Thus Stokes bands will be much more important than anti-Stokes ones. In addition, there is a sharp decrease of intensity as the vibrational quantum number  $v$  increases, due to the relative population of states as defined by the Boltzmann distribution. The laser excitation of  $N_2$ , and  $H_2O$  atmospheric molecules will give essentially Stokes type transitions. For illustration, the Raman spectra of a diatomic molecule is shown in Figure 2.6. Stokes and anti-Stokes branches of the rotational-vibrational structure are shown as well as the pure rotational one. The first Stokes band is shown in detail. The rotational structure of the Q-branch is also shown. Often the Q branch is considered as a "single" line because its rotational lines are much less widely spaced than in the O - or S - branches. Typically the width of the Q-branch ranges from tenths of  $cm^{-1}$  to tens of  $cm^{-1}$ . The intensity of a Raman line is determined by the scattering cross-section value of the transition between the energy levels. In the case of vibrational-rotational transitions, according to the polarizability theory [3], the scattering

cross section of a transition can then be expressed through the matrix elements of the polarizability tensor.

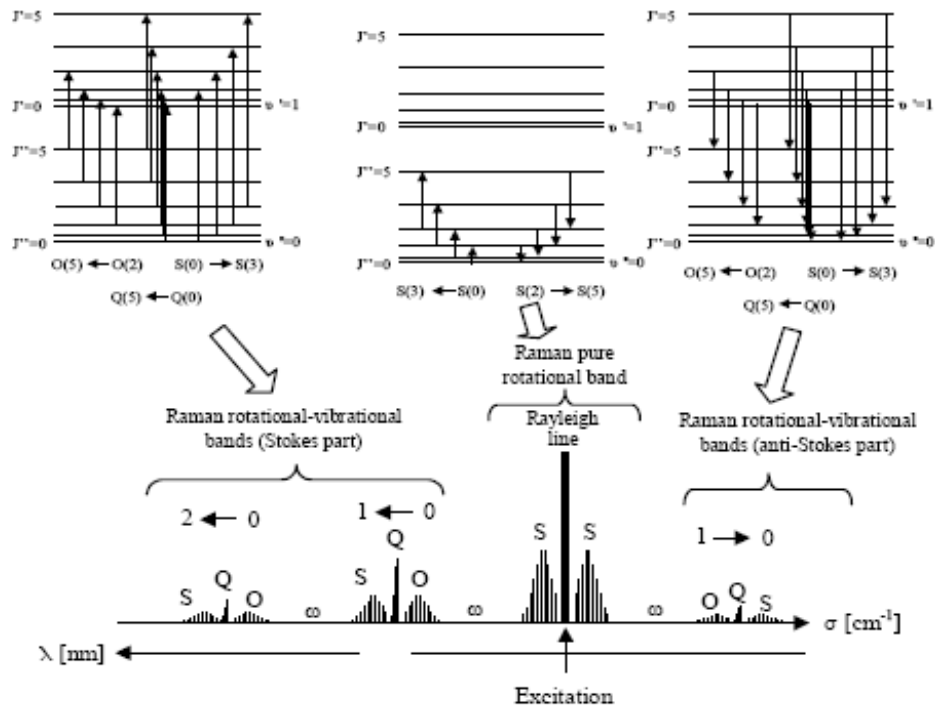


Figure 2.6 Energy levels diagrams and the correspondent Raman spectra for diatomic molecule

The expression for the total (sum of cross-sections of Q, O and S branches) Raman backscattering cross-section of a shifted vibrational-rotational Raman band  $\nu_j$  is given after [18] as follows:

$$\frac{d\sigma}{d\Omega}(\nu_j, \nu_0) = \frac{(2\pi)^4}{45} \frac{(\nu_0 - \nu_j)^4 b_j^2}{c^4 \left[ 1 - \exp\left(-\frac{hc\nu_j}{k_B T}\right) \right]} g_j (45\alpha_j^2 + 7\gamma_j^2) \quad (32)$$

where  $\nu_j$  [ $\text{cm}^{-1}$ ] is the frequency of the  $j^{\text{th}}$  vibrational mode of the molecule,  $b_j$  is the zero amplitude of the  $j^{\text{th}}$  vibrational mode,  $T$  [K] is the vibrational temperature of the molecules,  $g_j$  is the degree of degeneracy of the  $j^{\text{th}}$  vibrational mode,  $\alpha_j$  and  $\gamma_j$  are the

isotropic and anisotropic components of the polarizability tensor derived with respect to the normal coordinates, and  $k_B$  is the Boltzmann constant.

The Raman processes have relatively low efficiency (cross-sections ranges from  $10^{-32}$  to  $10^{-28} \text{ cm}^2 \cdot \text{molec}^{-1}$ ) compared with Rayleigh scattering which is  $\sim 3$ -5 orders of magnitude higher. Experimental measurements [4] resulted in extensive lists of values of the differential Raman backscattering cross section for a range of atmospheric constituents. These cross sections are experimentally evaluated relative to the  $2331 \text{ cm}^{-1}$  vibrational Q-branch of the Raman cross section of nitrogen. The absolute value of this cross section [4] for  $0 \rightarrow 1$  vibrational Q branch Raman transition in  $\text{N}_2$  gas when excited at  $514.5 \text{ nm}$  is  $\frac{d\sigma}{d\Omega} \approx (4.3 \pm 0.2) \times 10^{-31} \text{ cm}^2 \text{ sr}^{-1}$ . This corresponds to the value  $2.8 \times 10^{-30} \text{ cm}^2 \text{ sr}^{-1}$  and  $7.8 \times 10^{-30} \text{ cm}^2 \text{ sr}^{-1}$  for  $337.1 \text{ nm}$  excitation of  $\text{N}_2$  and respectively of  $\text{H}_2\text{O}$ , when allowance is made for the  $(\nu^4)\lambda^{-4}$  dependence of  $\frac{d\sigma}{d\Omega}$ . Therefore, since the Raman differential cross-section follows a  $\lambda^{-4}$  law, the efficiency of this process is higher in the UV, at shorter wavelengths. The choice of the excited wavelength is a key factor and a compromise has to be found between skipping the trace gases (i.e. ozone) molecular absorption in the solar - blind UV regions, avoiding the strong solar radiation influence in the VIS spectral range and accommodating the complexity of the laser source. The CCNY Raman lidar is detecting only the rotational-vibrational spectra of  $\text{N}_2$  at  $387 \text{ nm}$  and  $\text{H}_2\text{O}$  vapor at  $407 \text{ nm}$  but Raman lidar techniques based on pure rotational spectra is also a suitable method because of the higher intensity of the pure rotational lines ( $\sim 10^2$ - $10^3$  greater than the rotational-vibrational ones [18]).

The choice of the exciting wavelength has to be made carefully in order to avoid coincidences with the absorption wavelengths of the atmospheric components or with resonant molecular transitions. Possible interferences with fluorescence are generally negligible. The fluorescence process is efficient, due to cross-sections around  $10^{-20}$   $\text{cm}^2 \cdot \text{molec}^{-1}$ , but the lifetime of the excited levels, from  $10^{-6}$  to 1 s, is in general much longer than the time between two collisions. Quenching by collision reduces drastically the efficiency of the fluorescence at least in the troposphere. The Raman spectrum of molecule-dependent specific lines, shifted with respect to the excitation wavelength, is produced during the very short interaction lifetime ( $\sim 10^{-14}$  s) between the molecule and the electromagnetic exciting wave. One of the main advantages of Raman based techniques is the fact that using a single wavelength of the excitation radiation one may induce simultaneously Raman radiation from different molecules which are present in the sampled volume.

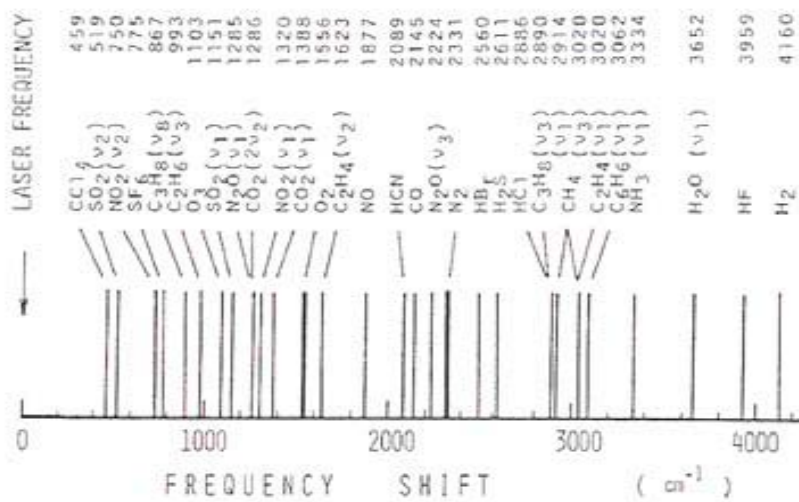


Figure 2.7 Raman frequency shifts of Q branch of the atmospheric molecules

In Figure 2.7 Q-branch Raman shifts for typical atmospheric molecules are shown. The study of such a spectrum allows simultaneous measurements of a wide range of components, and absolute determination of their mixing ratio.

In this work, rotational-vibrational Raman spectra of N<sub>2</sub> at 387 nm, H<sub>2</sub>O vapor at 407nm excited by 355 nm. The lidar equation [8,15] for the Raman process may be written as:

$$P_{RCS}(\lambda_R, z) = C_s(z) \cdot \beta_R(\lambda_R, z) \cdot \exp\left[-\int_{z_0}^z [\alpha_{atm}(\lambda_L, z) + \alpha_{atm}(\lambda_R, z)] dz\right] \quad (33)$$

where the Raman backscatter and extinction coefficients are given by

$$\begin{aligned} \beta_R(\lambda_L, \lambda_R, z) &= n_R(z) \frac{\pi d\sigma_R(\lambda_L, \lambda_R, z)}{d\Omega} \\ \alpha_{atm}(\lambda_{L,R}, z) &= \alpha_m(\lambda_{L,R}, z) + \alpha_a(\lambda_{L,R}, z) \end{aligned} \quad (34)$$

where R denotes a ‘‘Raman’’ processes,  $n_R(z)$  is the atmospheric profile number density of Raman active scattering molecules,  $\pi d\sigma_R/d\Omega$  is the differential Raman backscatter cross-section, and  $\alpha_{atm}$  is the total (molecular - m plus aerosol - a) atmospheric extinction coefficient.

The advantage of the Raman lidar approach is the use of one laser line for sensing a number of molecular species (different Raman shifts). The main disadvantage is its reduced sensitivity as the Raman cross sections are very low (e.g.  $\sim 10^{-30}$  cm<sup>2</sup>sr<sup>-1</sup> for nitrogen) compared with Rayleigh cross-sections which are 10<sup>3</sup> greater or with Mie cross-sections which are at least 10<sup>3</sup> up to 10<sup>20</sup> greater. The suppression of the Rayleigh and Mie interferences in the Raman lidar detection channels is crucial for properly recording the Raman atmospheric backscatters. Powerful laser sources, large telescopes, high performance optical filtering, and long integration times are requirements for the application of the Raman technique.

## 2.4 Optical parameters of atmospheric particles

The CCNY lidar allows us in principle to obtain the extinction and backscatter coefficients at three different wavelengths: 355nm, 532nm and 1064nm. However, in the case of elastic lidar channels, extra assumption in the form of the extinction to backscatter ratio is needed. This is illustrated in the Fernald method which we solve iteratively.

### Method I Fernald iterative method

- *Step 1.* The aerosol extinction coefficient is defined to be the product between aerosol backscatter and the lidar ratio as shown in equation 38

$$\alpha^a(\lambda_L, z) = \beta^a(\lambda_L, z) * S_1 \quad (35)$$

where  $S_1$  is the lidar ratio for aerosols and it has values in the range 10-100. In all applications,  $S$  is assumed constant. Some commonly used values of lidar ratios are presented in table 2.1

Table 2.1 Usual lidar ratios in visible (Ellsworth J. Welton, NASA)

<b>Aerosol type</b>	<b>Lidar ratio</b>
Salt	20-30
None	30(PBL), 40(Troposphere)
Dust	35.7
Dust_sulfate/carbon	48-63
Sulfate	50-65
Sulfate_carbon	53-68
Carbon	56-71

In this first iteration step, we assume no extinction is present  $\alpha_{k=0}^a(z_i) = 0$  and by necessity assume  $S_1$  and the ratio  $R = \beta_m + \beta_a / \beta_m$  values

- *Step 2* In the second step we need to use the lidar equation and the step one assumptions to obtain the calibration constant.

$$C_k = \frac{P(z_i)z_i^2}{[\beta_k^a(z_i) + \beta^m(z_i)] \exp\left(-2 \int_{z_i}^{z_{i+1}} \alpha_k^a(z_i) + \alpha^m(z_i) dz\right)} \quad (36)$$

where  $z_i$  is the max altitude where it is assumed a clear sky (see step one assumptions).

- *Step 3* Therefore the only variable that has to be solved in the equation is the aerosol backscatter. With the calibration constant obtained from step 3 and replaced back into the lidar equation, one can obtain the aerosol backscatter at the (k+1) iteration  $\beta_{k+1}^a(z)$  and continue to convergence. Clearly, the aerosol backscatter coefficient can be used therefore in the Fernald equation [16] to determine the aerosol extinction.

Unfortunately, the method requires an S ratio which must be assumed. However, if a raman channel is used together with the elastic channel, this assumption can be relaxed.

## Method II

- *Step 1* In method 2 [17] the aerosol backscatter coefficient is determined by combining the return signal at the laser wavelength (elastic signal) and inelastic (Raman) signal and forming the ratio:

$$\Lambda = \frac{P_r(\lambda_L, z)P_r(\lambda_R, z_0)}{P_r(\lambda_L, z_0)P_r(\lambda_R, z)} \quad (37)$$

where  $P_r(\lambda_L, z_0)$  and  $P_r(\lambda_R, z)$  are the lidar returns at the lidar and Raman wavelength from a height where the molecular backscatter is more predominant

- *Step 2* Replacing the terms in equation 7 by the equivalent expression given by equations 1 and 2 and using the approximation  $\beta^m(z_0) + \beta^a(z_0) \cong \beta^m(z_0)$  one can derive the backscatter radiation in the following form:

$$\beta^a(\lambda_L, z) + \beta^m(\lambda_L, z) = \beta^m(\lambda_R, z_0) \times \Lambda \times \frac{n(\lambda_R, z)}{n(\lambda_R, z_0)} \times \frac{\exp\left(-\int_{R_0}^R [\alpha^a(\lambda_R, z) + \alpha^m(\lambda_R, z)] dz\right)}{\exp\left(-\int_{R_0}^R [\alpha^a(\lambda_L, z) + \alpha^m(\lambda_L, z)] dz\right)} \quad (38)$$

where  $\alpha^a(\lambda_{R,L}, z)$  is the aerosol extinction coefficient at the Raman respectively laser wavelength and could be retrieved from step 3

- *Step 3* The aerosol extinction coefficient at the Raman respectively laser wavelength  $\alpha^a(\lambda_{R,L}, z)$  can be retrieved by using the formula presented below.

$$\alpha^a(\lambda_L, z) + \alpha^m(\lambda_L, z) + \alpha^a(\lambda_R, z) + \alpha^m(\lambda_R, z) = \frac{d}{dR} \left[ \ln \left( \frac{O(z)n(z)}{z^2 P_R(z)} \right) \right] \quad (39)$$

where  $O(z)$  is the overlap function and can be assumed to be 1 for heights above 0.4 in the CCNY lidar case and  $n(z)$  in the number concentration of particles.

Solving the above equation for the aerosol extinction would give:

$$\alpha^a(\lambda_L, z) + \alpha^a(\lambda_R, z) = \frac{d}{dR} \left[ \ln \left( \frac{O(z)n(z)}{z^2 P_R(z)} \right) \right] - \alpha^m(\lambda_L, z) - \alpha^m(\lambda_R, z) \quad (40)$$

If one uses the ratio  $\frac{\alpha^a(\lambda_L)}{\alpha^a(\lambda_R)} = \left( \frac{\lambda_R}{\lambda_L} \right)^\gamma$  in equation 40 would obtain the aerosol

extinction at the laser wavelength given by equation 41 below

$$\alpha^a(\lambda_L, z) = \frac{\frac{d}{dR} \left[ \ln \left( \frac{O(z)n(z)}{z^2 P_R(z)} \right) \right] - \alpha^m(\lambda_L, z) - \alpha^m(\lambda_R, z)}{1 + \left( \frac{\lambda_L}{\lambda_R} \right)^\gamma} \quad (41)$$

where  $\gamma$  is the Angstrom coefficient,  $\alpha^m(\lambda_L, z)$  represents the molecular Rayleigh extinction coefficient, given in section 2.1 of this paper, and  $\alpha^m(\lambda_R, z)$  expresses the molecular extinction coefficient at the Raman wavelength

- *Step 4* Thus, replacing the  $\alpha^a(\lambda_{R,L}, z)$  in the backscatter equation given in step two, the aerosol backscatter is also retrieved.

#### *Aerosol microphysics based on lidar determined aerosol optical. Properties*

Once the lidar-determined values of aerosol extinction and backscatter coefficients are obtained, they may be used via various methods [13,14] to determine the microphysical aerosol properties such as number-surface-volume size distributions, complex refractive index and single scattering *albedo*. The extinction and backscatter coefficients at a given altitude can be expressed by two Fredholm equations:

$$\alpha_a = \int_{r_{\min}}^{r_{\max}} \pi r^2 Q_{ext}(r, \lambda, m) n(r) dr; \beta_a = \int_{r_{\min}}^{r_{\max}} \pi r^2 Q_{\pi}(r, \lambda, m) n(r) dr \quad (42)$$

where  $n(r)$  is the volume concentration distribution [aerosols  $\text{cm}^{-3}$ ],  $r_{\min}$  and  $r_{\max}$  are the minimum and maximum radius of the particles,  $m$  is the complex refractive index and  $Q$  is the extinction and backscatter efficiency (i.e. ratio of scattering and geometric cross-sections). Basically  $\alpha_a$  and  $\beta_a$  are calculated cf. Eq. (35) iterating on a matrix of particle radius and complex refractive index, up to values that minimize the difference with the

lidar observed values [7]. To choose ranges for the radius, it should be noticed that only particles with radii of the order of the magnitude of the measurement wavelengths (355 to 1064 nm) possess particle-size-dependent scattering efficiencies and therefore are suitable for inversion. The key parameter that best describes the radiative properties of a given size distribution is the surface-area weighted effective radius  $r_e$  which is defined as:

$$r_e(z) = \frac{\int n(r, z)r^3 dr}{\int n(r, z)r^2 dr} \quad (43)$$

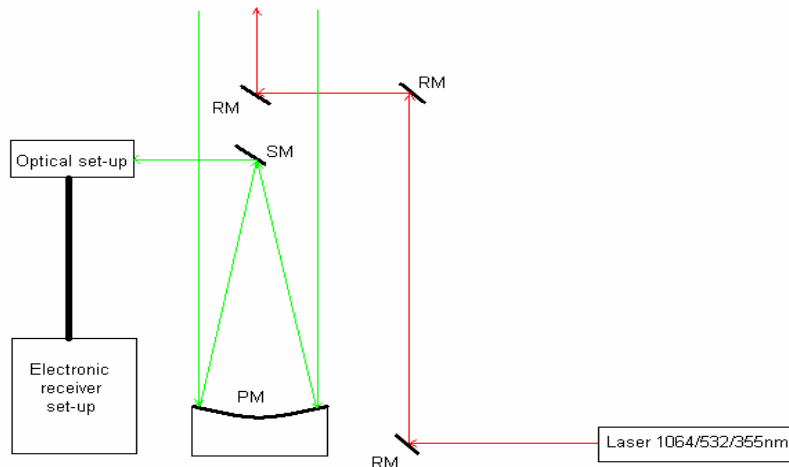
where  $r_e$  [ $\mu\text{m}$ ] is the effective radius and  $n(r, Z)$  [ $\text{cm}^{-3}\mu\text{m}^{-1}$ ] is the aerosol number concentration distribution. The total surface-area concentration at [ $\mu\text{m}^2\text{cm}^{-3}$ ], the total volume concentration  $v_t$  [ $\mu\text{m}^3\text{cm}^{-3}$ ], and the total number concentration  $n_t$  of particles [ $\text{cm}^{-3}$ ] are given, respectively, by

$$a_t = 4\pi \int n(r)r^2 dr; \quad v_t = \frac{4\pi}{3} \int n(r)r^3 dr; \quad n_t = \int n(r)dr \quad (44)$$

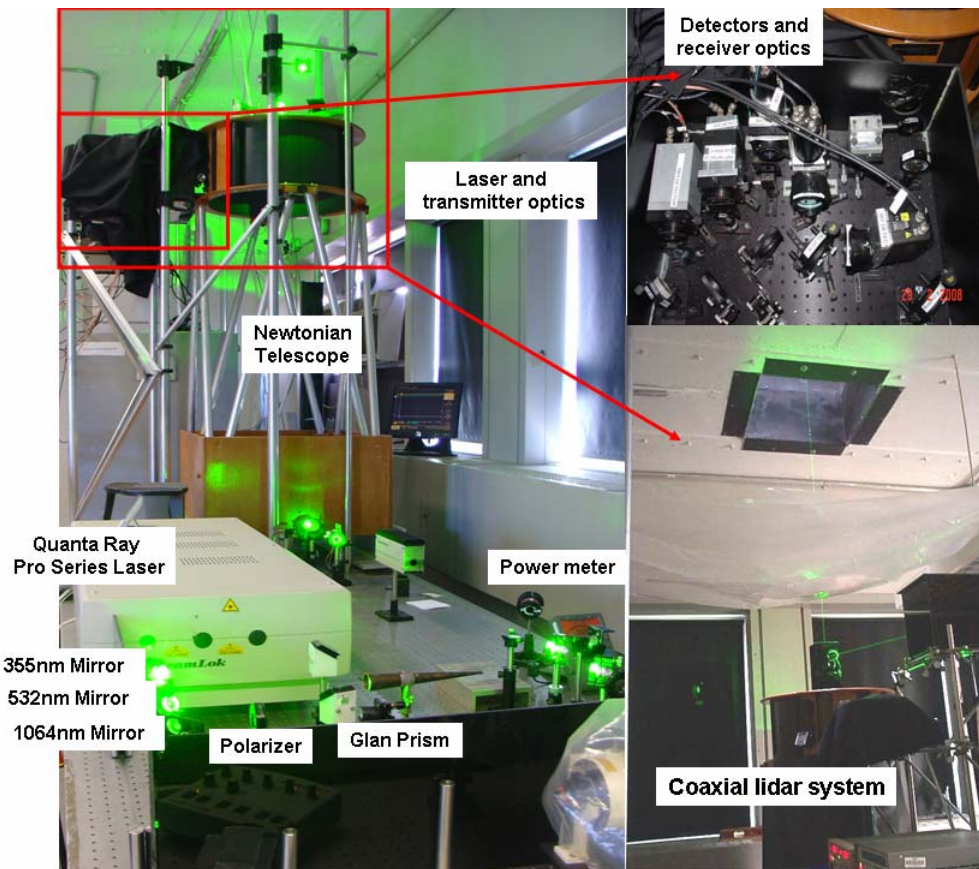
### 3. CCNY multiwavelength lidar system design

#### 3.1 Instrumentation diagram

A schematic of the CCNY lidar system is represented in fig 2.8



a)



b)

Figure 2.8.a) Schematic of the multi-wavelength Raman lidar installed at the CCNY station, b) Image of the lidar beam launched from the optics and remote sensing lab at CCNY

*Laser:* The transmitting laser is a Q-switched Spectra-Physics Quanta Ray Pro230 Nd-YAG with variable output power up to 475 mJ @ 532 nm, 950 mJ @ 1064 nm and 300 mJ @ 355 nm. This system currently has five channels with wavelengths at 1064 nm, 532 nm, 355 nm, including a Raman channel at 407 nm for water with a second Raman channel at 387 for nitrogen. Repetition rate of 30 Hz with 1-2 ns pulse duration @ 532 nm; <0.5 mrad beam divergence. Beam is separated in the three components to allow power measurements on separate channels and then regrouped and directed by three dichroic mirrors into the atmosphere above the system. The beam is on the axis of the telescope. The specifications of the laser transmitter are summarized in table 2 below:

Table 2.2 Technical specifications of the transmitter

Laser		Model Quanta-Ray Nd:YAG PRO 230, 30 Hz rep rate		
Wave length (nm)	Energy (mJ/p) <sup>2</sup>	Pulse width (ns)	Short term energy stability	Long Term Power Drift
1064	950	8-12	± 2%	<3%
532	475	1-2<1064	± 3%	<5%
355	300	2-3<1064	± 4%	<6%

The role of the Glan-Foucault is to diminish the intensity of the infrared radiation which at full power saturates the detectors. Further attenuation of the intensity is obtained at the receiving optics by insertion of neutral density filters in front of the interferometer filters. The Glan-Foucault prism illustrated in figure 2.9 achieves polarization by removing one plane of polarization by total internal reflection. It is made of two prisms of calcite with no other intervening material, i.e., with air between them. The O-ray (ordinary-ray) is removed and the E-ray (extraordinary-ray) continues straight through the device as shown.

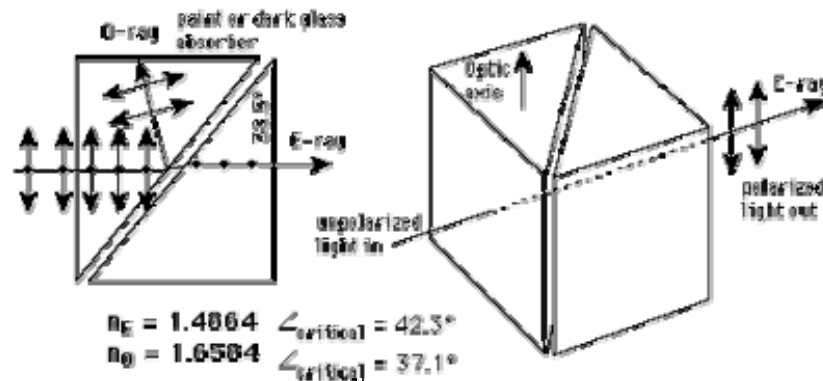


Figure 2.9 Glan Prism design

One of the advantages of the Glan-Foucault prism is that it can handle the high power densities (about 100 watts/cm<sup>2</sup>) characteristic of laser work. One disadvantage is a narrow field of view, about 10°. That field of view is widened in the Glan-Thompson prism, which has similar geometry but is cemented together. This extends the angle of view to about 30°, but cuts the maximum continuous power density by a factor of 100 to about 1 watt/cm<sup>2</sup>. The presence of the cement in the Glan-Thompson prism means that the angles must be different, since the critical angle for total internal reflection depends upon the indices of refraction of both materials at an interface.

After separating the the usual measured powers from the three separated channels are shown in table 2.3

Table 2.3 Lidar measured powers

Wavelength nm	Power from the QR Laser(W)	Usual measured powers(W)
1064	950mJ/pulse*30pulses/s=28.5W	4.12W
532nm	475mJ/pulse*30Hz=14.25W	1.72W
355nm	300mJ/pulse*30Hz=9W	4.81W

*Telescope:* 20 inch Newtonian Reflector, F3.5, FOV=detector size/effective focal length

*Detectors:* Due to the different wavelength channels, different detectors are used. A APD (silicon enhanced avalanche photodiode) for the 1064 nm (infrared) channel. A PMT (Hamamatsu photomultiplier tubes) for the 532 nm (green), 386 nm (Raman) and 355 nm (UV) channels. The optical components of the receiver are specified in table 3 and the set-up is schematically presented in figure 2.10

The system also requires various ND (neutral density) filters according to the intensity of the solar radiation at the time of measurement(0.1-3 mm).

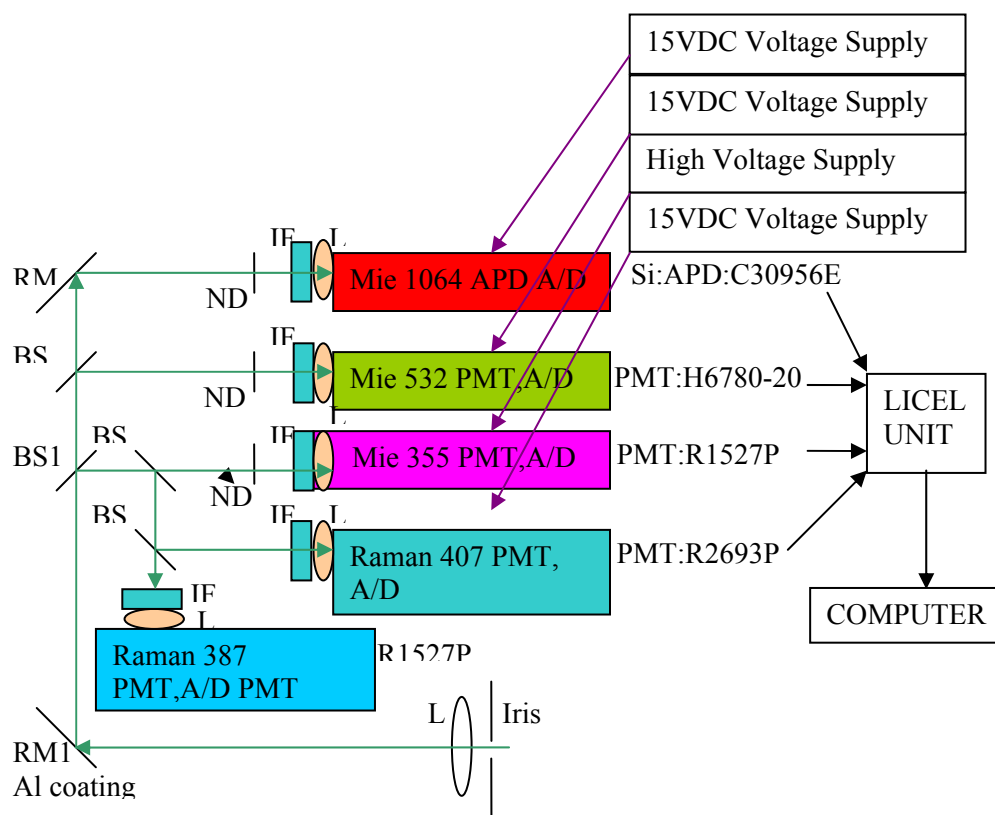


Figure 2.10 a) Schematic of the optical set-up of the receiver

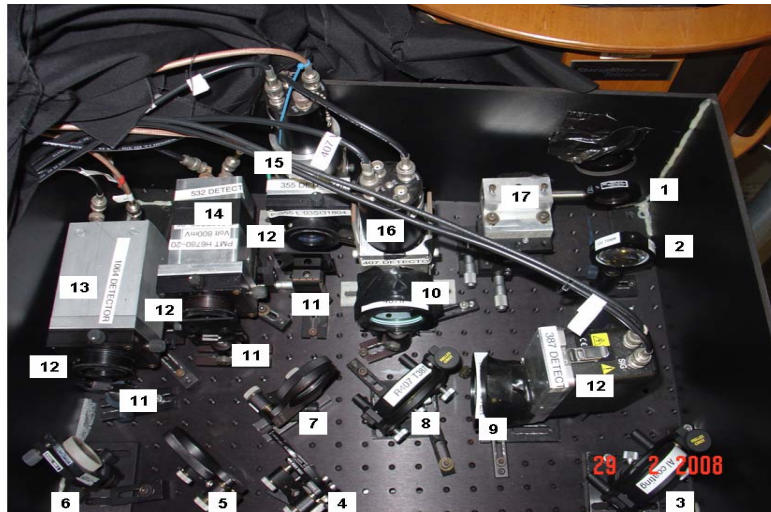


Figure 2.10b) Optical set up of the detectors

- |                             |                            |                |
|-----------------------------|----------------------------|----------------|
| 1. Field stop               | 7. $T 532 / R 355-407$     | 13. 1064nm APD |
| 2. Beam collimator          | 8. $T 387 / R 407$         | 14. 532nm PMT  |
| 3. Al coated mirror         | 9. $T 387\text{nm}$        | 15. 355nm PMT  |
| 4. $T 532-1064 / R 355-407$ | 10. $T 407 \text{ nm}$     | 16. 407nm PMT  |
| 5. $T 1064 / R 532$         | 11. Neutral Density Filter | 17. 387nm PMT  |
| 6. $R 1064$                 | 12. Interference Filter    |                |

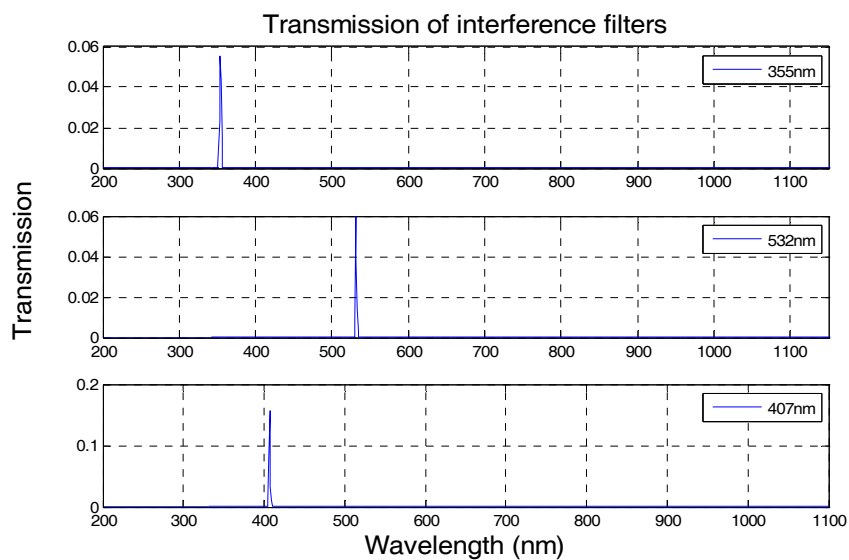


Figure 2.11 Transmission of interference filters

*Digitizing System:* Lidar Transient Recorder TR 40-16 (LICEL) with 12-bit, 40 MHz A/D converter for signals between 10 MHz and 200 MHz, 64-level fast discriminator for signals in the high frequency domain above 200 MHz.

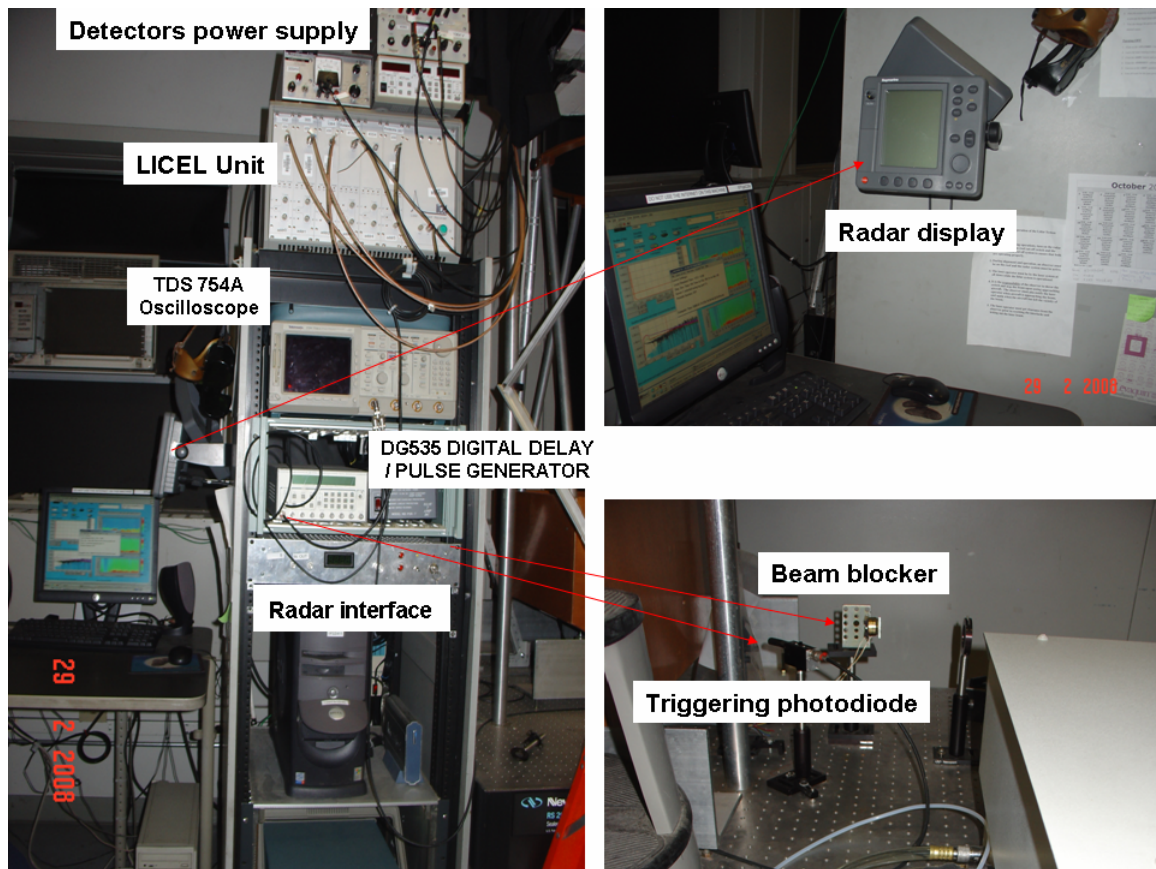


Figure 2.12 Receiver components

*RangeResolution:* 500 m to 15 km

Due to the overlap function the range below 300-500m is practically impossible to monitor. Sources that can lead to the low degree of spatial recovering between the emitted beam and the receiver field of view are the interference filters. The interference filters have narrow transmission functions around the specified wavelengths as could be noticed in figure 2.11. The light coming at different angles is transmitted at shifted

wavelengths and a convolution of the laser transmission function and interference filter shifted transmission curve (at high angles of incidence) leads to lower intensity detected by the photomultiplier tubes or avalanche photodiodes. This is the case when the light is backscattered by low altitude particles and the angle at which it arrives at the detector is slightly off the normal incidence (see Fabry Perot Etalons in chapter 6 of this thesis). The geometry of the telescope is another important factor of the overlap function. The presence of the secondary mirror in the center of the optical path and the holding bars could also obstruct the incoming radiation from below this height. Also the image formed from an object at a closer distance has a larger size than one at infinity. When this image is reflected by several mirrors with possible non-uniform reflectance (or defects) it can lead to poor detection of the signal.

*Data Acquisition:* Acquisition system is configured by using the TR 40-160 Transient Recorder modules for all channels in a five-channel rack comprising power supplies and interface ports to a PC computer equipped with a National Instruments digital I/O card, DIO-32F. Each channel can be configured and controlled separately by the host computer. The data acquisition is performed using LICEL transient recorders working at (40 Mega samples /sec)40MHz, 12 bit resolution of the recorder in analog (A/D) mode and a discriminator which detects voltage pulses above a selected threshold in the range 0-500mV. Typically an acquisition file contains 1800 shots averaged for each wavelength in A/D and P.C modes of 16000 bins. The acquisition sampling rate of 40Hz the pulse width is  $2.5 \times 10^{-8}$  s which results in a spatial resolution of 3.75 m resolution/1 bin) agrees with the response time of the detectors of 25.4ns ( $d=ct/2=(3 \times 10^8) \times (25 \times 10^{-9})/2=3.75\text{m}$ ).

As mentioned before it is also crucial that the repetition rate be sufficiently slow to allow the echo to return without interference to the next pulse. In the CCNY case, a rep rate of 30 Hz is clearly more than sufficient to increase detection SNR. Suitable averaging of the shots is required in the CCNY lidar system the average is performed over 1800 files. This is particularly true for weak raman signals in daylight.

In the acquisition mode of the lidar backscatter signal the LICEL is externally triggered by the triggering photodiode. This photodiode is facing the mirror that reflects the laser beam from the optics table to the upper mirror above the secondary mirror of the telescope. During the dark noise background measurement process the LICEL is internally triggered by the DG535 Digital Delay/Pulse generator as shown in figure 2.10. Figure 2.13 illustrates the front face of the LICEL unit where in the bottom right hand corner we can notice the cable connection to the trigger input of the LICEL unit.

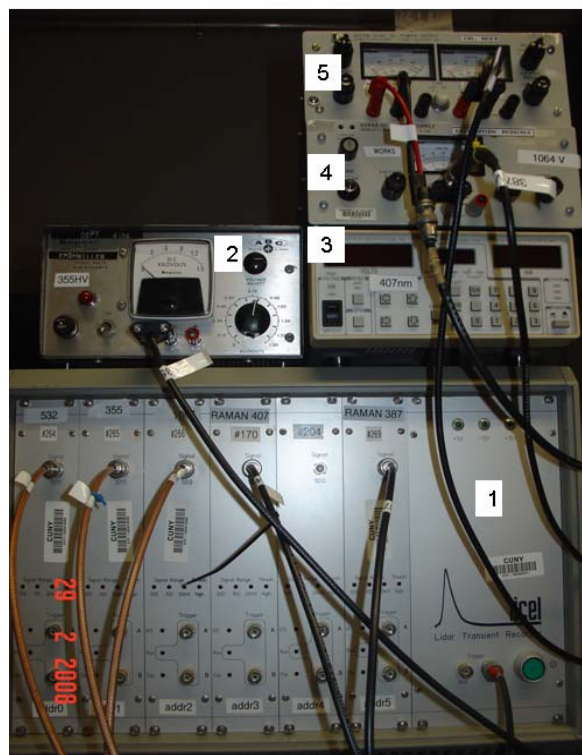


Figure 2.13 Input (power supply) and Output (LICEL) of the receiver optical detectors

1. LICEL TR 40-250
2. Power supply for 355nm
3. High Voltage power supply 407nm
4. Power supply for 387nm
5. Power supply for 532nm/1064nm

*Radar Interface:* A vertical radar emitter and antenna continually search for the presence of aircraft and provide a failsafe interlock for the beam while the laser is in operation. On detection of aircraft, the laser beam is automatically disabled and lidar data acquisition halted. When the airspace is again clear, the system can be reset by the operator after observer confirmation and data collection will automatically resume.

A summary of the main specifications of the multivalength Lidar system at CCNY is presented in table 2.4

Table 2.4 Specifications of the Mie-Raman lidar system at CCNY

Laser	Quanta Ray PRO-230 Nd:YAG, 30Hz 950 mJ at 1064 nm, 475 mJ at 532nm, 300 mJ at 355 nm
Telescope	Newtonian, f/3.5, Diameter: 50.8cm, FOV: 2mrad
Interference filters	Barr Associates Inc, Central wavelength(nm)/ Bandwidth(nm)/ Peak Transmission Mie channel: 1064, 532, 355/ 0.3~1 / T>50% N <sub>2</sub> -Raman : 386.7 / 0.3 / T=65% H <sub>2</sub> O(vapor)-Raman :407.5 / 0.5 / T=65%
Detectors	EG& G APD for 1064nm Hamamatsu PMT: H6780-20, R2693P, R1527P
Data acquisition	LICEL TR 40-250, 12 bits and 40 MHz A/D 250 MHz Photon-counting
Range resolution	3.75m

### 3.2 Typical profiles

The first Raman lidar water vapor profile (resolution 3.75m) was obtained at CCNY August 10, 2006, only 2 days before the below plot (improvements have been done since then). The laser emission is specified in table 1 and the repetition rate was of 30 Hz with 1800 averaged shots. The profile plotted in figure 2.14 is the vertical profile background subtracted of 532nm, 407nm, 1064nm and 387nm.

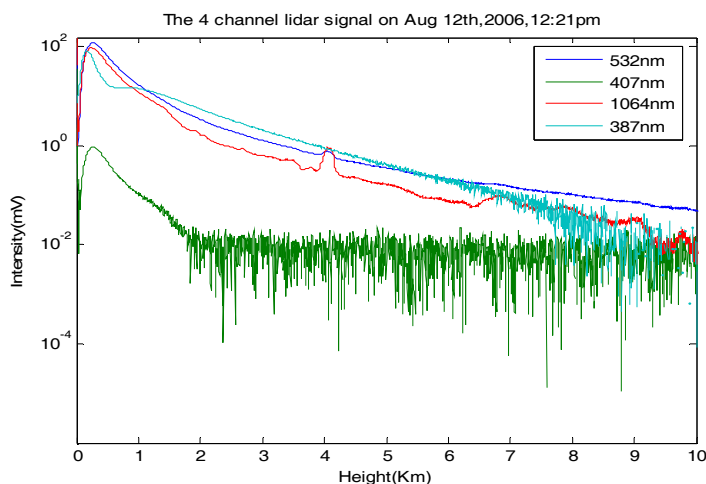


Figure 2.14 Vertical profiles of 4 different channels measured above CCNY station using a 60 min average at 12:21pm on 12<sup>th</sup> of August 2006

The Mie/Rayleigh 1064nm signal measured on September 7<sup>th</sup>,2006 is plotted for the whole day in figure 2.15. This day has been considered for calibration due to the relatively high PBL(planetary boundary layer) that can be observed in figure 2.14 and contains most of the atmospheric water.

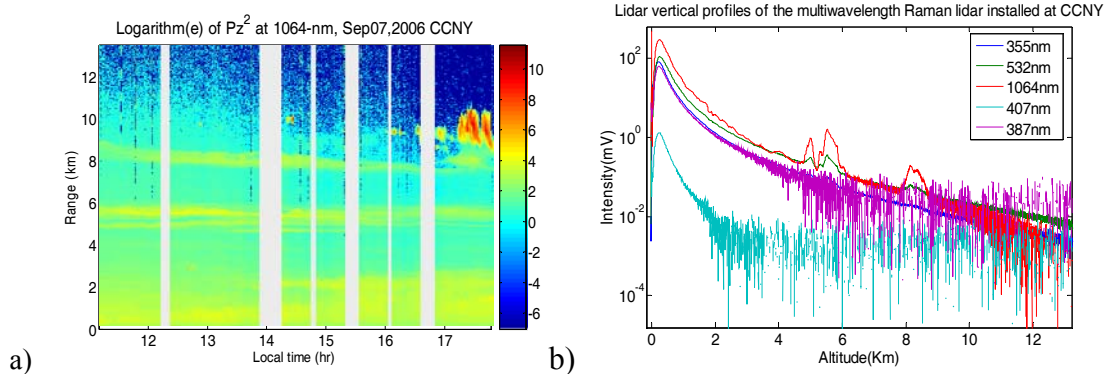


Figure 2.15. Lidar image and vertical profile measured at CCNY station over the day of Sept 7th, 2006

The background subtracted vertical profiles of the 5 channels are plotted in figure 2.15 b). During daytime measurements the solar radiation induces a high noise in the measurements.

#### 4. Conclusions and References

All these lidar system details presented above are of crucial importance to the aerosol retrievals presented in the future chapters. For example the 12 bit resolution, that is  $2^{12}=4096$ bytes and a maximum of 500mV allowed by the detectors we obtain a minimum of 0.112mV/bin (or byte). This value is useful in the calculations of the calibration constant of water vapor mixing ratio profile above CCNY (see chapter 3). A proper understanding of the system leads to correct measurements and therefore data analyses.

#### References:

- [1] Inventory of New York City Greenhouse Gas Emissions. New York City Office of Long-term Planning and Sustainability, April 2007.
- [2] <http://icerd.engr.ccnyc.cuny.edu/noaa/wc/index.html>
- [3] G.L. Stephens, *Remote Sensing of the Lower Atmosphere, An Introduction*, New York, Oxford University Press, 1994

- [4] R. Measures, *Laser Remote Sensing, Fundamentals and Applications*, Krieger Publishing Company; Reprint edition ,1992
- [5] B.A. Bodhaine et.al, “*On Rayleigh Optical Depth Calculations*”, Journal of Atmospheric and Ocean Technologies, Am. Meteo. Soc., Vol 16, p.1854-1861, 1999
- [6] H.C. van de Hulst, *Light Scattering by Small Particles*, Dover Publications, NY, 1981
- [7] I. Balin, “*Measurement and analysis of aerosols, cirrus contrails, water vapor and temperature in the upper troposphere with the Jungfraujoch lidar system*”, École Polytechnique Federale de Lausanne, These No 2975, 2004
- [8] V. Kovalev et.al, *Elastic Lidar, Theory, practice, and analyses methods*, John Wiley and sons, New Jersey, USA 2004
- [9] G.A. d’Almeida et al, *Atmospheric aerosols, Global climatology and radiative characteristics*, A Deepak Publishing, Virginia USA, 1991
- [10] M. Diem, *Modern vibrational spectroscopy*, Wiley Interscience, USA, 1993
- [11] I.N. Levine, *Quantum Chemistry*, Prentice Hall, New Jersey, USA, 2000
- [12] D.W. Hahn, *Raman Scattering Theory*,  
<http://plaza.ufl.edu/dwhahn/Raman%20Scattering%20Theory.pdf>
- [13] C. Bockmann, “*Hybrid regularization method for the illposed inversion of multiwavelength lidar data in the retrieval of aerosol size distributions*”, Applied Optics, Vol.40, No.9, 2001
- [14] D. Muler et al, “*Comprehensive particle characterization from three wavelength Raman lidar observations: case study*”, Applied Optics, Vol 40, No 27, 2001

- [15] D.N. Whiteman, “*Examination of the traditional Raman lidar technique. I Evaluating the temperature-dependant lidar equations*”, Applied Optics Vol. 42, No. 15, 2003
- [16] F.G. Fernald, “*Analyses of atmospheric lidar observations: some comments*”, Applied Optics , Vol. 23, No. 5, 1984
- [17] R. Tardif, “*Boundary layer aerosol backscattering and its relationship to relative humidity from a combined Raman –Elastic backscatter lidar*”, [http://www.rap.ucar.edu/staff/tardif/CUprojects/ATOC5235/ATOC5235class\\_project.pdf](http://www.rap.ucar.edu/staff/tardif/CUprojects/ATOC5235/ATOC5235class_project.pdf)
- [18] H. Inaba et al., “*Laser –Raman Radar-Laser Raman scattering methods for remote detection and analysis of atmospheric pollution*”, Opto-Electronics, Vol 4, pp 101-123, 1972.

## Chapter III

### **Water vapor retrieval based on Raman lidar technique**

Water vapor is an important greenhouse gas due to its high concentration in the atmosphere (parts per thousand) and its interaction with tropospheric aerosols particles. The upward convection of water vapor and aerosols due to intense heating of the ground lead to aggregation of water particles or ice on aerosols in the air forming different types of clouds at various altitudes. The condensation of water vapor on aerosols is affecting their size, shape, refractive index and chemical composition. The warming or cooling effect of the clouds hence formed are both possible depending on the cloud location, cover, composition and structure. The effect of these clouds on radiative global forcing and therefore on the short and long term global climate is of high interest in the scientific world. A major interest is manifested in obtaining accurate vertical water vapor profiles simultaneously with aerosol extinction and backscatter in the meteorological and remote sensing fields all around the globe. A reliable method of retrieving atmospheric water vapor profiles and aerosols in the same atmospheric volume is the use of Raman lidar that can provide high spatial resolution measurements in different wavelengths. The accuracy of the measurements is obtained by calibration techniques based on water vapor measurements presented in this paper along with aerosol backscattering measurements.

## 1. Introduction

The chemical property of water vapor of condensation on different types of aerosols, found in the atmosphere, is changing the chemical composition, shape and size of this particles, and at the same time it affects their optical properties and their contribution to the direct radiative forcing [1]. High cirrus clouds and contrails created by airplanes are formed from amalgams of water or ice crystals suspended in air cooled below the saturation temperature, allowing the moisture to form into small drops on microscopic particles called condensation nuclei that can be water molecules (homogeneous nucleation) or other metallic nitrogen oxides, etc (heterogeneous nucleation). The impact of high altitude clouds on global warming is larger than their cooling effect, the lower altitude clouds in change have an overall cooling effect [1-3]. Therefore good measurements of water vapor in the atmosphere with high spatial resolution are necessary. Among the wide range of methods described in section 1.2, the lidar system is capable of monitoring the water vapor mixing ratio in the atmosphere with high spatial resolution. The possible lidar interactions are split in two big mechanisms the elastic and inelastic ones. The elastic mechanism described by the Rayleigh and Mie scattering theories and inelastic mechanism described by the Raman process have been detailed in second chapter. The lidar system is collecting data in both analog to digital (A/D) format and Photon counting (PC mode). Data are typically averaged for approximately 1800 laser shots, which corresponds to 1-min datasets (a small amount of time is needed to clear the multi-channel cards). Since Raman scattering is a relatively weak process compared to elastic scattering, an important attribute of any successful Raman lidar is the ability to block the backscatter at the laser wavelength in the Raman channels. For this

beam splitters and filters have been used in front of the Raman channels detectors (see section 3 in chapter 2)

The theory that represents the base of the two calibration methods and aerosol backscatter radiation is explained in detail in section 2. The two calibration techniques are compared and validated in section 3 and the statistical analyses are performed in section 4.

The first part of this paper discusses and compares a set of two calibration techniques of the multi wavelength Raman lidar installed at the CCNY station. The calibration algorithms are based on a data fusion algorithm from different sources: day and night Raman Lidar measurements, CIMEL sunphotometer, global positioning meteorological system (GPS-MET) and radiosonde data from the OKX station (Brookhaven National Laboratory) in NYS, USA. The water vapor mixing ratio measured by the CCNY (City College of New York) Raman lidar is then validated with hygrometers surface measurements of the water vapor mixing ratio and NOAA meteorological predicted profiles. The hygrometers are collocated with the CCNY lidar system. The results of our calibrations are then presented to illustrate both short term and long term stability capabilities.

### **1.1 Climate impacts of atmospheric water vapor**

Due to its unique physical and chemical properties, water is crucial for the Earth system both on the local-short time scale (weather) and in long-term (global climate) related processes. Water is an universal solvent and is the main transport vector of matter and energy from the microscale of molecules and individual cells to the planetary scale. In the range of the pressure and temperature values encountered on the Earth's surface

and in its atmosphere, a water molecule can change phase easily between solid, liquid and gas, releasing or absorbing heat in the process (latent heat). Water vapor is the primary heat exchanger on the planet Earth. Because of its high latent heat value, and large thermal inertia, water also acts as a climatic thermostat [1]. Water circulation at the global scale (the hydrological cycle [2]) is solar powered and is connected with the rotation of the Earth. The global redistribution of precipitation occurs via atmospheric water vapor transport, synoptic-scale wind formations (jet stream), the southern oscillation (El Niño and La Niña) phenomena, and many others.

Water participates in all its three phase states in a multitude of chemical reactions in the atmosphere. Water vapor is involved in the formation of the ice content polar stratospheric clouds (reservoirs of halogenated molecules involved in the spring polar ozone depletion).

Water vapor is also the main source of the OH radical, an important atmospheric oxidant that is obtained from a homogeneous gas phase reaction of the water vapor molecule with the single-D excited state oxygen resulting from ozone photodissociation. Acid rain ( $\text{H}_2\text{CO}_3$ ,  $\text{HNO}_3$ ,  $\text{H}_2\text{SO}_4$ , etc) is formed by reactions of  $\text{CO}_2$ ,  $\text{NO}_2$  or  $\text{SO}_2$  in their aqueous phase with the OH radical. A schematic of the hydroxyl radical with chemical constituents in the atmosphere is presented in fig.3.1 [3].

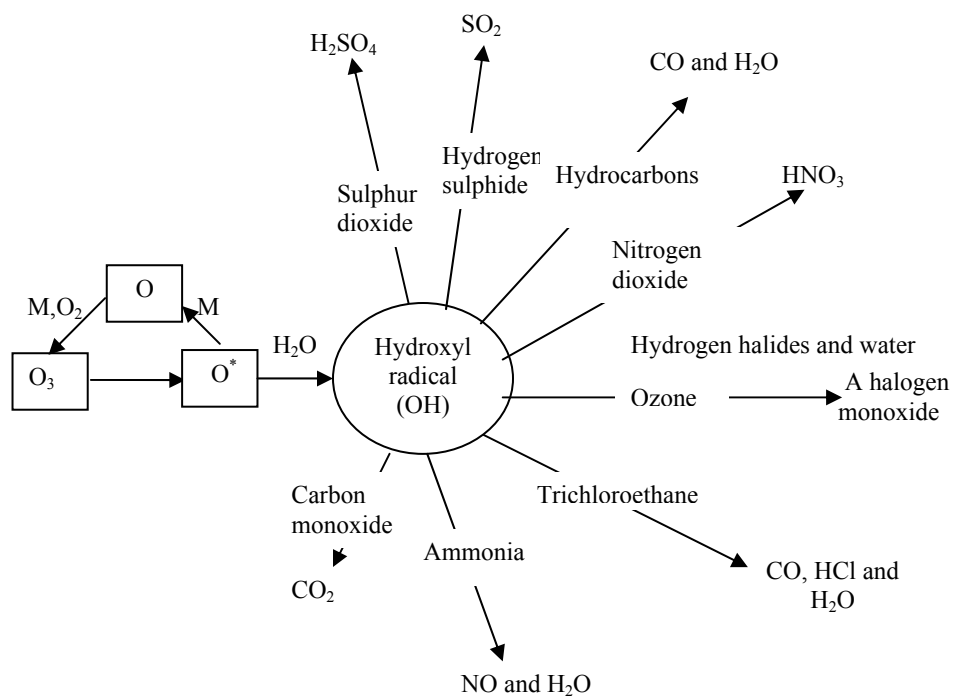


Figure 3.1 Illustration of the central role of OH radical in the oxidation of tropospheric trace gases [3]

Compared to other atmospheric trace greenhouse gases such as carbon dioxide ( $\text{CO}_2$ ), methane ( $\text{CH}_4$ ), nitrous oxide ( $\text{N}_2\text{O}$ ), or chlorofluorocarbons (CFCs), water vapor is the most efficient greenhouse gas because of its global concentration and its spectral properties (i.e transparent to incoming short-wave radiation from the Sun and opaque to long-wave radiation leaving the Earth). Indeed the electronic absorption spectrum of water vapor is located in the far UV ( $< 186 \text{ nm}$ ) while its vibrational-rotational spectrum contains three main bands centered at  $\nu_1 \sim 3657 \text{ cm}^{-1}$  ( $\lambda_1 \sim 2.73 \text{ }\mu\text{m}$ ),  $\nu_2 \sim 1595 \text{ cm}^{-1}$  ( $\lambda_2 \sim 6.3 \text{ }\mu\text{m}$ ), and  $\nu_3 \sim 3756 \text{ cm}^{-1}$  ( $\lambda_3 \sim 2.66 \text{ }\mu\text{m}$ ), with overtones, combinations and hot bands in the infrared and visible parts of the spectrum. The most intensive and broad  $\text{H}_2\text{O}$  vibration-rotation band is  $\nu_2$  centered at  $6.3 \text{ }\mu\text{m}$  that completely absorbs solar radiation between  $5.5$  and  $7.5 \text{ }\mu\text{m}$ . The overlap of the  $\nu_1$ ,  $\nu_3$  and the overtone of  $\nu_2$  ( $3.14 \text{ }\mu\text{m}$ ) also absorb completely the radiation from  $2.6$  to  $3.3 \text{ }\mu\text{m}$ . Other vibration-rotation bands are centered

close to 1.87, 1.38, 1.10, 0.94, 0.81 and 0.72  $\mu\text{m}$  and even some weaker bands are present in the visible part of the spectrum. The large dipole moment of  $\text{H}_2\text{O}$  and its isotopes are responsible for an intensive rotational spectrum that occupies a very broad region, extending from  $8\mu\text{m}$  to wavelengths of several cm [3]. The contribution of water vapor to the total greenhouse effect is estimated from 50- 60% [4] up to ~95% [5] and is still a controversial subject. The positive feedback between atmospheric temperature and water vapor is of crucial importance. To a first approximation, a  $1^\circ\text{C}$  increase in atmospheric temperature will cause a 6% increase in water vapor concentration, leading to further warming and thus initiating a positive feedback. This direct effect combined with the indirect effect (through cloud formation) of the water vapor on the Earth budget radiation is still poorly quantified [6] and scientific consensus is only qualitative at this point. The uncertainties stem from a lack of information on the high space-time variability of water vapor, which is difficult to measure due to the complex natural processes involved. Water vapor averages about one per cent by volume in the atmosphere and its distribution in time and space is highly variable: it comprises about 4 percent of the atmosphere by volume near the surface, but only 3-6 ppmv (parts per million by volume) above 10 to 12 km. Nearly 50% of the total atmospheric water is trapped in the planetary boundary layer (PBL, from 0 to 1-3 km) while less than 6% of the water is above 5 km, and only 1 % above 12 km. The annual average precipitation over the globe is about 1 meter, while the water-vapor column density (precipitable water) averages about 5 cm in the tropical regions and less than 1 mm at the poles. The average lifetime of the water vapor molecule in the atmosphere is about 9 days [7]. At any given location in the atmosphere, the water vapor content can vary markedly in a relatively short time span, owing to the passage of

cold or warm fronts, precipitation, etc. Because of the critical role that water vapor plays in most atmospheric processes, accurate water vapor profiles are needed in atmospheric modeling applications. Water vapor profiles are also needed for basic meteorology applications (i.e. the identification and study of frontal boundaries, dry lines,...), boundary layer studies (such as cloud formation/dissipation), development of climatological records, and for radiative transfer calculations. Therefore, as a most important greenhouse gas, water vapor concentration in the atmosphere should be determined along with the size, chemical composition and hygroscopic properties of the constituent aerosols of the atmosphere derived from their physical and optical characteristics. In this regard next section is briefly presenting a variety of atmospheric water vapor measurement techniques.

## **1.2 Water vapor measurement techniques**

Measurements of water vapor through the troposphere have proven to be difficult to obtain with good accuracy. A large variety of observational technologies have been developed to address this needs. Inexpensive *in situ* sensors (ground, towers) provide reasonably accurate water vapor measurements, but do not provide information on the water vapor content of the atmosphere at higher altitudes. *In situ* sensors have also been installed on commercial and research aircraft to measure water vapor. Measurements from commercial aircraft are promising but data would only be available when and where scheduled flights occur – a significant limitation. Research aircraft can provide high-quality measurements at any location but the cost is high for dedicated aircraft flights.

Another well established approach that provides a detailed vertical profile is radiosounding. In this technique, sondes are carried in the atmosphere by meteorological balloons and equipped with appropriate humidity sensors. However, the temporal and global coverage resolution is typically fairly coarse (launches every 12 h at specific meteorological stations). Moreover, radiosondes are expensive because their implementation is labor-intensive. Satellites can provide excellent global coverage of water vapor distribution, but the horizontal, vertical and temporal resolution is very coarse. Water vapor measurement sensors have evolved from goldbeater skin, hairs, lithium chloride, carbon hygistor, and thin film capacitors to the more recent frost point hygrometers (chilled mirror). Different types of Lyman - hygrometers have been developed based on the photo dissociation of H<sub>2</sub>O at  $\lambda < 137$  nm and the detection of the fluorescence ( $\lambda \sim 305$ - $325$  nm) of the excited OH radical. Open path measurements have also been made with tunable diode laser spectroscopy (TDLS) technique[8], which is based on the laser absorption in the near and mid infrared water vapor rotation-vibration spectrum. Microwave instruments using the H<sub>2</sub>O emission lines at 22.2 GHz or even 183 GHz are used mainly for the estimation of the stratosphere – mesosphere humidity [3]. The inversion techniques for retrieving vertical profiles are still in development, and the results have very poor vertical resolution. The FTIR spectrophotometers and the precision filter radiometers (PFR) are used to estimate the integrated total column water vapor based on various IR absorption bands and on VIS (719, 817 and 946 nm) atmospheric absorption. Based on the delays induced by the atmospheric water vapor on the paths between the antennas of the receiver and the satellites of the GPS network, the total column may be estimated. The continuous profiling of the water vapor dynamics with

high spatial and temporal resolution is possible with the use of the lidar techniques – both differential absorption (DIAL) [10] or rotational-vibrational Raman techniques [11, 12, 21].

The DIAL technique, first demonstrated in 1966 [10], exploits the differential absorption of water vapor in the VIS and NIR using two lidar emitted wavelengths: one on the peak of the absorption ( $\lambda_{ON}$ ) and other in the wing of the absorption line ( $\lambda_{OFF}$ ). The average absolute water vapor molecular number density  $n_{H_2O}(z)$  between  $z$  and  $z + \Delta z$  is retrieved as given in the relationship below:

$$n_{H_2O} = \frac{1}{2\Delta\sigma\Delta z} \ln \frac{P_{on}(z)P_{off}(z + \Delta z)}{P_{on}(z + \Delta z)P_{off}(z)} \pm \delta N_{H_2O}(z)$$

where  $P$  are the lidar backscatter signals and  $\Delta\sigma = \sigma_{on} - \sigma_{off}$  is the differential absorption cross-section. The DIAL technique is self-calibrated, providing absolute water vapor concentration in both daytime and nighttime. In addition, the OFF signal can be simultaneously considered for aerosol investigations. In spite of these advantages the water vapor DIAL technique requires specific laser sources emitting at various and precise  $\lambda_{ON}$ , (tunable lasers), having relatively narrow ( $\sim 10^{-4}$  nm) bandwidths, and precise, stable and well-known line shapes. In addition, the knowledge and accuracy of the absorption cross-section values is a systematic challenge due to their variation within a normal range of atmospheric temperature and pressure. In Eq. (1) the correction term  $\delta N_{H_2O}(z)$  is due to the interference (differential extinction) from various atmospheric gases and aerosols; and thus for a precise calculation, the atmospheric composition (aerosols and gases) has to be relatively well known. Several DIAL systems, ground based or airborne, using the water vapor absorption bands at 724, 815, 830 and 940 nm were developed [3],[10],[22],[23] and they provide troposphere and stratosphere water

vapor profiles. Due to the high absorption of the on-line in the lower troposphere, the ground based DIAL is less frequently used than the airborne or space nadir systems.

The Raman technique is based on the Raman effect. When a substance is subjected to an incident exciting wavelength, it exhibits the Raman effect; it reemits secondary light at wavelengths that are shifted from the incident radiation. The magnitude of the shift is unique to the scattering molecule, while the intensity of the Raman band is proportional to the molecular number density. The water vapor Raman lidar technique uses the ratio of rotational-vibrational Raman scattering intensities from water vapor and nitrogen molecules [12], which is a direct measurement of the atmospheric water vapor mixing ratio. The water vapor profile retrieval is presented in detail in section 2 of this second chapter.

Despite the small amount of water vapor in the free troposphere (above 2-3 km), recent studies [13,14] have shown that the middle and upper troposphere (600 - 200 hPa) water vapor content contributes as ~27-35% of the absolute greenhouse forcing due to the strong absorption in  $100\text{-}600\text{ cm}^{-1}$  spectral region which is within the spectral band of Earth surface infrared re-emission. Another study [15] shows that the contribution of water vapor in layers of equal mass to the climate sensitivity varies by about a factor of two with the height. The largest contribution comes from layers between 450 and 750 hPa, and the smallest, from layers above 230 hPa. The water vapor positive feedback is of crucial importance but poorly understood. The positive feedback of water vapor on the global mean surface temperature is also altitude sensitive. For example, the response of water vapor to the doubling of  $\text{CO}_2$  concentrations is 2.6 times greater above 750 hPa than below 750 hPa in terms of its effects on the Earth surface temperature[3]. High

resolution and more accurate upper troposphere and low stratosphere water vapor measurements are also needed for investigations into tropopause phenomena, vertical troposphere-stratosphere exchanges, nucleation processes, cirrus/contrail cloud formation, and lower stratosphere water vapor increasing concentrations (e.g. already observed increasing partially related to the CH<sub>4</sub> oxidation). In this context, this chapter presents the implementation of the Raman lidar technique at the CCNY station for water vapor profile measurements. Section 2 addresses the principle of the water vapor retrieval by Raman lidar technique. Section 3 presents a set of two calibration methods along with errors, corrections. Validations of the measurements with collocated GPS techniques and the closest space-time radiosounding are discussed. Typical daytime and night time water vapor profiles are also presented. Finally statistical analyses of the calibration methods are presented in section 4 and the conclusions and recommendations for the perspectives are given in section 5.

## **2. Raman lidar water vapor measurement methodology**

The Rayleigh scattering is relevant for molecular gases including N<sub>2</sub>, O<sub>2</sub> where the diameter is much smaller than the transmitted lidar radiation and can be defined by Measures (1992) as “Laser radiation elastically scattered from atoms or molecules is observed with no change of frequency”. The Mie scattering theory is for particulates (spherical) where the diameter is proportional to the laser wavelength and is defined in the same book as “Laser radiation elastically scattered from small particulates or aerosols (of size comparable to wavelength of radiation) is observed with no change in frequency [11,16]. There is no wavelength change in either mechanism described above

The elastic lidar equation is written as:

$$P_L(z) = \frac{K_s(\lambda_L, z)}{z^2} n_L(z) \frac{\pi d\sigma(\lambda_L, z)}{d\Omega} * \exp\left[-2 \int_0^z \alpha_{\lambda_L}^m(z) + \alpha_{\lambda_L}^a(z) dz\right] + b_{\lambda_L}(z) \quad (1)$$

where  $P_L$  is the detected lidar backscatter signal corresponding to both molecules and aerosols,  $K_s$  is a system function that is dependent on the optical transmission and detector efficiency, the overlap function and the area of the collector mirror of the telescope,  $n_L$  is the number density of active molecule,  $\frac{\pi d\sigma(\lambda_L, z)}{d\Omega}$  is the differential backscatter cross-section at the laser wavelength,  $\alpha_{\lambda_L}^a(z)$  and  $\alpha_{\lambda_L}^m(z)$  are the aerosol and molecular extinction coefficient at the laser wavelength and  $b_{\lambda_L}(z)$  is the background signal.

The second interaction mechanism where the ‘‘Laser radiation inelastically scattered from molecules is observed with a frequency shift characteristic of the molecule ( $h\nu - h\nu^f = E$ )’’ is called Raman Scattering which was detailed in the second chapter of the paper. The considered Raman transition is the radiation generated at longer wavelength from excitation (Stokes or red shift) due to its stronger response [12]. The water vapor Raman lidar technique uses the ratio of rotational-vibrational Raman scattering intensities from water vapor and nitrogen molecules, which is a direct measurement of the atmospheric water vapor mixing ratio. The backscatter radiation detected by the lidar is expressed as a function of range.

The water vapor and nitrogen Raman signals(inelastic lidar equation) are given by:

$$P_R(z) = \frac{K_s(\lambda_R, z)}{z^2} n_R(z) \frac{\pi d\sigma(\lambda_L, \lambda_R, z)}{d\Omega} * \exp\left[-\int_0^z (\alpha_{\lambda_L}(z) + \alpha_{\lambda_R}(z)) dz\right] + b_{\lambda_R}(z) \quad (2)$$

where  $P_R$  is the detected Raman lidar backscatter signal corresponding to nitrogen and water vapor,  $K_s$  is a system function that is dependent on the optical transmission and detector efficiency, the overlap function and the area of the collector mirror of the telescope,  $n_R$  is the number density of Raman active molecule,  $\frac{\pi d\sigma(\lambda_L, \lambda_R, z)}{d\Omega}$  is the differential Raman backscatter cross-section,  $\alpha_{\lambda_L}(z)$  is the aerosol and molecular extinction coefficient at the laser wavelength and  $\alpha_{\lambda_R}(z)$  is the aerosol and molecular extinction coefficient at the Raman wavelength and  $b_{\lambda_R}(z)$  is the background signal.

By taking the ratio of the two signals one can obtain the water vapor mixing ratio profile, equation 3.

$$\frac{P_{H_2O}(z)}{P_{N_2}(z)} = \left[ \frac{K_{H_2O}}{K_{N_2}} \left[ \frac{\left( \frac{d\sigma}{d\Omega} \right)_{H_2O}}{\left( \frac{d\sigma}{d\Omega} \right)_{N_2}} \right] \frac{T_{H_2O}}{T_{N_2}} \right] * q_{H_2O}(z) \frac{M_{air}}{M_{H_2O}} \quad (3)$$

where T is the transmission for the two wavelengths through the atmosphere and M represents the mass of water vapor in atmosphere and dry air. The water vapor mixing ratio profile may be retrieved using equation (4).

$$q_{H_2O}(z) = \frac{K_{N_2}}{K_{H_2O}} \frac{\left( \frac{d\sigma}{d\Omega} \right)_{N_2}}{\left( \frac{d\sigma}{d\Omega} \right)_{H_2O}} \frac{T_{N_2}}{T_{H_2O}} \frac{M_{H_2O}}{M_{N_2O}} \frac{P_{H_2O}}{P_{N_2}} \quad (4)$$

where  $q$  is the water vapor mixing ratio in [g/Kg dry air] or in [ppmv].

Hence

$$q_{H_2O}(z) = C * \Gamma * \left[ \frac{P_{H_2O}}{P_{N_2}} \right] \quad (5)$$

where  $\Gamma = \frac{T_{N_2}}{T_{H_2O}} \cong 1$  and C is the calibration function. Due to no aerosol influence on the 407nm and 387nm Raman channels this technique is relatively free of systematic errors (aerosol effects), can be operated from the ground (the radiation is not absorbed by the water vapor itself) and its use is relatively simple. Its main limitation is the relatively small backscatter Raman cross- sections, that result in weak Raman signals compared with the elastic backscatters or the electronic noise induced in daytime by solar radiation (see figures 2.11 and 3.11).

As mentioned above one might observe that the method requires the use of a calibration constant to be used in the retrieval.

$$C = \frac{K_{N_2} \left( \frac{d\sigma}{d\Omega} \right)_{N_2} M_{H_2O}}{K_{H_2O} \left( \frac{d\sigma}{d\Omega} \right)_{H_2O} M_{N_2O}} \quad (6)$$

There have been many calibration techniques proposed and used along time [3],[18-20]. Some methods suggest an approximate external calibration, a one point in situ value, or calibration based on horizontal lidar measurements. The method we adopt is discussed next.

### 3. Calibration and validation

#### 3.1 Data fusion

The water vapor profiles are based on the CCNY multi-wavelength Raman lidar measurements at 407nm and 387nm. In addition, a calibration is needed. Unfortunately, radiosondes are not available during daylight hours in close proximity (Brookhaven National Laboratory BNL (40°82' north latitude and 72°86' west longitude)). Therefore, we need an alternative method for calibration using total column water measurements as well as a correction factor which accounts for the fact that the Raman lidar path does not cover the entire atmosphere column. Total column measurements can be obtained either through the Cimel sun photometer (day only) or through global positioning meteorological data (GPS). To obtain correction factors defining the total column water over a finite path, we invoke large scale statistical measurements from radiosondes over our area generated from Hysplit. In this way, monthly averaged water vapor fraction in the atmosphere above CCNY location for a given altitude range can be obtained and used in the retrieval of the lidar water vapor vertical profiles.

#### 3.2 GPS/ sunphotometer and radiosonde based calibration technique

The calibration approach can be summarized as follows

Step #1 Calculate uncalibrated water mixing ratio profile  $\frac{P_{H_2O}}{P_{N_2}}$

Step #2 Given air-pressure from radiosonde calculate total uncalibrated column water vapor using sunphotometer/GPS and multiply by fraction parameter describing the amount of total water vapor in lidar path to obtain the true lidar path water content

$$W_{Tot}^{Lidar} = f(z_0, z_{max}) W_{tot}^{GPS/Aeron} = C \int_{z_0}^{z_{max}} \frac{\overline{P_{H_2O}}}{\overline{P_{N_2}}} * \rho_{N_2} dz$$

Once the calibration constant is obtained, the mixing ratio relative to dry air density is simply

$$q_{H_2O}(z) = C * \frac{\overline{P_{H_2O}}}{\overline{P_{N_2}}} * \frac{\rho_{N_2}}{\rho_{air}} \quad (7)$$

To assure a realistic water vapor fraction in the retrieval process analyses have been performed on water vapor variability in the planetary boundary layer for different months and lidar path ranges. Figure 3.2 indicate the amount of variability of the water vapor mixing ratio over the four seasons and for 3 different lidar range heights.

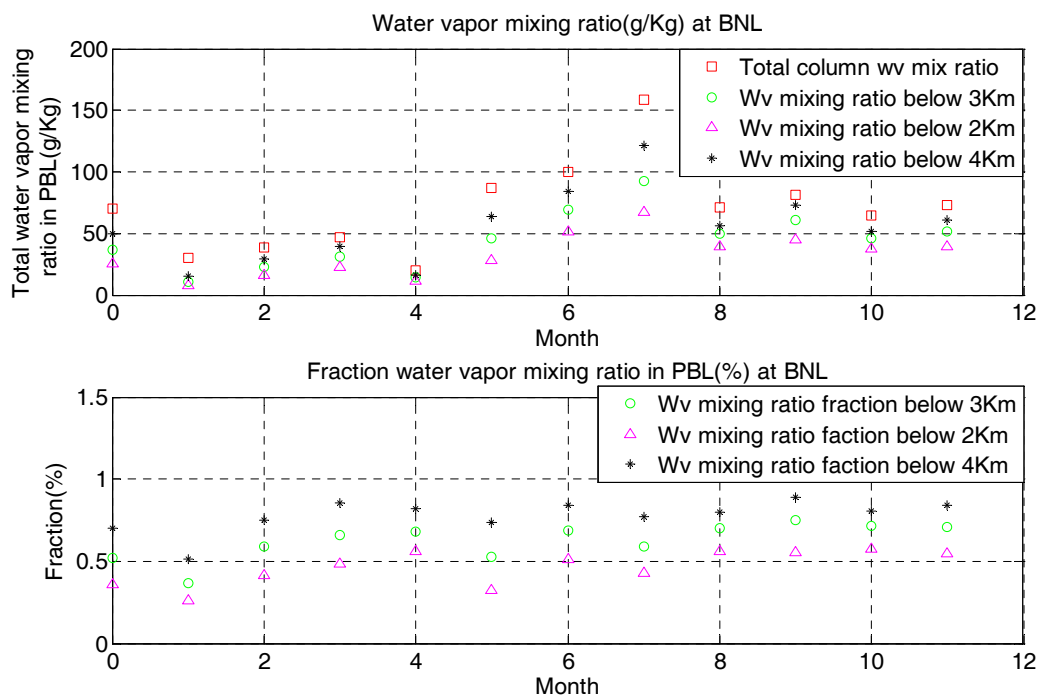
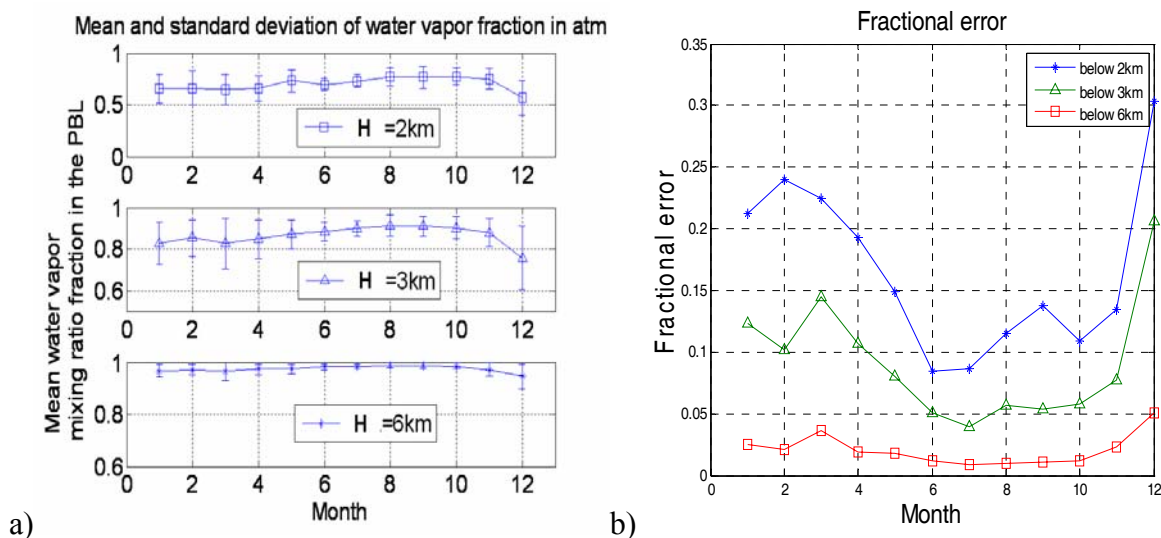
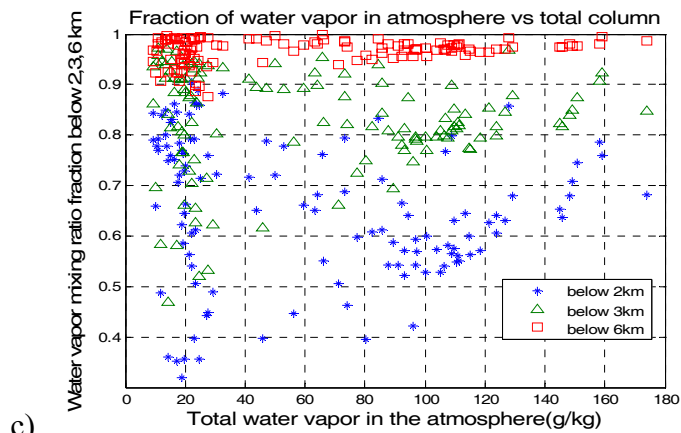


Figure 3.2. Measured water vapor mixing ratio and fraction of it below 2km, 3km and 4km, above Brookhaven National Laboratory (BNL), during 2007

Statistical analyses of the modeled water vapor fraction in atmosphere by Hysplit is presented in figure 3.3a) for different heights in atmosphere. In figure 3.3b) the fractional error which is defined as the standard deviation over the mean has been plotted for different altitude. Figure 3.3c) plots the fraction of water vapor vs total integrated water vapor. Also, comparisons of the errors between the CCNY station water vapor retrievals below 2km at 12pm/8pm and similar retrievals at BNL at 8pm (evening radiosonde launching time) indicate errors above 30% in figure 3.3 d) and e). Due to these high errors the used water vapor fraction is the one indicated by the Hysplit model above CCNY and not the one measured by the radiosonde.

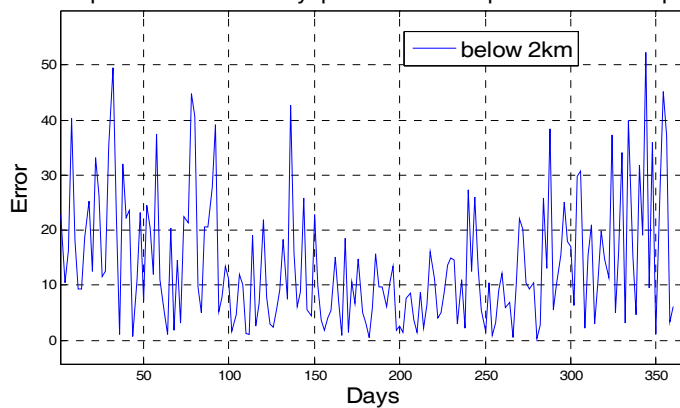
The results of this analysis show that for sufficiently high water vapor loadings (i.e warmer conditions), fractional error estimates as low as 10% can be achieved in day time conditions where  $z_{max} \sim 2km$ . On the other hand, a clear improvement is seen with  $z_{max}$  to 6km. Finally, a spread in the fraction for low water loading conditions is seen for daytime conditions.





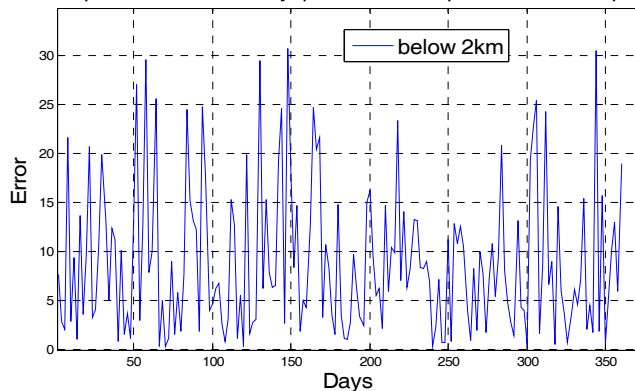
c)

Water vapor error between Hysplit CCNY at 12 pm and BNL at 8pm,2007



d)

Water vapor error between Hysplit CCNY at 8 pm and BNL at 8pm, 2007



e)

Figure 3.3 a) Water vapor as fraction from the total column integrated water vapor in the atmosphere  
 b) Fractional error (standard deviation/mean) by month, c) Water vapor mixing ratio fraction versus total column  
 d) Error of water vapor amount between CCNY at 12pm and BNL at 8pm (radiosonde evening launching time) stations at below 2km  
 e) Error of water vapor amount between CCNY at 8pm and BNL at 8pm (radiosonde evening launching time) stations at below 2km

Finally, we should address the accuracy of the total water column. An inter-comparison of the GPS integrated water vapor column with the AERONET corresponding reading show good correlation with a small percentage error deviation standard deviation ( $<0.05$ ) as noticed in figures 3.4 .

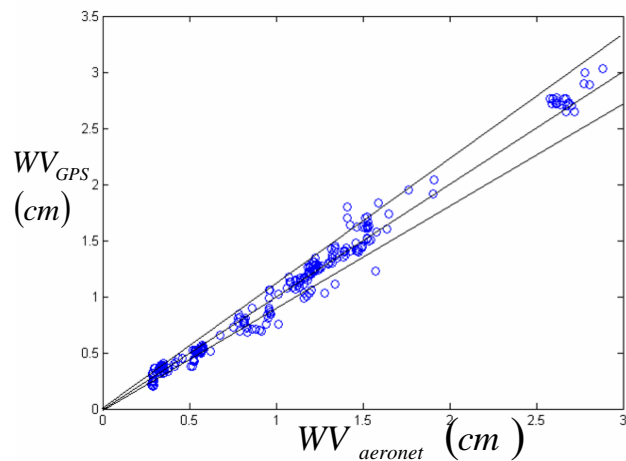


Figure 3.4 GPS-Aeronet intercomparison with 10 percent error bars

Furthermore, a histogram analysis below shows no bias.

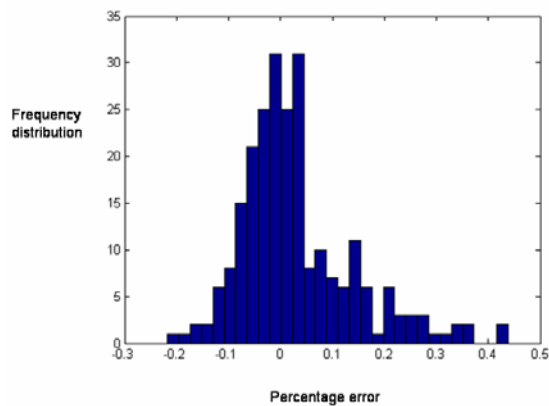


Figure 3.5 Frequency distribution of the aeronet percentage error with respect to GPS measurements

### 3.3 Validation of measurements

#### 3.3.1 Daytime water vapor measurements

As a preliminary test, we match our derived water vapor mixing ratio using the technique discussed above in figure 3.6 to the 2 Brookhaven radiosondes bracketing our measurements.

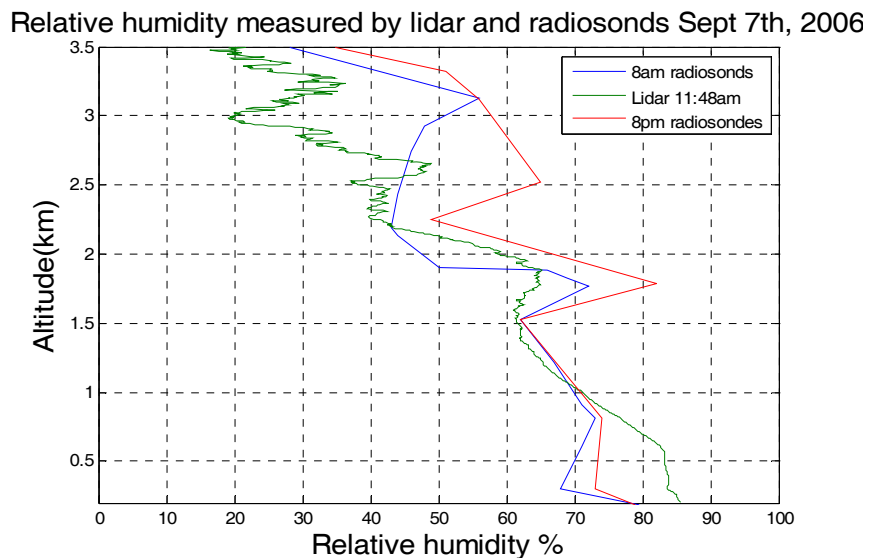


Figure 3.6 Water vapor mixing ratio profile measured by the CCNY lidar and radiosondes at the BNL station at 11:48am, 09/07/06

We observe good agreement below 2.5 km. The vertical profile above this height is unreliable due to the electronic noise induced by the solar background. Other cases are presented below.

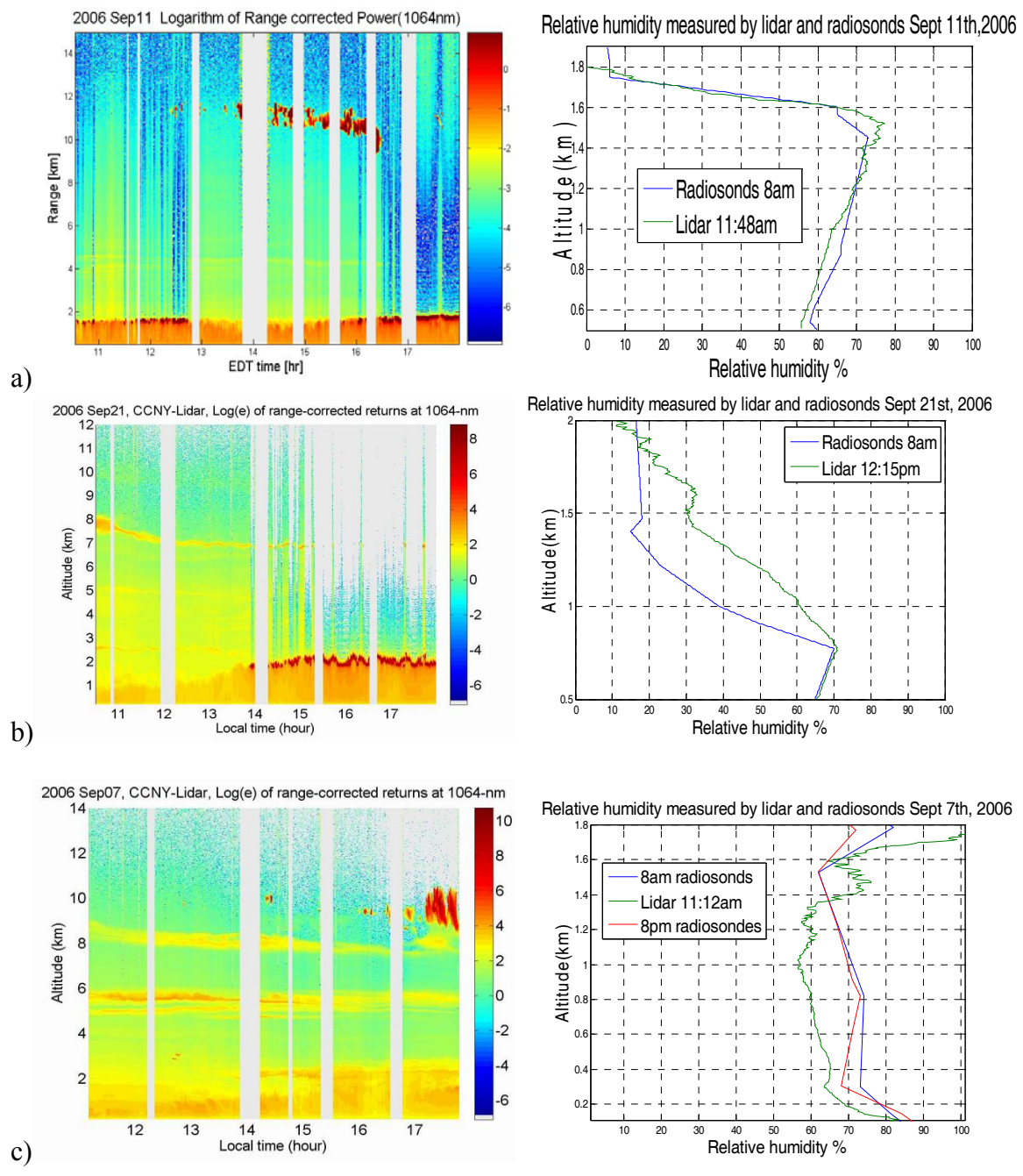


Fig. 3.7. Relative humidity retrieved on different days at morning time around 11:30am

In addition, we have made some preliminary comparisons (October 4<sup>th</sup> and 5<sup>th</sup>, of 2007) of the lidar data with WRF (weather research and forecasting model) which indicate reasonable agreement as seen in figure 3.8

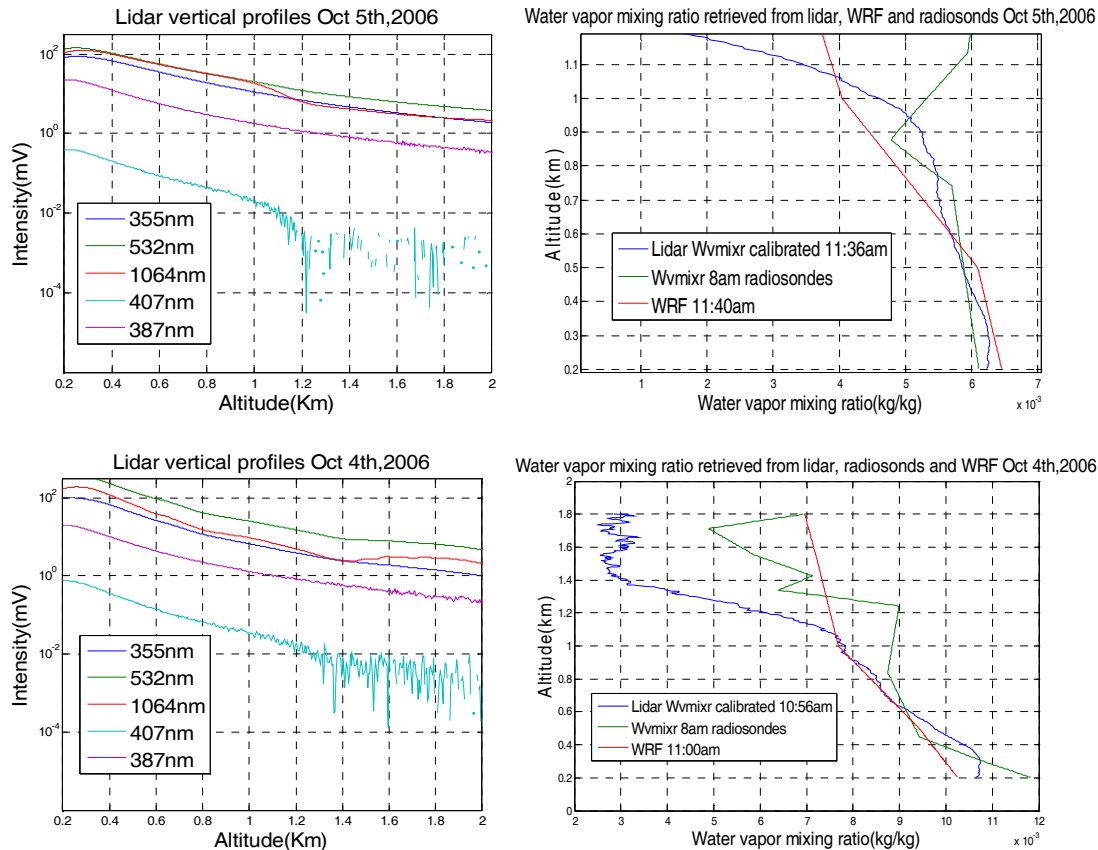


Figure 3.8 Lidar, radiosonde and WRF (weather research and forecasting model )

On clear observation is the range limitations for daytime observations. Clearly, night measurements are desirable.

### 3.3.2 Nighttime water vapor measurements

We considered for analyses two cases October 31, 2006 and May 23<sup>rd</sup>, 2007. The lidar image obtained during late evening hours has been plotted for the 1064nm channel in figure 3.9

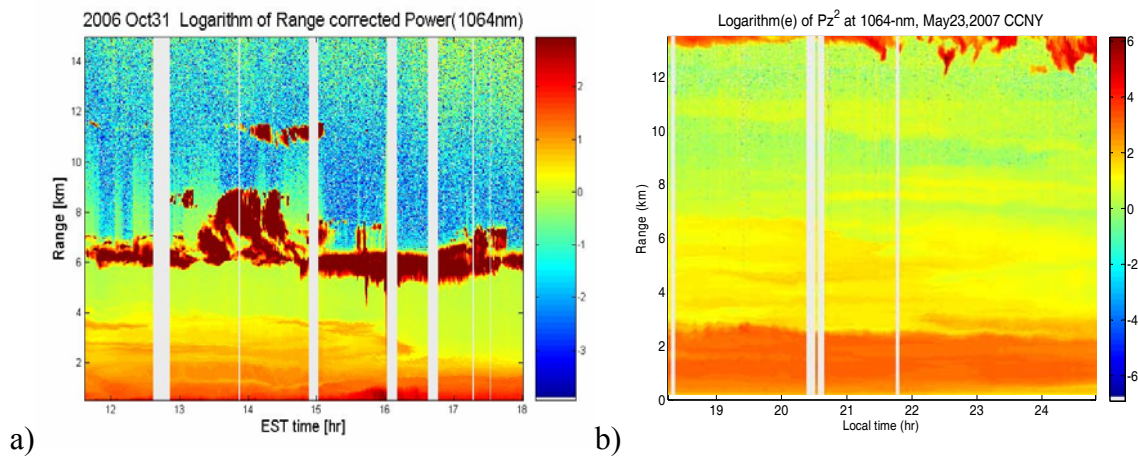


Figure 3.9 .Lidar image on a)October 31<sup>st</sup> 2006 between 12pm and 6 pm and on b) May23 between 6:15pm until 12:50am on May24,2007

This day was chosen due to the useful air patterns seen by hysplit. In particular, as seen in Figure 3.10, the wind patterns are generally pushing the air to NYC from Brookhaven at the time of measurement increasing the likelihood that the air parcels are likely to be similar.

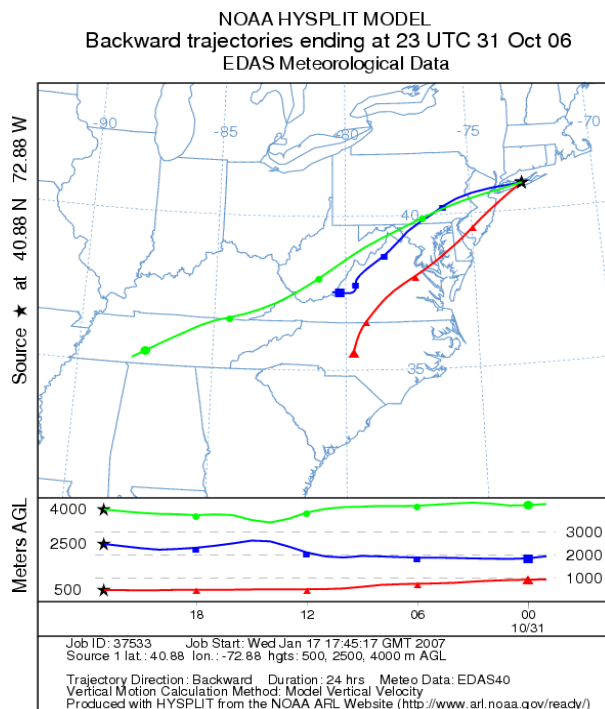


Figure 3.10 Backward trajectories plotted for October 31<sup>st</sup>, 2006 at 8pm

The night time measurements performed in both the analog to digital mode(A/D) and photon counting(PC) mode plotted in figure 3.11. The first case is a twilight case while the second is a show an obvious improvement in the height to which the water vapor can be determined. As it can be noticed the green and UV, PC channels are saturated at close range where the signal is very strong and thus we must transfer to A/D data in this region. Therefore, we must knit the PC and A/D data appropriately. For this we selected a small region between 1 to 1.2km in the A/D signal where the Raman water vapor has values above 0.1mV. This value was chose such that for a maximum of 500mV per  $2^{12}$  digital bins there is at least 1 digital bin used towards retrieval (i.e.  $500\text{mv}/4096\text{bytes}=0.122\text{mV}/1\text{byte}$ ).

Between 1.2km and 10km we used PC data only. In the end the data was smoothed using a sliding average method over 30 data values and calibrated using the above described technique.

The power signals are plotted in fig 3.9 the altitude at which the water vapor can be determined with relative good accuracy is around 6km during twilight time increasing to 10km for complete night conditions.

Background subtracted lidar signal Oct 31st, 2006, 5:32pm

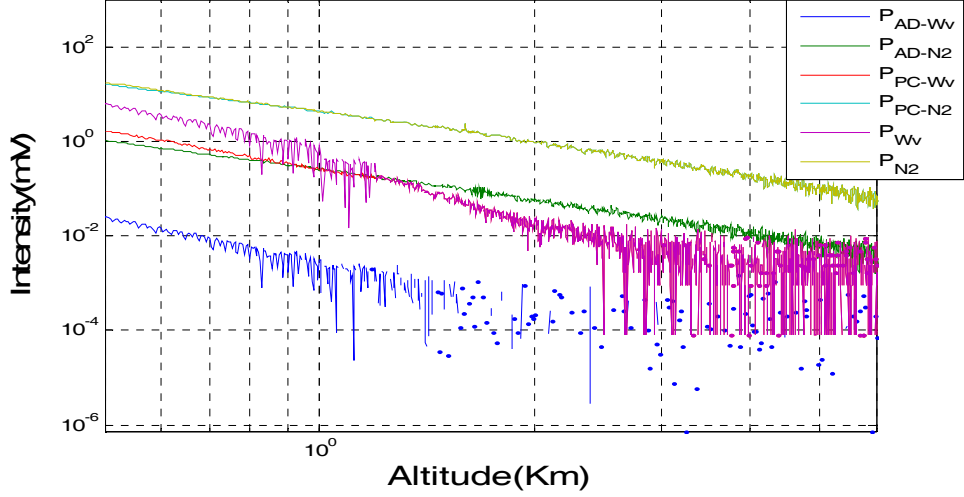


Figure 3.11a Night time vertical profiles of the five lidar returns in the Analog to digital mode and Photon Counting mode respectively (October 31, 2006)

Background subtracted lidar signal May 23rd, 2007, 8:46pm

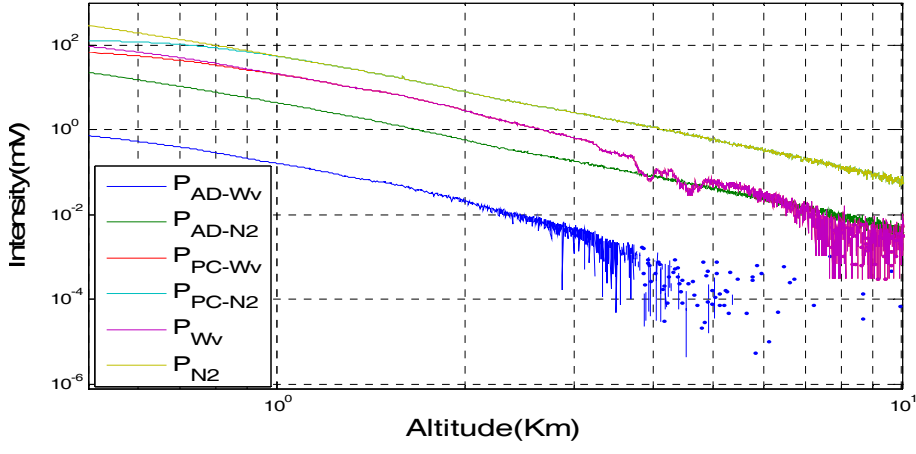


Figure 3.11b A/D and PC Raman lidar returns at 8:46pm on May 23<sup>rd</sup>, 2007

Comparisons with radiosonde profiles are illustrated in fig 3.12

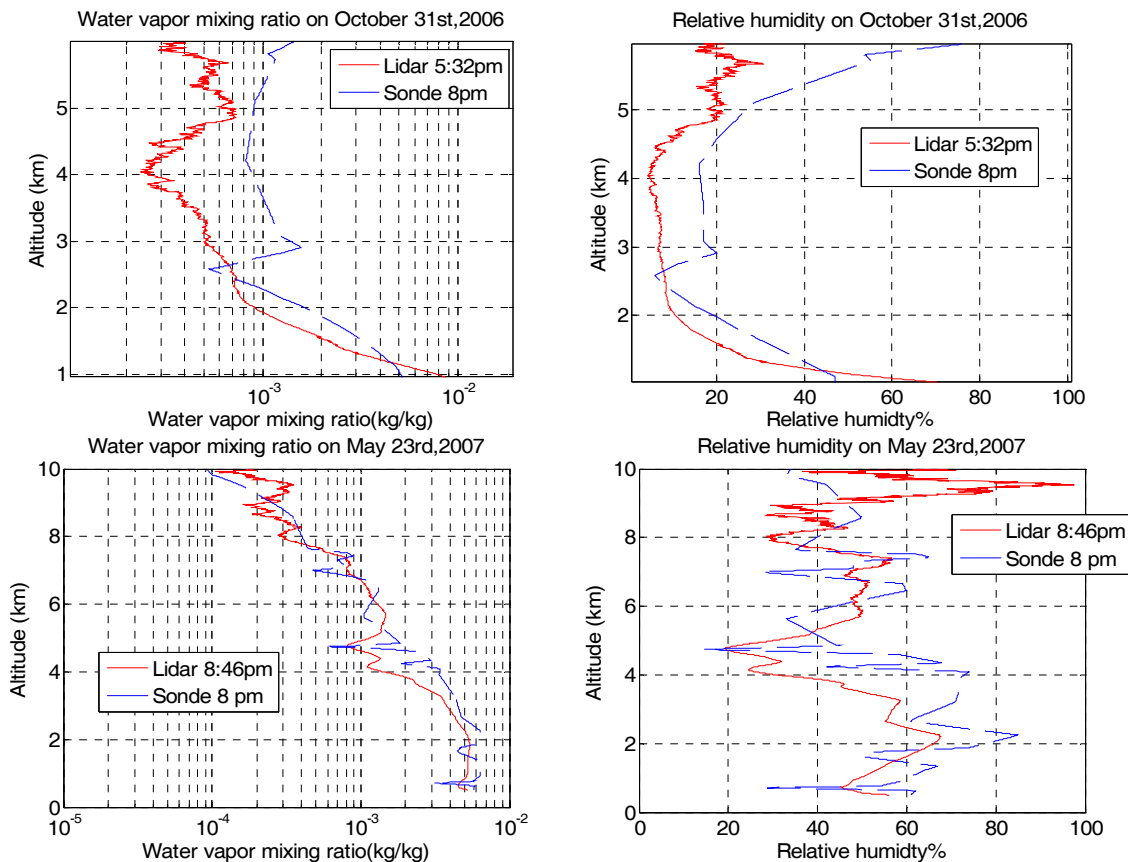


Figure 3.12 Water vapor mixing ratio measured in the photon counting mode and calibrated by the above detailed method. Water vapor mixing ratio vertical profile obtained from an average of 60 lidar files collected before 8:46pm on May 23<sup>rd</sup>, 2007

In general, for the case where the weather is fairly uniform, the water vapor and RH vertical profile for both twilight and night time conditions, the matchup is quite good with night time measurements to 10km possible.

However, there are days when the radiosondes and the lidar measurements do not entirely agree. The days observed when the two calibration constants lead to big discrepancies in the relative humidity profile have been carefully analyzed. Two of such

days are September 25<sup>th</sup>, 2006 and April 25<sup>th</sup>, 2007 displayed in figure 3.24. Analyzing the meteorological conditions at the two locations (BNL and CCNY) the divergences can be easily justified.

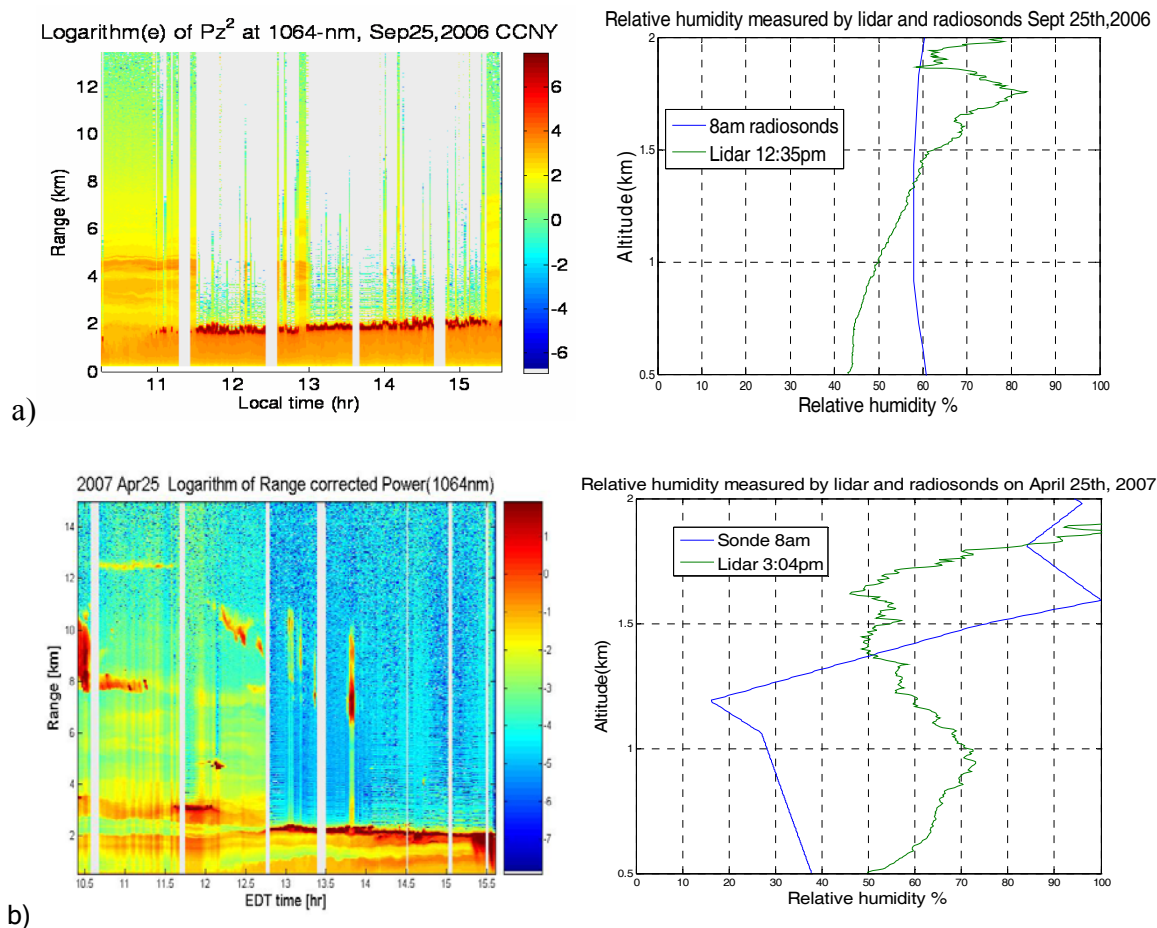


Figure 3.13 Lidar images and relative humidity profiles retrieved on

a) September 25<sup>th</sup>, 2006 and b) April 25<sup>th</sup>, 2007

In particular, it is expected to see higher humidity at CCNY below 2000m due to the atmospheric currents that are pushing the clouds above BNL which are discernable from MODIS and hysplit datasets. An additional indication of higher humidity above Brookhaven is the plot in fig. 3.14 that show temperatures close to the saturation (cloud or fog) up to 2.5km in the morning and 1.8km in the evening while the human observers at CCNY indicate no fog or clouds present during the measurements (this can also be

verified by AERONET Hysplit sounding models of dew point temperature and temperature above CCNY).

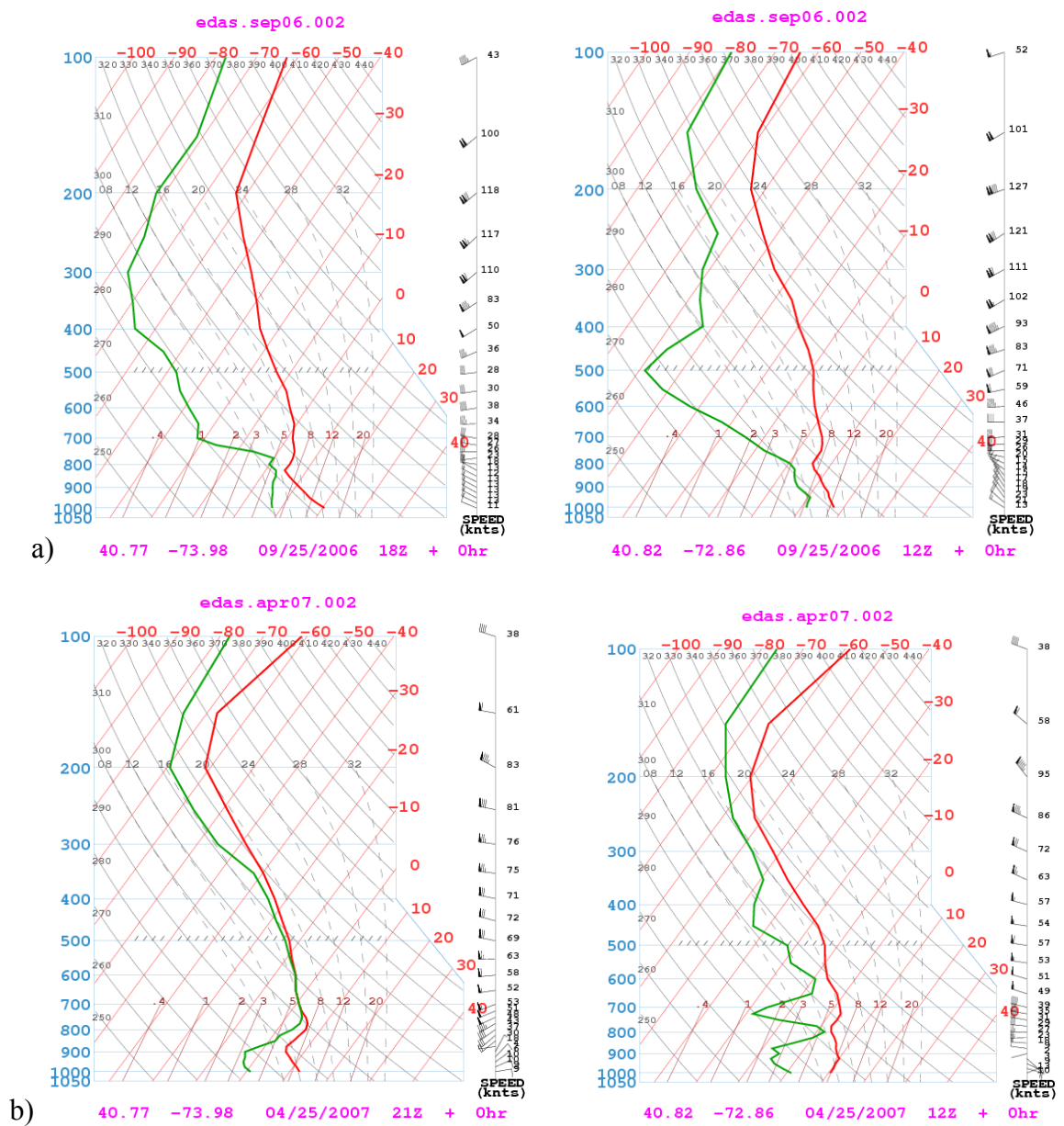


Figure 3.14 Temperature and dew point temperature profiles measured above CCNY and BNL on  
a)09/25/06 at 1pm at CCNY and 8am at BNL; b)04/25/07 at 4pm at CCNY and 8am at BNL

Finally, we examine surface measurements of the relative humidity using our MET Station Hygrometer and comparing with low altitude retrievals.

Table 3.1 Comparison of surface relative humidity as retrieved  
by hygrometer and lidar

Day Instrument	August 12th	September 11th	September 21th	October 5th
Hygrometer (surface relative humidity ~90 m above the surface)	28%	42%	40%	51.5%
Lidar calibrated water vapor measurements (~500 m above the ground)	28%	55%	65%	51%

Table 3.1 displays a summary of 4 days of hygrometer surface measurements and lidar calibrated water vapor measurements.

#### 4. Conclusions and References

Validation of the retrievals is achieved by comparing the water vapor mixing ratio measurements at CCNY with the vertical profiles of the mixing ratios measured by the radiosondes at Brookhaven National Laboratory, NY. Therefore the backward trajectories of the wind circulation from/to CCNY station to/from Brookhaven weather station played an important role in deciding the suited days for validation. The first conclusion that has to be studied in more detail is that calibrating the lidar by use of radiosonds alone is not a reliable method due to the high horizontal variability of the water vapor in the atmosphere that can lead to big discrepancies in estimations. One can use the temperature profile of the day (less horizontal variability) to determine for example air density but not water vapor mixing ratio for stations that are approximately 70 miles away.

Instead, we choose to use a method based on total water column and a fraction parameter determined by statistical radiosondes. Estimated based on fraction variability and total water retrieval are quite better than the variability seen between water profiles observed at different locations and site positions.

As observed, day time measurements limit the water vapor signal to less than 2.5 km due to the strong solar background . On the other hand, night measurements of the water vapor mixing ratio in the photon counting mode have been performed allowing retrievals of water vapor vertical profiles to much higher altitudes.

### *References*

- [1] P.S. Eagleson, “*The role of water in climate*” Proceedings of the American philosophical society, 2000.
- [2] D J Seidel, “*Water Vapor: Distribution and Trends*“, Encyclopedia of Global Environmental Change, John Wiley & Sons, 2002
- [3] I. Balin, *Measurement and analysis of aerosols, cirrus contrails, water vapor and temperature in the upper troposphere with the Jungfraujoeh lidar system*, École Polytechnique Federale de Lausanne, These No 2975, 2004
- [4] C. Minghang et al., “*Assimilating TOVS Humidity into the GEOS-2 Data Assimilation System*”, Vol 12, pp. 2983–2995,1999
- [5] J. T. Kiehl et al., *Earth’s Annual Global Mean Energy Budget*, American Meteorological Society, 1997
- [6] L.Bernstein et al, Intergovernmental Panel on Climate Change Fourth Assessment Report, Climate Change: 2007, <http://www.ipcc.ch/ipccreports/ar4-syr.htm>

- [7] J.M. Wallace, P.V. Hobbs, *Atmospheric Science An introductory survey*, Second edition, Academic Press Elsevier , 209-262, 2006
- [8] C S. Edwards et. al, “Development of an IR tunable diode laser absorption spectrometer for trace humidity measurements at atmospheric pressure”, *Applied Optics*, Vol 38, pp. 4699-4704, 1999
- [9] A. Giez et al, “Water Vapor Flux Measurements from Ground-Based Vertically Pointed Water Vapor Differential Absorption and Doppler Lidars”, *American Meteorological Society*, Vol 16, Issue 2, pp.237-250,1999
- [10] J.R. Measures, *Laser Remote Sensing: Fundamentals and Applications*, Krieger Publishing Company, Reprint Edition ,1992
- [11] A. Ansmann et al, “*Independent measurement of extinction and backscatter profiles in cirrus clouds by using a combined Raman elastic-backscatter lidar*”, *Applied Optics*, Vol. 31, 1992
- [12] R. Measures, “*Laser Remote Sensing: Fundamentals and Applications*”, Krieger Publishing Company, 1992
- [13] L.Palchetti et al., “*Measurement of the water vapour vertical profile and of the Earth’s outgoing far infrared flux*”, *Atmospheric Chem. And Phys. Discussions*, 2007
- [14] A. Stenke et al., “*Impact of stratospheric water vapor trends on ozone chemistry*”, *Atmos. Chem. Phys.*, Vol. 5, pp. 1257–1272, 2005
- [15] E.K. Schenider,” *Tropospheric Water Vapor and Climate Sensitivity*”, *Am. Met Soc.*, Vol 56, pp1649-1658, 1998
- [16] Kovalev, *Elastic Lidar*,

- [17] M. Triola, *Elementary Statistics*, Pearson Custom Publication, MA, USA, 2006
- [18] J.A. Reagan, *Fellow, IEEE*, X. Wang, and M. T. Osborn, *Spaceborne Lidar Calibration From Cirrus and Molecular Backscatter Returns* IEEE Transactions on Geoscience and Remote sensing, vol. 40, No.10, October 2002
- [19] Z. Liu, M. McGill, Y. Hu, C. Hostetler, M. Vaughan, and D. Winker, *Validating Lidar Depolarization Calibration Using Solar Radiation Scattered by Ice Cloud*, IEEE, Geoscience and Remote sensing letters, vol.1, No.3 July 2004
- [20] D. N. Whiteman@ all, *Scanning Raman Lidar Error Characteristics and Calibration For IHOP*, NASA/HQ
- [21] D. D. Turner et al, “*Automated Retrievals of Water Vapor and Aerosol Profiles from an Operational Raman Lidar*”, Journal. of Atm. And Oc. Technology, Vol 19, pp.37-50, 2001
- [22] V. Wulfmeyer et al., “*Investigations of Humidity Skewness and Variance Profiles in the Convective Boundary Layer and Comparison of the Latter with Large Eddy Simulation Results*”, American Meteorology Society, Vol 56, pp 1077-1087, 1999
- [23] C.J. Grund et al., “*Feasibility of Tropospheric Water Vapor Profiling Using Infrared Heterodyne Differential Absorption Lidar*”, Proceedings of the Fifth Atmospheric Radiation Measurement (ARM) Science Team Meeting, San Diego California, 1995

## Chapter IV

### **Aerosol hygroscopic properties**

The affinity of aerosol particles to water, as measured by the relative humidity (RH), plays an important role in several processes. It influences visibility reduction in the atmosphere, modifies aerosol gas chemistry through multiphase reactions, modifies the particles ability to act as cloud condensation nuclei resulting in an influence to the Earth's radiation budget.

Knowledge of the aerosol optical properties (backscatter, absorption or emission) in the infrared and microwave region, and their influence on electromagnetic propagation, are of particular interest to a wide range of scientific disciplines. In the environmental study of the atmosphere the major interest is manifested towards understanding the radiative transfer budget. The presence of atmospheric water vapor triggers water-soluble particles to act as cloud condensation nuclei and to initiate the cloud formation process. Once generated, cloud particles also attenuate atmospheric radiation to emphasize the indirect effect of aerosol particles. Other disciplines interested in the hygroscopic properties of the aerosols have military or communication applications. The use of electro-optical systems in military hardware has made the study of aerosols a favorite military research subject. Also short term forecasts of aerosol and optical conditions become feasible when the influence of humidity on aerosol is well understood and therefore a relation of weather to weapons performance is well understood. [1]

## 1. Introduction

The optical properties, health effects, atmospheric lifetime, and climate impact of ambient aerosols are influenced directly by their size distribution, chemical composition, and phase. The aerosol hygroscopicity, which is also a function of composition, governs the size and phase changes of these particles when subjected to varying ambient relative humidities (RH). In this chapter we presented the relationship between aerosol backscattering properties and relative humidity and identification of different types of aerosol sources based on their hygroscopic behavior. In previous work, simultaneous measurements of relative humidity (RH) with backscatter measurements from a surface nephelometer were used to probe the hygroscopic properties of aerosols. However, most of these measurements were not able to probe the high RH domain since such high RH (95% and above) is very difficult to control. For this reason, experiments using a 355nm Raman water vapor and aerosol lidar at the Atmospheric Radiation Measurements (ARM) site were used [2]. The measurements were capable of providing simultaneous backscatter and RH profiles, and performing the experiments under low altitude cloud decks insured stable well mixed layers as well as probing RH profiles to above 95%. The later is required for the separation of different aerosol hygroscopic models.

The proposed research here is based on the use the water vapor and aerosol backscatter measurements in the exploration of the nature and variability of urban aerosol hygroscopic properties using multi-wavelength Raman lidar measurements at 355nm, as well as backscatter measurements at 532nm and 1064nm. The addition of the longer wavelength channels allows us to more accurately validate the homogeneity of the aerosol layer as well as provide additional multi wavelength information that can be used

to validate and modify the aerosol models underlying the hygroscopic trends observed in the Raman Channel. In particular, we show that aerosols backtracked to different sources (bio-mass, maritime) have different hygroscopic behavior which are compared to theoretical models.

### **1.1 Basics of the aerosol hygroscopic properties**

Atmospheric aerosols (also referred to as particulate matter or simply PM) are a complex chemical mixture of solid and/or liquid particles suspended in the air. Their presence is often directly observable by the human eye as haze in many industrial regions, as well as the rural areas subjected to heavy biomass burning, caused by the scattering and absorption of sunlight. The sizes of the atmospheric aerosols widely range from a few nanometers (nm) to tens of micrometers ( $\mu\text{m}$ ) in diameter. The so-called superfine particles (less than about  $0.1\mu\text{m}$ ) mainly arise from gas-to-particle conversion whereby gases such as sulfur dioxide ( $\text{SO}_2$ ), nitric oxide and nitrogen dioxide ( $\text{NO}_x$ ) and volatile organic carbon (VOC) are oxidized and condensed. The so-called coarse particles (greater than  $1\mu\text{m}$ ) are usually produced mechanically, e.g. wind blowing over dusty region, evaporation of sea spray, etc. Between the superfine and the coarse mode particles are the fine particles (about  $0.1 \sim 1\mu\text{m}$ ). This mode is also referred to as the accumulation mode because the aerosols in this size range accumulate from the coagulation and condensational growth of superfine particles and tend to remain in the atmosphere for relatively long times (i.e., a few days) because of their relatively low sedimentation and coagulation rates. This mode is of particular interest in regard to the Earth's energy budget and climate change due to their efficient interaction with the solar

radiation, (i.e., most of the solar energy is in the visible part of the spectrum  $\sim 0.5\mu\text{m}$ , and the particles of about the same size as the wavelength scatter light efficiently), and their optimum size as cloud condensation nuclei (CCN) and as ice nuclei (IN)[3]

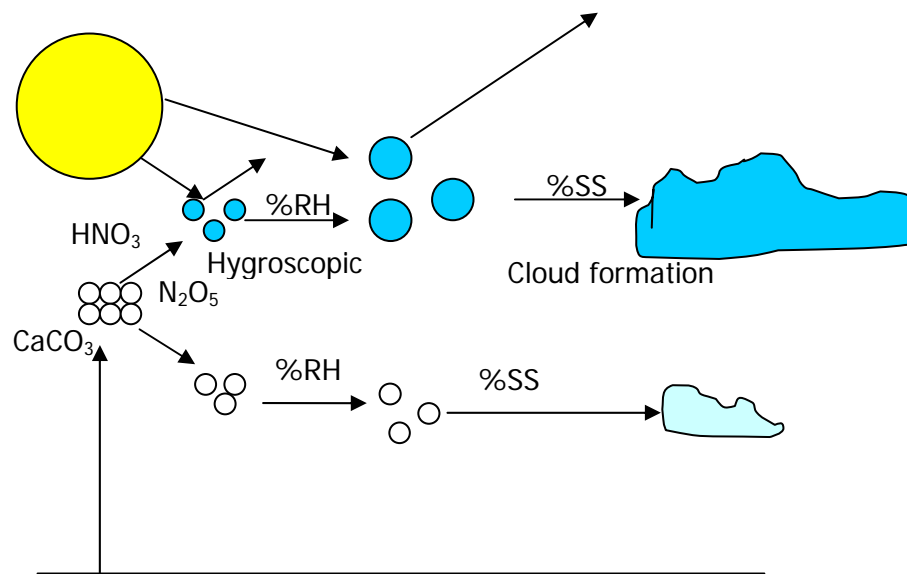


Figure 4.1 Radiation forcing of atmospheric aerosols and their impact on precipitation

A schematic pictogram of the direct and indirect effects of aerosols in the atmosphere is presented in figure 4.1 where %SS is the percentage supersaturation, RH stands for relative humidity in the atmosphere.

Fine mode aerosols generally have atmospheric lifetimes of days to about a week [3], and, as a result, can be highly variable in the spatial and temporal distributions. As discussed in the introductory chapter, the atmospheric aerosol particles may be emitted directly as particles (primary sources) or formed from gaseous precursors (secondary sources) via the aforementioned gas-to-particle conversion of  $\text{SO}_2$ ,  $\text{NO}_x$ , and VOC, etc. Some of the atmospheric sources are natural, e.g. volcanic emission and ocean sea spray; while others, such as industrial emissions, biomass burning and soil dust emissions from

agriculture activities are anthropogenic. Globally, the atmospheric aerosol flux is estimated at about 3440 Tg per year, of which 10% comes from anthropogenic sources [4-5].

However, the anthropogenic aerosols, mainly consisting of sulfate and carbonaceous aerosols (black carbon and organic carbon), has substantially increased since preindustrial times, and even exceeds the natural sources globally, and dominates over the urban/industrial areas [6,7], etc. Such a large perturbation of the global and regional aerosols from the anthropogenic sources is a major climatic and environmental concern.

The water vapor property of coating particles in the atmosphere and finally forming soluble solutions is called hygroscopicity. The hygroscopicity is changing the aerosols optical and microphysical characteristics enabling researchers to differentiate between different types of aerosols [8,9]

Several studies have been performed on laboratory simulated atmospheric constituents and numerous papers have been published. Based on a good knowledge of the atmospheric chemistry researchers have developed laboratory models for hygroscopic growth for different types of aerosol like urban, marine and continental. Hygroscopic properties of aerosols have been determined for atmospheric constituents like  $\text{CaCO}_3$ ,  $\text{CaMg}(\text{CO}_3)_2$ ,  $(\text{NH}_4)_2\text{SO}_4$ ,  $(\text{NH}_4)_2\text{SO}_4$ ,  $\text{NaCl}$ ,  $\text{CaSO}_4$ , at different sizes that they can be found in the atmosphere, i.e., Aitken Nuclei  $<0.2 \mu\text{m}$ , Large Nuclei  $0.2$  to  $1.0 \mu\text{m}$ , Giant Nuclei  $>1.0 \mu\text{m}$ . The conclusions of [10] show that the component of mineral dust aerosol ( $\text{CaCO}_3$  and  $\text{CaMg}(\text{CO}_3)_2$ ) are particularly reactive with  $\text{HNO}_3$  and  $\text{N}_2\text{O}_5$ . According to the results, the rate and extent of reaction are RH dependent. [10]

The process of hygroscopic growth is simple and is briefly explained here. As the relative humidity increases, the first water to be added is the water of hydration. The water molecules chemically combine with a substance in such a way that it can be removed, as by heating, without substantially changing the chemical composition of the substance. While the water of hydration can be sum of both structured and bound water subfractions, the structured water would appear to follow the bound water; however, in the case of extremely dry, tightly bound aerosols, the structured water may come first as the bound water may take some time to react with the ions. Once this water has entered the aerosol system, the soluble parts dissolve and the droplet becomes a highly concentrated solution. Under typical conditions  $\text{Ca}(\text{NO}_3)_2$  has a greater water to solute ratio than  $(\text{NH}_4)_2\text{SO}_4$ . As observed by E. Gibson et al (2006)[11], the nitrate salts are significantly more hygroscopic than the carbonate component of mineral dust aerosol. Increased water content will provide a more aqueous environment for heterogeneous reactions to occur in the atmosphere. Some of the laboratory studies concluded that the CCN activity of nitrate aerosol is much larger than that of carbonate aerosol and mineral dust aerosol that has been transported and aged, and will have a larger impact on direct and indirect climate forcing than freshly emitted mineral dust aerosol.

Melfi et al. (2005)[12] have been able to produce in situ hygroscopic models for different types of aerosols: clean maritime, polluted maritime, continental/urban.

The relations staying at the bases of the hygroscopical behavior of particles are given by the equations below. The relationship between the relative humidity and the particle size according to Hanel [1] is

$$RH = \exp \left( \frac{2\sigma}{\rho_w R_w T r} - \frac{\eta \frac{\rho_0}{\rho_w}}{\left( \frac{r}{r_0} \right)^3 - 1} \right) \quad (1)$$

where RH stand for relative humidity expressed as a ratio of the actual water vapor pressure of the air and that of the air when saturated;  $\sigma$  is the surface tension of the particle against surrounding air;  $R_w$  is the specific gas constant of water;  $T$  is the absolute temperature;  $\rho_w$  is density of pure water;  $\rho_0$  is the mean bulk density of the particle in dry state (RH=0);  $r$  is equilibrium equivalent volume radius of particle;  $r_0$  is the equivalent volume radius of the dry particle (RH=0) and  $\eta$  is the exponential mass increase coefficient of the particle.

The first part of the exponential function describes the increase of the equilibrium RH over the particle surface with curvature, known as well as the curvature effect. The second term describes the decrease of the equilibrium relative humidity due to action of dissolved material in water and presented below as  $a_w$ .

#### *Water activity*

The influence of the dissolved material is described in terms of the water activity  $a_w$  that can be interpreted as equilibrium relative humidity over the particle when its surface would be a plane; meaning its radius is approaching infinity. The water activity is obtained from the following formula:

$$a_w = \exp \left[ \left( \frac{-\bar{v} \cdot \bar{\phi} \cdot \varepsilon \cdot \gamma \cdot M_w}{\bar{M}_s} \right) \left( \frac{m_0}{m_w} \right) \right] \quad (2)$$

where  $\bar{v}$  is the mean number density of moles of ions and undissociated molecules per mole of salt mixture,  $\bar{\phi}$  is the observed particle osmotic coefficient,  $\varepsilon$  is the mass fraction of soluble material in the aerosol particle,  $\gamma$  is a correction factor taking into account absorption (or desorption),  $M_w$  is the molecular weight of water,  $\bar{M}_s$  is the mean molecular weight,  $m_0$  is the mass of particle in dry state,  $m_w$  is the mass of water condensed on the particle. The first multiplication term of the exponential expression (2) is known as the exponential mass increase coefficient.

$$\eta = \frac{\bar{v} \cdot \bar{\phi} \cdot \varepsilon \cdot \gamma \cdot M_w}{\bar{M}_s} \quad (3)$$

Therefore the water activity can also be expressed as

$$a_w = \exp\left(-\eta \frac{m_0}{m_w}\right) \quad (4)$$

According to Hanel the RH can be approximated to  $a_w$  (water activity) for  $r/r_0 < \sqrt[3]{2}$ .

#### *Activity parameter*

The activation parameter is described by the following relation:

$$B = \frac{\eta(a_w)}{\eta^0} B^0 \quad (5)$$

where  $B^0 = \eta^0 \frac{\rho_0}{\rho_w}$ . The exponential mass increase coefficient  $\eta^0$  and the hygroscopic parameter  $B^0$  are defined at infinitely dilute solution ( $a_w = 1$ ). The exponential increase coefficient,  $\eta(a_w)$  is a function of the solute concentration and it can be obtained from the equation (3)

### *Mean bulk density*

The mean bulk density of a particle is one of the parameters affecting its settlement to the ground, relative to the moving air [1]. Therefore, its dependence on relative humidity must be known. By assuming additivity of the volumes of dry particle and of the condensed water [13], it is

$$\rho(RH) = \rho_w + (\rho_0 - \rho_w) \left[ \frac{r(RH, r_0)}{r_0} \right]^{-3} \quad (6)$$

The mean bulk density decreases with increasing relative humidity. When the atmosphere is nearly saturated, the mean bulk density of a particle attains values close to density of water. Hanel [13] shows that like the particle radius presented below, the mean bulk density shows also a hysteresis effect; in a specified range, the mean bulk density of the particle is for decreasing relative humidity smaller than that for increasing relative humidity. According to Andre et al.(1980) [14] the  $\rho_0$  values range between 1.8 and about 3.0g/cm<sup>3</sup>.

### *Surface tension*

The surface tension of the particle is mostly dependent on the surface tension of pure water and the effect of dissolved material which is very small and is negligible at saturation ratios at and above unity. Therefore

$$\sigma = \sigma_w - \frac{\beta \ln a_w}{B} \quad (7)$$

where B is the aerosol activity parameter (also known as the hygroscopicity parameter)

and  $\beta = b\varepsilon \frac{\rho_0}{\rho_w}$ . The terms forming the second part of the surface tension formula are  $\varepsilon$ ,

the mass fraction of soluble material in the aerosol particle,  $b$  is the coefficient describing the dependence of the surface tension from the dissolved material.

*Mean complex refractive index*

Among the many mixture rules for the real part of refractive index or functions of it, the following mixture rules [1] combine a minimum of inaccuracy for a wide range of applications with formal simplicity.

$$n(RH) = n_w + (n_0 - n_w) \left( \frac{r(RH, r_0)}{r_0} \right)^{-3} \quad (8)$$

Where  $n$  is the real part of mean refractive index of a particle,  $n_0$  is the real part of mean refractive index of a dry particle, and  $n_w$  is the real part of mean refractive index of water.

$$n_0 = \rho_0 \sum_j \frac{n_{0j} m_{0j}}{\rho_{0j} m_0} \quad (9)$$

where  $n_{0j}$  is the real part of refractive index of the pure component  $j$  of the particle. The above (8) and (9) relations are derived supposing volume additivity of the components. According to [1], the maximum inaccuracies of both formulas commonly are in order of  $\pm 1$  to  $\pm 3\%$ .

Formerly, the same type of mixture rule has been used for the imaginary as for the real part of the real part of the refractive index. However a more accurate mixture rule has been evaluated by applying an approximation for the absorption coefficient of an ensemble of airborne particles to the components of a single particle [1, 14]. By assuming volume additivity for the components, the imaginary refractive index relation is given as

$$\frac{k(RH)}{n^2(RH) + 2} = \frac{k_w}{n_w^2 + 2} + \left( \frac{k_0}{n_0^2 + 2} - \frac{k_w}{n_w^2 + 2} \right) \left( \frac{r(RH, r_0)}{r_0} \right)^{-3} \quad (10)$$

where  $k$  is the imaginary part of the mean refractive index of the particle,  $k_0$  is the imaginary part of mean refractive index of the dry particle, and  $k_w$  is the imaginary part of the refractive index of water. In the above expression we have

$$\frac{k_0}{n_0^2 + 2} = \rho_0 \sum_j \frac{k_0}{n_0^2 + 2} \frac{1}{\rho_{0j}} \frac{m_{0j}}{m_0} \quad (11)$$

where  $k_{0j}$  is the imaginary part of refractive index of component  $j$  of the dry particle.

### *Settlement of particles in the atmosphere*

Studies have been made to estimate the settlement of particles relative to the moving air and removal of particulate matter by and due to precipitation (dominant sinks of particles in the atmosphere). Lehman and Hanel (1980)[1] have investigated the settling velocities of single particles in stagnant air as functions of relative humidity. The mean settling velocity of dry material is

$$\bar{w}_{s,dry} = \frac{\sum_{j=1}^1 \bar{m}_{j,dry} \cdot \bar{w}_{sj}}{\sum_{j=1}^1 \bar{m}_{j,dry}} \quad (12)$$

where  $\bar{m}_{j,dry}$  is the mean mass of particles of class  $j$  per unit volume of air,  $\bar{w}_{sj}$  is the amount of mean relative velocity between the particles of class  $j$  and surrounding air.

The relative humidity does not affect the  $\bar{w}_{s,dry}$  largely below RH=0.8. In this region the effects of radius increase and bulk density decrease partly balance out each other. At RH >0.8 the radius increase determines mostly the increase of  $\bar{w}_{s,dry}$ . When the relative humidity has reached 0.99, the value of  $\bar{w}_{s,dry}$  is about 15-20 times larger than at low and medium relative humidity. During the effects of episodes of clouds or fog or of high relative humidity during the night and in the early morning, the particulate matter is

removed very effectively from the atmosphere by settlement. When these episodes are not existing or not efficient ( the settling velocities are relatively low) in removing these particles, a residual layer can be observed in the morning PBL layer as indicated by the lidar images in figures 4.2a) and b).

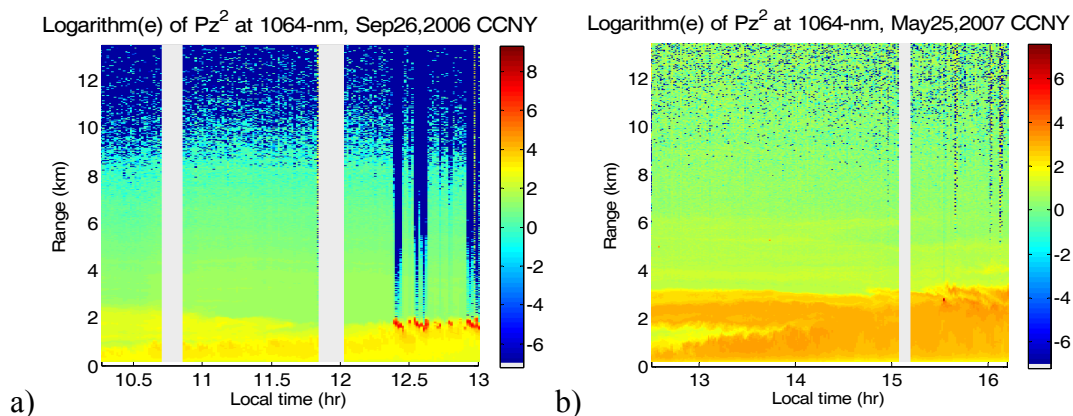


Figure 4.2 Lidar images on a) September 26<sup>th</sup>, 2006 and b) May 25<sup>th</sup>, 2007

indicating a clear residual layer from the anterior day

### *Particle growth*

Using the approximation in (4), one can obtain the relation for particle radius as function of the RH as follows:

$$r = r_0 \left( 1 + \frac{\rho_0}{\rho_w} \frac{m_w}{m_0} \right)^{1/3} \quad (13)$$

To provide reliable measurements of ambient aerosol particle properties and to reduce uncertainties in the estimated radiative forcing by ambient aerosol particles (in particular meteorological air-pollution predictions) the development of hygroscopic models are essential. Aerosols can have their optical properties modified in the presence of water vapor with different classes of aerosols being modified in different manners. As the intensive (refractive index) and extensive characteristics (optical depth) of the aerosols

vary with the effective radius, relative humidity, wavelength of light and composition, the use of the optical parameters obtained from the multivavelength Raman lidar returns should allow us to validate (with higher accuracy) the homogeneity of the aerosol layer as well as provide additional multi wavelength information. This information can be used to validate and separate or modify the aerosol models underlying the hygroscopic trends observed in the Raman channel. In particular, we show that aerosols backtracked to different sources (bio-mass, maritime) have different hygroscopic behavior which are compared to theoretical models. The need to identify hygroscopic properties from measurements is complicated by the fact that most dramatic effects occur at high relative humidity values which are difficult to control for *in situ* measurement by instruments like nephelometers. Therefore lidar measurements near cloud base offer a chance at looking at hygroscopic properties. In particular, the ability of the multiwavelength Raman lidar of performing simultaneous atmospheric measurements at three different wavelengths 355nm, 1064nm and 407nm (Raman water vapor) provides the opportunity of isolating the hygroscopic effect from the number of density variations which plague the single channel approach since the normalized backscatter (to the dry state) retrieved at 355nm and 1064nm is independent of the total number of particles (for small spatial ranges). In this chapter we investigate the possibility of using the ratio optical scatter measurements which eliminate the inherent problem of variable particle number and illustrate the sensitivity of different hygroscopic aerosols to these measurements and find that combining both extinction and backscatter with color ratios improves the accuracy of the retrieval.

## **2. Mathematical modeling relating optical scattering coefficients to the hygroscopic properties of aerosols**

One of the most frequent questions among aerosol and climate modelers is weather and to what extent aerosol particles influence the regional and the global climate [17]. A reliable answer to this question supposes the availability of both an aerosol model and ocean and atmospheric models along with an appropriate radiation code flexible enough to allow aerosol properties to be incorporated and “sensitive” enough to indicate the possible perturbations induced by them later. To quantify hygroscopic properties, a model of aerosol changes in size and refractive index are needed as a function of the ambient RH and the dry state properties. Therefore, it is crucial to obtain simultaneous optical properties as function of RH which may be accomplished using a Raman – Mie Lidar.

Hygroscopic models are a suitable way of quantitatively and qualitatively evaluate the backscatter outputs of lidars and other instruments that measure hygroscopic properties of aerosols. In this chapter an aerosol model that takes into account the hygroscopic properties of atmospheric particles is presented. Some of the problems in creating such models are:

- the lack in information regarding composition of the atmosphere at different altitudes, because the measurements of the physic-chemical properties of the aerosols is difficult and foster a wide range of uncertainty
- atmospheric aerosol stems from localized and sparse sources, remains only a few days in the atmosphere, and is therefore subject to a high variability in space and time. The extent of this variability has not been really

investigated[17]

The hygroscopic model presented here have been based on the measurements performed by Hanel (1976) [13] and measurements collected at the CCNY weather station. The hygroscopic model can be used as part of a climate modeling or solely as a mean for calculating optical properties of hygroscopic aerosols and identifying the existing atmospheric states under study. The models are based on measured dry particle densities [13] with their corresponding real and imaginary refractive indexes at different wavelengths. The radius and the real and imaginary refractive indexes used in the above relation are relative humidity dependent and are described by the following relations derived by Hanel [13]:

$$r = r_0 \left( 1 + \frac{\rho_0}{\rho_w} \mu(RH) \frac{RH}{1 - RH} \right)^{1/3} \quad (14)$$

$$n = n_w + (n_0 + n_w) \left( \frac{r_0}{r} \right)^3 \quad (15)$$

$$k = k_w + (k_0 - k_w) \left( \frac{r_0}{r} \right)^3 \quad (16)$$

In the above 14 to 16 relations RH represents the relative humidity,  $\mu(f)$  is the linear mass increase coefficient,  $\rho_0$  and  $\rho_w$  represent the dry air and water vapor density respectively,  $n_0$  and  $n_w$  represent the real refractive index of dry particles and water vapor respectively, and the imaginary refractive indexes of dry air and water vapor are represented by  $k_0$  and  $k_w$  respectively. Equation (16) is an alternative form to equation (10).

A description of the used atmospheric models is found in Hanel [13] and described again for convenience: model 1 is represented by average aerosol in summer 1966 at Mainz, model 2 by sea-spray aerosol, model 3 by maritime aerosol over Atlantic, 13-16<sup>th</sup> of April 1969, model 4 Maritime aerosol over Atlantic containing Saharan dust, 16-25<sup>th</sup> of April 1969, model 5 Urban aerosol at Mainz in January 1970, model 6 Aerosol on top of the Hohenpeissenberg, elevation 1000m above MSL in the foothills of the Alps, in summer 1970.

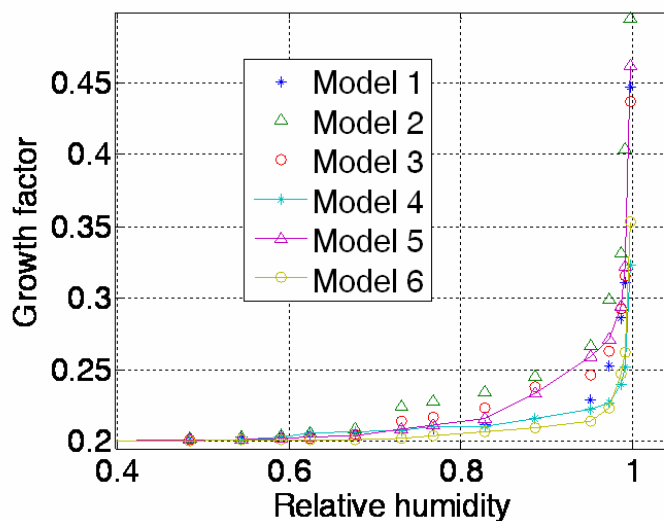


Fig. 4.3 Growth factor for the 6 atmospheric models with a dry radii of  $0.2\mu\text{m}$

Figure 4.3 presents the particles hygroscopic radius growth for a dry particle radius of  $0.2\mu\text{m}$  for the six different atmospheric models described above. The plot indicate very little change in particle growth below 80% relative humidity.

From figure 4.3, we see the nature of hygroscopic aerosols is a growth which can change the radii by a factor of 2. While it is difficult to model a realistic aerosol model requiring parameters which are laboratory based, we can explore a simplified model which is reasonable for the accumulation mode for aerosols.

In particular, we assume a single particle size in our model (no size distribution) with particles having dry state radii of .2  $\mu\text{m}$  (representative of the aerosol accumulation mode) but we vary the complex refractive index. Since the models seem to behave in much the same way in terms of growth, we can examine the backscatter signature for a fixed growth factor which we choose to be 2.0. In particular, we are interested in the ratio of backscatter ratios for different wavelengths.

$$\frac{\bar{\beta}_1}{\bar{\beta}_2} = \frac{\left(\frac{\beta(RH)}{\beta_0}\right)_{\lambda_1} \left[ \frac{Q_{sca}\left(\frac{2\pi r_w}{\lambda_1}, m_w\right)}{Q_{sca}\left(\frac{2\pi r_0}{\lambda_1}, m_w\right)} \right]}{\left(\frac{\beta(RH)}{\beta_0}\right)_{\lambda_2} \left[ \frac{Q_{sca}\left(\frac{2\pi r_w}{\lambda_2}, m_w\right)}{Q_{sca}\left(\frac{2\pi r_0}{\lambda_2}, m_w\right)} \right]} \quad (17a)$$

or backscatter to extinction ratio

$$\frac{\bar{\beta}_1}{\bar{\alpha}_1} = \frac{\left[ \frac{Q_{sca}\left(\frac{2\pi r_w}{\lambda_1}, m_w\right)}{Q_{sca}\left(\frac{2\pi r_0}{\lambda_1}, m_w\right)} \right]}{\left[ \frac{Q_{ext}\left(\frac{2\pi r_w}{\lambda_1}, m_w\right)}{Q_{ext}\left(\frac{2\pi r_0}{\lambda_1}, m_w\right)} \right]} \quad (17b)$$

The bar in equation 17 stands for normalization of the scatter of the wet particle (at a given relative humidity) with respect to the scatter of the same particle in dry state. In the above equation,  $r_w$  is the equivalent radius of the wet particle,  $r_0$  is the radius of the dry particle,  $Q_{sca}$  is the backscattering efficiency,  $\lambda_1$  and  $\lambda_2$  are the wavelengths considered in the ratio,  $m$  is the refractive index, While these results are based only on homogeneous

distributions, we note significant qualitative differences between absorbing and non absorbing aerosol particles. These results are illustrated in figure 4.4

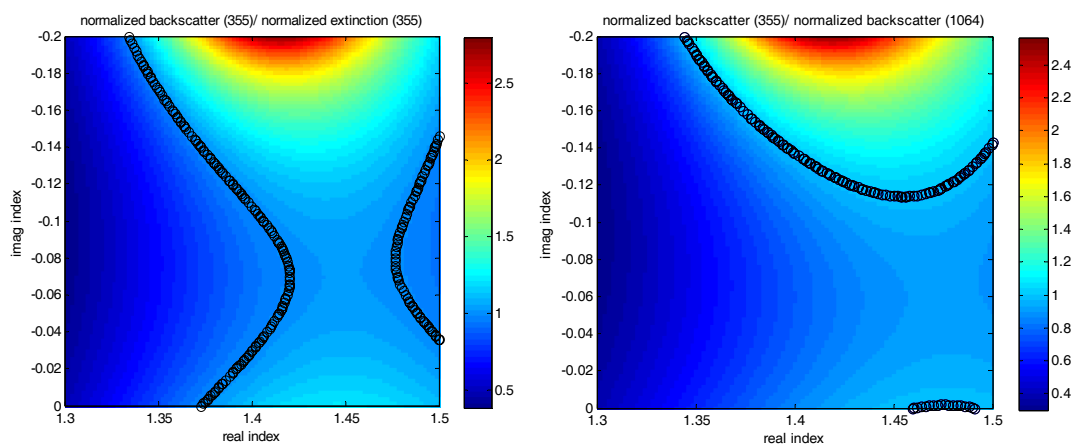


Fig 4.4 Normalized (wet to dry) ratios a) backscatter (355) /extinction (355) b) backscatter (355) / backscatter (1064)

We note first of all that the qualitative behavior of the two types of ratio measurements are nearly identical which clearly shows a limit in using both measurements to deduce more information than either ratio alone. On the other hand, there does seem to be some differentiation when the absorption properties are high.

## 2.1 Analyses and Results

The analyses of the hygroscopic properties of the aerosols have been made for the day of September 25<sup>th</sup>, 2006 and April 25<sup>th</sup>, 2007 due to the low cloud presence in the planetary boundary layer and the expected increase relative humidity with height. In particular, the low clouds allow us to have a fairly stable atmospheric state which can be probed vertically to high RH. The lidar image at 1064nm on September 25<sup>th</sup>, 2006 is presented in figure 4.5a).

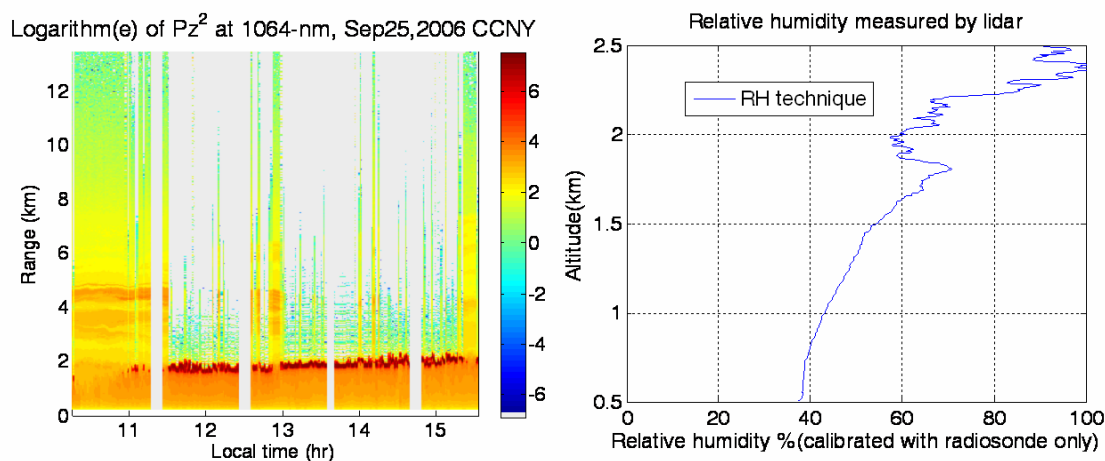


Fig. 4.5. a) Lidar image at the 1064nm and b). Relative humidity vs. altitude on Sept 25<sup>th</sup>, 2006 at 12:35pm

As discussed earlier, well mixed conditions are optimal and are assumed to occur under cloud capped conditions. It is important that the aerosol layer is well mixed so that changes in optical properties due to RH effects are not confused with variations in aerosol concentrations. For example, in ref [2], they try to validate the well mixed condition using the hypsometric form of the ideal gas law. This approach calculates the RH for a constant mixing ratio derived from the surface alone. If the RH reaches 100 % for a height which matches the lidar derived cloud base value, we can infer well mixed conditions. However, no attempt was made to validate procedure directly by monitoring the water vapor directly from raman lidar. To satisfy this missing piece, we simultaneously compare the predictions of the hypsometric eqn to our lidar below.

The results of the hypsometric analysis are presented in figure 4.6a which relates the RH to the pressure level. Converting to altitude units using the standard pressure profile indicates that the saturating RH level of 100% occurs  $\sim$  800 hPa or 2 km which agrees within 10% with the lidar determination of cloud base as seen in figure 4.5a

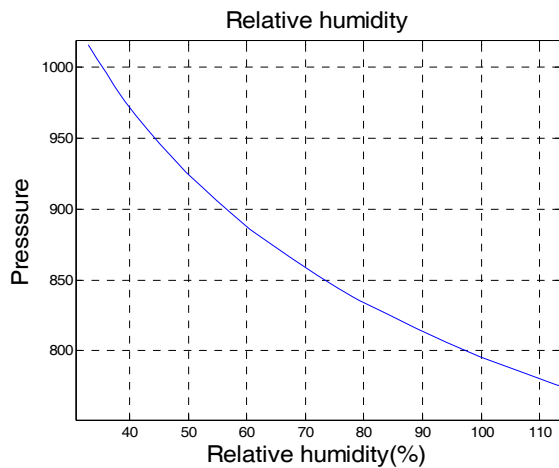
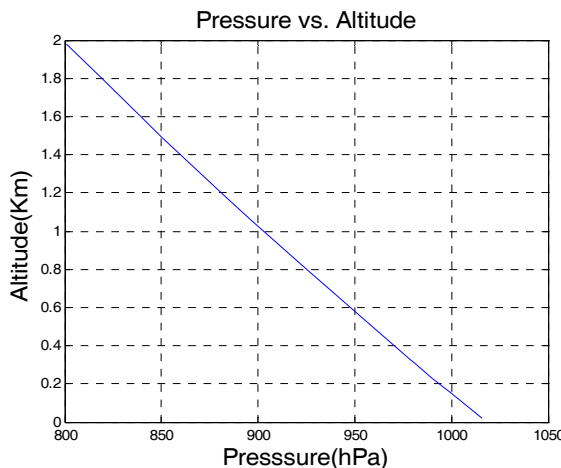


Fig 4.6a) RH vs Pressure based on hypsometric eqn.



b) Pressure vs Altitude scale

At the same time, we are in a position to directly test if the water vapor is well mixed. The results in figure 4.7 show that for the height range of interest, the mixing ratio is constant to within 10-15%

The lidar retrieved relative humidity and calibrated by methods described in the third chapter, section 3.1 and [15] is plotted in fig 4.5b). The local surface measurements obtained from a GPS instrument confirm the 39%-40% relative humidity at the ground confirming the lidar measurements. The relative humidity obtained this way is then used in

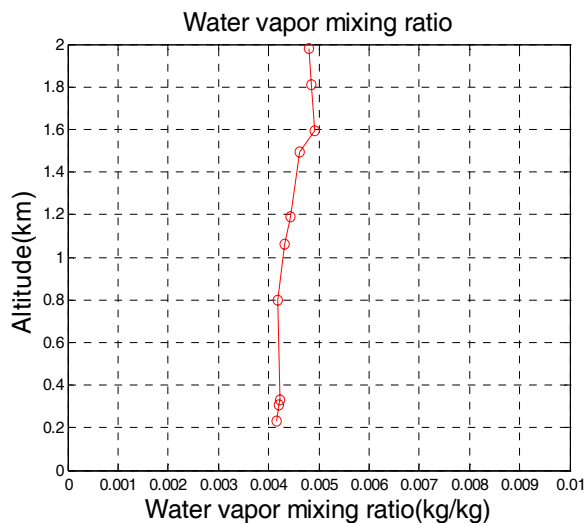


Fig4.7 Lidar retrieved water vapor mixing ratio

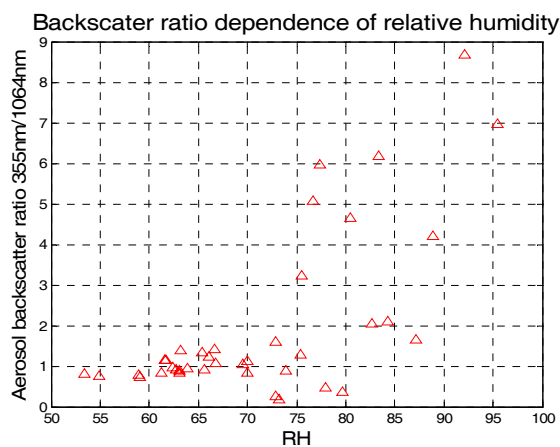


Fig 4.8 Aerosol backscatter ratio

combination with the lidar returns at 355 nm and 1064 nm to determine aerosol hygroscopic properties.

The increase in the backscatter ratio of the 355 nm and 1064 nm channels is shown in figure 4.8.

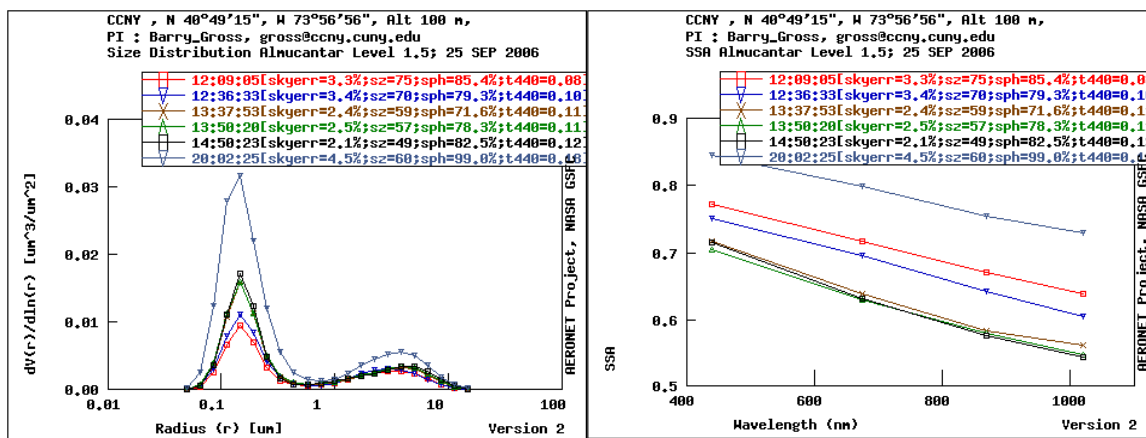


Fig. 4.9 Aeronet retrievals for hygroscopic aerosols a) PSD showing accumulation mode b) low albedo

Interestingly, the results seem to be quite reasonable based on the fact that the particle size distribution was heavily dominated by the accumulation mode together with low albedo (absorbing) conditions as illustrated by our aeronet retrievals for this day.

While this analysis was performed for a simplified homogeneous model, it is clearly important to attempt a more realistic modeling based on aerosol models. In particular, we focus on including reasonable aerosol size distributions. This complication is performed by replacing the scattering efficiencies by a full integration over the given size distribution

$$\frac{\bar{\beta}_1}{\bar{\beta}_2} = \frac{\left(\frac{\beta(RH)}{\beta_0}\right)_{\lambda_1} \frac{\int \left[ Q_{sca} \left( \frac{2\pi r}{\lambda}, m \right) * N_s * \frac{dn(r)}{d \log r} * \pi^2 \right] d \log r}{\int \left[ Q_{sca} \left( \frac{2\pi r_0}{\lambda}, m_0 \right) * N_s * \frac{dn(r_0)}{d \log r_0} * \pi_0^2 \right] d \log r_0} \Big|_{\lambda_1}}{\left(\frac{\beta(RH)}{\beta_0}\right)_{\lambda_2} \frac{\int \left[ Q_{sca} \left( \frac{2\pi r}{\lambda}, m \right) * N_s * \frac{dn(r)}{d \log r} * \pi^2 \right] d \log r}{\int \left[ Q_{sca} \left( \frac{2\pi r_0}{\lambda}, m_0 \right) * N_s * \frac{dn(r_0)}{d \log r_0} * \pi_0^2 \right] d \log r_0} \Big|_{\lambda_2}} \quad (18)$$

Here,  $n(r)$  is the number density (number of particles per volume) and  $\frac{dn(r)}{d \log r}$  is the

aerosol size distribution. We note that for a given aerosol size distribution mode, the ratio eliminates the vertical concentration effects.

In addition, instead of assuming a given particle growth, we attempt to include the particular growth rate for an aerosol model as a function of the ambient RH. In particular, the water vapor density used in (14-16) is calculated at 20°C temperature based on the relative humidity indicated by [13] for each individual mass of water vapor to mass of dry substance and linear mass increase coefficient. A table of measured values for the six models and used in the hygroscopic model validation is available in Hanel(1976) [13] where  $\bar{\alpha}_\lambda$  is the aerosol extinction normalized to the extinction of the dry particle at wavelength  $\lambda$ ,  $Q_{ext}$  is the extinction efficiency. Using the given ratios in (18) one can identify the dry state aerosol by constructing a table of ratio scattering properties for different models and dry state conditions as a function of the RH. While the models are not extensive in the literature, we hope that they will capture some of the real life behavior of different types of atmospheric aerosols (different combinations of

atmospheric gases and particulates or particulates alone) under different atmospheric conditions (humidity, temperature, particle density etc).

Once the microphysical model parameters are estimated, the aerosol backscatter ratio normalized with respect to the dry particles backscatter can be calculated using equation 17 and 18. The results obtained using equations (17),(18) have been plotted in fig 4.6. The two plots represent the logarithm of two normalized ratios as function of model number and radii. In fig.4.10a has been represented the logarithm of the ratio of normalized backscatter at 1000nm to the normalized backscatter at 300nm,  $\log_{10}(\bar{\beta}_{1064}(fH=.95)/\bar{\beta}_{355}(fH=.95))$ , while in fig.4.10b. has been plotted the normalized backscatter to extinction ratio at 355 nm,  $\log_{10}(\bar{\beta}_{355}(fH=.95)/\bar{\alpha}_{355}(fH=.95))$ . The bar means the quantity is normalized to the dry state value.

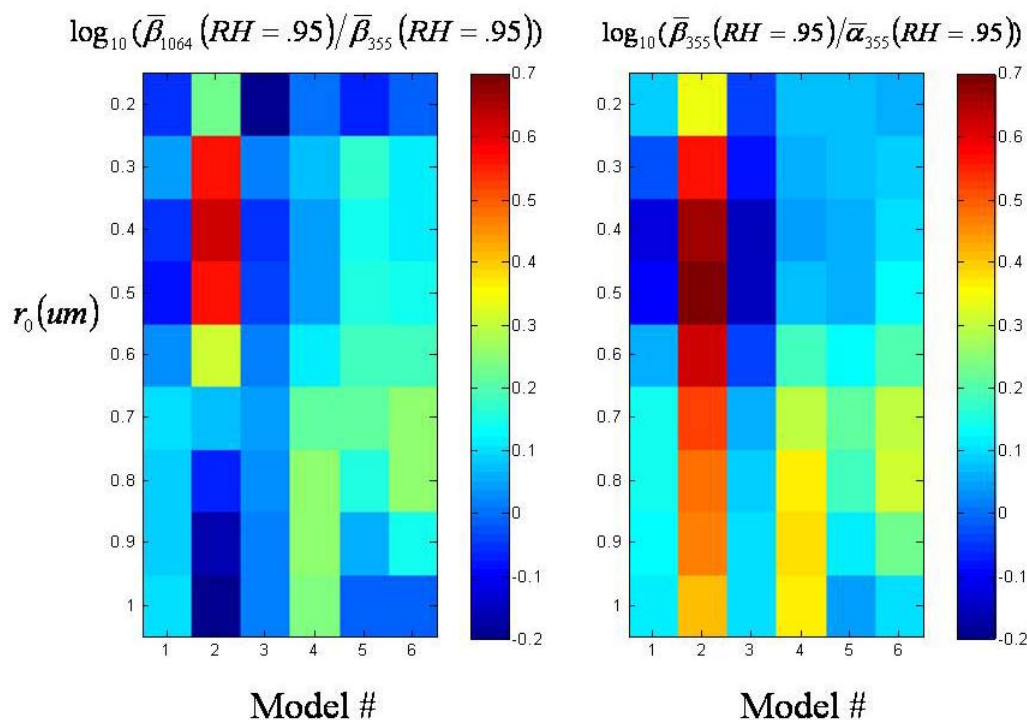


Fig. 4.10. Normalized color ratio(355 nm to 1064 nm) for six atmospheric models (left) and normalized lidar ratio (right) for six atmospheric models and radii from 0.2 to 1  $\mu\text{m}$

Our space of admissible is represented by the 54 cells (6 models x 9 dry radii). The dry radii range from  $0.2\mu\text{m}$  to  $1\mu\text{m}$  and logarithmic standard deviation is kept constant at  $1.2\mu\text{m}$  since the mode width has a much weaker effect on the hygroscopic effects. When examining the results, we note a significant variation seen between models and the different ratio types. Unfortunately, the plethora of atmospheric states behaviors is so rich that determination of a particular model for a given data set is quite a task and requires in essence large statistical data sets which can be tracked to a particular source to make any real assessment of a particular model. However, as seen in the next section, we seem to see some agreement with aerosol models and lidar retrievals.

## **2.2 Comparison of lidar measurements to existing models**

By performing ratios of the normalized backscatter ratio, the number concentration of particles in the atmosphere is cancelled as seen from formula (18). Therefore, we may perform vertical profile analysis on the scattering ratios without concern for the actual number density of the scattering objects in the backscattering ratio dependence of relative humidity. Using conventional lidar algorithms to determine the backscatter and extinction coefficients at 355nm and 1064nm [18-22], one can obtain the ratio of the two obtained backscattered profiles at the two wavelengths as described by (8).

Preliminary results of the atmospheric models normalized backscatter ratio have been plotted in fig 4.11. The ratio of the normalized backscatter ratios of the 355nm to the 1064nm have been plotted for models 1,3,5,6 [13] and CCNY aerosol measurements on April 25<sup>th</sup>, 2007. The ratio of the normalized backscatter coefficients at CCNY were retrieved from the vertical profiles measured by the multiwavelength Raman lidar. Models 2 and 4 have not been used for comparison due to the lack of information in the

measured data in [13].

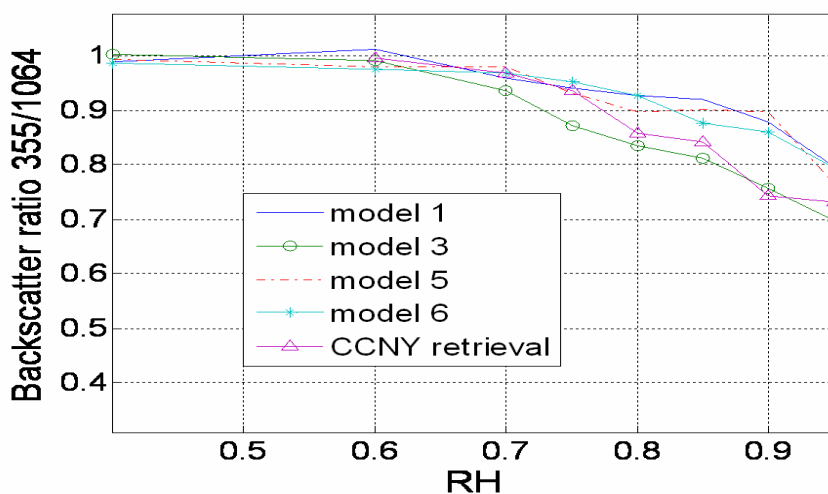


Fig. 4.11. Normalized aerosol backscatter ratio of the 355nm and 1064nm lidar returns on April 25<sup>th</sup>, 2007

As it can be noticed the CCNY measured backscatter ratio is in the interval between model 3 and the cluster formed by the other models on April 25<sup>th</sup>, 2007. While no data set from aeronet is available, we see the data seems to agree with non absorbing particle models with large radius.

### 3. Sensitivity of optical scattering coefficients to the hygroscopic properties of aerosols

Considering the significant variation that can occur between atmospheric models and the different ratio types, we explore an inversion approach using multiple channels at variable RH levels to provide information in disentangling the size and hygroscopic properties. To assess this possibility, we need to fix our approach for inversion which can be simply described as a brute force identification of all possible states satisfying all possible scattering combinations within a particular measurement sensitivity. However, we do expect that due to some of the qualitative commonalities between these two

measurements, the combination of both measurements should have somewhat restricted benefit.

### 3.1 Multiwavelength inversion of hygroscopic models and dry state radii

To begin, we calculate the optical backscatter coefficients for each radii index ( $i_0$ ) and aerosol model index ( $j_0$ ) at all RH levels for a particular ratio  $k$ . We can then determine the inversion set as the set that satisfies all backscatter measurements simultaneously. In mathematical terms, the set of admissible solutions is obtained by determining all states indices that satisfy “all” optical coefficient constraints where  $R$  is a particular ratio of optical coefficient

$$S(i_0, j_0) \equiv \left\{ (i, j) \text{ s.t. } \frac{[R_k(i_0, j_0) - R_k(i, j)]}{R_k(i_0, j_0)} \leq \varepsilon_k \right\} \quad (19)$$

In these calculations, the ratios  $R_k$  are a combination of two channel optical coefficient ratios as seen in equations (17) and (18) and given by (20) and (21) respectively:

$$R_1 \equiv \left[ \frac{\alpha_{355}(RH)/\beta_{355}(RH)}{\alpha_{355}(RH_0)/\beta_{355}(RH_0)} \right] \rightarrow \left[ \frac{\alpha_{355}(RH)}{\alpha_{355}(RH_0)} \right] \left[ \frac{\beta_{355}(RH_0)}{\beta_{355}(RH)} \right] \quad (20)$$

$$R_2 \equiv \left[ \frac{\beta_{1064}(RH)/\beta_{355}(RH)}{\beta_{1064}(RH_0)/\beta_{355}(RH_0)} \right] \rightarrow \left[ \frac{\beta_{1064}(RH)}{\beta_{1064}(RH_0)} \right] \left[ \frac{\beta_{355}(RH_0)}{\beta_{355}(RH)} \right] \quad (21)$$

where  $R_1$  is the lidar normalized ratio and  $R_2$  is the backscatter normalized ratio.

To calculate the ratio constraint error, we use the propagation of errors for the noise on the optical coefficients. Assuming independence of the optical coefficient errors, the combined error for ratio  $R$  can be written as a RMS sum of the individual channel errors as shown in equations (22) and (23)

$$\varepsilon_1 = \sigma_{R_1} = \sqrt{\sigma_{\alpha,355}^2 + \sigma_{\beta,355}^2} \quad (22)$$

$$\varepsilon_2 = \sigma_{R_2} = \sqrt{\sigma_{\beta,1064}^2 + \sigma_{\beta,355}^2} \quad (23)$$

where the uncertainties are provided in table 4.1. The first ratio in the table has high error due to high noise on Raman channel. The second ratio error is due to both far end condition and to smaller extend extinction error (no data available at a reference  $z_{\max}$ , - note the lidar retrieval methods in chapter II for more details). The smallest error is the one in channel 1064nm due to small uncertainty in the calibration constant retrieval and extinction is low.

Table 4.1 Individual channels uncertainties

Optical ratio	$\frac{\alpha_{355}(RH)}{\alpha_{355}(RH_0)}$	$\frac{\beta_{355}(RH)}{\beta_{355}(RH_0)}$	$\frac{\beta_{1064}(RH)}{\beta_{1064}(RH_0)}$	$\frac{\beta_{2300}(RH)}{\beta_{2300}(RH_0)}$
Uncertainty	20%	20%	5%	25%

Once the set is constructed, we can define a metric describing the size of the retrieval set as

$$P(i_0, j_0) = \text{size}(S(i_0, j_0)) / \text{total number of states} \quad (24)$$

In particular, the smaller the fraction of states that can be mistaken for the reference state P, the better the retrieval. In figures 4.9a and b, we plot the probability metric as a function of dry state radius and model number using two possible ratio schemes. All cases include the use of two high RH levels (80% and 95%). After setting the constraints as described above, we see in fig 4.12a that the fraction of atmospheric states that seem to be the least ambiguous belong to the sea-spray aerosol model which makes the identification of this state most likely. As explained before the bar used in  $\bar{\beta}_{1064}/\bar{\beta}_{355}$  ratio (also referred to as UV-NIR ratio or color ratio) stands for normalized to dry state,

meaning that both backscatter and extinction at 355nm have been estimated at 95% RH and then normalized to backscatter / extinction of particles in the dry state, (i.e 40% RH).

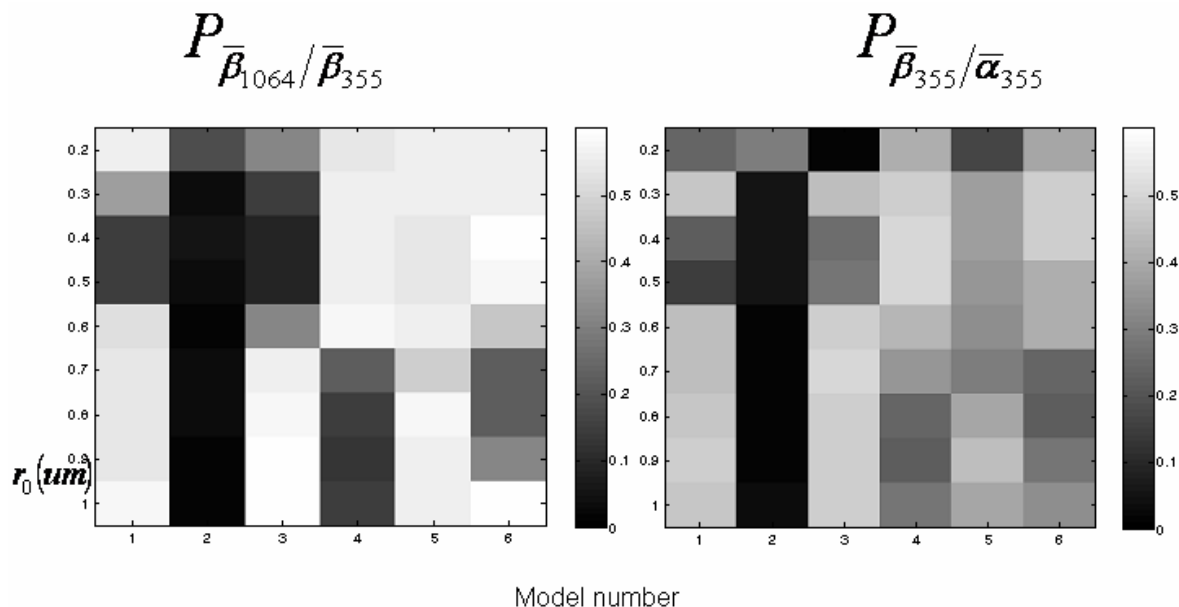


Fig. 4.12.a) Probability metric as a function of the ratio of normalized backscatter at 1064nm to normalized backscatter at 355nm for different atmospheric states (model and radii) at 80% and 95% RH,  
 b) Probability metric as a function of the ratio of normalized backscatter at 355 to normalized extinction at 355nm for different atmospheric states (model and radii) at 80% and 95% relative humidity.

In fig.4.12b the constraint has been forced on the ratio of normalized backscatter at 355nm to normalized extinction at 355nm (meaning normalized to backscatter of the particles in dry state at the corresponding wavelengths). An inversion sensitivity comparison between fig. 4.12a and fig.4.12b indicates the  $\bar{\beta}_{355}/\bar{\alpha}_{355}$  ratio (also referred to as UV ratio or the lidar ratio) constrain in fig. 4.12b performing better than the color ratio constrain in fig. 4.12a .

The probability metric using a combination of measurements to include both UV normalized ratio and UV-NIR normalized ratio constraints for the combinations of relative humidities already defined earlier is illustrated in figure 4.10. By forcing the

unknown atmospheric state to undergo restrictions from all four constraints (UV normalized ratio at 80% and 95%, and UV-NIR normalized ratio at 80% and 95% simultaneously) simultaneously the probability of mistaking the unknown state for other states than the correct one is much smaller.

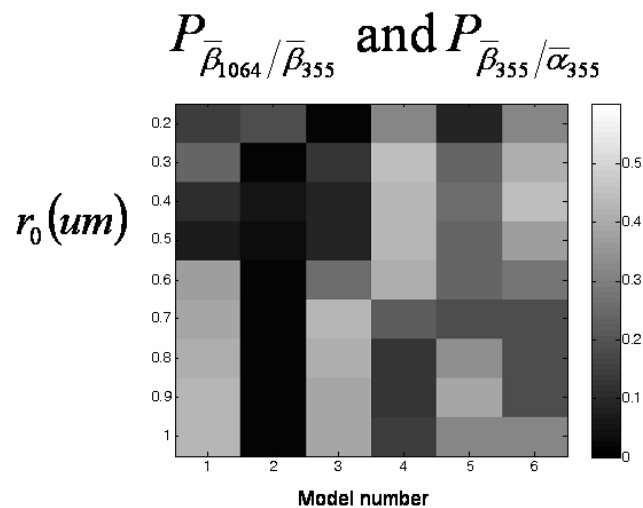


Fig. 4.13. Probability metric as a function of lidar and color ratio at 80% and 95% relative humidity

The fractional improvement when the four constraints mentioned above are used has been plotted in fig. 4.14.

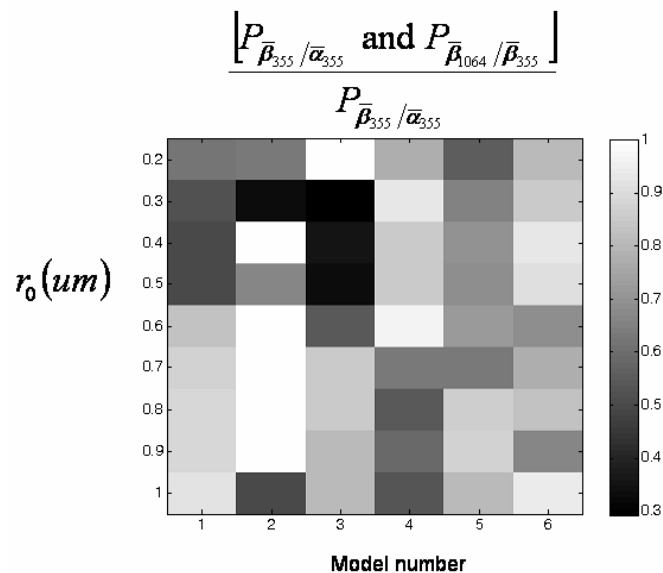


Fig. 4.14. Fractional improvement using four constraints

The states corresponding to model 2 (radii 0.6-0.9  $\mu\text{m}$ ) show little improvement while the ones corresponding to model 2 (radius 0.2) and model 3 (radii 0.3 to 0.5 $\mu\text{m}$ ) indicate a significant improvement in isolating the correct states by setting simultaneously the four constraints.

#### **4. Conclusions and References**

In this chapter, we explored the possibility of determining the nature and variability of urban aerosol hygroscopic properties using multi-wavelength Raman lidar measurements at 355nm, as well as backscatter measurements at 532nm and 1064nm. The addition of these longer wavelength channels allow us to more accurately validate the homogeneity of the aerosol layer as well as provide additional multiwavelength information that can be used to validate and modify the aerosol models underlying the hygroscopic trends observed in the Raman channel. The results of the model analysis taken at wavelengths 355nm and 1064nm (those nearest our experimental arrangement) indicate a clear dependence of the backscattering and total geometric cross section on relative humidity. In addition, a sensitivity analysis was performed which showed that a combination of UV normalized ratio(lidar ratio) and UV-NIR ratio (color ratio) data should improve hygroscopic model assessment. More mathematical investigations of the new proposed analyses should be performed on the lidar data to determine the degree of agreement of the measurements to the theoretical models based on the different models inputs. In addition, some qualitative features of the hygroscopic properties is demonstrated from lidar measurements under low cloud conditions. However, further efforts are needed to update the aerosol hygroscopic models. An updated model database

together with backward trajectory analysis is needed to develop a suitable climatology of hygroscopic aerosols. Further validation using a ground based multiwavelength nephelometer, TSI SMPS (Scanning Mobility Particle Sizer spectrometers) for size distribution, TEOM (Tapered Element Oscillating Microbalance) for mass of particles and Aeronet (NOAA ARL) refractive indexes analyses will also be explored.

### *References*

- [1] L.H Rhunke et al., *Hygroscopic aerosols*, A. Deepak Publishing, VI, USA, 1984
- [2] M.Phallow et al., “*Comparison between lidar and nephelometer measurements of aerosol hygroscopicity at the Southern Great Plains Atmospheric Radiation Measurement site*”, Journal of Geophysical Research, Vol 111, 2006
- [3] Yan Huang, “*Assessments of the Direct and Indirect Effects of Anthropogenic Aerosols on Regional Precipitation over East Asia Using a Coupled Regional Climate-Chemistry-Aerosol Model*”, Georgia Institute of Technology, 2005
- [4] Houghton, J. T. et al. eds, *Climate Change 2001: The Scientific Basis*(Houghton, J. T. et al. eds, Cambridge, U.K.: Cambridge University Press, 2001). Cambridge University Press, New York, United States (2001)
- [5] L. Bernstein et al, Intergovernmental Panel on Climate Change Fourth Assessment Report, Climate Change: 2007, <http://www.ipcc.ch/ipccreports/ar4-syr.htm>
- [6] R.J .Charlson et al., “*Climate forcing by anthropogenic aerosols*”,. Science, Vol. 255, pp. 423-430, 1992.

- [7] S. Twomey, " *The influence of pollution on the shortwave albedo of clouds*", Journal of the Atmospheric Sciences, Vol 34. Issue 7, pp. 1149–1152, 1997
- [8] S. E. Schwartz, *Cloud droplet nucleation and its connection to aerosol properties*, Proceedings of the 14<sup>th</sup> International Conference on Nucleation and Atmospheric Aerosols, 770-779, Elsevier Science Ltd., Oxford, UK, 1996.
- [9] V. Ramanathan et al. , *Aerosols, Climate, and the Hydrological Cycle*, Science, Vol. 294, 2119, 2001
- [10] B.J. Krueger et al, "*The transformation of solid atmospheric particles into liquid droplets through heterogeneous chemistry: Laboratory insights into the processing of calcium containing mineral dust aerosol in the troposphere*"; Geophys. Res. Lett., Vol. 30, No. 3, 2003
- [11] E. R. Gibson, "*Aerosol chemistry and climate: Laboratory studies of the carbonate component of mineral dust and its reaction products*", Geophysical Research Letters, Vol. 33, No. 13, L13811, 2006
- [12] S.H. Melfi et. al, "*Raman Lidar Measurements of Aerosol and Water Vapor, 2nd Symposium on Lidar Atmospheric Applications*", The 85<sup>th</sup> AMS Annual Meeting, San Diego, CA, Jan. 8-14, 2005
- [13] G. Hanel , "*The properties of Atmospheric aerosol particles as functions of the relative humidity at thermodynamic equilibrium with the surrounding moist air*", Adv. Geophy., Vol. 19, pp. 73-188 , 1976
- [14] K. Andre et al, "*Absorption of visible radiation by atmospheric aerosol particle, fog and cloud water residues*", American Meteorological Society, Vol. 38, pp141-155, 1981

- [15] D. V. Vladutescu et al, "*Analyses of Raman lidar calibration techniques based on water vapor mixing ratio measurements*", WSEAS Trans. on Syst., vol. 2, issue 4, pp. 651–658, Apr. 2007
- [16] G. d'Almeida et al, *Atmospheric aerosols. Global climatology and radiative characteristics*, A Deepak Publishing, VI, USA ,1991
- [17] D.N. Whiteman et al, "*Raman lidar system for the measurement of water vapor and aerosols in the Earth's atmosphere*" Applied Optics, Vol. 31, No. 16, 1992
- [18] G. Feingold et al., "*Feasibility of Retrieving Cloud Condensation Nucleus Properties from Doppler Cloud Radar, Microwave Radiometer, Lidar*", Journal of Atmospheric and Oceanic Technology, Vol.15, pp. 1188-1194, 1998
- [19] R. Measures, *Laser Remote Sensing: Fundamentals and Applications*, Krieger Publishing Company, Reprint Edition ,1992
- [20] A. Ansmann et al., "*Independent measurement of extinction and backscatter profiles in cirrus clouds by using a combined Raman elastic-backscatter lidar*", Applied Optics, Vol. 31, No. 33, 1992
- [21] F. G. Fernald, "Analyses of atmospheric lidar observations: some comments", Applied Optics, vol. 23, no. 5 ,1984
- [22] C. Weitkamp, *LIDAR range-resolved optical remote sensing of the atmosphere* , Springer, pp.100-190, 2005

## Chapter V

### **Atmospheric trace gas concentrations using Fourier Transform Interferometer measurements**

The determination of greenhouse gases and other molecular pollutants is important in process control as well as environmental monitoring. Since many molecular vibrational modes are in the infrared, molecules can absorb light from an infrared source (such as the sun or an artificial source such as a glow rod) and therefore, if the source spectrum is known, the absorption spectra of the sample can be measured. Therefore, any spectroscopy method needs a well characterized infrared source as well as an accurate high resolution spectrometer. The standard technique for open-path detection is Fourier Transform Infrared Spectroscopy (FTIR). Unlike a diffraction grating based spectrometer which directs different frequencies to different detectors (pixels), the interference spectrometer generates an interferogram that is then Fourier Transformed to obtain spectra. The finite sampling of the FFT results in an instrument resolution function which needs to be taken into account when resolving sharp absorption features. Therefore, the absorption spectra seen by the instrument is a convolution of the spectral line shape and the instrument response.

## 1. Introduction

### 1.1 Spectroscopic properties of atmospheric gases

The ability of measuring and consequently obtain information about the different gases in the atmosphere requires knowledge of the interaction of radiation and matter. This process is known as molecular spectroscopy and its aim and goal is to elucidate information on concentration, structure, dynamics, interactions of molecules (or atoms) with other particles. Molecular spectroscopy is usually classified by the wavelengths ranges of the electromagnetic radiation. The interaction of the radiation with the molecules or atoms is usually written in terms of a resonance condition, which implies that the energy difference between two stationary states,  $m$  and  $n$ , in a molecule or atom must be matched exactly by the energy of the photon (also known as elastic interaction):

$$(h\nu)_{\text{photon}} = E_m - E_n \quad (1)$$

A photon can only be absorbed to produce vibrational and rotational movements in the molecule if the charge around a molecule is separated in some way to produce dipole moment. However, radiation interacts with matter even if its wavelength is far different from the specific wavelength at which an absorption occurs (known as inelastic interaction). Therefore a more general classification of spectroscopy than that given by the wavelength range alone would be resonance/ off-resonance distinction. Some of the off-resonance models are the Raman effect described in section 2 of the second chapter, attenuated total reflection (ATR) spectroscopy, and others [1]

Levine shows in Molecular Spectroscopy that usually that the interaction between the radiation's magnetic field and the atom or molecule's charges is much weaker than the interaction of the radiation's electric field and the charges[2]. The exception is in the

NMR region where the interaction is between the magnetic dipole moments of the nuclei and the radiation's magnetic field, as seen in the diagram 5.1

Change of spin		Change of orientation	Change of configuration	Change of electron distribution		Change of nuclear configuration
N.m.r.	E.s.r.	Microwave	Infra-red	Visible and ultra-violet	X-ray	$\gamma$ -ray
$10^{-2}$	1	100	$10^4$	$10^6$	$10^8$	$10^8$
	$\text{cm}^{-1}$					
10 m	100 cm	1 cm	100 $\mu\text{m}$	1 $\mu\text{m}$	10 nm	100 pm
$3 \times 10^6$	$3 \times 10^8$	$3 \times 10^{10}$	$3 \times 10^{12}$	$3 \times 10^{14}$	$3 \times 10^{16}$	$3 \times 10^{18}$
				Hz	Frequency	
$10^{-3}$	$10^{-1}$	10	$10^3$	$10^5$	$10^7$	$10^9$
				joules/mole	Energy	

Figure 5.1 Electromagnetic(EM)-spectrum and types of interactions with EM-radiation

In the microwave and far infrared, the molecules undergo rotations and the component of the dipole in a given direction fluctuates like as the atom presented in the figure 5.2 where the atom is an oscillating dipole and its charge distribution in the coherent state  $1s+2p_0$  is presented as a function of time.

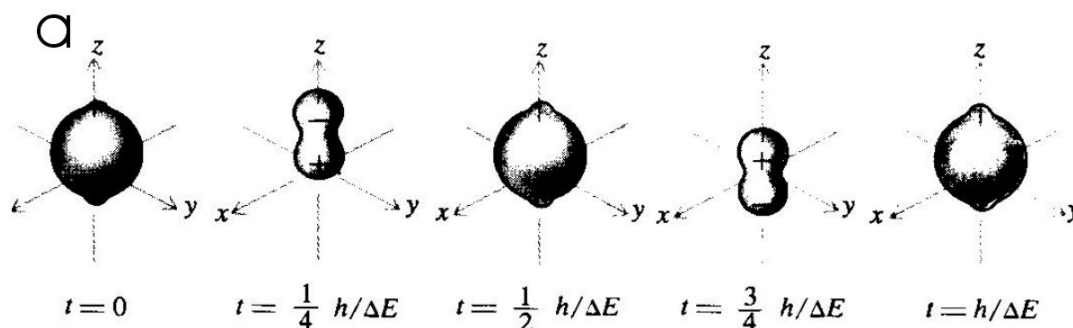


Figure 5.2 Electron cloud oscillations during optical transitions in an atom. The emitted radiation follows a very similar pattern.

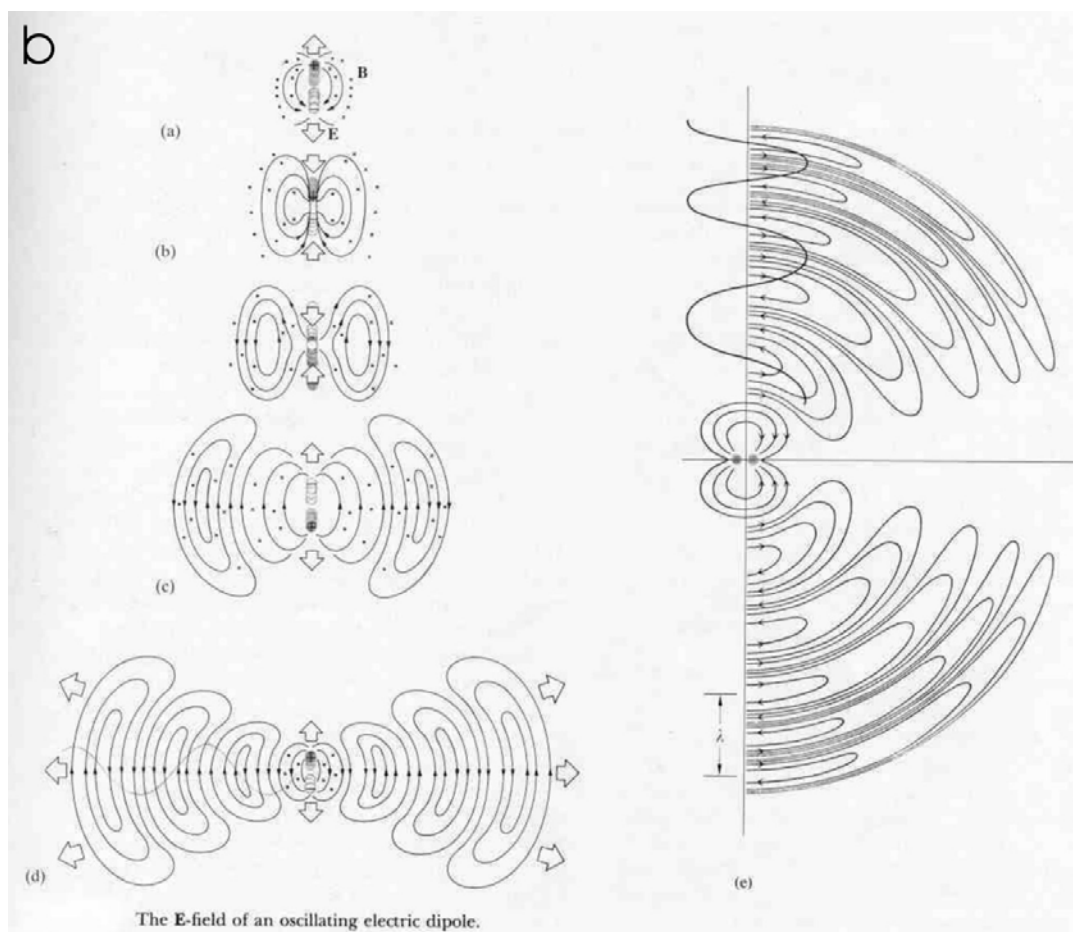


Figure 5.2 b) Electric field patterns of a classically oscillating dipole. Electromagnetic radiation is emitted. The atomic dipole shown above exhibits exactly the same pattern.

The fluctuations are more sluggish than are the fluctuations associated with vibrations or electronic transitions. Rotational lines usually take place in the longer infrared wavelengths beyond  $20\mu\text{m}$  extending in the microwave region where individual rotational lines can be resolved.[3]

In the mid-and near infrared the absorption of the radiation by molecules occurs by vibration or a mixture of vibrations and rotations.

Several vibrational modes of  $\text{CO}_2$  and  $\text{H}_2\text{O}$  can be identified and are presented in figure 5.3a) and b)

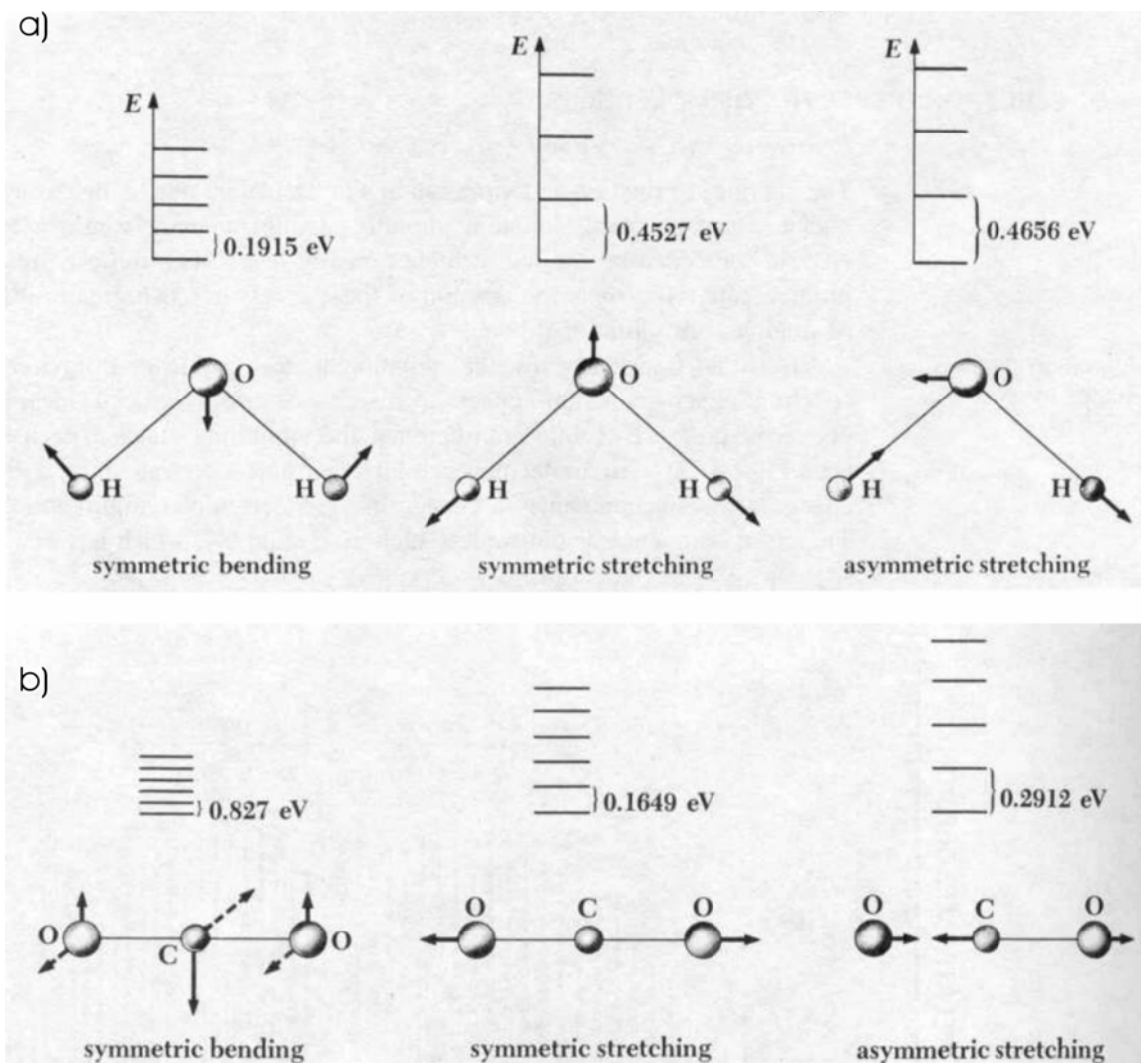


Figure 5.3 The normal modes of vibration of the a)  $\text{H}_2\text{O}$  and b) of  $\text{CO}_2$  and the energy levels of each mode

At higher energy (in the visible and ultraviolet region) the absorption is associated with electronic transitions. The valence electrons are excited and move in the molecule.

At even shorter wavelengths like x-rays or gamma-rays, the photons can actually disrupt the absorbing molecules by photodissociation or respectively produce photoionization of individual atoms (as is occurring in the ionosphere)

### *Atmospheric absorption spectra*

A schematic overview of the atmospheric absorption spectra is given in figure 5.5. The absorption in the ultraviolet beyond  $0.1\mu\text{m}$  and the visible is dominated by transitions in the electronic bands of molecular oxygen and ozone. The vibrational-rotational absorbing bands of six absorbing gases are also presented and they are applied to vertical paths through the whole atmosphere.

Because of its symmetry, the oxygen molecule has no permanent dipole, but it does possess a permanent magnetic dipole moment as a result of unpaired orbital electrons. This insures that the molecule is radiatively active through magnetic dipole transitions. These transitions are typically orders of magnitude less intense than the electric dipole transitions. The great abundance of the oxygen molecule, relative to the other absorbing molecules, compensates for these weak transitions, ultimately producing a large atmospheric absorption. Molecular oxygen is referred to as a triplet with a ground electronic state and two excited electronic states. The electronic transitions from the ground state to either of these other states, accompanied by vibrational-rotational transitions, produces bands referred to as the infrared and the red bands, observed in the diagram below.

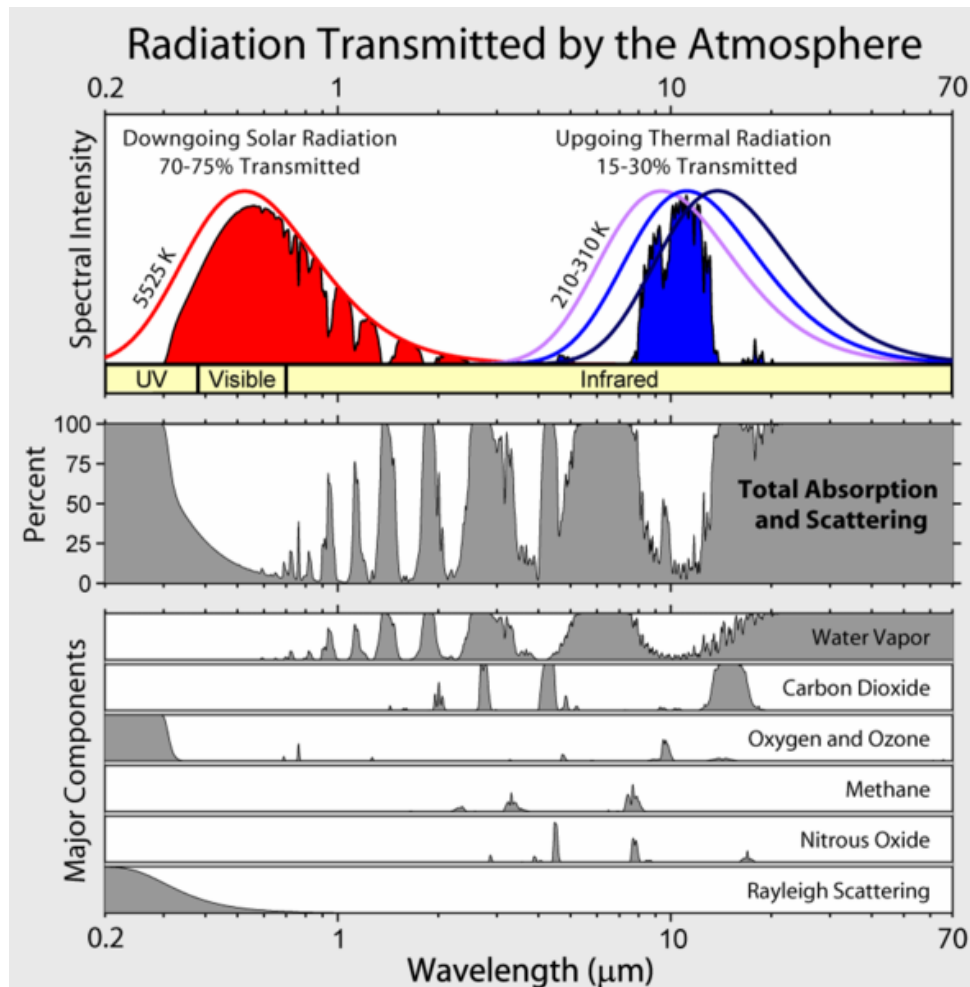


Figure 5.4 Radiation transmitted by the atmosphere

Absorption by atmospheric ozone is dominated by electronic bands in visible and ultraviolet spectral regions (centered at  $0.255\mu\text{m}$ ) and the vibrational-rotational transitions in the infrared region with a strong band centered at  $9.6\mu\text{m}$ .

Vibrational-rotational absorption by carbon dioxide occurs in a number of spectral regions. The infrared absorption of spectrum of carbon dioxide is dominated by the very strong  $15\mu\text{m}$  and  $4.3\mu\text{m}$  bands. The  $15\mu\text{m}$  is particularly important to temperature sounding techniques. The complex vibrational-rotational absorption spectrum of water vapor together with relatively large concentrations of water vapor in the lower

atmosphere, account for the dominance of this gas in the spectrum extending from the near infrared into the microwave region. [4]

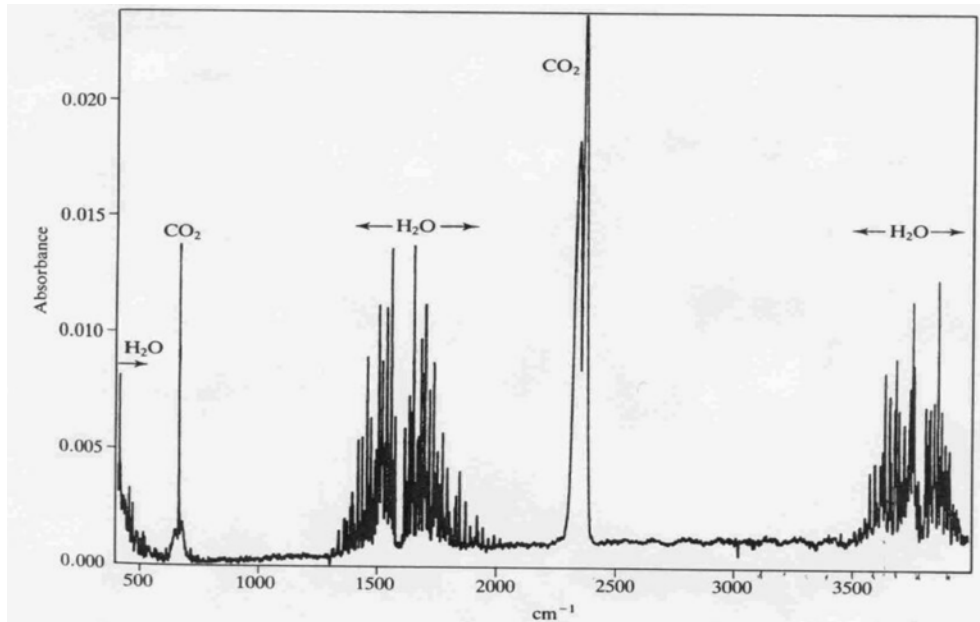


Figure 5.5 Infrared spectrum of humid air.

The fine scale structure is due to molecular rotations. These can only be seen in low pressure samples in the gas phase, in liquid (or solid) samples. In the atmosphere these spectral lines are blurred out by interactions (collisions) with molecules close by, through three main processes: natural, pressure and Doppler broadening that characterize the line shape. The other two factors that characterize the line absorption are the position and the strength.

#### *Spectral line shape*

The shape factor  $f(\nu - \nu_0)$  together with the line strength  $S$  and position combine to define the absorption parameter

$$k_\nu = Sf(\nu - \nu_0) \quad (2)$$

where  $S$ , the line strength is the product of two distinct factors. The first factor represents the probability that a single molecule in its original lower state absorbs a photon to jump

to an upper state. This probability is measured in terms of the line cross section  $\sigma$ . The second factor represents the relative populations of the lower and upper states such that  $S = \sigma(n_l - n_u)$ , where  $n_{l,u}$  are the molecules in the lower and upper states relative to the total number of molecules in all states. It is usually assumed that  $\sigma$  is the same for both the upper and lower states and that the populations are governed by the Boltzmann distribution so that the line strength is temperature dependent.[3] By convention the shape factor is defined such that  $\int_{-\infty}^{\infty} f(\nu - \nu_0) d\nu = 1$  and is found based on the following principles

A photon is absorbed or emitted whenever atoms undergo transition between energy levels by radiative means. Each atomic energy level has a lifetime  $\tau$ , which is the inverse of the rate at which its population decays, radiatively or nonradiatively, at all lower levels. The lifetime  $\tau$  of an energy level is related to the time uncertainty of the occupation of that level and is in essence a Fourier transform effect. As seen in ANEXA B the Fourier Transform of an exponentially decaying harmonic function of time  $e^{-t/2\tau} e^{j2\pi\nu_0 t}$ , which has an energy that decays as  $e^{-t/\tau}$  (with time constant  $\tau$ ), is proportional to  $1/[1 + j4\pi(\nu - \nu_0)\tau]$ . The full width at half-maximum (FWHM) of this Lorentzian function of frequency is  $\Delta\nu = 1/2\pi\tau$ . This spectral uncertainty corresponds to an energy uncertainty  $\Delta E_1 = h\Delta\nu = h/2\pi\tau_1$  for level 1 and respectively  $\Delta E_2 = h\Delta\nu = h/2\pi\tau_2$  for level 2, provided that we can model the decay process as a simple exponential. [5]. The spread in the energy difference between this is known as the natural broadening of the line. Therefore

$$\Delta E = \Delta E_1 + \Delta E_2 = \frac{h}{2\pi} \left( \frac{1}{\tau_1} + \frac{1}{\tau_2} \right) = \frac{h}{2\pi} \frac{1}{\tau} = h\Delta\nu \quad (3)$$

where  $\Delta\nu$  is called the lifetime broadening and represents the spread of the transition frequency. This spread is centered about the frequency  $\nu_0 = E_2 - E_1 / h$ , and the shape factor is called *Lorentz line shape* (pressure (collision) broadening):

$$f_L(\nu - \nu_0) = \frac{\alpha_L / \pi}{(\nu - \nu_0)^2 + \alpha_L^2} \quad (4)$$

where  $\alpha_L$  is referred to as the Lorentz half width and is  $(2\pi t)^{-1}$  and  $t$  is the mean time between collision. When typical kinetic theory is adopted to describe molecular collisions

$$\alpha_L \approx \alpha_{L,s} \left( \frac{p}{p_s} \right) \left( \frac{T_s}{T} \right)^{1/2} \quad (5)$$

where  $p_s=1000\text{mb}$ ,  $T_s=273\text{K}$ , and  $\alpha_{L,s}$  is the half value at these standard temperatures and pressures. However the temperature dependence on the line shape is usually of secondary importance compared to the temperature dependence of the line strength, as it will be shown below.

The pressure dependence of absorption has a profound effect on the remote sensing of the atmosphere. Consider a downward-looking radiometer which receives radiation through a filter which has a spectral width narrower than the line width and is capable of detecting radiation emitted at three neighboring spectral regions in the absorption line. For a line of suitable strength when the line is close to the center, the radiation detected by the instrument originates mainly from the higher levels of the troposphere. Further out from the line center, the radiation detected by the instrument arrives from lower down, perhaps in the middle levels of the atmosphere. Still further out into the wings of the line,

little of the radiation emitted from the broadened line is absorbed by the atmosphere above owing to the narrowing of the absorption line at higher altitudes. Thus the radiation detected at these wavelengths originates largely from emission in the lower troposphere.

Variations of the line shape from the Lorentz model occur in the microwave regions where the width of the of the rotational line is comparable to the central frequency of the line. At these wavelengths the van Vleck-Weisskopf function

$$f_{vw}(\nu - \nu_0) = \frac{1}{\pi} \left( \frac{\nu}{\nu_0} \right)^2 \left[ \frac{\alpha_L}{(\nu - \nu_0)^2 + \alpha_L^2} + \frac{\alpha_L}{(\nu + \nu_0)^2 + \alpha_L^2} \right] \quad (6)$$

is a better approximation to the laboratory measurements.

Finite line width arise also simply due to the motions of the molecules themselves. The frequency shift depends on whether the dipole is moving toward or away from the observer. It is this shift in frequency that gives rise to Doppler broadening. The distribution function describing the Doppler shifts (resulting from the distribution of particle velocities) is given by

$$f_D(\nu - \nu_0) = (\pi\alpha_D)^{-1/2} \exp\left[-(\nu - \nu_0)^2 / \alpha_D^2\right] \quad (7)$$

where  $\alpha_D = \frac{u_m \nu_0}{c}$ ,  $u_m = \left( \frac{2k_B T}{m_a} \right)^{1/2}$  and  $m_a$  is the molecular mass;  $u_m$  is essentially the

root mean square molecular velocity. We note from this broadening formula that the absorption lines of heavy molecules broaden less than do light molecules.

The relative importance of the Doppler broadening compared to pressure broadening can be appreciated in terms of the ratio

Due to the dependence of the Doppler width on the center frequency, Doppler broadening of the line at 2.5mm wavelength (or about 118GHz) is two orders of

magnitude smaller than that of the CO<sub>2</sub> line at 15μm. The transition between regions dominated by pressure broadening and regions dominated by Doppler broadening occurs approximately 40km higher up in the atmosphere for O<sub>2</sub> at 2.5mm.

In the transition region where both Doppler and Lorentz broadening are important, that is where  $\alpha_D = \alpha_L$ , the shape factor maybe represented as a combination of both line shapes according to a function referred as Voight line shape.

The spectral analyses presented in this work are based on infrared absorption window of gases using Fourier transform infrared spectroscopy. The measurement of the trace gases in the atmosphere by means of spectrometers is based on the diagram presented in figure 5.6.

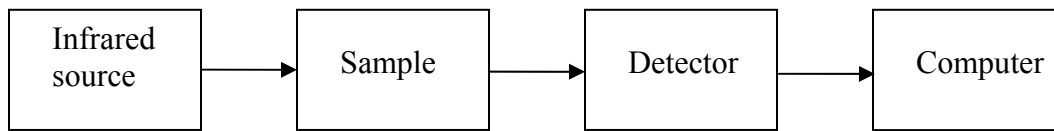


Figure 5.6 Schematic illustration of infrared spectroscopy

### *Transmission function*

Absorption of radiation by gases in the Earth's atmosphere is described in terms of transmission functions. This function arises from Lambert's law which states that the change in intensity along a path (of gas)  $ds$  is proportional to the amount of matter (gas) along the path according to

$$dI_{\bar{\nu}} = -k_{\bar{\nu},v} I_{\bar{\nu}} ds \quad (8)$$

where  $k_{\tilde{\nu},v}$  is the volume absorption coefficient. The dependence of the absorption coefficient on the density of the gas gives rise to a number of possible ways of specifying the absorption coefficient: the molecular absorption coefficient,  $k_{\tilde{\nu},n} = k_{\tilde{\nu},v} / n$  where  $n$  is number density of absorbing molecules; the mass absorption coefficient  $k_{\tilde{\nu},m} = k_{\tilde{\nu},v} / \rho_a$ , where  $\rho_a$  is the density of the absorbing gas; and the absorption coefficient at s.t.p.,  $k_{\tilde{\nu},s} = k_{\tilde{\nu},v} n / n_s$ , where  $n_s$  is the Loschmidt's number (also known as the Avogadro's number  $6.8 \times 10^{23}$  molecule per gram molecule). The product  $k_{\tilde{\nu}} ds$  is unitless so that for each type of coefficient there is a different measure of path length. Integrating between  $s_1$  and  $s_2$  provides a general solution to Lambert's law in the form

$$I_{\tilde{\nu}}(s_2) = I_{\tilde{\nu}}(s_1) \mathfrak{T}_{\tilde{\nu}}(s_1, s_2) \quad (9)$$

where  $\mathfrak{T}_{\tilde{\nu}}(s_1, s_2)$  is referred to as monochromatic transmission function and is defined as

$$\mathfrak{T}_{\tilde{\nu}}(s_1, s_2) = \exp \left[ - \int_{s_1}^{s_2} k_{\tilde{\nu},v} ds \right] \quad (10)$$

And refer to this as the optical path. This quantity is basic to the mathematical description of how radiation interacts with matter. There are a variety of different forms of this quantity throughout this book. It is customary to idealize the atmosphere as a horizontally stratified medium in the manner as shown in figure 5.7 and to define the path relative to the vertical.

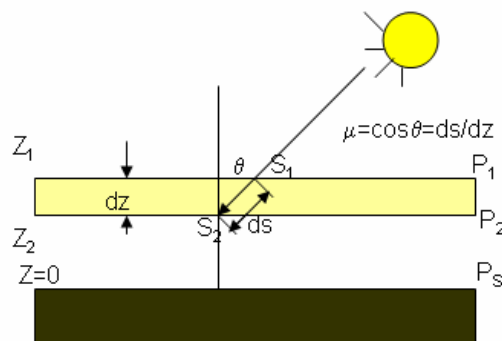


Figure 5.7 Plane parallel atmosphere and the relationship between slant and vertical paths.

Thus transmission along a path tilted from the vertical by an angle, the zenith angle, is simply related to the transmission along the vertical path according to

$$\mathfrak{T}_{\bar{\nu}}(s_1, s_2) = \mathfrak{T}_{\bar{\nu}}(s_1, s_2, \mu = \cos \theta) = \exp[-\tau_{\bar{\nu}}(z_1, z_2) / \mu] = \exp\left[\frac{\int_{z_1}^{z_2} k_{\bar{\nu}, \nu} dz}{\mu}\right] \quad (11)$$

where  $\tau_{\bar{\nu}}(z_1, z_2)$  is now measured along the vertical and is referred to as the optical depth [3 see ch2]. Therefore the final radiance detected by the sensor is the convolution of this monochromatic transmission function with the instrument band transmission function and radiation before entering the gas. For more information on instrument transmission function please refer to section 2.[3]

## 2. Basics of the FTIR technique

### 2.1 Interference and Autocorrelation

The open path FTIR process can be mathematically described by three main contributing components:

1. The polychromatic wave (a superposition integral of harmonic functions of different frequencies, amplitudes and phases known as an inverse fourier transform) produced by the source travels through the atmosphere with different harmonic components being absorbed by the different gases in the atmosphere.
2. The resultant polychromatic wave is collected by a telescope and focused into a Michelson interferometer that separates the beam into two components and then based on the correlation theorem recombines the two waves into an interferogram.
3. The interferogram thus obtained is fourier transformed by the operating software and the resulting spectrum is analyzed and processed to retrieve the concentration of the atmospheric gases present between the source and the detector.

A mathematical detailation of the above 3 process is given below.

### *1. Polychromatic wave*

A polychromatic wave can be expanded as a sum of monochromatic waves by the use of Fourier methods. An arbitrary function of time, such as the wavefunction An arbitrary optical wave is described by a wave function  $E'(z,t)$  at a fixed position  $z$ , can be analyzed as a superposition of harmonic functions of different frequencies, amplitudes, and phases.

$$E'(z,t) = \int_{-\infty}^{\infty} E_0 \exp j[\omega t - kz]d\nu = \int_{-\infty}^{\infty} E_\nu(z) \exp j2\pi\nu t d\nu \quad (12)$$

where  $E_\nu(z)$  can be determined by carrying out the Fourier transform and will be detailed in the third process below[5].

Since  $E'(z,t)$  is real then  $E_\nu(z)$  must be a symmetric function of  $\nu$ , i.e.  $E_{-\nu}(z) = E_\nu^*(z)$ .

The integral in equation (12) may therefore be simplified by use of the relation

$$\int_{-\infty}^0 E_\nu(z) \exp(j2\pi\nu t) d\nu = \int_0^{\infty} E_{-\nu}(z) \exp(-j2\pi\nu t) d\nu = \int_0^{\infty} E_\nu^*(z) \exp(-j2\pi\nu t) d\nu \quad (13)$$

so that  $E'(z,t)$  is the sum of a complex function and its conjugate,

$$E'(z,t) = \int_0^{\infty} [E_\nu(z) \exp(j2\pi\nu t) + E_\nu^*(z) \exp(-j2\pi\nu t)] d\nu \quad (14)$$

The complex wavefunction is defined as twice the first term

$$E(z,t) = 2 \int_0^{\infty} E_\nu(z) \exp(j2\pi\nu t) d\nu \quad (15)$$

So that its real part is the wave function

$$E'(z,t) = \text{Re}\{E(z,t)\} = \frac{1}{2} [E(z,t) + E^*(z,t)] \quad (16)$$

The intensity of this wavefunction is given by

$$I(z,t) = 2 \langle E^2(z,t) \rangle = 2 \left\langle \left\{ \frac{1}{2} [E(z,t) + E^*(z,t)] \right\}^2 \right\rangle = \frac{1}{2} \langle E^2(z,t) \rangle + \frac{1}{2} \langle E^{*2}(z,t) \rangle + \frac{1}{2} \langle E(z,t)E^*(z,t) \rangle \quad (17)$$

## 2. Autocorrelation and interferogram

The polychromatic wavefunction arrives at the Michelson interferometer after passing through the atmosphere. At the Michelson's interferometer (figure 5.8) light is split into two beams by using a beam splitter to generate two identical waves, one of which is made to travel a longer optical path before the two waves are recombined using another (or the same beamsplitter). The schematic diagram of the Michelson interferometer is shown in the figure 5.8a).

The ability of a wave to interfere with a timed delayed replica of itself is governed by its *complex degree of temporal coherence* at that time of delay. If  $E'_1(z, t)$  and  $E'_2(z, t) = E'_1(z, t + \tau)$  are the two resultant coherent fields obtained by separation with a beamsplitter and reflected by the fixed and the moving mirrors than the total resultant autocorrelation function obtained from the two waves is given as follows

$$G(\tau) = \langle E_1'^*(t)E_1'(t + \tau) \rangle = \lim_{T \rightarrow \infty} \frac{1}{2T} \int_{-T}^T E_1'^*(t)E_1'(t + \tau) dt \quad (18)$$

This function describes the extent to which the wavefunction fluctuates in unison at two instants of time separated by a given time delay, so that it establishes the time scale of the process that underlies the generation of the wavefunction. In the language of optical coherence theory, this function is also known as *temporal coherence function*.

The *temporal coherence function*  $G(\tau)$  carries information about both the intensity and the degree of correlation (coherence) of stationary light. A measure of coherence that is insensitive to the intensity is provided by the normalized autocorrelation function

$$g(\tau) = \frac{G(\tau)}{G(0)} = \frac{\langle E_1'^*(t)E_1'(t + \tau) \rangle}{\langle E_1'^*(t)E_1'(t) \rangle} = \frac{\langle E_1'^*(t)E_1'(t + \tau) \rangle}{I_0} \quad (19)$$

which is called the complex degree of temporal coherence. Its absolute value cannot exceed unity,

$$0 \leq |g(\tau)| \leq 1 \quad (20)$$

The value of  $|g(\tau)|$  is a measure of the degree of correlation between  $E'_1(z, t)$  and  $E'_1(z, t + \tau)$ . When the light is coherent and monochromatic ( $E_0 \exp(j2\pi\nu_0 t)$ ) gives  $g(\tau) = \exp(j2\pi\nu_0 \tau)$ . Usually  $|g(\tau)|$  drops from its largest value  $|g(0)| = 1$  as  $\tau$  increases and the fluctuations become uncorrelated for sufficiently large time delay  $\tau$ .

### Interferogram

At a given position  $z$  and time  $t$ , the intensities of the two waves are

$$I_1 = \langle |E_1'(t)|^2 \rangle \quad \text{and} \quad I_2 = \langle |E_1'(t + \tau)|^2 \rangle, \quad I_1 = I_2 = I_0 \quad (21)$$

whereas their cross correlation is described by the statistical average  $G_{12}$  given by (18), and its normalized version  $g_{12} = g(\tau)$  given by (19).

When the two waves are superposed,  $E_{tot} = E_1'(t) + E_1'(t + \tau)$ , the average intensity of their sum is

$$\begin{aligned} I_{tot} &\propto E_{tot} \cdot E_{tot}^* = \langle |E_1'(t) + E_1'(t + \tau)|^2 \rangle = \\ &= \langle |E_1'(t)|^2 \rangle + \langle |E_1'(t + \tau)|^2 \rangle + \langle E_1'(t) E_1'^*(t + \tau) \rangle + \langle E_1'^*(t) E_1'(t + \tau) \rangle = \\ &= I_0 + I_0 + G_{12} + G_{12}^* = 2I_0 + 2\text{Re}\{G_{12}\} = 2I_0 + 2\sqrt{I_0 \cdot I_0} \text{Re}\{g_{12}\} \end{aligned} \quad (22)$$

therefore 
$$I = 2I_0 [1 + \text{Re}\{g(\tau)\}] = 2I_0 [1 + |g(\tau) \cos \varphi(t)|] \quad (23)$$

where  $\varphi = \arg\{g_{12}\}$  is the phase of  $g_{12}$ . The second term in on the right hand side of (23) represents the optical interference.

For two completely correlated waves with  $g_{12} = \exp(j\phi)$ , with  $\phi = \phi_2 - \phi_1 = 2\pi\nu t - 2\pi\nu(t + \tau) = -2\pi\nu\tau$  and  $|g_{12}| = 1$ , we obtain

$$I = 2I_0 [1 + \cos \varphi(\tau)] \quad (24)$$

For two uncorrelated waves with  $g_{12} = 0$ ,  $I = 2I_0$ , so there is no interference.

The strength of the interfere is measured by the visibility  $V$ , also called the modulation depth or the contrast of the interference pattern

$$V = \frac{I_{\max} - I_{\min}}{I_{\max} + I_{\min}} = \frac{2\sqrt{I_0 \cdot I_0}}{(I_0 + I_0)} |g_{12}| = |g_{12}| \quad (25)$$

where  $I_{\min}$  and  $I_{\max}$  are the minimum and maximum values that  $I$  takes as  $\varphi(\tau)$  is varied

### 3. Interferogram deconvolution (Spectrum)

The relation between  $I$  and  $\tau$  is known as an interferogram. Using the Fourier transform relation between  $G(\tau)$  and  $S(\nu)$ ,

$$G(\tau) = I_0 g(\tau) = \int_0^{\infty} S(\theta) [\exp(j2\pi\nu\tau)] d\nu \quad (26)$$

equation (24) can be expressed in terms of the power spectral density  $S(\nu)$  as

$$I = 2 \int_0^{\infty} S(\theta) [1 + \cos(2\pi\nu\tau)] d\nu \quad (27)$$

where  $\int_0^{\infty} S(\nu) d\nu = I_0$ . This equation can be interpreted as a weighted superposition of interferograms produced by each monochromatic components of the wave. Each component  $\nu$  produces an interferogram with period  $1/\nu$  and unit visibility, but the composite interferogram has reduced visibility as a result of different periods. Equation (27) suggests a technique for determining the spectral density of the light source by measuring the interferogram  $I$  versus  $\tau$  and then inverting it by means of Fourier-Transform methods. This technique is known as Fourier Transform Spectroscopy. The spectrum is finally obtained using the fourier Transform relationship below

$$I(\nu) = \int_{-\infty}^{\infty} I(\tau) \cos(2\pi\nu\tau) d\tau$$

## 2.2 Michelson Interferometer

A schematic diagram of the Michelson Interferometer is shown in figure 5.8. Waves emanating from the source get partially reflected and partially transmitted by the beam splitter, and the resulting beams get reflected by the moving and fixed mirrors. The reflected beams recombine after passing through the beam splitter and get collected by the detector. A linear representation of the optical path is illustrated in figure 5.8b). where the waves emanating from the source appear to get reflected by  $M_2$  and  $M_1'$  separated by a distance  $\Delta d$ . If the source is extended than no definite pattern is detected at the focal plane. The whole illuminated area of the detector is uniformly lit. Instead, if the wave is emanated by a point source or the detector is focused at infinity, circular fringes will be observed at the focal plane, each circle corresponding to a definite value of  $\theta$ (29).[6]

If  $M_2$  is tilted at an angle  $\theta/2$  then straight fringes will appear to the axes of the tilt

$$\begin{aligned} E_1 &= E_0 \exp i[k(z + 2\Delta d) - \omega t] \\ E_2 &= E_0 \exp i[kz \cos \theta + kx' \sin \theta - \omega t] \end{aligned} \quad (28)$$

The resultant field is obtained by plugging (28) in (22).

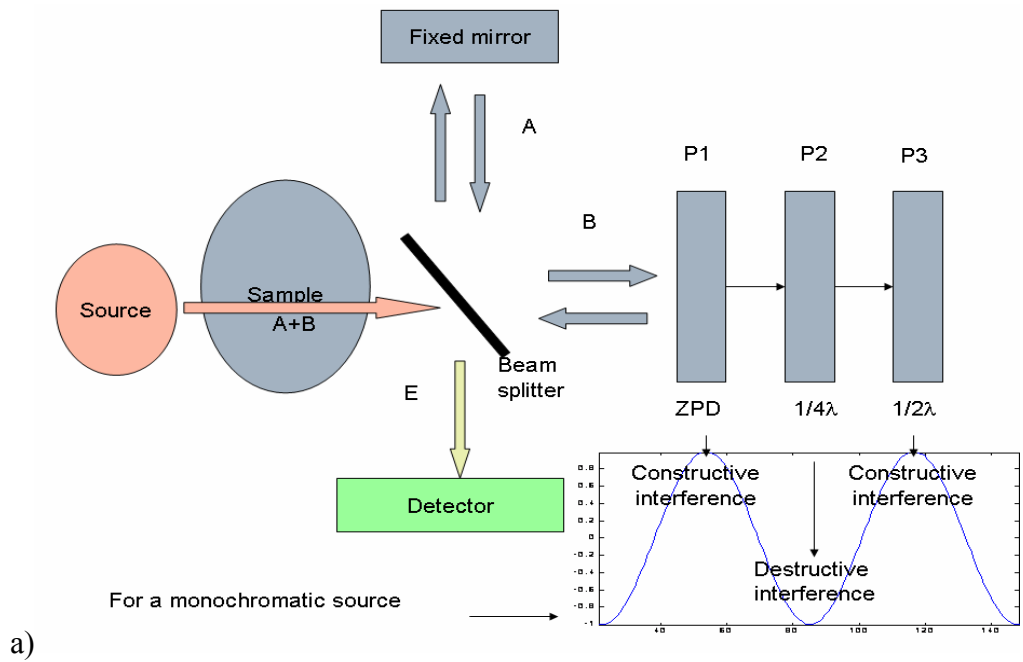


Figure 5.8 a) Michelson Interferometer,

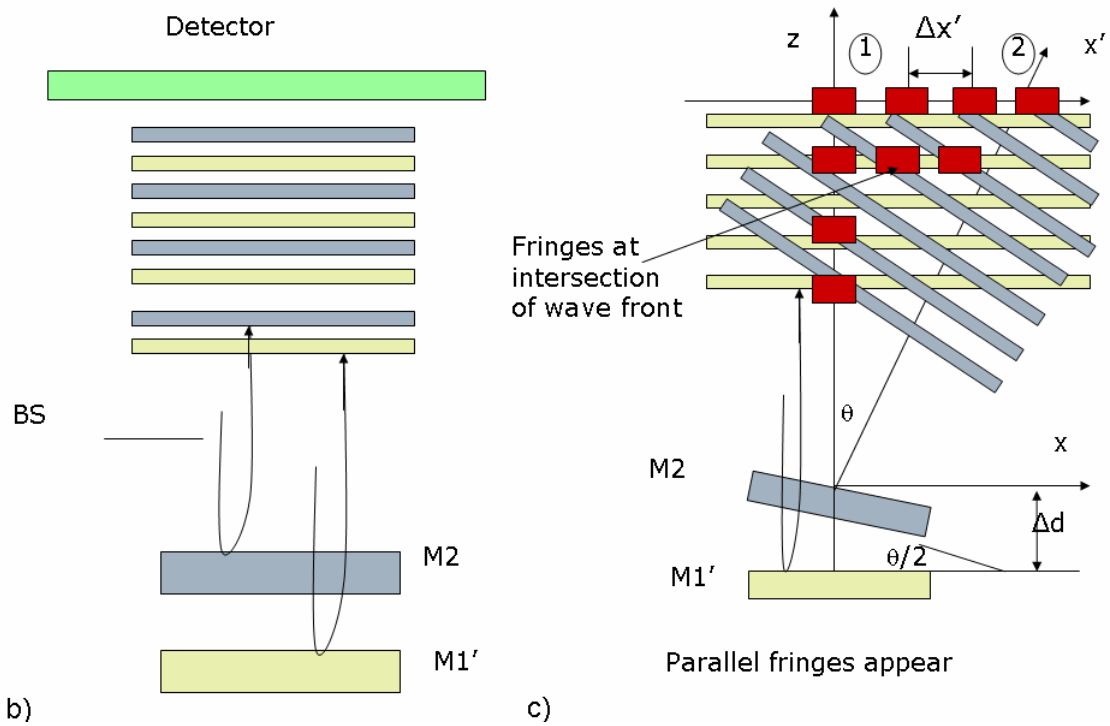


Figure 5.8 cont'd b)Linear equivalent of the optical path; c) moving mirror tilted at an angle  $\theta$

### *Resonance*

Condition for minimum intensity between rings

$$2\Delta d \cos \theta = n\lambda \quad (29)$$

where  $n=0,1,2,3,\dots$  and  $\Delta d$  is the path difference traveled by the two interfering beams.

The condition for a bright ring is

$$2\Delta d \cos \theta = \left(n + \frac{1}{2}\right)\lambda \quad (30)$$

### *Resolving power of the Michelson interferometer*

The resolving power of interferometers is function of the path difference of the two beams. This can be appreciated by considering the Michelson interferometer illuminated by a source of light at two adjacent wavelengths,  $\lambda$  and  $\lambda+\Delta\lambda$ . As the mirror move, the bright fringes periodically appear, disappear, and then reappear again. If a small displacement of the mirror in its travel is  $\Delta x$ , the resolution of the instrument is  $\Delta\lambda$  in terms of this displacement. Since the MIDAC instrument presented in this paper is using a mercury cadmium telluride (MCT) sensor that detects only the center interference(fringe),  $\Delta x$  is considered as the displacement of the mirror that causes a one-cycle variation in the visibility of the fringes. The fringe visibility is high when the bands of  $\lambda$  overlies those of  $\lambda+\Delta\lambda$  and poor when the bright fringes of the former coincide with the dark fringes of the latter. This situation occurs when  $\lambda$  is an odd number of half wavelengths of  $\lambda+\Delta\lambda$ . For a path of travel  $2x$ , the condition of maximum visibility is

$$2x = n_1\lambda = \left(n_2 + \frac{1}{2}\right)(\lambda + \Delta\lambda) \quad (31)$$

where  $n_1$  and  $n_2$  are odd integers. Noting that  $n_1 = \frac{2x}{\lambda}$ ,  $n_2 + \frac{1}{2} \approx \frac{2x}{\lambda} \left(1 - \frac{\Delta\lambda}{\lambda}\right)$

For  $\Delta\lambda \ll \lambda$ , then subtraction yields

$$n_2 - n_1 + \frac{1}{2} \approx -\frac{2x\Delta\lambda}{\lambda^2} \quad (32)$$

If  $n_2 - n_1$  increases by 1 as  $x$  goes from  $x$  to  $\Delta x$  and

$$n_2 - n_1 + \frac{3}{2} \approx -\frac{2(x + \Delta x)\Delta\lambda}{\lambda^2} \quad (33)$$

Subtracting these equations and rearranging follows that

$$\Delta x \approx \frac{\lambda^2}{2\Delta\lambda} \quad (34)$$

In terms of wavenumber  $\tilde{\nu}$ ,  $d\tilde{\nu}/d\lambda = -1/\lambda^2$  and

$$d\tilde{\nu} \approx \frac{1}{2x} \quad (35)$$

The high spectral resolution of the MIDAC spectrometer is 0.5cm<sup>-1</sup> leads to a displacement of approximately 1cm.

#### *Instrument transmission function*

For remote sensing, is important to distinguish between transmission of radiation at one selected wavelength (see section 1 in this chapter on monochromatic transmission functions) and transmission averaged over a range of wavelengths as specified, for example, by spectral response of the instrument (band transmission functions).

The radiation received at the detector is of the form:

$$I_{\Delta\tilde{\nu}} = \int_{\Delta\tilde{\nu}} g(\tilde{\nu}) I_{\nu} d\tilde{\nu} \quad (36)$$

where  $g(\nu)$  is the spectral response function of the instrument over its spectral band pass

$$I_{\Delta\tilde{\nu}}(s_2) = \int_{\Delta\tilde{\nu}} g(\tilde{\nu}) I_{\tilde{\nu}}(s_1) \mathfrak{T}_{\nu}(s_1, s_2) d\tilde{\nu} \quad (37)$$

where  $I_{\tilde{\nu}}(s_1)$  and  $\mathfrak{T}_{\tilde{\nu}}(s_1, s_2)$  were presented in section 1.1 of this chapter and they are the intensity of the signal after it passed through the gas and the monochromatic transmission respectively. If the spectral band is sufficiently narrow that the incident intensity is constant across the band, then the band transmission function becomes

$$\mathfrak{T}_{\Delta\tilde{\nu}}(s_1, s_2) = \int_{\Delta\tilde{\nu}} g(\tilde{\nu}) \mathfrak{T}_{\tilde{\nu}}(s_1, s_2) d\tilde{\nu} \quad (38)$$

Therefore the instrument properties (in this case the response function  $g(\nu)$ ) directly influence the transmission derived from measurements and must be accounted for in the retrieval schemes. In the analyses presented here (section 3 of chapter V), the response function used is

$$\phi(\tilde{\nu}) = \frac{1}{\tilde{\nu}_0} \operatorname{sinc}\left(\frac{\tilde{\nu}}{\tilde{\nu}_0}\right) \quad (39)$$

where  $\bar{\nu} = \pi\nu$  is the instrument effective bandwidth and  $\tilde{\nu}_0$  is the central wavenumber to be detected.[7]

### 2.3 Open path FTIR

In a laboratory environment (Closed Path FTIR), a controlled set of calibration spectra (for each molecule of interest) and a reference spectra (taken when the source is off) allows an unambiguous measurement of absolute spectra. In addition, only the gases of interest are placed in the sample cell. Open-path Fourier transform infrared (OP-FTIR) spectroscopy is a versatile analytical technique for filling an important gap in real-time methods available for occupational and environmental monitoring applications [1-3]. OP-FTIR spectrometers are remote sensing instruments that can non-invasively scan large

areas and simultaneously monitor multiple atmospheric pollutants at low limits of detection. OP-FTIR spectrometer systems use an interferometer, transfer optics, an infrared (IR) source, and a detector. Among the Open-Path FTIR configurations the most common are the mono-static, bi-static, and Aries. The difference between the monostatic and bistatic is that the bistatic uses an external source that sends photons to the instrument and then to the interferometer and then detector. The monostatic uses an internal source to send photons to the interferometer and then to an external retro-reflector and back to the detector. The disadvantage of the monostatic unit is that only half of the photons are sent to the retro reflector so that the maximum distance that you can use the system is cut in half. The advantage is that it is easier to align the retro reflector because the infrared beam is reflected back to its source although it may be slightly off axis. Retro reflectors are typically three mutually perpendicular surfaces available in different types of reflective materials typically being gold or silver. Retro reflectors are typically referred to as corner cubes or prismatic retro reflector. The systems can also be set-up to measure actively (with an external source or corner cube) or passively (using external stray light, solar energy, or an object that is hotter than ambient temperatures). Typically, it is more difficult although not impossible to quantify without an external source if the pathlength is not known.

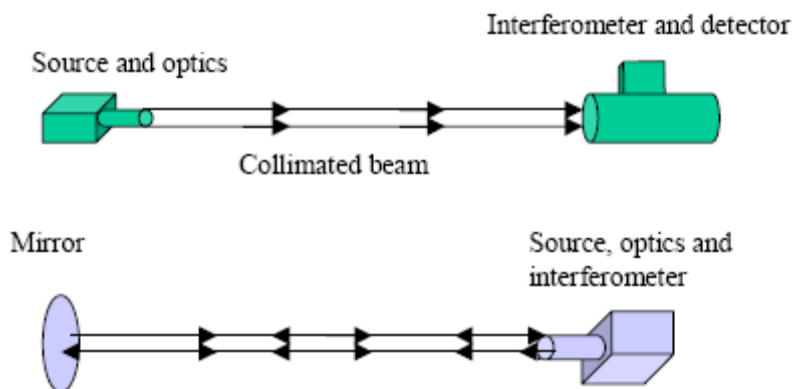


Figure 5.9 Bistatic and monostatic FTIR configurations

In the open-path design, there is no gas cell, and the infrared light (IR) is transmitted through a long open-air path that contains the ambient gases of interest. Since the excitation is continuous, the concentrations of pollutants are integrated over the entire length of the optical path. [8]

#### 2.4 MIDAC M2401-C FTIR characteristics

MIDAC Corp. manufactures 3 types of Open-Path systems, mono-static, bi-static, and Aries. The main working principles of these systems have been described in section 2.2 of this chapter. MIDAC Systems are in use throughout the world for fenceline monitoring of industrial facilities, rocket plume analysis, and studies of volcanic emissions. MIDAC Air Monitoring Systems are available in two basic configurations: Emissions package and remote source package (bistatic). The emissions configuration is primarily intended for qualitative analysis, while the active bistatic configuration can be used for quantitative and/or qualitative analysis. In this work we used a MIDAC M2401-C open-path FTIR instrument whose major characteristic are described below.

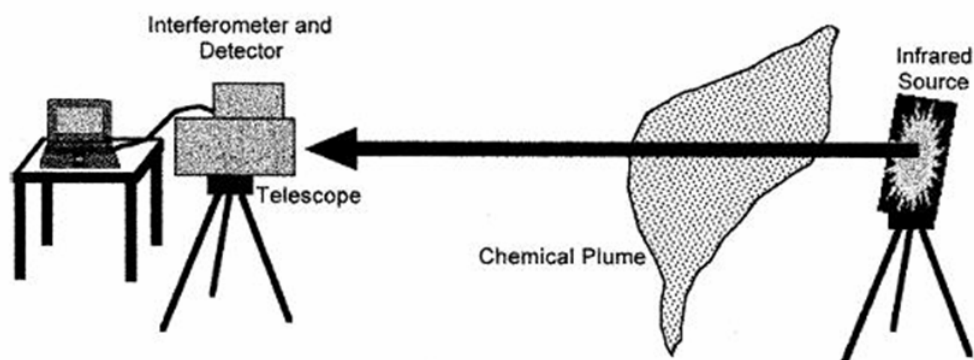


Fig. 5.10 FTIR instrument in Bistatic mode, the IR source is placed at the opposite end of the optical path

As specified above, the advantage of open-path systems is that they can be set-up to measure over very long optical pathlengths typically 1000 meters. The longer the pathlength, the lower the detection limit of the target compound being measured. The disadvantage is that interferences, typically ambient moisture and carbon dioxide can quickly saturate in their regions making it impossible to measure detector response in those regions

The FTIR measures molecules within the pathlength between the detector and source but the software reports the same number for a small plume of higher concentration (e.g. 100 ppm over a 1 meter pathlength) as a low concentration plume over a longer path length (10 ppm over 10 meters). This effect may lead to bias in the results, and is illustrated schematically in the figure below.

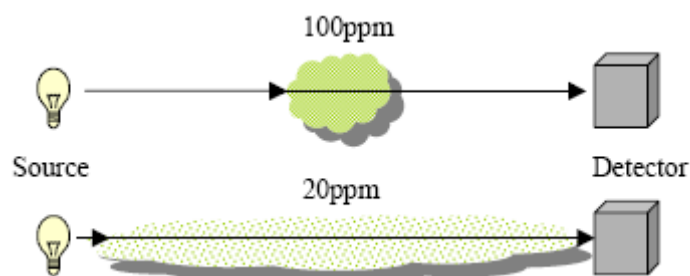


Fig 5.11 Plume concentration in the FTIR field of view

In more formal terms, the reported concentration of a matrix component is the average concentration value in the space between the source and detector.

Images of the MIDAC M2401-C system and outdoor measurements performed with this instrument are shown in figures 5.12 a), b), c).

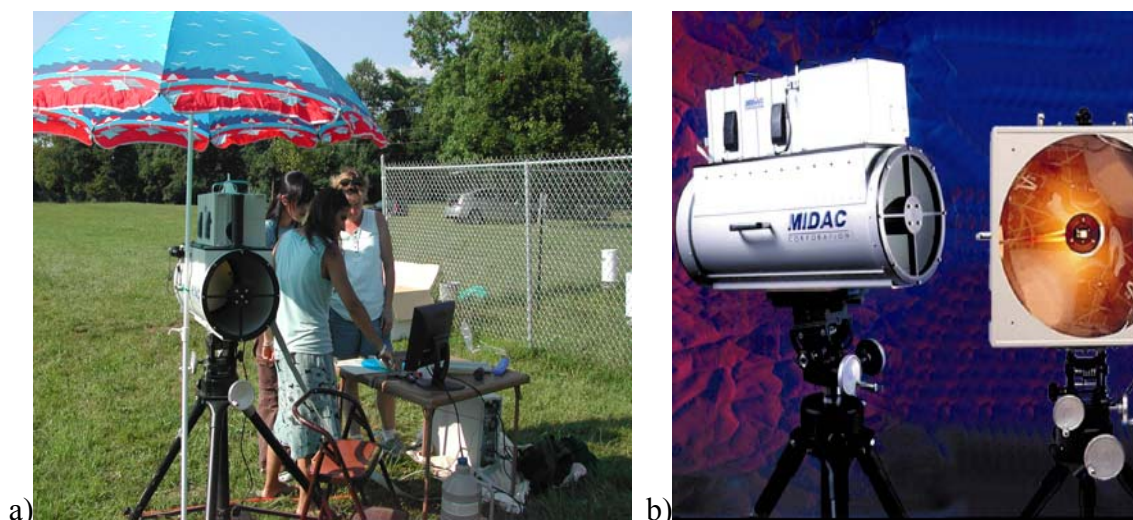


Figure 5.12 a) Spectroscopic field measurements with the open path bistatic MIDAC FTIR system.

b) MIDAC M2401-C open-path FTIR instrument



Figure 5.12 cont'd c) Illuminator (Spectrometer) without telescope

The system consist of an IR sources emit broadband electromagnetic radiation and operate at temperatures from 1200 to 1500K. The bistatic sources are 12VDC external

sources with a silicon carbide glower or quartz halogen source mounted in the center of a parabolic mirror. A summary of the main components of the FTIR system is presented in table 5.1

Table 5.1 Technical data of the FTIR system

FTIR System Components	Description
Source	12VDC, parabolic mirror
Telescope	Newtonian, D=12 in, Part#A2400, Serial#103
Spectral resolutions	0.5, 2, 4, 8, 16, 32 $\text{cm}^{-1}$
Spectral range	650-4500 $\text{cm}^{-1}$
Spectrometer	M2401-C Illuminator (Michelson Interferometer), Serial #166, 12VDC, 4cc
Optics	ZnSe
Detector	Graseby, 5/18/1994, N <sub>2</sub> cooled MCT, Model FTIR M16-1.00
Operating software	AutoQuantPro

### System Alignment

Accurate FTIR measurements are obtained when both the optical and electrical alignments are performed correctly. The optical alignment consists in the correct positioning of the source in the field of view of the detector.

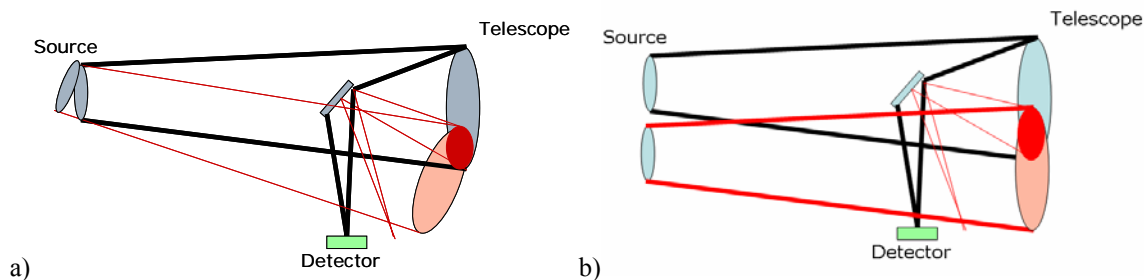


Figure 5.13 Two of the possible causes of misalignment a) source is tilted with respect to the detector,

b) source is off the main field of view axis

Improper alignment (see figure 5.13) can lead to poor or no signal detected by the signal. The alignment interferogram signal is displayed in either voltage or data bit

format in the Align window displayed by the AQ software in figure 5.14. The purpose of alignment is to maximize signal at the detector without overflowing the ADC capacity. Since the interferogram is rarely symmetrical at the centerburst, alignment should be done by observing either the minimum or maximum signal value, whichever is greatest. Optimally, the absolute value of the Max or Min should fall between 70% and 90% of the A/DC capacity (this translates to approximately 23,000 – 29,500 data bits, or 1.75 – 2.25 Volts). To avoid the loose of data points in the ADC, careful attention has been paid during alignments. The Min or Max value or “clipping,” were restricted to a range of +32,760 or -32,760. In figure below are illustrated the screens indicating the correct alignment voltage and number of points. The Min, Max, and Peak to-Peak values are displayed in large red characters on the Align screen for easy reference as adjustment is made on the source mirror or the telescope.

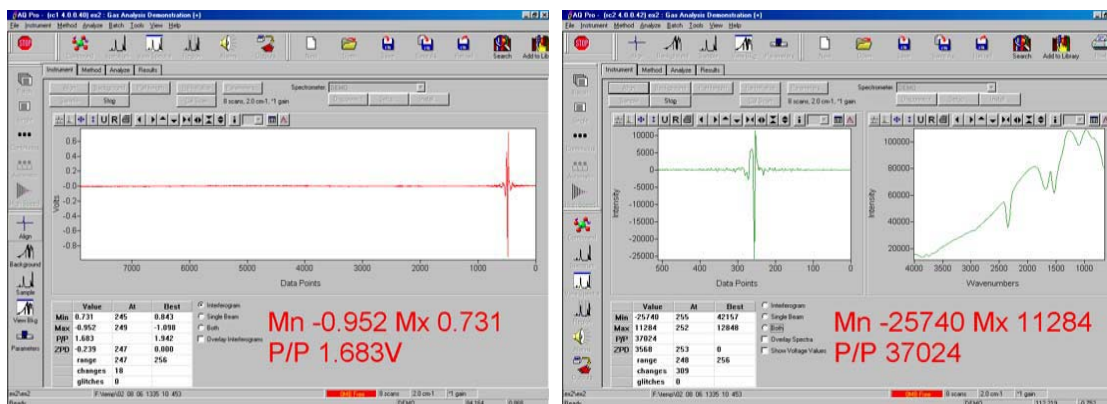


Figure 5.14 Peak to peak volts on the left and data points on the right obtained during correct alignments displayed by the AutoQuant Pro (AQ) Software

The interferogram measured with the open path MIDAC system and fourier transformed by the AQ are illustrated in figure 5.15.

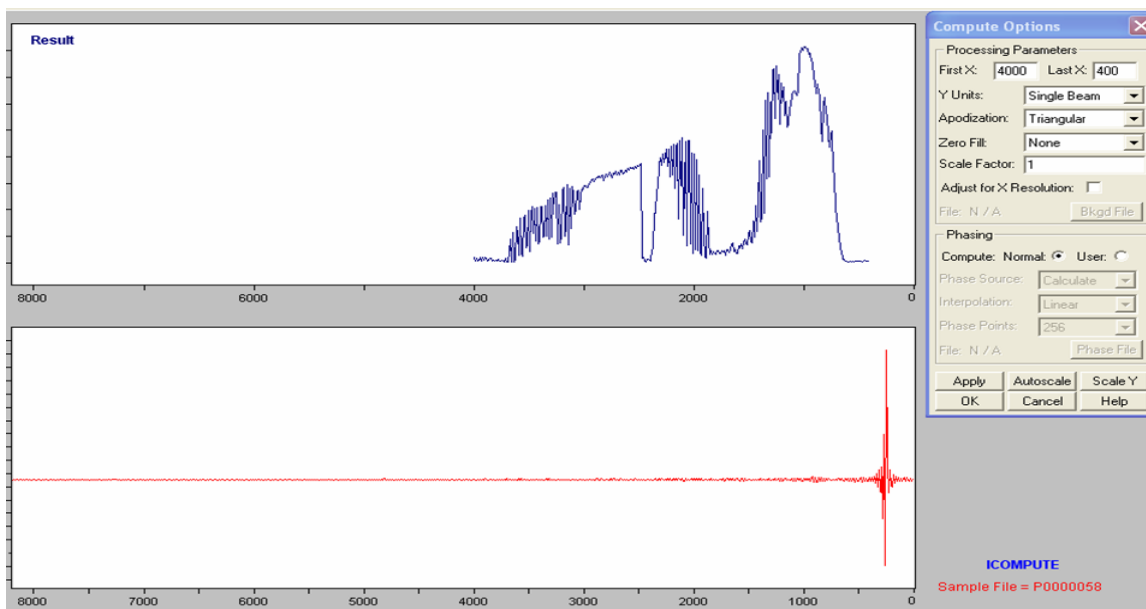


Figure 5.15 Interferogram (bottom) measured with the MIDAC M2401-C FTIR system and Fourier transformed by the AQ software into the IR spectrum (top)

The absorption lines retrieved from the spectrum above is baseline corrected and presented in the figure below

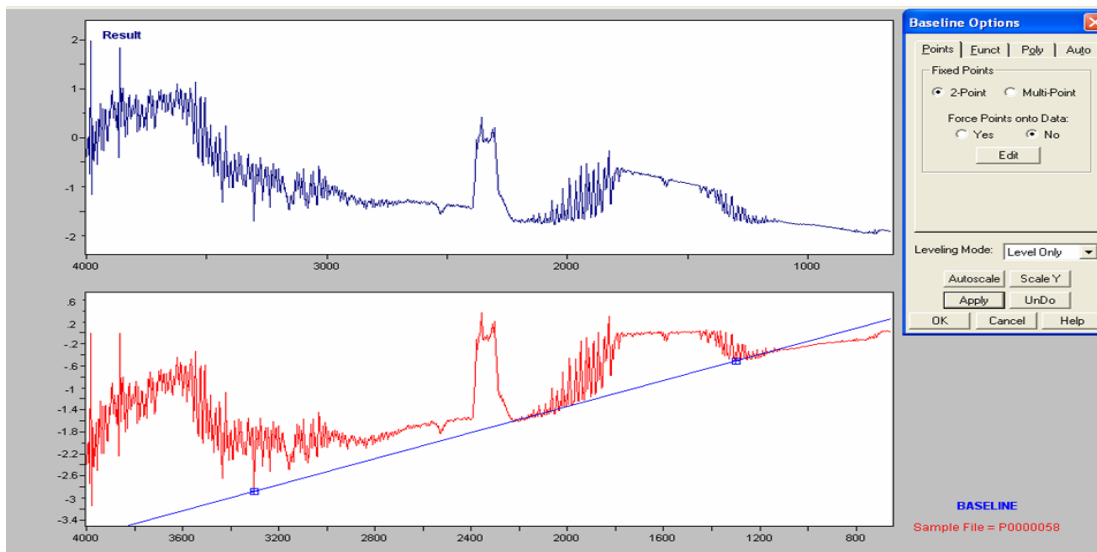


Figure 5.16 Baseline corrected absorption spectrum retrieved by the AQ software

The absorption spectrum obtained by the AQ software does not allow the disentangling of the different atmospheric gases contributions to the absorption spectrum. The overlap of the absorption lines and the saturation of the 3500-4000  $\text{cm}^{-1}$  and 1300-2000 $\text{cm}^{-1}$  spectral ranges by atmospheric water vapor and 2200-2400  $\text{cm}^{-1}$  by carbon dioxide makes the detection of atmospheric gases concentration practically impossible. Considering this we propose an algorithm for the determination of the atmospheric gases concentrations.

### **3 Results and discussions**

#### **3.1 Retrieval algorithm**

In the analysis of FTIR spectra, the standard approach is to subtract the single spectra directly from the calculated background power spectrum. Obviously underestimates of the background can lead to negative transmissions. To eliminate these spurious reading, we have developed an approach to reconstruct the background using the measurement spectrum directly. With this customized background approach, we obtain a significantly improved background which avoids the underestimation problem as seen in figure 5.17.

The approach used to create this background is simple.

1. Subdivide the spectral window into intervals with a width significantly longer than the expected feature line widths but much narrower than the expected background spectrum. In our case, the window  $\sim 10\text{cm}^{-1}$
2. Find the maximum value for the power spectrum in each window and the location of the maximum point and save all data points.

- From the coarse envelope, obtain the fine envelope using cubic-spline interpolation which will serve as background.

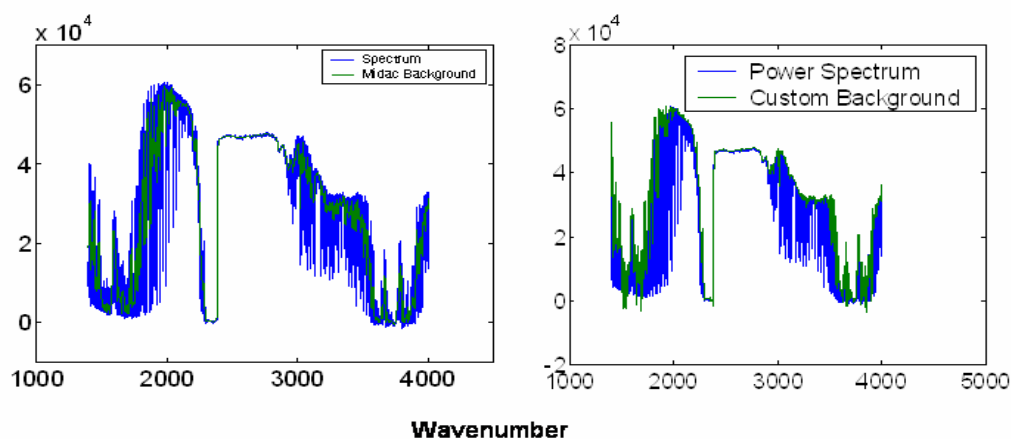


Figure 5.17. Spectrum overlaid with background spectra. a) standard processing b) custom background

The results of applying the custom background in the calculation of the absorption spectra are illustrated in figure 5.18. In particular, we note that using the standard processing can lead to spurious results in the absorption spectra. In fact, taking the logarithm of the ratio output to input power ( $P_{out}/P_{in}$ ) often leads to complex numbers with negative real part which must be filtered out. However, this occurrence is much less frequent using the custom background approach.

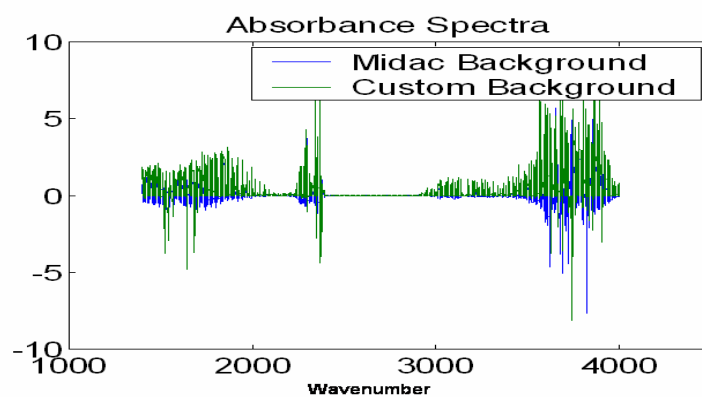


Fig. 5.18 Absorbance spectra calculated using the standard processing and the custom background processing

Once the system is calibrated by recalculating the background, the instrument function which defines the width of convolution in the processing of the theoretical lineshapes must be calculated. Based on the apodization used in the instrument, the instrument transfer function has the form

$$\phi(\bar{\nu}) = \frac{1}{\bar{\nu}_0} \operatorname{sinc}\left(\frac{\bar{\nu}}{\bar{\nu}_0}\right) \quad \bar{\nu} = \pi\nu \quad (40)$$

Using the spectral lineshape in equation above with different instrument line widths and convolving with the methane line between  $2626 \text{ cm}^{-1}$  and  $2629 \text{ cm}^{-1}$ , we examine the residuals in figure 5.19. The methane line was chosen as the spectrum has multiple inflection points.

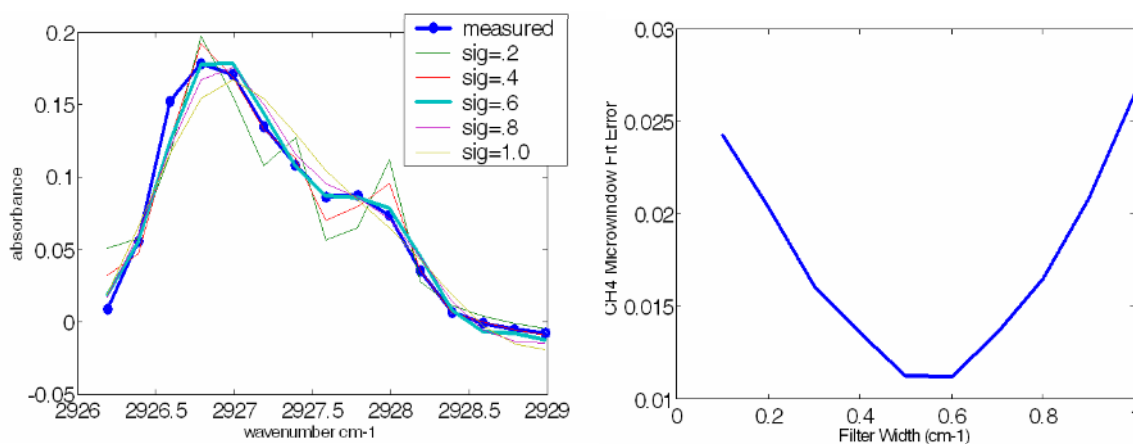


Figure 5.19. Convolved methane line to test instrument width. a) overlaid spectra with different widths b) residuals as function of width.

An illustration of the spectral fitting is given in figure 5.22 and 5.24 for 6 different species. From the above results, we determine the instrument linewidth to be  $\pi\nu_0 = .2\pi$

Absolute calibration of Open Path FTIR is difficult. Aerosol extinction, sensor quantum efficiency and source irregularities occur on much longer spectral scales than gas absorbance profiles. Therefore, in performing the analysis, a least squares fit is used

on each micro-window of interest. In particular, since we are not confident in the calibration approach, we ratio all absorbing signals to the signal strength of a non absorbing feature **in the vicinity of the microwindow**. In this way, a relative (ratio) measurement allows us to disentangle gas from background spectral signatures.

$$\begin{aligned} P_{out}(\lambda_{on}) &= T_{gas}(\lambda_{on})T_{back}(\lambda_{on})P_{in}(\lambda_{on}) \\ P_{out}(\lambda_{off}) &= T_{gas}(\lambda_{off})T_{back}(\lambda_{off})P_{in}(\lambda_{off}) \end{aligned} \quad (41)$$

where  $T_{gas}(\lambda_{on})/ T_{gas}(\lambda_{off})$  is the transmission of the gas in the ON/OFF band,  $T_{back}(\lambda_{on})/ T_{back}(\lambda_{off})$  is the transmission of the background in the ON/OFF bands and  $P_{in}(\lambda_{on})/ P_{in}(\lambda_{off})$  is the input power in the ON/OFF band. Therefore

$$\Rightarrow \frac{P_{out}(\lambda_{on})}{P_{out}(\lambda_{off})} \approx T_{gas}(\lambda_{on}) \quad (42)$$

assuming  $\lambda_{on} \approx \lambda_{off}$  the absorbance defined by the Beer-Lambert law is

$$\Rightarrow \tau_{meas}(\lambda) \approx -\log\left(\frac{P_{out}(\lambda)}{P_{out}(\lambda_{off})}\right) \quad (43)$$

where  $\lambda_{off}$  is at the reference wavelength where background absorption is negligible. [9].

Even with this precaution, we can still expect some issues with poor background compensation so an effort is made to fit both a constant background as well as a small linear spectral tilt which might occur in any reasonable spectral efficiency curve into our theoretical model as written by equation 44:

$$\tau_{meas}(\nu) = c_0 + c_1(\nu/\nu_0) + \sum_j c_j \tau_j(\nu) \quad (44)$$

where  $\tau_j = \exp(-C_{ref,j}\sigma_j L)$  is the optical depth of the  $j$ th species along the optical path the  $c_j$  are the retrieval coefficients normalized to the input concentrations used to calculate the ambient path optical depth (i.e.  $c_j = C_j/C_{ref,j}$ )

The solution of the normalized concentration vector in the LSQ formulation is given as

$$\mathbf{c}_{ret} = [\mathbf{T}'\mathbf{T}]^{-1}\mathbf{T}'\boldsymbol{\tau}_{meas} \quad (45)$$

where the matrix  $\mathbf{T} = [\mathbf{t}'_1 \wedge \mathbf{t}'_n]$ . In assessing retrieval error, we use the standard formula

$$\Delta c_j = \Delta \tau_{fit} * \text{sqrt}([\mathbf{Z}^{-1}]_{jj}) \quad (46)$$

where  $\Delta \tau_{fit}$  is the residual optical depth after fitting and we use the canonical LSQ matrix  $\mathbf{Z}^{-1} = [\mathbf{T}'\mathbf{T}]^{-1}$ .

### 3.2 Results

All trace gas spectra are calculated by the Line-Line Radiative Transfer Package GENSPECT for standard atmosphere conditions. All monochromatic spectra are convolved with the instrument function prior to LSQ retrieval. For choosing the spectral windows we developed an automated algorithm that searched for all microwindows in which no more than 2 ambient absorption features are present and all other features contribute  $< 0.1\%$  together with a requirement

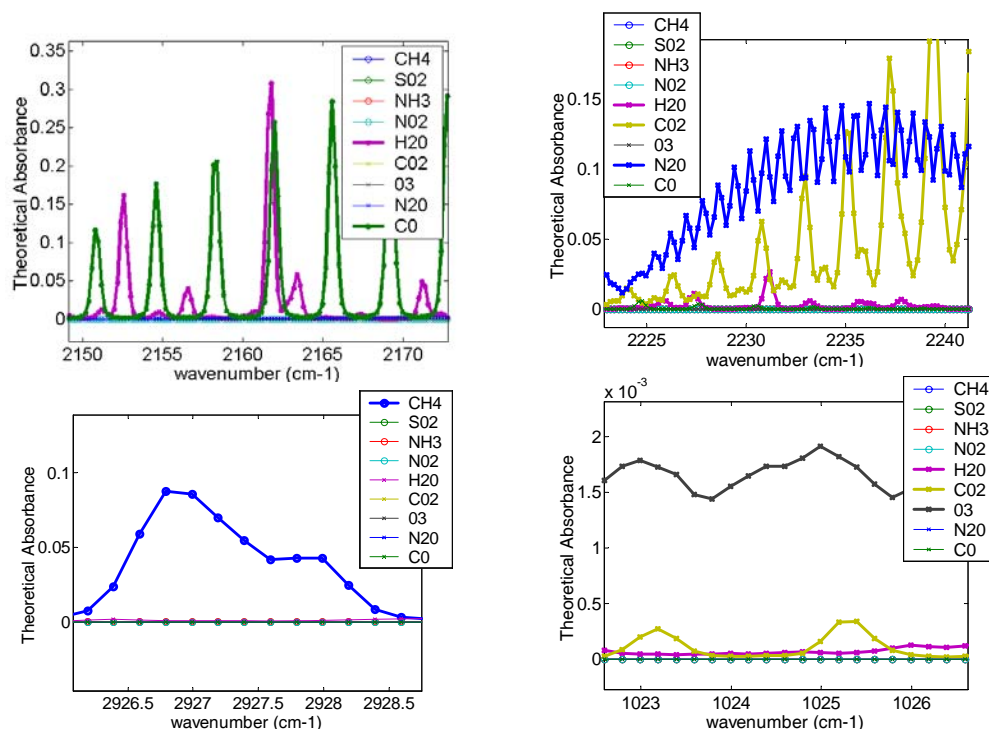


Fig. 5.20 Spectral microwindow with 2 ambient absorption features and all other features contribute  $< 0.1\%$

Ozone microwindow ( $1023\text{-}1025\text{ cm}^{-1}$ ) needs estimate of  $\text{CO}_2$  which comes from the ( $2225\text{-}2240\text{ cm}^{-1}$ ) window. The  $\text{CO}_2$  was obtained after a preliminary subtraction of the CO and  $\text{H}_2\text{O}$  concentrations determined from the  $2150\text{-}2170\text{ cm}^{-1}$ . In the end, methane was retrieved in the  $2926\text{-}2929\text{ cm}^{-1}$  window after preliminary subtraction of the all the gases whose concentrations were calculated above.

The absorption lines presented here were retrieved on two different days and locations: at CCNY station on April 22<sup>nd</sup>, 2003 and Princeton University on October 5<sup>th</sup>, 2007.

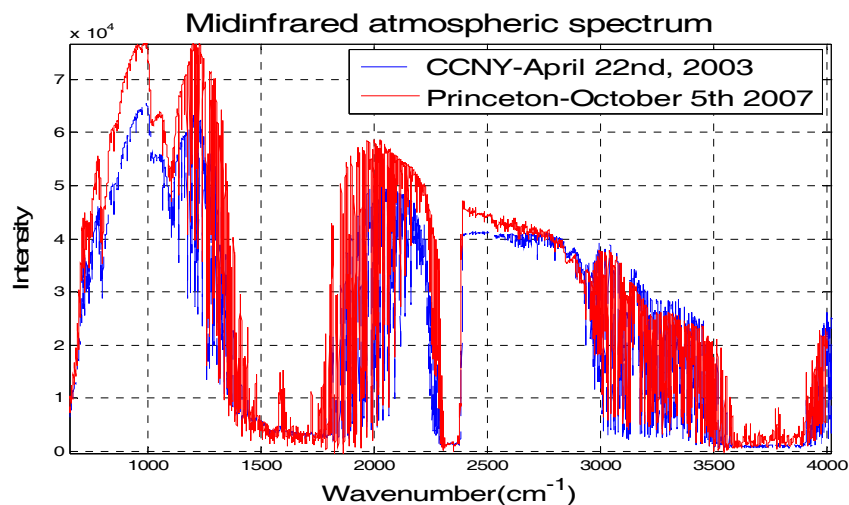


Figure 5.21 Comparison of mid IR spectrum measured at two different locations

(Princeton University and CCNY) and 4 years time difference (2003 and 2007 respectively)

The absorbances of the gases mentioned above retrieved on April 22<sup>nd</sup>, 2003 at the CCNY station are plotted in figure 5.22

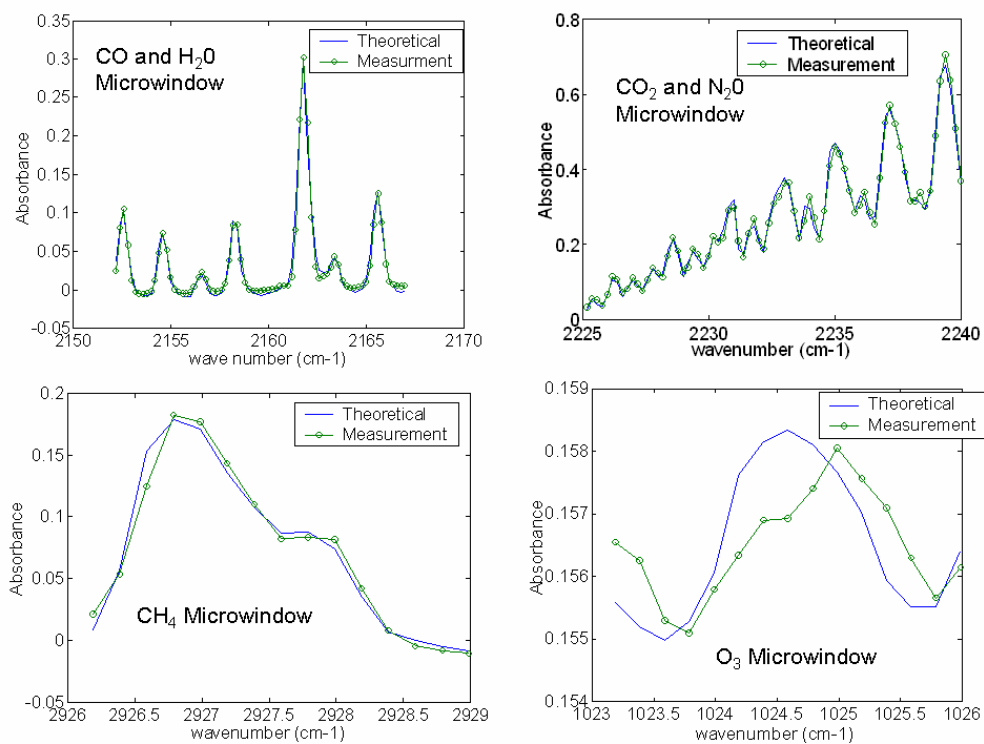


Figure 5.22 Match-ups based on least square fitting (LSQ) of theoretical spectra

and experimental spectra for 4 different micro-windows at CCNY station on April 22<sup>nd</sup>, 2003.

We see that the spectral fits on both days are more than adequate to measure almost all of the trace gases except ozone. This is because the absorption spectrum for ozone lies on a background continuum which is significantly larger than the spectral features of the ozone absorption at ambient concentrations.

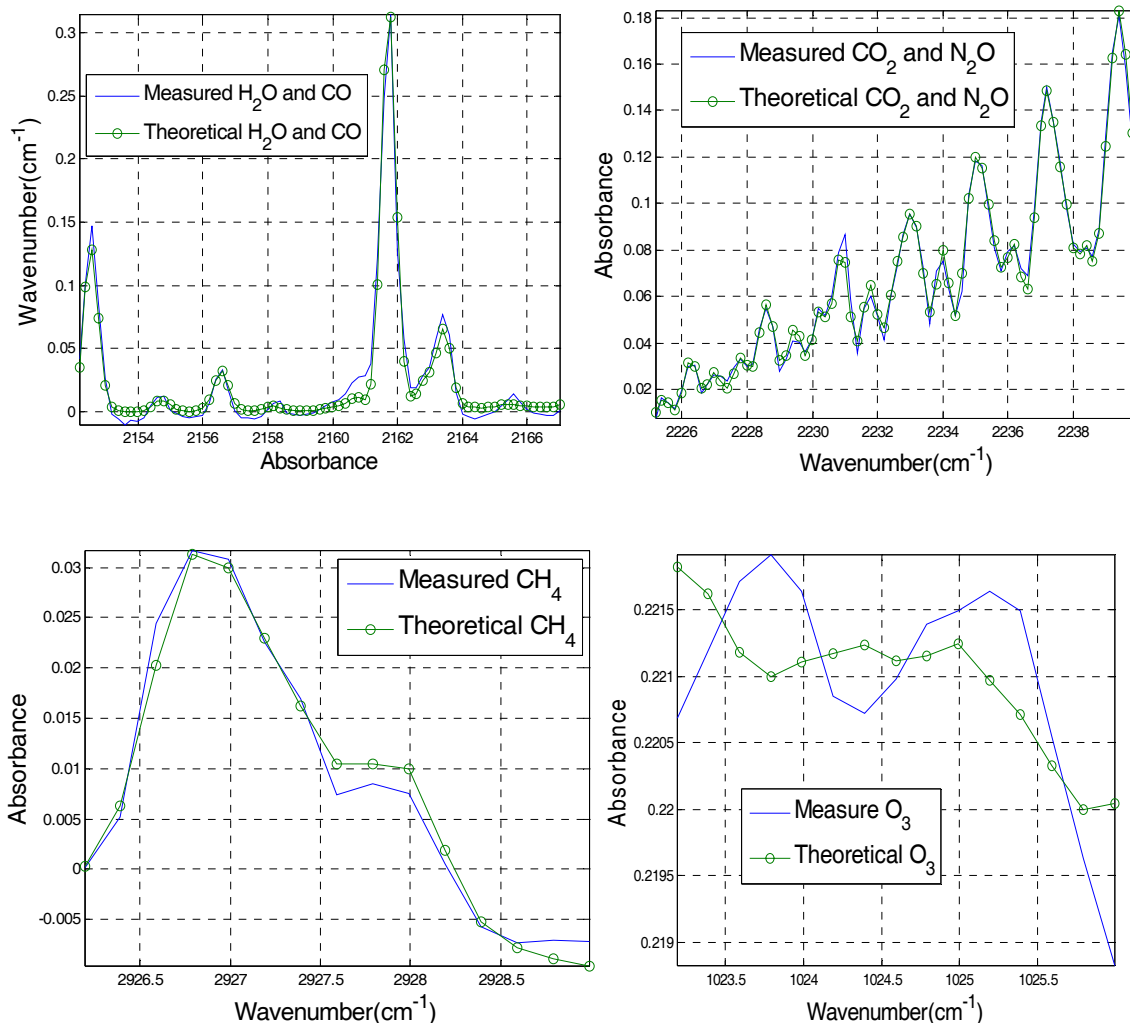


Figure 5.23 Match-ups based on least square fitting (LSQ) of theoretical spectra and experimental spectra for 4 different micro-windows at Princeton University on October 5<sup>th</sup>, 2007

The results of the least squares analysis over the 4 different micro-windows considered in figure 5.21 and 5.23 are presented in table 5.2

Table 5.2 Retrieved atmospheric gases concentrations

Species	Assumed Concentration (ppm)	Retrieved Concentration (ppm) April 22 <sup>nd</sup> , 2003 CCNY	Retrieved Concentration(ppm) October 5 <sup>th</sup> , 2007 Princeton University	Worst Error
H <sub>2</sub> O	10000	3567	17445	±50
CO <sub>2</sub>	370	357	399	±18
O <sub>3</sub>	0.024	0.06	0.12	±0.04
N <sub>2</sub> O	0.3	0.26	0.31	±0.03
CO	1.5	0.33	0.04	±0.02
CH <sub>4</sub>	1.8	1.85	1.83	±0.01

In column 2, we state the conditions in which the theoretical lineshapes were constructed. Clearly, these should be reasonably chosen to correspond to likely outputs although no noticeable difference was detected when the lines were calculated at slightly different concentrations except for the water vapor (~.2%). As discussed before, the ozone results have significant error even when the concentration of ozone is high.

#### 4. Conclusions and References

Conventional FTIR Spectroscopy in the midinfrared is suitable for several abundant ambient trace gases CH<sub>4</sub>, CO<sub>2</sub>, CO and H<sub>2</sub>O can be retrieved with uncertainties < 3% N<sub>2</sub>O can be retrieved within 10% and non-episodic ozone within 30%. We find the accuracy of the ozone should be sufficient when using as baseline for comparison to quantum cascade lasers (QCL)-based differential absorption spectroscopy (DOAS) measurements. However, the difficulty in retrieving ozone with sufficient accuracy is a major incentive in the development of such DOAS instruments.

Further comparisons of water vapor to ground humidity measurements should be performed and simultaneous measurements of CO<sub>2</sub> with the FTIR system and the Eddy Covariance station located at Princeton University should be performed for validations of

the retrievals. Also a subtraction of trace gas absorbance is suggested in an attempt to retrieve aerosol extinction. Present applications of the FTIR systems include measurements in the vertical pointing mode for temperature and water vapor profiles that could therefore inter-compared with Raman Lidar profiles.

### *References*

- [1] M. Diem, *Modern vibrational spectroscopy*, Wiley Interscience, USA, 1993
- [2] I.N. Levine, *Quantum Chemistry*, Prentice Hall, New Jersey, USA, 2000
- [3] G. L. Stephens, *Remote sensing of the lower atmosphere. An Introduction*, Oxford University Press, NY, USA 1994
- [4] J. Steinfeld, "*An introduction to Modern Molecular Spectroscopy*", MIT Press, Cambridge, Massachusetts, Second edition, 1993
- [5] B.E.A. Saleh, M. C. Teich, *Fundamentals of Photonics*, John Wiley & Sons, USA, 1991
- [6] A. Ghatak, *Optics*, 3<sup>rd</sup> edition, Tata McGraw-Hill, New Delhi, 2005
- [7] B. Gross et al., "*Assessment of a QCL Laser approach for the simultaneous measurement of ambient ammonia and ozone.*", Infrared, Mid-IR, and THz Technologies for Health and the Environment II, SPIE Optics East, Sept 2007
- [8] "*FTIR Spectrometer. Operator manual. M2000 Series*", Midac Corporation, April 1999
- [9] V. Vladutescu et al., "*DOAS Spectroscopy using a tunable MIR QCL for simultaneous Ozone and Ammonia detection*" Mirthe, Annual Midterm Review, Princeton, NJ, USA, 2006

## Chapter VI

### **High Spatial Spectral Resolution VIS-NIR Scanning Fabry Perot Imager for Geostationary spaceborne applications**

High spatial-spectral resolution space based observations in visible-near infrared VNIR portion of the spectrum are required for a variety of remote sensing applications including ocean color, land surface classification, and atmospheric monitoring. In conventional approaches, the spectral selectivity is accomplished by means of interferometry, a series of pass-band filters (channels), or grating based spectrometers selectively designed to cover the spectral domain of interest for a given application.

Unfortunately, these schemes are not able to modify the spectral channels for different applications as may be required for an all purpose imager. To accomplish tunability, we examine the feasibility of using Fabry Perot technology and show that by using a dual etalon system, we can achieve sufficient sensitivity and spectral filtration for ocean color observations which are the most difficult radiometrically. System specifications are outlined and signal to noise ratio (SNR) estimates are developed as a function of the pixel-pixel integration time. Finally, the effects of out of band signals are considered and it is shown that a signal inversion scheme can be used for accurate retrieval of signals.

## **I. Introduction**

### **1.1 Theoretical considerations of Fabry-Perot etalons**

In the previous chapter we have been discussing the Michelson Interferometer which is based on the interference between two beams derived from a single beam by division of the amplitude.

In this chapter, we show that a multiple Fabry-Perot etalon technique can be adapted to provide hyperspectral imaging capabilities for a Geostationary Satellite over the entire VNIR range from 400-800nm without the need for additional interference filters with the etalon lengths above 1.6 $\mu$ m. The use of Fabry Perot etalons for spectral discrimination is not new. For example, a multi-etalon planar Fabry-Perot (PFP) filter with an array imager has been developed for the Advanced Technology Solar Telescope (ATST). Unlike a single FP etalon, the free-spectra-range of the system can be made extremely large. This is accomplished by a careful selection of etalon optical pathlengths to allow constructive interference of the periodic pass bands of each etalon at a single resonance while destructively canceling other transmission resonances. This method effectively increases the free spectral range ( $f \sim 1000$ ) providing pico-meter resolution to probe over 25 molecular spectral lines in the VIS-NIR. Another instrument based on this concept which is being considered within the NASA Instrument Incubator Project (IIP) is the Tropospheric Trace Species Sensing Fabry- Perot Interferometer (TTSS-FPI) whose main goal is the detection of tropospheric ozone by picometer interrogation of a pressure broadened ozone line in the infrared (IR). However, the planar Fabry Perot(PFP) in these cases were designed to work within the passbands of additional filters which should be avoided for the broad band case.

Unlike conventional grating spectrometers and interferometers that need to process the entire spectrum, this instrument can be tasked to selected spectral features and for given resolving power is the most luminous instrument. Practical issues for the multi-etalon technique that will be considered include signal-to-noise ratio requirements, spatial and spectral resolution, image acquisition time and corrections for out of band signals. In section 2, the system components are described including the optical requirement needs, and the signal to noise ratio (SNR) estimates relevant. Single and multiple cavity designs are presented and the correct Fabry Perot Interferometer (FPI) system is obtained. In section 3, the signal processing is detailing characteristics of the temporal behavior of the system and error budget.

To understand the proposed system we first introduce the working principle of the Fabry Perot Interferometer.

#### *Fabry-Perot interferometer*

When a plane wave falls on a parallel glass plate, then the beam would undergo multiple reflections at the two surfaces and a large number of beams successively diminishing amplitude will emerge on both sides of the plate. These beams (on either side) interfere to produce an interference pattern at infinity. The so formed fringes are much sharper than those by two beam interference and, therefore, the interferometers involving multiple beam interference have a higher resolving power and hence find applications in high resolution spectroscopy. The Fabry-Perot interferometer is a system based on the principle of multiple beam interference.

The interferometer consists of two plane glass (or quartz) plates which are coated on one side with a partially reflecting mettalic film (of aluminum or silver or one suitable to the reflection of the wavelengths of interest) of about 80-90% reflectivity. This two plates are kept in such that they enclose a plane parallel slab of of air between their coated surfaces. If the reflecting glass plates are held paralle; to each other at a fixed separation, we have what is known as a Fabry-Perot etalon. If one of the mirrors is is kept fixed while the other is capable of moving to change separation between the two mirrors, the system is called a Fabry-Perot interferometer (FPI). As the etalon, the interferometer is characterized by its, reflectivity( $\mathfrak{R}$ ), transmission (T), coefficient of finesse(F) and the resolving power ( $\Delta\lambda$ ).

The reflectivity of a Fabry Perot etalon is derived from the reflectivity and transmissivitty at each interface, and phase diference (between two successive waves emanating from the plate) as is described below.

As a wave of complex amplitude  $E_{in}$  is incident on the FPI, it undergoes multiple reflections and transmissions at the two interfaces as shown in figure 6.1

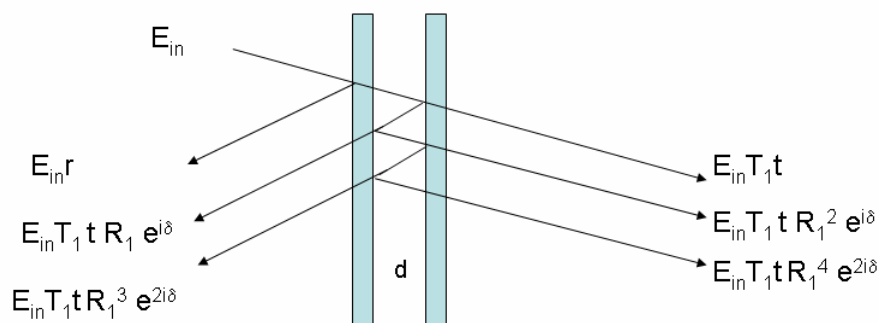


Figure 6.1 Reflection and transmission of a beam incident at an angle  $\theta_i$  on a FP etalon of with a distance between plates of d

The resultant complex transmitted and reflected amplitude will be

$$E_T = E_{in} T_1 t [1 + R_1^2 e^{i\delta} + R_1^4 e^{2i\delta} + \dots] \quad (1)$$

$$E_R = E_{in} \left[ r + T_1 t R_1 e^{i\delta} (1 + R_1^2 e^{i\delta} + R_1^4 e^{2i\delta} + \dots) \right] \quad (2)$$

where  $R_1$  and  $T_1$  are the reflection and transmission ( the transmission coefficient of the medium between the plates) coefficients inside the cavity,  $r$  and  $t$  are the reflection and transmission outside of the cavity plates and  $\delta$  is the phase difference between two successive waves emanating from the plates given by the following relation:

$$\delta = \frac{2\pi}{\lambda_0} \Delta = \frac{4\pi n_{cavity} d \cos \theta}{\lambda_0} \quad (3)$$

where  $n_{cavity}$  is the refractive index of the medium in the cavity [8].

If the reflectors are lossless, the reflectivity and the transmissivity at each interface are

$$\begin{aligned} R &= R_1^2 = r^2 \\ \tau &= T_1 t = 1 - R \end{aligned} \quad (4)$$

Thus the reflectivity of the Fabry-Perot etalon is given by

$$\begin{aligned} \mathfrak{R} &= \left| \frac{E_R}{E_{in}} \right|^2 = \left[ R_1 \left( 1 - \frac{(1-R)e^{i\delta}}{1 - R e^{i\delta}} \right) \right]^2 = R \left| \frac{1 - e^{i\delta}}{1 - R e^{i\delta}} \right|^2 = \\ &= R \frac{(1 - \cos \delta)^2 + \sin^2 \delta}{(1 - R \cos \delta)^2 + R^2 \sin^2 \delta} = \frac{4R \sin^2 \frac{\delta}{2}}{(1-R)^2 + 4R \sin^2 \frac{\delta}{2}} = \frac{F \sin^2 \frac{\delta}{2}}{1 + F \sin^2 \frac{\delta}{2}} \end{aligned} \quad (5)$$

where

$$F = \frac{4R}{(1-R)^2} \quad (6)$$

is called the coefficient of finesse.

One can see that when  $R \ll 1$ ,  $F$  is small and the reflectivity is proportional to  $\sin^2 \frac{\delta}{2}$

The transmissivity  $T$  is given by

$$T = \left| \frac{E_T}{E_{in}} \right|^2 = \frac{(1-R)^2}{(1-R \cos \delta)^2 + R^2 \sin^2 \delta} = \frac{1}{1 + F \sin^2 \frac{\delta}{2}} \quad (7)$$

It is immediately seen that the reflectivity and the transmittivity of the FP etalon add up to unity.

Further T=1 when

$$\delta = 2m\pi \quad \text{where } m=1,2,3,\dots \quad (8)$$

To get an estimate of the width of the transmission resources, more exactly  $\Delta\delta$  the full width at half maximum(FWHM), we let T=1/2 for  $\delta = 2m\pi \pm \frac{\Delta\delta}{2}$ .

$$\text{Thus } F \sin^2 \frac{\Delta\delta}{4} = 1.$$

In almost all cases  $\ll 1$  and therefore, to very good approximation it is given by

$$\Delta\delta \approx \frac{4}{\sqrt{F}} = \frac{2(1-R)}{\sqrt{R}} \quad (9)$$

Thus the transmission resources become sharper as F increases.

### *Cavity resonance*

For an incident beam of specific wavelength  $\lambda_0$ , to be totally transmitted (T=1), the angle of incidence is described in eq 8 and given below in eq(10)

$$\delta = \frac{4\pi}{\lambda_0} n_{cavity} d \cos \theta = 2m\pi \quad (10)$$

where  $\cos \theta = \frac{m\lambda_0}{2n_{cavity}d}$ , and  $\theta$  is the angle of incidence. For a given wavelength, at the

focal plane of the lens L, we will obtain a fringe pattern consisting of concentric rings, where each ring will correspond to a particular value of m. As mentioned above the sharpness of the bright rings will increase with the value of F. Also to have sharp fringes,

the coated surfaces should be flat within about  $\lambda/50$ . If there is a variation in the spacing between the plates, the fringes of different wavelengths will start overlap. [8]

For a normally incident polychromatic beam on a FP etalon with fixed distance and a refractive index between the plates of 1, the transmission resonance in terms of the wavelength or frequency occurs at

$$\lambda = 2md \quad \text{or} \quad \nu = \nu_m = m \frac{c}{2d} \quad (11)$$

where frequency spacing of two adjacent modes would be given by

$$\Delta\lambda = 2d \quad \text{or} \quad \Delta\nu = \frac{c}{2d} \quad (12)$$

### *Resolving power*

For two frequencies to be just resolved, assume that the half intensity point of  $\nu_1$  falls on the half intensity point of  $\nu_2 = \nu_1 + \Delta\nu_1$ . When this happens, the minimum of the resultant intensity distribution is about 74% of the corresponding maximum value [8]. The half intensity point occurs at

$$\delta = \delta_{1/2} = 2m\pi \pm \frac{\Delta\delta}{2} \quad (13)$$

Then  $\Delta\delta \approx \frac{4}{\sqrt{F}}$  (9). If intensity maximum of the beam of frequency  $\nu_1$  occurs at

$h=h_1$  then

$$\delta_1 = \frac{4\pi h_1 \nu_1}{c} = 2m\pi \quad (14)$$

The intensity maximum of the second beam of frequency  $\nu_1 + \Delta\nu_1$  occurs at  $h=h_2=h_1+\Delta h_1$ . Thus

$$\delta_2 = \frac{4\pi(h_1 + \Delta h_1)(\nu_1 + \Delta \nu_1)}{c} = 2m\pi \quad (15)$$

Using equations (14) and (15), we get  $h_1\Delta\nu_1 + \nu_1\Delta h_1$  or

$$\Delta h_1 = -\frac{h_1}{\nu_1} \Delta \nu_1 \quad (16)$$

Equation (16) implies that for  $\Delta h_1$  to be positive  $\Delta \nu_1$  should be negative.

If the half intensity point of  $\nu_1$  occurs at  $h = h_1 + \delta h_1$  (the corresponding value of  $\delta = 2m\pi + 1/2\Delta\delta_1$ ), thus using (14)

$$\frac{4\pi\nu_1\delta h_1}{c} = \frac{1}{2}\Delta\delta_1 \approx \frac{2}{\sqrt{F}} \quad \text{or} \quad \Delta h_1 \approx \frac{c}{2\pi\nu_1\sqrt{F}} \quad (17)$$

For the two frequencies to be just resolved

$$\Delta h_1 = 2 * \delta h_1 = \frac{c}{\pi\nu_1\sqrt{F}} \quad (18)$$

Using (16) we get the resolving power in terms of frequency and wavelength respectively.

$$\left| \frac{\nu_1}{\Delta \nu} \right| = \frac{h_1}{\Delta h} = \frac{\pi h_1 \nu_1 \sqrt{F}}{c} \rightarrow \left| \frac{\nu}{\Delta \nu} \right| = \frac{\pi h \nu \sqrt{F}}{c} ; \left| \frac{\lambda_0}{\Delta \lambda} \right| = \frac{\pi h \sqrt{F}}{\lambda_0} \quad (19)$$

## 2. System Components

The main components of the system are the Schmidt Cassegrain Telescope , a Fabry Perot Interferometer system and a 2048x2048 charged coupled (CCD) detector array with typical pixel dimensions  $\sim 13\mu\text{m} \times 13\mu\text{m}$  , the telescope system and the spectral filtration system designed to provide 2nm resolution in a scanning mode over the range from 400nm to 800nm. Unlike conventional filter designs or complex grating spectrometers,

we employ a cascade Fabry Perot system. This approach is chosen due to its capability to reconfigure the spectral range/number of channels used which is necessary for a Taskable (Special Event) that can process in either Multispectral or Hyperspectral Imager.

### 2.1. Optical design

For a given Schmidt Cassegrain telescope with an F#=10 and an object at a distance  $l=\infty$  (for a geostationary satellite at 32000km above ground) and a D=11” diameter (of the primary mirror) we can calculate the focal length using the relation

$F\# = \frac{\text{focal distance}}{\text{aperture diameter}} = 10$ . Therefore the effective focal distance is calculated to be

approximately 2800mm. Using the lens formula:

$$\frac{1}{l'} - \frac{1}{l} = \frac{1}{f} \quad (20)$$

where  $l'$  is the distance the distance between the lens and the image and  $l$  is the distance between the lens and the object, and  $f$  is the focal length we can get. Therefore the distance between the lens (our primary mirror) and image is  $l' = 2800 \text{ mm}$ .

The Schmidt Cassegrain telescope characteristics are obtained based on a set of formulas given below

$$f = \frac{f_1 \times f_2}{f_1 + f_2 - d} \quad (21)$$

$$f_2 = \frac{-(d+b)}{M-1}, M = \frac{f}{f_1} \quad (22)$$

$$bfl = d + b \quad (23)$$

$$D_2 = \frac{D_1 \cdot (d+b)}{f} + D_F \cdot \frac{d}{f} \quad (24)$$

where  $f$  is the effective focal length of the telescope of 2800mm,  $f_1$  is the focal length of the primary mirror,  $f_2$  is the focal length of the secondary mirror, bfl is the back focal distance,  $M$  is the magnification, DF is the field diameter at the focal plane,  $d$  is the distance between the primary and the secondary mirror and  $b$  is the distance between the back of the primary mirror and the focal plane,  $D_1$  and  $D_2$  are the diameters of the primary and respectively the secondary mirrors.

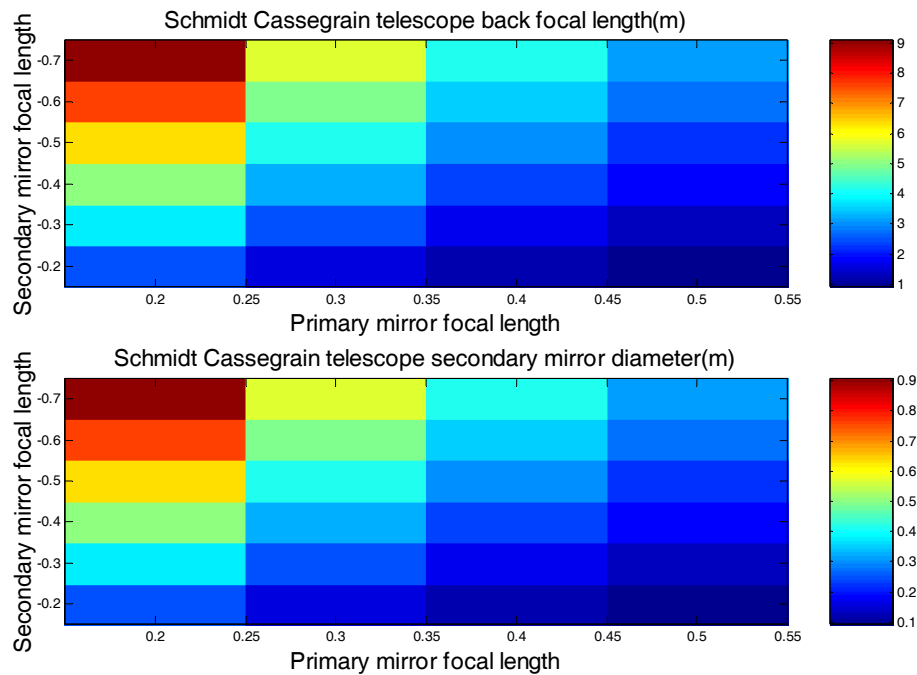


Figure 6.2 Schmidt Cassegrain telescope back focal length(bfl) and secondary mirror diameter for different focal lengths of primary and secondary mirrors.

As seen in figure above the minimum back focal length (b.f.l) and secondary mirror diameter could be achieved for primary mirror of focal length of 0.5m and for a secondary mirror of focal length -0.7. The resulting b.f.l. is therefore 0.92m with a distance between the mirrors of 0.33571m and a distance between the primary mirror and the focal plane of 0.58429m as seen in the figure below. The obtained secondary mirror

diameter is 0.0916m. An illustration of the Schmidt Cassegrain telescope is presented in figure 6.3

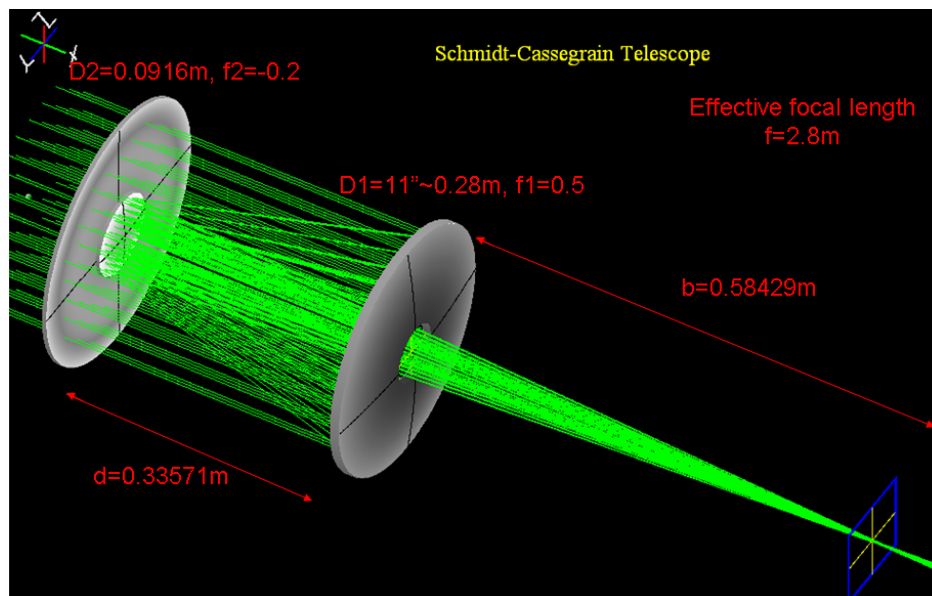


Figure 6.3 Schematic of the Schmidt Cassegrain Telescope design

For the wavelength of 400nm we get a theoretical resolution limit in the image space of  $4.89 \mu\text{m}$  and a resolution limit in the object space of 55.891m. These parameters were obtained using the formula for the resolving power of the telescope is given as

$$RL' = 1.22\lambda' / D \quad (25)$$

For the upper limit of the spectral region of interest (800nm) we just need to multiply the above obtained resolutions by a factor of 2 and we would obtain  $9.78 \mu\text{m}$  for the image resolution limit and and respectively 111.78m for the object resolution limit. As observed timage resolution limits are smaller than the selected  $13 \mu\text{m}$  CCD pixel size (see table 6.1), making the retrievals possible.

The image size is calculated using the relation

$$\frac{h'}{h} = \frac{l'}{l} \quad (26)$$

where  $h'$  is the height of the image (image of the object considered to be the cross track/2) and  $h$  is the cross track divided by two. For a half cross track of 100km, this calculation leads to  $h' = 8.75 \text{ mm}$ . The angle at the beam waist is found by taking the tangent of angle  $C$  in the  $ABC$  triangle shown

$$\text{above: } \tan \frac{\theta}{2} = \frac{AB}{BC} = \frac{130.95}{2800} = 0.04676 \Rightarrow \theta = 5.355^\circ$$

Using the angle and the image size we can obtain the distance between the image and the thin biconvex lens L1 for a spot size of 50mm at the lens. In the triangle  $AB'H'$  we have

$$\tan \beta = \frac{AB'}{B'H'} = \frac{148.5 \text{ mm}}{2800 \text{ mm}} = 0.053$$

All these specifications and the ones in the table below can be observed in the optical train taking into account realistic optical elements shown in figure 6.1.

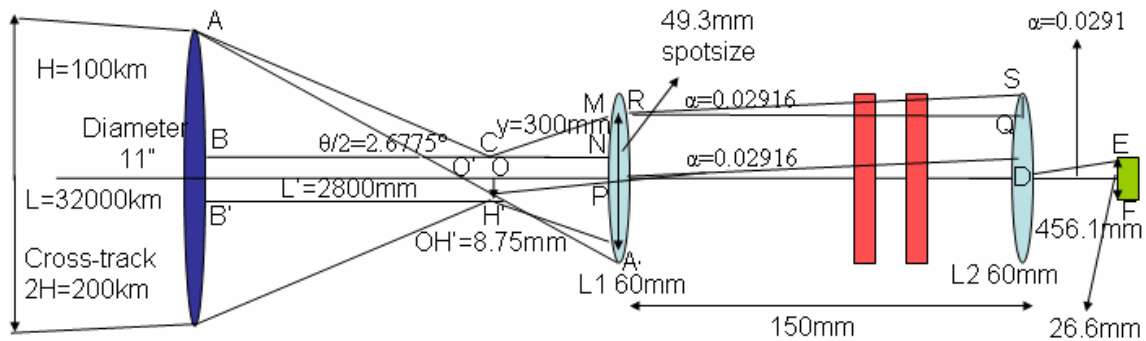


Figure 6.4 Optical set up of the Fabry Perot Interferometer

For an  $f\#$  at lens L1 of 5 we get a focal length of  $f=300\text{mm}$ (distance between L1 and image  $h'$ ). This would give us a spot size at the first lens of 49.3mm:  $Spotsize(L1) = (h' + f * \tan \beta) * 2 = 49.3 \text{ mm}$ .

For this distance between the image and the lens and the found height we obtain a divergence angle from the tangent in the triangle OH'P  $\Rightarrow \alpha = 1.67^\circ$ . This divergence would result in a final beam size of 58.05mm after it travels through the 3 FP cavities spread over a distance of 150mm. The calculation for the beam size at lens L2 is given by

$$\tan \alpha = \frac{SQ}{RQ} \Rightarrow SQ = 0.02916 * 150 \text{ mm} = 4.375 \text{ mm} .$$

The total beam size at lens two (L2) is  $2 * SQ + \text{spotsize}(L1) = 58.05\text{mm}$  For a beam size of 58.05mm and an image of no more than #pixels\*pixel size=2048\*13um=26.6mm In the DEF triangle at the lens L1 we observe angle D being equal to the divergence angle  $\alpha=0.02916\text{rad}$ . The  $\text{tg}\alpha=EF/DF$ , and therefore the  $DF=13.3\text{mm}/0.02916=456.1\text{mm}$ . From the lens formula we obtain a focal length for the second L1 of 220.7mm.

The field of view is calculated by dividing the detector size by the effective focal distance as follows  $\text{FOV}= 13\mu\text{m}/2800\text{mm}=4.64\mu\text{rad}$ . The footprint is calculated by multiplying the field of view (FOV) by the range

**Table 6.1. Preliminary Instrument/ System Specification**

Instrument Parameter	Size
Smidth Cassegrain Telescope Aperture	612.8cm <sup>2</sup> (d=11inches=28cm)
Lenses	60mm
Etalon diameter	60mm
CCD Pixel size	13umx 13um
Spectral Range	400-800nm
Platform Altitude	32000km
F/#	10
Effective focal distance	2800mm
Etalon scan range	1.6÷3.19um-cavity 1 1.8÷3.59um-cavity 2
Effective Spectral Resolution	2nm

Spatial resolution	98m x 98m
Footprint	200km x 200km
FOV	4.64μrad

### *Detector*

The detector used is a charged coupled device (CCD) with 2048x2048 pixels where each pixel has a 13umx13um size. The irradiance at the detector is related to the irradiance at the aperture by the following relation:

$$h_d = \frac{\tau h_a}{4F\#^2 + 1} \quad (27)$$

where  $h_a$  is the irradiance at the principal plane (aperture of the telescope) and  $\tau$  is the optical throughput (transmission through the lenses and other optical components in the optical train) and is usually around 0.7.

The ultimate determination of threshold operation is the S/N operation in the case of the most stringent operating conditions. Since we are on a Geostationary platform, we are to some degree able to control the ultimate S/N through control of the data acquisition time for the scan. The CCD total noise is given as  $N_T = \sqrt{N_R^2 + N_D^2 + N_S^2}$ , where  $N_T$  is the total CCD system noise,  $N_R$  is the read noise,  $N_D$  is the dark noise and  $N_S$  is the shot noise. The read out noise is due to the noise of the electronics (can not be removed completely) and it depends on the readout rate and as well as on temperature. It does not depend on exposure. In general the readout noise is only significant at signal levels  $< \sim 300$  electrons.

For a high speed CCD as the sampling frequency increases, the root mean square value of the read out noise increases (the sampling frequency corresponds to the rate at which each pixel is read). The variation in dark current with temperature for a CCD has an exponential behavior for which the number of  $e^-$ /pixel/sec decreases as the temperature decreases. For a fast application we referred to DALSA Camera with a frame rate of 60fps and data rate of 2x40 MHz with selection of one or two output taps. According to the manufacturer the dc offset (dark current) is 52DN on a 12 bit scale(data format) and the random noise (readout noise) is 1.75DN on the same scale at 495nm. To relationship between S/N, irradiance and exposure time can be found by including all the noise terms as defined below.

$$SNR = \frac{PQ_e t}{\sqrt{PQ_e t + Dt + N_R^2}} \quad (28)$$

where  $Q_e=50\%$  is the quantum efficiency of a CCD at 400nm, P is the flux incident on the CCD (photons/pixel/second), t is the integration time(seconds), D is the dark current ( $N_D$  is square root of Dt),  $N_R$  is the readout noise.

Converting from flux to irradiance using  $P = \left( \frac{I}{h\nu} \right) S$ , we have

$$SNR = \frac{\frac{I}{h\nu} * S * Q_e t}{\sqrt{\frac{I}{h\nu} * S * Q_e t + Dt + N_R^2}} \quad (29)$$

For a fixed SNR=100 and TOA sensor irradiance taken to be representative of an optically thin atmosphere over an ocean signal (see fig 6.22) we can plot in figure 6.5, the exposure time for different wavelengths. It is clear that a fixed integration time of less than 1 millisecond is sufficient to capture a signal with a signal to noise ratio of 100

which we will show to be sufficient for a dual-etalon cavity to resolve even weak ocean water leaving radiance signals.

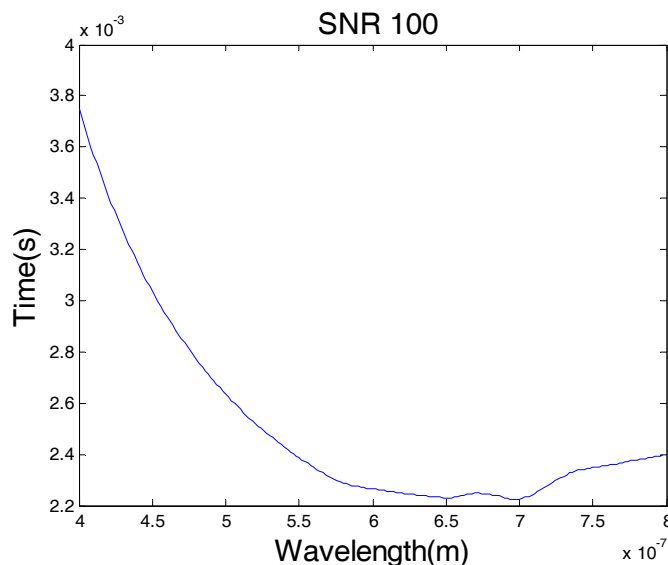


Figure 6.5 Required exposure time across the spectrum for an SNR=100

assuming an optically thick aerosol layer covering a typical deep ocean signal

### 3. Spatial-spectral response of Fabry Perot Etalons

The theory of the FPI system has been addressed in the first section of this chapter. The most relevant fact in our application is that in order to extend the Free – Spectral range in the VIS from 400-800 nm and use Fabry – Perot Etalons of reasonable length requires a large number of synchronized pass- bands to reject multiple resonance

To handle the case of multiple resonances, we purpose two possible systems. The first is based on the simple approach of designing a set of interference filters which will each pass only a single resonance order within the spectral region of interest. The specification of the interference filters in this case will depend on the specified minimum cavity length.

The use of multiple interference filters requires a rotating filter wheel that can place one filter at a time in the optical train, and adds complexity to the design.

In a second approach, similar to the method proposed in [10-11], a synchronized set of interferometers are employed whose optical path lengths are chosen to allow constructive interference of the periodic pass bands of each etalon at a single resonance while destructively canceling other transmission resonances. This method effectively increases the free spectral range of the multi-stage etalon system while allowing for high spectral resolution. Similar to the multiple interference filter design, a system can be designed in this way to operate over the entire VIS-NIR range from 400-800nm. The complexity in this case is to accommodate synchronized scanning while maintaining alignment of multiple etalon system.

The systems described in this paper are preliminary conceptual instrument designs that address the main issues needed for a flexible multi- or hyper-spectral sensor with high spatial resolution from a geostationary platform.

### *Imaging Considerations*

A Fabry Perot Filter allows a comb of frequencies to propagate separated by the free spectral range. In our application, we need the free spectral range to be sufficiently big so that the entire visible-NIR spectrum can fit within it thereby requiring very small separations. Scanning is accomplished by increasing  $L$  in a controlled way. As  $L$  increases, multiple resonances will occur which would make a spectral determination difficult. Therefore, we propose to store the spectral information obtained during the beginning of the scan to subtract out the contributions

One of the most important aspect to observe is that the rays going to different CCD pixels pass the Fabry Perot Filter at different angles and that different angles will affect the spectral response.

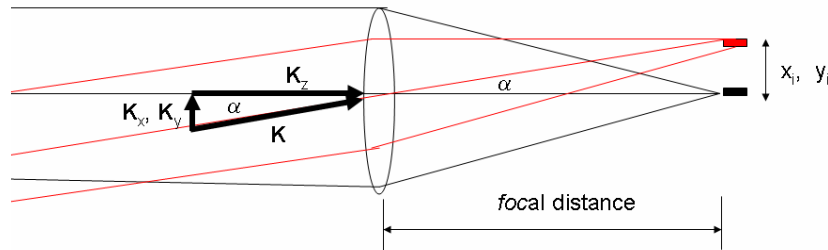


Figure 6.6 Imaging angles and light vectors

To understand how the resonances are affected by different angles, a theory of the spectral response due to off-axis rays needs to be given. From the multiple path interaction of the plane wave with the etalon, the  $m^{th}$  path accounts for  $m$  reflections, one transmission and the free-space diffraction operator applied to  $m$  path lengths [12]. Beams of “ $a$ ” diameter hitting the resonator get diffracted and then transmitted through the movable mirror (set at distance  $L+\Delta\xi$ ) and then detected at the CCD according to the following relations

$$\begin{aligned}
 E(x, z) &= \sum_{m=0}^{\infty} TR^m E_{diff}(x, z_m) \text{ or in fourier space} \\
 \hat{E}(k_x, z) &= \sum_{m=0}^{\infty} TR^m \hat{E}_{diff}(k_x; z_m) \text{ where} \\
 \hat{E}_{diff}(k_x; z_m) &= \exp(iz_m \sqrt{k^2 - k_x^2}) \hat{E}_{in}(k_x; 0) \quad z_m = m(2L) \\
 \hat{E}_{out}(k_x, z) &= T \left[ \frac{1}{1 - \text{Re} \exp(i2L \sqrt{k^2 - k_x^2})} \right] \hat{E}_{in}(k_x; 0)
 \end{aligned} \tag{30}$$

where

$$E_{out}(k_x, k) = H_{FP}(k_x, k) E_{in}(k_x, k) \tag{31}$$

$$\hat{E}_{in} = E_0 \exp\left(-\frac{k_x^2}{2(\Delta k_x)^2}\right) \quad (32)$$

In the above equations the off axis rays are denoted by  $k$  composed by the two components  $k_z$  and  $k_x$ (or  $k_y$ ) denoted by  $k_{\perp}$  for generalization.

$$\bar{k} = \bar{k}_{\perp} + \bar{k}_z \quad (33)$$

$$\bar{k}_{\perp} = \bar{k} \sin \alpha$$

$$x = f \tan \alpha = f \frac{\sin \alpha}{\cos \alpha} = \frac{\frac{\bar{k}_{\perp}}{\bar{k}}}{\sqrt{1 - \left(\frac{\bar{k}_{\perp}}{\bar{k}}\right)^2}} = f \frac{\bar{k}_{\perp}}{\sqrt{\bar{k} - \bar{k}_{\perp}^2}} \quad (34)$$

For a very small  $\alpha$  angle

$$\bar{k}_{\perp} = \bar{k} \alpha$$

$$x = f \alpha = f \frac{\bar{k}_{\perp}}{\bar{k}} \quad (35)$$

From the above expression, the term in the rectangular brackets can function as a spatial-spectral response function. If we re-write the transfer function in terms of spectroscopic variables such as the angle of the ray and the spectral detuning, we obtain the following representation.

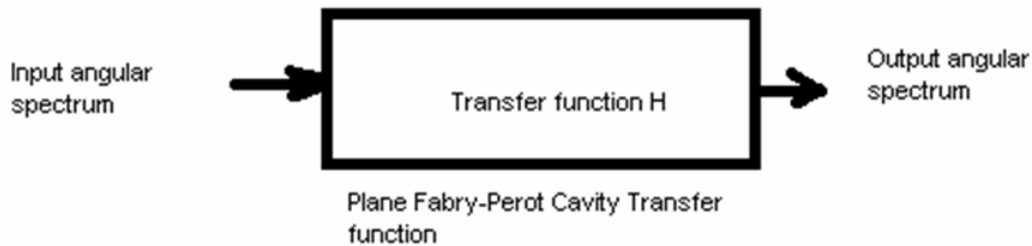


Figure 6.7 Plane FP cavity transfer function

In diagram 6.7 the transfer function is found as follows

$$H_{FP}(k_x, k_y, k, \theta) = \frac{T}{1 - R * \exp\left(iz_r(\theta)\sqrt{k^2 - k_x^2 - k_y^2} - k_x x_r(\theta)\right)} \quad (36)$$

$z_r(\theta) = 2L \cos(\theta)$   $x_r(\theta) = 2L \sin(\theta)$  can be written as

$$H_{FP}(k_x, k_y, k) = \frac{1 - R}{1 - R * \exp\left(i2kL\sqrt{1 - \left(\frac{k_x}{k}\right)^2 - \left(\frac{k_y}{k}\right)^2}\right)} \quad (37)$$

For  $k = \frac{2\pi}{\lambda_0} \Rightarrow kL = \frac{2\pi}{\lambda_0} * \frac{c}{c} * L = \frac{\pi f_0}{f_s}$  equation (37) can be written as

$$\begin{aligned} H_{FP}(k_x, k_y, k) &= \frac{1 - R}{1 - R * \exp\left(2\pi i \left[\frac{f}{f_s}\right] \sqrt{1 - \left(\frac{k_x}{k}\right)^2 - \left(\frac{k_y}{k}\right)^2}\right)} \\ &= \frac{T}{1 - R * \exp\left(2\pi i \left[\frac{f}{f_s}\right] \sqrt{1 - \left(\frac{x_i}{foc}\right)^2 - \left(\frac{y_i}{foc}\right)^2}\right)} \end{aligned} \quad (38)$$

where  $f_s = \frac{c}{2L}$  is the free spectral range and  $T \equiv \|H\|^2$  is the transmissivity and R is the

reflectivity;  $x_i, y_i$  ( $x_i = \frac{(i-1)x}{1024} \text{ cm}, y_i = \frac{(i-1)y}{1024} \text{ cm}$ ) are the CCD pixel locations and f is

the optical frequency.

$$\begin{pmatrix} x_i \\ y_i \end{pmatrix} = \begin{pmatrix} -f \\ H \end{pmatrix} \begin{pmatrix} x_o \\ y_o \end{pmatrix} \leftrightarrow \frac{\bar{k}_\perp}{|k|} \approx \frac{(k_x, k_y)}{|k|} \approx \frac{(x_i, y_i)}{foc} \quad (39)$$

To see the effect of the transverse wave number on the spectral response, we plot the transfer function contour lines in figure 6.8 below.

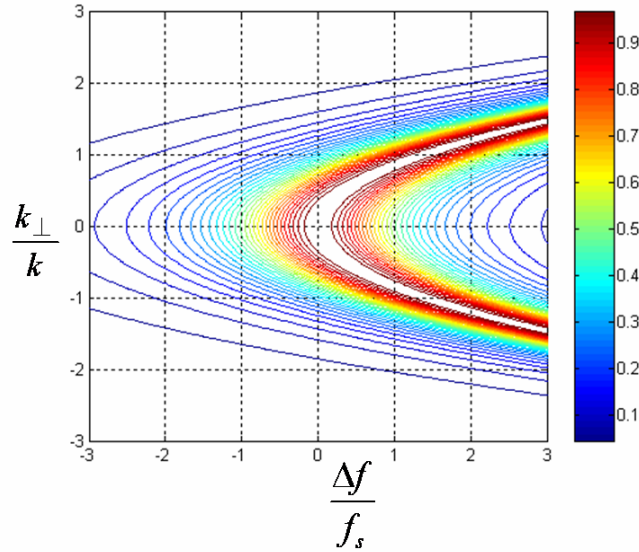


Figure 6.8 Fabry Perot Transfer Function contour representation

It is clear that the spectral response shifts in a symmetric way for different angles away from the plane incidence case. The signal detected at the pixel of coordinates  $(x_i, y_i)$  is given by equation

For *Transmission in center* ( $\theta=0$ )=*Transmission in center* ( $\theta=\theta_x$ ) we have

$$\frac{T}{1 - R^* \exp\left(2\pi i \left[\frac{f_0}{f_s}\right] \sqrt{1 - (0)^2}\right)} = \frac{T}{1 - R^* \exp\left(2\pi i \left[\frac{f_c}{f_s}\right] \sqrt{1 - \theta^2}\right)}$$

$$\frac{T}{1 - R^* \exp\left(2\pi i \left[\frac{f_0}{f_s}\right]\right)} = \frac{T}{1 - R^* \exp\left(2\pi i \left[\frac{f_c}{f_s}\right] \sqrt{1 - \theta^2}\right)}$$

which is true if the below condition is satisfied

$$\begin{aligned} \frac{f_0}{f_s} &= \frac{f_c}{f_s} \sqrt{1 - \theta^2} \Rightarrow \overline{f_0} = \overline{f_c} \sqrt{1 - \theta^2} \Rightarrow \overline{f_c} = \frac{\overline{f_0}}{\sqrt{1 - \theta^2}} \Rightarrow \overline{f_c} = \overline{f_0} \left(1 + \frac{1}{2} \theta^2\right) \Rightarrow \\ &\Rightarrow \overline{f_c} - \overline{f_0} = \overline{f_0} \frac{1}{2} \theta^2 \Rightarrow \Delta \overline{f_{shift}} = \overline{f_0} \frac{1}{2} \theta^2 \Rightarrow \frac{\Delta \overline{f_{shift}}}{\overline{f_0}} = \frac{\Delta \overline{\lambda_{shift}}}{\overline{\lambda_0}} = \frac{1}{2} \theta^2 \end{aligned} \quad (40)$$

The FOV specifications are critical since beam angular dispersion leads to spectral shifts which may be approximately calculated as  $\frac{\Delta\lambda}{\lambda} \approx \frac{1}{2} \alpha_{\max}^2$ . For the system in figure 6.4 the maximum angle of divergence is 0.02916 radians. Therefore the maximum wave number shifts are below 0.34 nm, an order of magnitude superior to current specifications for existing or planned instruments. Even then, such spectral shifts may be compensated by pre-calibration with a narrow laser source.

### *Reflectance*

The reflectance for a full width half maximum (FWHM) of  $\Delta\lambda=5\text{nm}$  can be calculated using the finesses formula given in equation (6). The FWHM in radians can be obtained using the relation below

$$\gamma = \frac{4}{\sqrt{F}} = \frac{4}{\sqrt{\frac{4R}{(1-R)^2}}} \Rightarrow R\gamma^2 = 4 - 8R + R^2 \quad (41)$$

which gives two solutions

$$R_{1,2} = \frac{8 + \gamma^2 \pm \sqrt{(8 + \gamma^2)^2 - 64}}{8} \quad (42)$$

Where

$$\gamma = 2\delta_{1/2} \text{ and } \delta = \frac{4\pi L}{\lambda_0} \Rightarrow \delta_{1/2} = \frac{4\pi L}{\lambda_0 + \frac{1}{2}\Delta\lambda} \quad (43)$$

This can be calculated in terms of the free spectral range as follows

$$\Delta\delta = -\frac{4\pi}{\lambda^2} L\Delta\lambda \Rightarrow \Delta\lambda = -\frac{\lambda^2}{4\pi} \Delta\delta \quad (44)$$

but is also known the frequency can be expressed as

$$f = \frac{c}{\lambda} \Rightarrow \Delta f = -\frac{c}{\lambda^2} \Delta \lambda \quad (45)$$

Plugging (45) in (44) we obtain

$$\Delta f = -\frac{c}{\lambda_0^2} \left( -\frac{\lambda_0^2}{4\pi L} \right) \Delta \delta = \frac{c}{4\pi L} \Delta \delta \quad (46)$$

Which can be written as

$$\delta_{1/2} = \frac{4\pi L}{c} f_{1/2} = \frac{2L}{c} 2\pi f_{1/2} = \frac{2\pi f_{1/2}}{f_s} \quad (47)$$

Replacing equation (47) in (43) and afterwards in (42) we obtain  $R=0.852$  for a FWHM of  $\Delta\lambda=5\text{nm}$ .

To get spatial response seen by a CCD pixel, the spatial frequency response must be inverse fourier transformed to the space domain. The processing steps are iterated below

$$\begin{aligned} E_{in}(x, y) &\xrightarrow{FFT} \hat{E}_{in}(k_x, k_y) \xrightarrow{H_{FP}(k_x, f)} \\ \hat{E}_{out}(k_x, k_y, f) &\xrightarrow{IFFT} \hat{E}_{out}(x, y, f) \xrightarrow{y=0(\text{symmetry})} \\ P_{out}(x, f) &\xrightarrow{\text{normalization}} \bar{P}_{out}(x, f) \end{aligned}$$

The spatial-spectral response can then be determined by looking at the 1% “leakage” contour to see the output spot at the CCD plane.

Before considering the case relevant to our imager, it is instructive to see the impact of these expressions on tightly focused beams to explore how the plane wave theory breaks down when illuminated by tightly focused beams. By the Fourier Transform theorem, images with high spatial resolution create fields with large transverse spatial wavenumber spectrum which can be mathematically equivalent to a tightly focused beam. Therefore, the traditional FP lorentzian spectral response is no longer valid since it is expected that the resonance condition for off-axis waves will be different. It is clear

that the condition for this to occur is that the spatial wave number divergence be sufficiently large so that  $\Delta k_T \approx \frac{2\pi\Delta f}{c}$  where  $\Delta f$  is the traditional plane wave spectral response. To see how the effect of increasing angular divergence changes the spectral and spatial characteristics, we plot the 99% power contours as a function of increasing angular divergence for a range of ratios  $L$ (distance between the etalon mirrors)/ $a$ (beam size) between  $\frac{1}{2}$  and  $\frac{1}{20}$ . On the inner contour where the input beam spot size is decreasing the diffraction effects go to zero

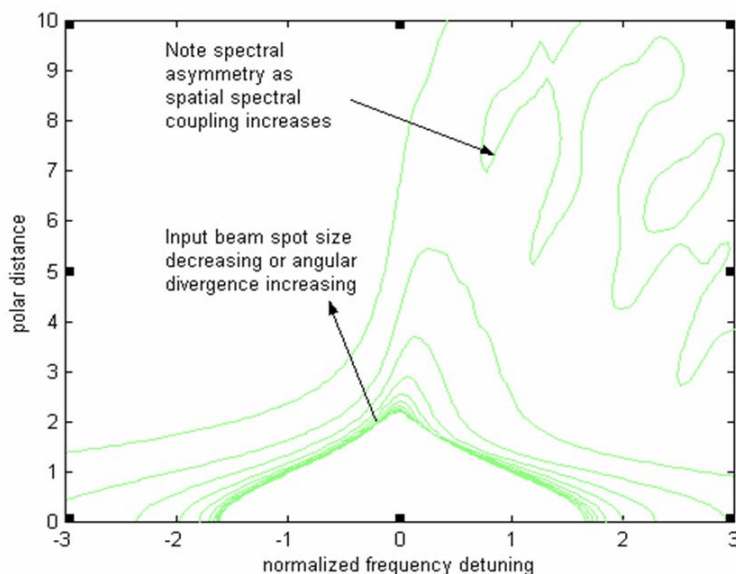


Figure 6.9 Spatial Spectral 99% power contours signifying response

of a FP filter for different plate separation to beam radii ratios  $\frac{1}{2} \geq L/a \geq \frac{1}{20}$

It is clear from this graph that coupling between the spatial and spectral components due to the frequency resonance selection of the filter result in a general broadening and of the spectral and spatial response. The effects of the spatial spectral coupling can be most clearly seen in the spectral broadening and asymmetry as the spatial beam size decreases

as seen in figure 6.9. Note also asymmetric shift of resonance with increased spatial harmonics.

Mirror jitter can cause angle discrepancies consider angle jitter in x-z plane (y-z plane is similar to the x-z ).Using equation (36) one can calculate the transfer function of the FPI system modified by the beam misalignment. An illustration of the frequency detuning with respect to the angular misalignment has been plotted in figure 6.10.

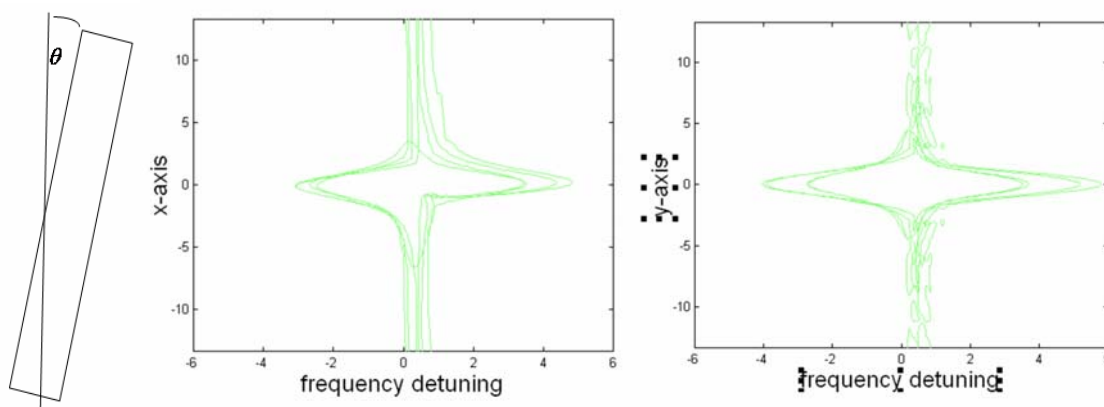


Figure 6.10 Beam misalignment

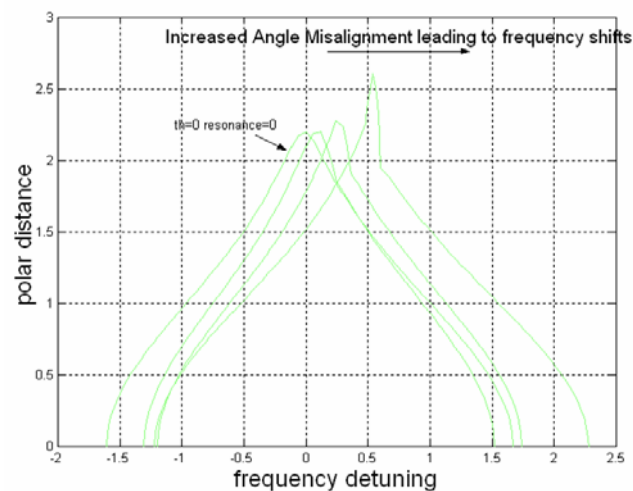


Figure 6.11 Frequency detuning versus x(or) y axis for angle misalignment varied from

$$0 \leq \theta \leq .1 \text{ for a ratio } L/a=1/20$$

The total field description is also necessary for cavity misalignment joined by mirror defects as shown in figure 6.12. Therefore the detected field at the CCD is calculated using equation (48)

$$\begin{aligned}
 E_{out}(x, z) &= \sum_{m=0}^{\infty} TR^m E_{m,diff}(x - x_m(L), z + z_m(L)) \\
 x_m(L) &\sim 2m^2 L \varepsilon \quad z_m(L) \sim 2mL \left( 1 + \frac{4m^2 \varepsilon^2}{3} \right) \\
 E_{m,diff}(x - x_m(L), z + z_m(L)) &= E_{diff}(x \cos(2m\varepsilon), z + x \sin(2m\varepsilon)) \sqrt{\cos(2m\varepsilon)}
 \end{aligned} \tag{48}$$

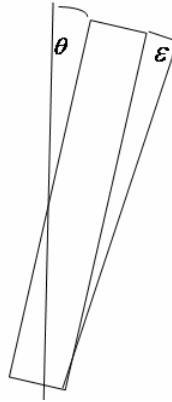


Figure 6.12 Imperfect cavity design

## 4. Fabry Perot System Configuration

### 4.1. Single cavity Fabry Perot Interferometer in series with a passband filter

In order to extend the free spectral range (FSR) from 400-800 nm using an etalon of reasonable length requires a large number of synchronized pass- bands to reject multiple resonance orders. An illustration of the single FP etalon is given in figure 6.13 a) To see the constraints on the pass band filters for maintain single resonance operation, we plot in figure 6.13b) , the boundaries of the different resonance orders for a given etalon.

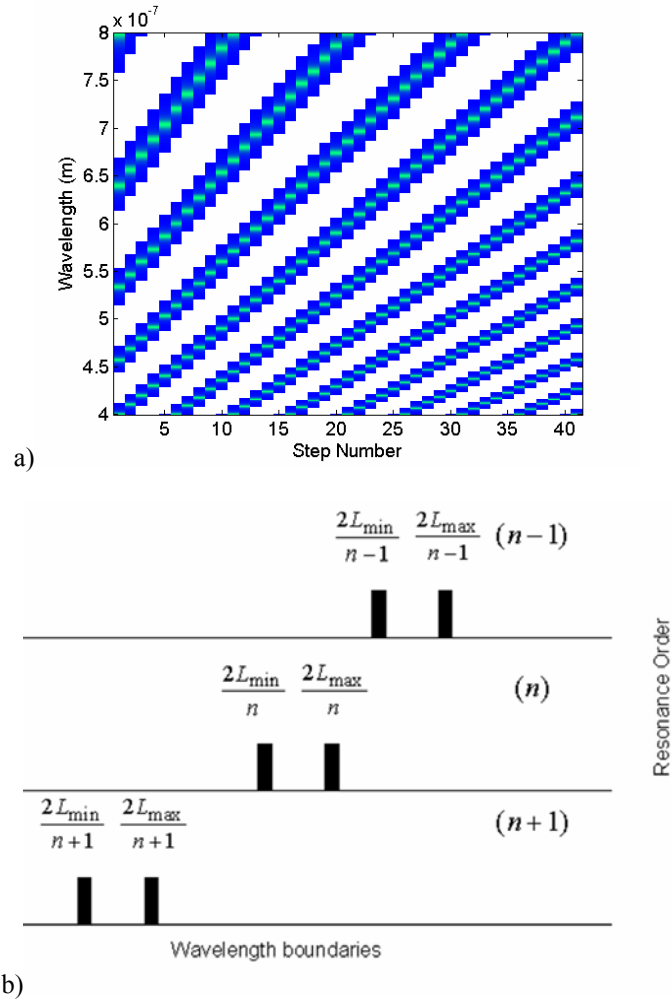


Figure 6.13 a)Spectral response of a single FP etalon. The diagonals represent multiple resonances occurring with the same intensity b)Resonance Boundaries of FP

Simple algebra shows that the single resonance conditions:

$$\frac{2L_{\min}}{n-1} > \frac{2L_{\max}}{n} \quad \text{and} \quad \frac{2L_{\min}}{n} > \frac{2L_{\max}}{n+1} \quad (49)$$

Lead to

$$\lambda_{\max} \leq \frac{n+1}{n} \lambda_{\min} \leq \frac{n}{n-1} \lambda_{\min}$$

$$\text{where } \lambda_{\min} = \frac{2L_{\max}}{n} \quad \lambda_{\max} = \frac{2L_{\max}}{n} \quad (50)$$

This observation allows us to define a simple algorithm to determine the passbands for each order that will allow continuous single resonance operation over the range of interest. The main point of this algorithm is that the minimum wavelength of a resonance order  $n$  must be larger than the maximum wavelength of the next resonance order  $(n+1)$ . The procedure is as follows:

1. Input as a limiting value, the minimum FP cavity length  $L_{cav}^{\min}$

Starting at the minimum wavelength of the passband required, determine the minimum resonance number needed for the first filter stage for the desired cavity length

$$n_1 = \left\lceil 2L_{cav}^{\min} / \lambda_{\min}^1 \right\rceil$$

2. Determine the maximum wavelength for the first stage as  $\lambda_{\max}^1 = \left\lceil [n_1 + 1] / n_1 \right\rceil - \Delta\lambda_{bound}$  where a buffer of bandwidth  $\Delta\lambda_{bound} \approx \Delta\lambda_{FP}$  is added to account for the finite bandwidth of the FP etalon.

3. Once the maximum wavelength of the first section is determined, the next section is considered where the minimum wavelength of this stage is given as

$$\lambda_2^{\min} = \lambda_1^{\max} + \Delta\lambda_{bound}$$

This algorithm is then iterated over the stages until we fill the entire passband. Each filter stage ( $k$ ) calculated above, would then require an interference filter covering the stage bandwidth. By rotating over all interference filters, complete single resonance coverage is obtained.

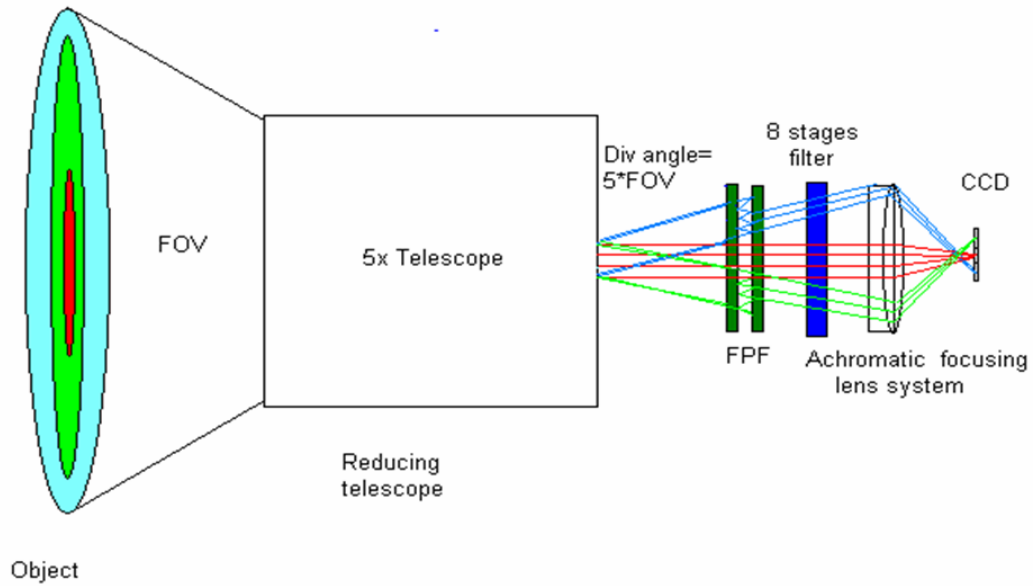


Figure 6.14 Schematic of the optical train containing single Fabry Perot Interferometer

In figure 6.15, we plot both the order of each Fabry Perot stage and the cavity length needed to cover each stage's passband assuming that the minimum cavity length is limited to  $L_{cav}^{Limit} = 2500nm$ . It can be seen that a minimum of 8 stages are needed to cover the range from 400nm to 800 nm where each stage covers a subsequently larger spectral band.

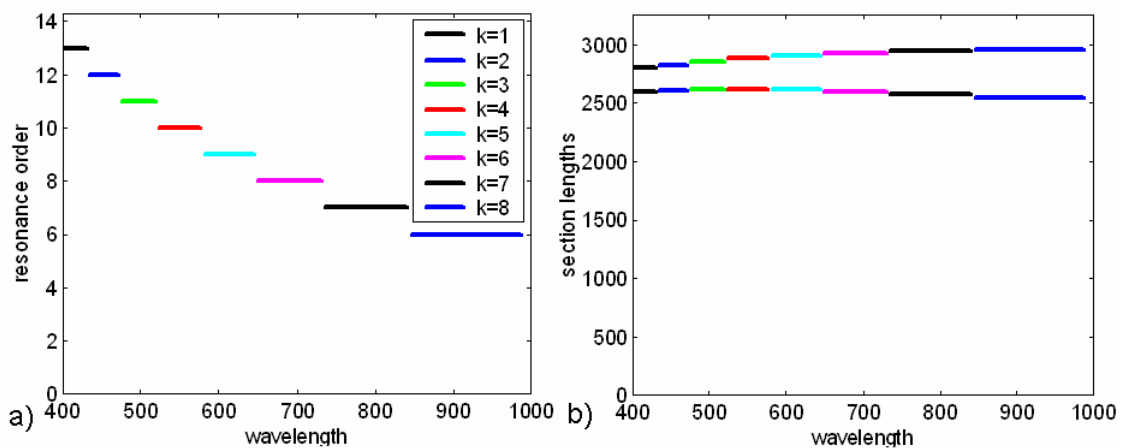


Figure 6.15 a) Filter stage resonance order for each passband and

b) Filter stage length range for each passband

In this configuration, it is clear that no changes have to be made to the cavity length sweep. Therefore, all that is required is a filter wheel mechanism to select each relevant passband over the same operational scan.

#### 4.2 Multicavity Fabry Perot Interferometer Design

A high resolution single wavelength Fabry Perot Interferometer with no interference filters will result in multiple resonance orders. However, it has been shown that multiple cascade etalons can increase the free-spectral range [15-17]. In our scheme, the wide tunability and the need for side band leads us to consider multiple etalon cavities. Reduction of the coupling due to multiple interference is obtained by suitable placement of a neutral density filter as illustrated in figure 6.16, The three etalons are positioned in series with the isolating medium attenuating the possible reflections between cavities.

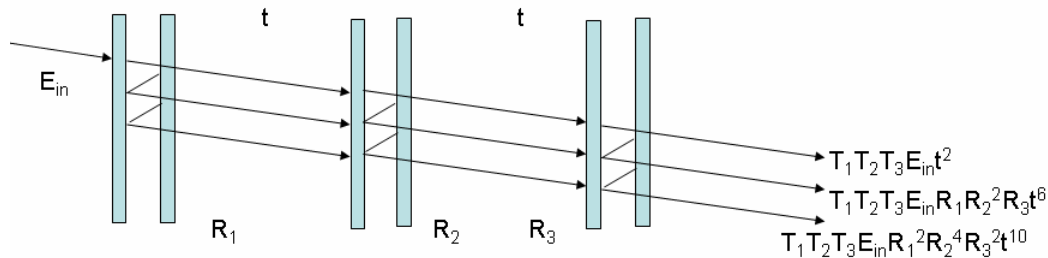


Fig 6.16. Three-etalon series configuration. The transmission between consecutive cavities is denoted by  $t$ , the etalons reflectivities are denoted by  $R_j$  and the input spectrum by  $E_{in}$ . The transmission of each cavity is represented by  $T_j$

The transmission of the attenuating medium between consecutive cavities is denoted as  $t$ , the etalons reflectivities are denoted by  $R_j$  and the input spectrum by  $E_{in}$ . The transmissions of each cavity are represented by  $T_{j.(j=1,2,3)}$

The derived transmission function for a triple etalon system taking in consideration all multiple reflections  $R_1, R_2, R_3$  between parallel cavities used at normal incidence is given as

$$T = \frac{T_1 T_2 T_3 t^2}{(1 - R_1 R_2 t^2)(1 - R_2 R_3 t^2) - R_1 R_3 T_2^2 t^4} \quad (51)$$

where  $t$  is the attenuation of the isolating medium and  $R_j = (1 - T_j)$  the reflectivity of cavity  $j$ [4]. The transmission of the attenuating medium between consecutive cavities is denoted as  $t$ , the etalons reflectivities are denoted by  $R_j$  and the input spectrum by  $E_{in}$ . The transmissions of each cavity are represented by  $T_j$ . For double cavity the above equation is changed by making  $T_3 = 1$  and  $R_3 = 0$ .

To examine the limits of single mode operation for a multiple etalon system, we note that at a particular wavelength (in our case 600nm) a ( $p$ ) order resonance of one cavity will constructively interfere with the ( $q$ ) resonance of a second cavity when the following relationship holds:

$$\lambda_{res} = \frac{2L_p}{p} = \frac{2L_q}{q} \rightarrow \frac{L_p}{L_q} = \frac{p}{q} \quad (52)$$

Therefore, we see that a transmission resonance of the coupled system requires that the cavity lengths are chosen correctly. The lengths are connected by the so called “vernier” ratio whose value is near unity for sufficiently high resonance orders (which is the case for the cavity lengths considered)[14]. Therefore if  $p = n$  and  $q = n + 1$ , it is easy to prove that all neighboring resonances are eliminated until

$$\frac{2L_p}{p \pm 1} \neq \frac{2L_q}{q \pm 1} \rightarrow \frac{2L_{2p}}{2p} = \frac{2L_{2q}}{2q} = \frac{\lambda_{res}}{2} \quad (53)$$

It also follows that the maximum tuning range is limited so that  $\lambda_{\max} < 2\lambda_{\min}$  and only the region between 400 and 800nm can operate in a single resonance mode. Operation in this mode requires only a single fixed filter covering the entire passband. The resulting transmission of both a double and triple etalon system are represented in figure 6.17 where  $t=.8$  between the elements. It is clear that the sidelobe suppression increases for three etalons by an order of magnitude. The above results may be graphically for three coupled cavities as seen in figure 6.17a). It is clear that by matching the cavity lengths appropriately, only the desired spectral window transmissions are in phase and all other spectral channels have a significantly smaller throughput. It is evident that we may tune the cavities so that a particular set of resonances overlap. The three etalons agree on the central resonance tuned to 600nm. However, all neighboring resonances will no longer overlap, resulting in a large suppression of the sidelobes which depends on the resonance linewidth as seen in figure 6.17b). Note in particular that there is a significant suppression in the side bands when more etalons are used.

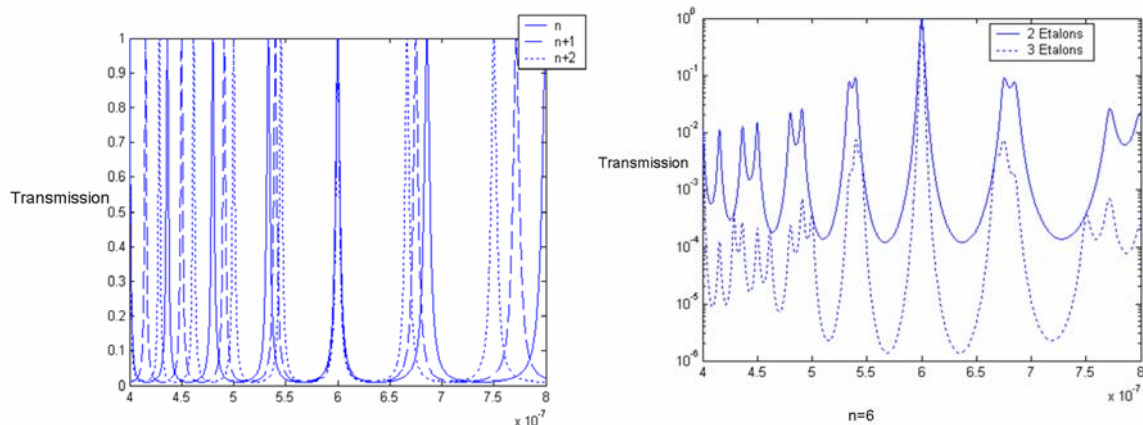


Figure 6.17 Single cavity etalon transmissions for three different spacings (uncoupled cavities)

b) Transmissions of 2 respectively 3 cavities etalons.

To function as a spectrometer, the vernier ratios must be maintained as the etalon cavity lengths (or phases) are swept. If this condition is met, the resultant transmission (i.e. transfer function) will have a main diagonal peak defining the resonant channel as well as a sequence of quasi-periodic side bands as seen in figure 6.20 a) for a double etalon system. It is clear that the sidelobe suppression occurs but that the out of band signal can still be quite significant.[10],[11] However, we will show in the next section that the out of band signal can be eliminated using suitable signal processing

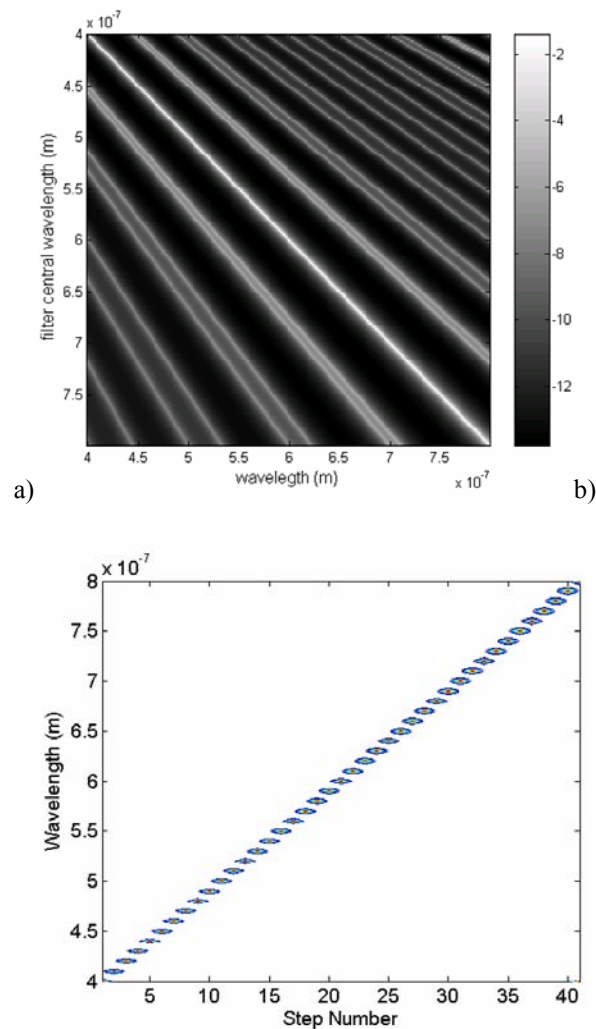


Figure 6.20 a) Spectral response of a dual etalon system and b) Triple etalon system

The diagonals represent multiple resonances occurring with same intensity. All multiple resonances eliminated and single wavelength is almost achieved. It is clear that for any scan position, multiple resonances will occur. In contrast, in figure 6.20 b), implementation of the three etalon configuration completely eliminates and multiple resonances. Therefore, we achieve single wavelength operation over the full bandwidth of interest and only one fixed broadband filter is needed. However, as we mentioned before the out of band signal of the dual system can be eliminated using suitable signal processing.

## 5. Signal Processing

### 5.1 Signal Processing

The total intensity after the Fabry Perot etalon can be mathematically represented as  $\bar{I}_j = \bar{T}_{j,k} \bar{I}_k$  where T represents the discretized transfer function. The solution to the retrieval of the true signal from the spectrometer output signal clearly has the form  $P_{in} = (T)^{-1} P_{out} = (I + \delta)^{-1} P_{out} = IP_{out} - \delta P_{out} + \Lambda$  and that the solution to this band matrix inversion may be obtained either through a direct inversion process or through an iterative scheme where as a first approximation, out of band signals are ignored and the TOA reflectance spectrum is used to estimate the first order correction to the signal.. If the retrieved signal is noiseless, it is clear that that there is no reason to process out the out of band signal but it is not immediately obvious how random noise is affected by the signal inversion. In section 2, we only considered the electronic random noise in the error budget but it is clear that out of band signals can have a major effect resulting in a significant overestimate of the reflected power. In figure 6.22, we plot a representative

deep ocean water leaving reflectance contaminated by a Rayleigh atmosphere. The lower trace is the correct in band signal while out of band contamination results in the upper trace. The curves include a 1% SNR component embedded onto the total TOA signal. Even if atmospheric contribution is accurately estimated, the out of band signals will result in a significantly overestimated water leaving reflectance. The lower trace is the result of accounting for the out of band signal directly by performing a signal inversion.

Simulated water and TOA reflectance: actual and measured with a double FPI

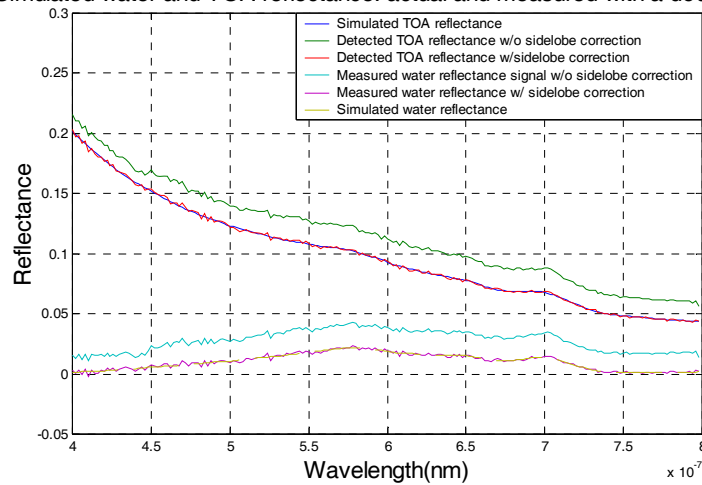


Figure 6.22 Detected and retrieved water leaving radiance

This analysis indicates that even significant out of band signal can be tolerated and processed without a significant increase in the processing noise. It may therefore be tempting to process the signal from a single etalon. Unfortunately, this is not realistic since the noise magnification is  $10^3$  which results in a  $10^6$  increase in the integration time which is obviously useless in any practical system.

## 5.2 Temporal behavior of the system

The overall response time for the image is governed by several factors. These include the integration  $t_{FPI}$  or stare time already estimated in section 2, the electronic response or dump time  $t_{CCD}$ , the scanning time for the piezoelectric motor stage  $t_{PZT}$  and the optical construction time needed to obtain the full spectral filter response function. The optical reconstruction time depends on the number of multiple internal reflections (beam orders) requires to construct the full spectral response and is obviously related to the finesse [15]. However, these multiple transit times over the small cavity length are on the order of picoseconds and therefore can be ignored. Therefore, the characteristic time of the system per image is  $T = t_{CCD} + t_{FPI} + t_{PZT}$ . Using  $t_{PZT} = 30ms$ ,  $t_{FPI} = 4ms$  and  $t_{CCD} = 16ms$  [20],[13], we can scan over the entire hyperspectral range from 400nm to 800nm in 2nm steps (200 channels) in approximately 10s.

## 5.3 Spectral Response Budget

The total effective finesse of the etalon configuration is defined by the following

relation:  $\frac{1}{F_e} = \sqrt{\frac{1}{F_r^2} + \frac{1}{F_d^2} + \frac{1}{F_{div}^2}}$ , where  $F_r$  is the reflective finesse

$F_r \approx \frac{\pi \sqrt{R}}{1 - R} = 37.5$ ,  $F_d$  is the overall defect finesse  $F_d = \lambda / \sqrt{4\delta_s^2 + 22\delta_{rms}^2 + 3\delta_p^2}$  and

$F_{div}$  the divergence finesse caused by the beam divergence. If the beam is sufficiently collimated, we can ignore the divergence effects and therefore the spectral line shapes will depend primarily on the cavity mirror characteristics (reflection and defects)[9],[13].

Current fabrication technology places limits on the defect finesse to about 50 across the

VIS-NIR range. Therefore, through simple algebra, an effective FWHM of 2nm may be obtained using mirror reflectivities on the order of 0.95.

## **6. Conclusions and References**

The system presented here describes the transmission of a dual cavity plane-mirror Fabry–Perot interferometer. We illustrate in principle the design for a VIS/NIR Fabry Perot Imaging Spectrometer and develop a procedure to calculate the characteristics of the needed components. We have also shown that if we use synchronously scanned multiple etalon cavities, we may significantly increase the FSR without decreasing the bandwidth of the resonance allowing single mode operation over the 400nm-800nm band with only a single fixed interference filter. The S/N between the main resonance and the sideband resonance is somewhat impacted by the multiple reflections of the cavities but we show that a moderate decoupling of the etalons is sufficient to reduce the sidebands. Furthermore, we have performed a SNR analysis and show that sufficient SNR may be achieved for limited integrations times on the order of 4 ms. With the inclusion of the scanning times and CCD dump times, an overall scan of 200 hyperspectral channels can be performed over 10 seconds. In addition, we show that the appearance of off resonant side bands in the spectrum need to be considered. If these bands are ignored, the overall water leaving radiance is extremely overestimated but by a suitable inversion taking into account the spectral details of the out of band signals, accurate water leaving radiances may be obtained even in the presence of noise.

## Acknowledgements

This work was in part supported under the NASA Center for Optical Sensing and Imaging (COSI) under grant number NCC-1-03009. We would also like to thank Raytheon and in particular Jeff Puschell for his assistance and support of this project.

## References

- [1] Larar A M., Hays P B., and Drayson S. R “*Global tropospheric and total ozone monitoring with a double-etalon Fabry–Perot interferometer.I. Instrument concept*”, [1998](#)
- [2] Larar A; and S. Drayson, “*Global tropospheric and total ozone monitoring with a double-etalon Fabry–Perot interferometer. II. Feasibility analysis*”, *Applied Optics*, Vol. 37, No. 21, 1998
- [3] Lee J.Y; and J. W. Hahn, H-W. Lee, “*Spatiospectral transmission of a plane mirror Fabry- Perot interferometer with nonuniform finite-size diffraction beam illumination*”, *J.Opt.Soc.Am.A* Vol. 19, No 5, 2002
- [4] Hecht E.; “*Optics*”, 3<sup>rd</sup> Ed. Addison Wesley, 1998
- [5] Mack J.E., McNutt D.P., Roesler F.L., and Chabbal R.,”*The PEPSIOS Purely Interferometric High-Resolution Scanning Spectrometer. I. The Pilot Model*”, 1963
- [6] Marinelli, W; C. Gittins, A. Gelb, and B. Green, “*A Tunable Fabry-Perot Etalon-Based Long-Wavelength Infrared Imaging spectroradiometer*” , *Applied Optics* Vol. 38, No. 16, pp. 2594-2604, 2000
- [7] Netterfield R. P., Freund C. H., Seckold J. A., and Walsh C. J., “*Design of a lithium niobate Fabry–Perot etalon-based spectrometer*”, 1997
- [8] A. Ghatak, *Optics*, 3<sup>rd</sup> edition, Tata McGraw-Hill, New Delhi, 2005

- [9] Gary G.A., Balasubramaniam K.S., and Sigwarth M., Science Group, “*Multiple Etalon Systems for the Advanced Technology Solar Telescope*”, Project Documentation, Technical Note #0005, <http://atst.nso.edu>, Tucson, AZ 85719, 2002
- [10] Larar A M., Hays P B., and Drayson S. R , “*Global tropospheric and total ozone monitoring with a double-etalon Fabry–Perot interferometer.I. Instrument concept*”, Applied Optics, Vol 37, No. 21, pp. 4721-4731, 1998
- [11] Larar A; and S. Drayson, “*Global tropospheric and total ozone monitoring with a double-etalon Fabry–Perot interferometer. II. Feasibility analysis*”, Applied Optics, Vol 37, No. 21, pp. 4732-4743 , 1998
- [12] Lee J.Y; and J. W. Hahn, H-W. Lee, “*Spatiospectral transmission of a plane mirror Fabry- Perot interferometer with nonuniform finite-size diffraction beam illumination*”, J. Opt. Soc. Am. A 19 #5, 973-984, 2002.
- [13] Hecht E.; *Optics*, 3rd Ed. Addison Wesley, 1998
- [14] Mack J.E., McNutt D.P., Roesler F.L., and Chabbal R., “*The PEPSIOS Purely Interferometric High-Resolution Scanning Spectrometer. I. The Pilot Mode*”l, Vol. 2, No. 9 , Applied Optics, pp.873-885,1963
- [15] Hernandez G., *Fabry-Perot Interferometers*, Cambridge University Press, 1986
- [16] Marinelli, W; C. Gittins, A. Gelb, and B. Green, “*A Tunable Fabry-Perot Etalon-Based Long-Wavelength Infrared Imaging spectroradiometer*” , Applied Optics Vol 38, No. 16, pp. 2594-2604, 2000
- [17] Netterfield R. P., Freund C. H., Seckold J. A., and Walsh C. J., ”*Design of a lithium niobate Fabry–Perot e´ talon-based spectrometer*”, Applied Optics, Vol. 36, No. 19, pp. 4556-4561,1997

- [18] Seelye Martin, *An introduction to ocean remote sensing*, Cambridge University Press, 2004
- [19] Curtis D. Mobley, *Light and Water. Radiative Transfer in Natural Waters*, Academic Press, 1994
- [20] T R Hicks, N K Reay and P D Atherton “The application of capacitance micrometry to the control of Fabry-Perot etalons”*J. Phys. E: Sci. Instrum.* 17 49-55, 1984
- [21] P.Falus, M.A. Borthwick, S.G.J. Mochrie,”Fast CCD camera for x-ray photon correlation spectroscopy and time- resolved x-ray scattering and imaging”, *Review to scientific instruments*, Vol.75, No.11, 4383-4400, 2004

## References by chapter

### *Chapter 1*

- [1] G. A. d'Almeida, P. Koepke, E.P. Shettle, *Atmospheric Aerosols. Global Climatology and Radiative Characteristics*, A. Deepak Publishing, Virginia, United States 1991
- [2] Robert J. Charlson, Francisco P. J. Valero, John H. Seinfeld, *In Search of Balance*, Science, Vol. 308. no. 5723, pp. 806 – 8076, 6 May 2005:
- [3] Charlson, R.J., S.E. Schwartz, J.M. Hales, R.D. Cess, J.A. Coakley, Jr., J.E. Hansen, and D.J. Hoffman, *Climate forcing by anthropogenic aerosols*,. Science, 255, 423-430, 1992.
- [4] S. E. Schwartz, *Uncertainty in Climate Change caused by Aerosols*, Science, Vol. 272, 24 May 1996
- [5] Yan Huang, *Assessments of the Direct and Indirect Effects of Anthropogenic Aerosols on Regional Precipitation over East Asia Using a Coupled Regional Climate-Chemistry-Aerosol Model*, Georgia Institute of Technology, 2005
- [6] Twomey S., *The influence of pollution on the shortwave albedo of clouds*, Journal of the Atmospheric Sciences, Vol 34. Issue 7, 1149–1152, July 1997
- [7] Albrecht B.A., *Aerosols, cloud microphysics and fractional cloudiness*, Science, 245, 1227-1230
- [8] S. E. Schwartz, Andreae M.O, *Uncertainty in Climate Change caused by Aerosols*, Science, Vol. 272, 24 May 1996
- [9] V. Ramanathan, P. J. Crutzen, J. T. Kiehl, D. Rosenfeld, *Aerosols, Climate, and the Hydrological Cycle*, Science, 294, 2119, 7 December 2001

- [10] Graf H.F., *The complex interaction of aerosols and clouds*, *Atm Science*, Vol 303, February 2004
- [11] Boucher et.al, Intercomparison of models representing direct shortwave radiative forcing by sulfate aerosols, *Journal of Geophysical Research*, 103, 16979-16998, July 1998
- [12] S. E. Schwartz, *Intercomparison of Radiation Transfer Models Representing Direct Shortwave Forcing by Sulfate Aerosols*, *Atmospheric Radiation Measurement*,
- [13] Beate G. Liepert,<sup>1</sup> Johann Feichter,<sup>2</sup> Ulrike Lohmann,<sup>3</sup> and Erich Roeckner, *Can aerosols spin down the water cycle in a warmer and moister world?*, *Geophysical Research Letters*, Vol. 31, L06207, ( 2004)
- [14] Dockery D. W., Pope III C. A. , *Acute respiratory effects of particulate air pollution*, *Annu. Rev. Public. Health.* , 15, 107-132, 1994
- [15] Ball R.J., Robinson G. D., *The origin of haze in the central United States and its effect on solar irradiation*, *American Meteorological Society* , 1982
- [16] Husar R.B., Husar J.D., Martin Laurent, Distribution of continental surface aerosol extinction based on visual range data, *Atmospheric Environment*, 34, 5067-5078, 2000
- [17] David G. Streets-Air quality during the 2008 Beijing Olympic Games
- [19] Mauzerall D.L., Wang X., *Protecting Agricultural Crops from the effects of tropospheric ozone exposure: Reconciling Science and Standard Setting in the United States, Europe and Asia*, *Annu. Rev. Energy. Environ.* 26, 237-268, 2001
- [18] NAPAP, National Acid Precipitation Assessment Program Report to Congress, An Integrated Assessment, 2005

*Chapter II*

- [1] Inventory of New York City Greenhouse Gas Emissions. New York City Office of Long-term Planning and Sustainability, April 2007.
- [2] <http://icerd.engr.ccnycunyc.edu/noaa/wc/index.html>
- [3] G.L. Stephens, *Remote Sensing of the Lower Atmosphere, An Introduction*, New York, Oxford University Press, 1994
- [4] R. Measures, *Laser Remote Sensing, Fundamentals and Applications*, Krieger Publishing Company; Reprint edition, 1992
- [5] B.A. Bodhaine et.al, “*On Rayleigh Optical Depth Calculations*”, *Journal of Atmospheric and Ocean Technologies*, Am. Meteo. Soc., Vol 16, p.1854-1861, 1999
- [6] H.C. van de Hulst, *Light Scattering by Small Particles*, Dover Publications, NY, 1981
- [7] I. Balin, “*Measurement and analysis of aerosols, cirrus contrails, water vapor and temperature in the upper troposphere with the Jungfraujoeh lidar system*”, École Polytechnique Federale de Lausanne, These No 2975, 2004
- [8] V. Kovalev et.al, *Elastic Lidar, Theory, practice, and analyses methods*, John Wiley and sons, New Jersey, USA 2004
- [9] G.A. d’Almeida et al, *Atmospheric aerosols, Global climatology and radiative characteristics*, A Deepak Publishing, Virginia USA, 1991
- [10] M. Diem, *Modern vibrational spectroscopy*, Wiley Interscience, USA, 1993
- [11] I.N. Levine, *Quantum Chemistry*, Prentice Hall, New Jersey, USA, 2000
- [12] D.W. Hahn, *Raman Scattering Theory*,

- <http://plaza.ufl.edu/dwhahn/Raman%20Scattering%20Theory.pdf>
- [13] C. Bockmann, “*Hybrid regularization method for the illposed inversion of multiwavelength lidar data in the retrieval of aerosol size distributions*”, Applied Optics, Vol.40, No.9, 2001
- [14] D. Muler et al, “*Comprehensive particle characterization from three wavelength Raman lidar observations: case study*”, Applied Optics, Vol 40, No 27, 2001
- [15] D.N. Whiteman, “*Examination of the traditional Raman lidar technique. I Evaluating the temperature-dependant lidar equations*”, Applied Optics Vol. 42, No. 15, 2003
- [16] F.G. Fernald, “*Analyses of atmospheric lidar observations: some comments*”, Applied Optics , Vol. 23, No. 5, 1984
- [17] R. Tardif, “*Boundary layer aerosol backscattering and its relationship to relative humidity from a combined Raman –Elastic backscatter lidar*”, [http://www.rap.ucar.edu/staff/tardif/CUprojects/ATOC5235/ATOC5235class\\_project.pdf](http://www.rap.ucar.edu/staff/tardif/CUprojects/ATOC5235/ATOC5235class_project.pdf)
- [18] H. Inaba et al., “*Laser –Raman Radar-Laser Raman scattering methods for remote detection and analysis of atmospheric pollution*”, Opto-Electronics, Vol 4, pp 101-123, 1972.

### Chapter III

- [1] P.S. Eagleson, “*The role of water in climate*” Proceedings of the American philosophical society, 2000.
- [2] D J Seidel, “*Water Vapor: Distribution and Trends*“, Encyclopedia of Global Environmental Change, John Wiley & Sons, 2002

- [3] I. Balin, *Measurement and analysis of aerosols, cirrus contrails, water vapor and temperature in the upper troposphere with the Jungfrauoch lidar system*, École Polytechnique Federale de Lausanne, These No 2975, 2004
- [4] C. Minghang et al., “*Assimilating TOVS Humidity into the GEOS-2 Data Assimilation System*”, Vol 12, pp. 2983–2995, 1999
- [5] J. T. Kiehl et al., *Earth’s Annual Global Mean Energy Budget*, American Meteorological Society, 1997
- [6] L. Bernstein et al, Intergovernmental Panel on Climate Change Fourth Assessment Report, Climate Change: 2007, <http://www.ipcc.ch/ipccreports/ar4-syr.htm>
- [7] J.M. Wallace, P.V. Hobbs, *Atmospheric Science An introductory survey*, Second edition, Academic Press Elsevier , 209-262, 2006
- [8] C S. Edwards et. al, “Development of an IR tunable diode laser absorption spectrometer for trace humidity measurements at atmospheric pressure”, *Applied Optics*, Vol 38, pp. 4699-4704, 1999
- [9] A. Giez et al, “Water Vapor Flux Measurements from Ground-Based Vertically Pointed Water Vapor Differential Absorption and Doppler Lidars”, *American Meteorological Society*, Vol 16, Issue 2, pp.237-250, 1999
- [10] J.R. Measures, *Laser Remote Sensing: Fundamentals and Applications*, Krieger Publishing Company, Reprint Edition , 1992
- [11] A. Ansmann et al, “*Independent measurement of extinction and backscatter profiles in cirrus clouds by using a combined Raman elastic-backscatter lidar*”, *Applied Optics*, Vol. 31, 1992

- [12] R. Measures, “Laser Remote Sensing: Fundamentals and Applications”, Krieger Publishing Company, 1992
- [13] L. Palchetti et al., “*Measurement of the water vapour vertical profile and of the Earth’s outgoing far infrared flux*”, Atmospheric Chem. And Phys. Discussions, 2007
- [14] A. Stenke et al., “*Impact of stratospheric water vapor trends on ozone chemistry*”, Atmos. Chem. Phys., Vol. 5, pp. 1257–1272, 2005
- [15] E.K. Schenider,” *Tropospheric Water Vapor and Climate Sensitivity*”, Am. Met Soc., Vol 56, pp1649-1658, 1998
- [16] Kovalev, Elastic Lidar,
- [17] M. Triola, Elementary Statistics, Pearson Custom Publication, MA, USA, 2006
- [18] J.A. Reagan, *Fellow, IEEE*, X. Wang, and M. T. Osborn, *Spaceborne Lidar Calibration From Cirrus and Molecular Backscatter Returns* IEEE Transactions on Geoscience and Remote sensing, vol. 40, No.10, October 2002
- [19] Z. Liu, M. McGill, Y. Hu, C. Hostetler, M. Vaughan, and D. Winker, *Validating Lidar Depolarization Calibration Using Solar Radiation Scattered by Ice Cloud*, IEEE, Geoscience and Remote sensing letters, vol.1, No.3 July 2004
- [20] D. N. Whiteman@ all, *Scanning Raman Lidar Error Characteristics and Calibration For IHOP*, NASA/HQ
- [21] D. D. Turner et al, “*Automated Retrievals of Water Vapor and Aerosol Profiles from an Operational Raman Lidar*”, Journal. of Atm. And Oc. Technology, Vol 19, pp.37-50, 2001

- [22] V. Wulfmeyer et al., “*Investigations of Humidity Skewness and Variance Profiles in the Convective Boundary Layer and Comparison of the Latter with Large Eddy Simulation Results*”, American Meteorology Society, Vol 56, pp 1077-1087, 1999
- [23] C.J. Grund et al., “*Feasibility of Tropospheric Water Vapor Profiling Using Infrared Heterodyne Differential Absorption Lidar*”, Proceedings of the Fifth Atmospheric Radiation Measurement (ARM) Science Team Meeting, San Diego California, 1995

#### *Chapter IV*

- [1] L.H Rhunke et al., *Hygroscopic aerosols*, A. Deepak Publishing, VI, USA, 1984
- [2] M.Phallow et al., “*Comparison between lidar and nephelometer measurements of aerosol hygroscopicity at the Southern Great Plains Atmospheric Radiation Measurement site*”, Journal of Geophysical Research, Vol 111, 2006
- [3] Yan Huang, “*Assessments of the Direct and Indirect Effects of Anthropogenic Aerosols on Regional Precipitation over East Asia Using a Coupled Regional Climate-Chemistry-Aerosol Model*”, Georgia Institute of Technology, 2005
- [4] Houghton, J. T. et al. eds, *Climate Change 2001: The Scientific Basis*(Houghton, J. T. et al. eds, Cambridge, U.K.: Cambridge University Press, 2001). Cambridge University Press, New York, United States (2001)
- [5] L. Bernstein et al, Intergovernmental Panel on Climate Change Fourth Assessment Report, Climate Change: 2007, <http://www.ipcc.ch/ipccreports/ar4-syr.htm>
- [6] R.J .Charlson et al., “*Climate forcing by anthropogenic aerosols*”,. Science, Vol. 255, pp. 423-430, 1992.

- [7] S. Twomey, " *The influence of pollution on the shortwave albedo of clouds*", Journal of the Atmospheric Sciences, Vol 34. Issue 7, pp. 1149–1152, 1997
- [8] S. E. Schwartz, *Cloud droplet nucleation and its connection to aerosol properties*, Proceedings of the 14<sup>th</sup> International Conference on Nucleation and Atmospheric Aerosols, 770-779, Elsevier Science Ltd., Oxford, UK, 1996.
- [9] V. Ramanathan et al. , *Aerosols, Climate, and the Hydrological Cycle*, Science, Vol. 294, 2119, 2001
- [10] B.J. Krueger et al, "*The transformation of solid atmospheric particles into liquid droplets through heterogeneous chemistry: Laboratory insights into the processing of calcium containing mineral dust aerosol in the troposphere*"; Geophys. Res. Lett., Vol. 30, No. 3, 2003
- [11] E. R. Gibson, "*Aerosol chemistry and climate: Laboratory studies of the carbonate component of mineral dust and its reaction products*", Geophysical Research Letters, Vol. 33, No. 13, L13811, 2006
- [12] S.H. Melfi et. al, "*Raman Lidar Measurements of Aerosol and Water Vapor, 2nd Symposium on Lidar Atmospheric Applications*", The 85<sup>th</sup> AMS Annual Meeting, San Diego, CA, Jan. 8-14, 2005
- [13] G. Hanel , "*The properties of Atmospheric aerosol particles as functions of the relative humidity at thermodynamic equilibrium with the surrounding moist air*", Adv. Geophy., Vol. 19, pp. 73-188 , 1976
- [14] K. Andre et al, "*Absorption of visible radiation by atmospheric aerosol particle, fog and cloud water residues*", American Meteorological Society, Vol. 38, pp141-155, 1981

- [15] D. V. Vladutescu et al, “*Analyses of Raman lidar calibration techniques based on water vapor mixing ratio measurements*”, WSEAS Trans. on Syst., vol. 2, issue 4, pp. 651–658, Apr. 2007
- [16] G. d’Almeida et al, *Atmospheric aerosols. Global climatology and radiative characteristics*, A Deepak Publishing, VI, USA ,1991
- [17] D.N. Whiteman et al, “ *Raman lidar system for the measurement of water vapor and aerosols in the Earth’s atmosphere*” Applied Optics, Vol. 31, No. 16, 1992
- [18] G. Feingold et al., “*Feasibility of Retrieving Cloud Condensation Nucleus Properties from Doppler Cloud Radar, Microwave Radiometer, Lidar*”, Journal of Atmospheric and Oceanic Technology, Vol.15, pp. 1188-1194, 1998
- [19] R. Measures, *Laser Remote Sensing: Fundamentals and Applications*, Krieger Publishing Company, Reprint Edition ,1992
- [20] A. Ansmann et al., “*Independent measurement of extinction and backscatter profiles in cirrus clouds by using a combined Raman elastic-backscatter lidar*”, Applied Optics, Vol. 31, No. 33, 1992
- [21] F. G. Fernald, ”Analyses of atmospheric lidar observations: some comments”, Applied Optics, vol. 23, no. 5 ,1984
- [22] C. Weitkamp, *LIDAR range-resolved optical remote sensing of the atmosphere* , Springer, pp.100-190, 2005

#### *Chapter V*

- [1] M. Diem, *Modern vibrational spectroscopy*, Wiley Interscience, USA, 1993
- [2] I.N. Levine, *Quantum Chemistry*, Prentice Hall, New Jersey, USA, 2000

- [3] G. L. Stephens, *Remote sensing of the lower atmosphere. An Introduction*, Oxford University Press, NY, USA 1994
- [4] J. Steinfeld, “*An introduction to Modern Molecular Spectroscopy*”, MIT Press, Cambridge, Massachusetts, Second edition, 1993
- [5] B.E.A. Saleh, M. C. Teich, *Fundamentals of Photonics*, John Wiley & Sons, USA, 1991
- [6] A. Ghatak, *Optics*, 3<sup>rd</sup> edition, Tata McGraw-Hill, New Delhi, 2005
- [7] B. Gross et al., “*Assessment of a QCL Laser approach for the simultaneous measurement of ambient ammonia and ozone.*”, Infrared, Mid-IR, and THz Technologies for Health and the Environment II, SPIE Optics East, Sept 2007
- [8] “*FTIR Spectrometer. Operator manual. M2000 Series*”, Midac Corporation, April 1999
- [9] V. Vladutescu et al., “*DOAS Spectroscopy using a tunable MIR QCL for simultaneous Ozone and Ammonia detection*” Mirthe, Annual Midterm Review, Princeton, NJ, USA, 2006

#### Chapter VI

- [1] Larar A M., Hays P B., and Drayson S. R “*Global tropospheric and total ozone monitoring with a double-etalon Fabry–Perot interferometer.I. Instrument concept*”, [1998](#)
- [2] Larar A; and S. Drayson, “*Global tropospheric and total ozone monitoring with a double-etalon Fabry–Perot interferometer. II. Feasibility analysis*”, Applied Optics, Vol. 37, No. 21, 1998

- [3] Lee J.Y; and J. W. Hahn, H-W. Lee, “*Spatiospectral transmission of a plane mirror Fabry- Perot interferometer with nonuniform finite-size diffraction beam illumination*”, J.Opt.Soc.Am.A Vol. 19, No 5, 2002
- [4] Hecht E.; “*Optics*”, 3<sup>rd</sup> Ed. Addison Wesley, 1998
- [5] Mack J.E., McNutt D.P., Roesler F.L., and Chabbal R.,”*The PEPSIOS Purely Interferometric High-Resolution Scanning Spectrometer. I. The Pilot Model*”, 1963
- [6] Marinelli, W; C. Gittins, A. Gelb, and B. Green, “*A Tunable Fabry-Perot Etalon-Based Long-Wavelength Infrared Imaging spectroradiometer*” , Applied Optics Vol. 38, No. 16, pp. 2594-2604, 2000
- [7] Netterfield R. P., Freund C. H., Seckold J. A., and Walsh C. J., “*Design of a lithium niobate Fabry–Perot etalon-based spectrometer*”, 1997
- [8] A. Ghatak, *Optics*, 3<sup>rd</sup> edition, Tata McGraw-Hill, New Delhi, 2005
- [9] Gary G.A., Balasubramaniam K.S., and Sigwarth M., Science Group, “*Multiple Etalon Systems for the Advanced Technology Solar Telescope*”, Project Documentation, Technical Note #0005, <http://atst.nso.edu>, Tucson, AZ 85719, 2002
- [10] Larar A M., Hays P B., and Drayson S. R , “*Global tropospheric and total ozone monitoring with a double-etalon Fabry–Perot interferometer.I. Instrument concept*”, Applied Optics, Vol 37, No. 21, pp. 4721-4731, 1998
- [11] Larar A; and S. Drayson, “*Global tropospheric and total ozone monitoring with a double-etalon Fabry–Perot interferometer. II. Feasibility analysis*”, Applied Optics, Vol 37, No. 21, pp. 4732-4743 , 1998
- [12] Lee J.Y; and J. W. Hahn, H-W. Lee, “*Spatiospectral transmission of a plane mirror Fabry- Perot interferometer with nonuniform finite-size diffraction beam illumination*”, J. Opt. Soc. Am. A 19 #5, 973-984, 2002.

- [13] Hecht E.; *Optics*, 3rd Ed. Addison Wesley, 1998
- [14] Mack J.E., McNutt D.P., Roesler F.L., and Chabbal R., “*The PEPSIOS Purely Interferometric High-Resolution Scanning Spectrometer. I. The Pilot Mode*”<sup>1</sup>, Vol. 2, No. 9 , Applied Optics, pp.873-885,1963
- [15] Hernandez G., *Fabry-Perot Interferometers*, Cambridge University Press, 1986
- [16] Marinelli, W; C. Gittins, A. Gelb, and B. Green, “*A Tunable Fabry-Perot Etalon-Based Long-Wavelength Infrared Imaging spectroradiometer*” , Applied Optics Vol 38, No. 16, pp. 2594-2604, 2000
- [17] Netterfield R. P., Freund C. H., Seckold J. A., and Walsh C. J., ”*Design of a lithium niobate Fabry-Perot e´ talon-based spectrometer*”, Applied Optics, Vol. 36, No. 19, pp. 4556-4561,1997
- [18] Seelye Martin, *An introduction to ocean remote sensing*, Cambridge University Press , 2004
- [19] Curtis D. Mobley, *Light and Water. Radiative Transfer in Natural Waters*, Academic Press, 1994
- [20] T R Hicks, N K Reay and P D Atherton “The application of capacitance micrometry to the control of Fabry-Perot etalons”*J. Phys. E: Sci. Instrum.* 17 49-55, 1984
- [21] P.Falus, M.A. Borthwick, S.G.J. Mochrie, ”Fast CCD camera for x-ray photon correlation spectroscopy and time- resolved x-ray scattering and imaging”, Review to scientific instruments, Vol.75, No.11, 4383-4400, 2004



are being explored. All the lidar data analyses were made using Matlab and data collection is done with Labview.

The research also involved operating various instruments for monitoring greenhouse gases present in the atmosphere using a Fourier Transform Interferometer with an AutoQuant Pro Interface. For instrument validation the data was analyzed and compared to eddy covariance station measurements collocated with the FTIR instrument at Princeton University. The work within the laboratory also included the development of different systems like an inexpensive, compact hyperspectral Planar Fabry Perot (PFP) land and ocean imager in conjunction with filters, conventional CCD detectors, and the system of lenses to accomplish spatial-spectral filtering over the visible /near infrared (VIS/NIR) band important for satellite imaging applications and outdoor measurements of the atmosphere. I have also conducted analyses of National Oceanographic and Atmospheric Administration (NOAA) satellite data to determine cloud heights, temperature using Matlab program and Linux platform of operation. Some of the instruments used in the research are:

- Mid-infrared MIDAC spectrometer (Fourier Transform Interferometer) to determine the concentration of different ambient greenhouse gases, temperature, water vapor retrieval using AutoQuant Pro, GRAMS AI, Matlab Fortran software(Genspec);
- LIDAR (Light Detection And Ranging ) system for measuring of the aerosol distribution using Mie and Raman channels(uses Matlab and Labview)
- mid-infrared Quantum Cascade Laser systems for analyses and simulations of simultaneous atmospheric ozone and ammonia measurements using DOAS (Differential optical absorption spectroscopy) spectroscopy
- Shadowband instrument to measure the solar radiation using Yesdas software.
- Cimel Sunphotometer CE318 (Matlab) for solar radiation measurements in different bands.

### **Electrical Engineer / Measurements Coordinator**

Testing Laboratory for Type and Reliability , MILTON IMPEX SRL, Bucharest,  
Romania; 1995-2001

Supervised the measuring and testing process,

- Issued certified bulletins on electro security standards for different devices and apparatus produced and imported in Romania by Kenwood, General Electrics, Panasonic and other Romanian and abroad manufacturers.

### **Laboratory research**

National Institute of Metrology, Continuous Measurement Systems

Laboratory, Bucharest, Romania

Summer 2000

- Conducted measurements and maintained measurement laboratory instruments like: ampermeters, voltmeter, frequency generators, multimeters, oscilloscopes etc

**TEACHING EXPERIENCE:****Adjunct Professor**

City College of The City University of New York, Electrical Engineering Department  
2002- Present

The teaching involves lecturing and preparing the material for

- **Electromagnetics I & II** class, guiding the students through the complex vectors, Maxwell's equations, boundary conditions, wave equation, uniform plane waves, polarization, propagation in lossless and lossy media, Poyting vector, reflection and transmission of waves at normal and oblique incidence, transmission lines (propagation, SmithChart, transients) and topics in waves, introduction to microwaves, fiber optics, waveguides and antennas for wired and wireless communication and power transfer.
- **Measurement Laboratory** involved the supervision of the measurements tests and measurement instruments, Virtual instruments and computer instrumentation, Electric and electronic circuits. The topics covered Transient and frequency response, Logic circuits, Discrete circuits, Operational amplifiers
- **Computer aided analyses tools for engineers** is intended to assist the students in solving engineering problems with computer programming language Matlab.
- **Teaching assisted** *Photonic Engineering, Probability & Stochastic Processes and Linear Systems*

**Adjunct Professor**

La Guardia Community College (LAGCC/CUNY), Mathematics Department,  
2003-Present

As an active lecturer within the department I have been teaching

- **Linear Algebra** This course is designed to introduce the students to the theory and applications of algebraic structures. This is done by studying the structure and properties of the matrix. The matrix is viewed both as an object possessing algebraic structure and an aid to computation. Systems of equations and their solutions are studied, and the concepts of basis and dimension are developed. Applications are discussed, including linear programming and computer programs in BASIC.
- **Calculus I**, This course is designed to provide students with an appreciation of the usefulness and the power of calculus. Among the topics studied are the definite integral, area, integration techniques and applications, elementary differential equations, and power series expansions.
- **Statistics I & II**, This course serves as a study of fundamental concepts and computational techniques of elementary statistics. Among the topics studied are: measures of central tendency, standard deviation, percentiles, statistical graphs, binomial and normal distributions, probability, confidence intervals, hypothesis testing, regression and correlation, inferences about proportions, means and variances, prediction intervals, multinomial experiments,

contingency tables and analyses of variance. A SPSS package is used by students to obtain basic sample statistics, to simulate fundamental theorems and to assist with hypothesis testing

Other classes taught at LAGCC were **Precalculus, Mathematics and the Modern World, Mathematics for Health Science, Mathematics in Action II**. As an active lecturer I participated in different professional development programs. Being a part of the Center for Teaching and Learning seminars that offered a wide range of classroom-focused professional development programs I had the chance to give my students the opportunity to understand mathematics through the SENCER (Science Education for New Civic Engagements and Responsibilities) approach. The SENCER project is promoting mathematical and statistical reasoning in compelling contexts under the umbrella of environmental sciences.

### **Comments of Students**

- Definitely one of the best professors. She explains things very well, she is clear, she knows the material and what's most important she cares about her students. She is always available to answer your questions and she is understanding in case you have any problems. Her exams are reasonable, she gives credit if you show that you know what your doing.
- This professor is into her work and thus makes the course very interesting. EE330 is a very involved: your Physics, Calc, Chem. and "imagination" have to be in tip-top shape if you want to be challenged and receive a good grade. 1-semester is definitely not enough for any professor to cover this course. IT WAS A WONDERFUL SEMESTER PROF.THANKS AND GOOD LUCK!!

### **PUBLISHED PAPERS and CONFERENCES:**

- “High Spatial Spectral Resolution VIS-NIR Scanning Fabry Perot Imager for Geostationary spaceborne applications”, Viviana Vladutescu, Mustapha Abdulfattah, Fred Moshary, Barry Gross, Photon 04 Conference , Glasgow Caledonian University, Glasgow , UK, September 6– 9,2004
- “Analysis of a Dual Etalon Fabry Perot Cavity for application in a Geostationary Coastal Water Imager”, Daniela Viviana Vladutescu, Fred Moshary, Barry Gross, Samir Ahmed, 12<sup>th</sup> International Symposium, Remote Sensing Conference, SPIE Europe, Bruges, Belgium, September 19-22, 2005
- “System Design of a Multiple Cavity Fabry Perot Interferometer for Visible, NIR Applications”, Viviana Vladutescu, Fred Moshary, Barry

Gross, Samir Ahmed , Einstein Conference, City College of City University of New York, NY, USA, April 11-12, 2005

- “DOAS Spectroscopy using a tunable MIR QCL for simultaneous Ozone and Ammonia detection” Viviana Vladutescu, Barry Gross, Fred Moshary, Samir Ahmed, Mirth, Annual Midterm Review, Princeton, NJ, USA, November 14<sup>th</sup>, 2006
- ”Water vapor mixing ratio used in lidar calibration technique” Daniela Viviana Vladutescu, Yonghua Wu, Leona Charles, Barry Gross, Fred Moshary, Samir Ahmed, The 2nd WSEAS International Conference on Remote Sensing (Remote’06), Tenerife, Spain, December 16-18, 2006
- “Analyses\_of\_Raman\_lidar\_calibration\_techniques\_based\_on\_water\_vapor\_mixing\_ratio\_measurements” Daniela Viviana Vladutescu, Yonghua Wu, Leona Charles, Barry Gross, Fred Moshary, Samir Ahmed, WSEAS Transactions on Systems, Issue 4, Volume 6, April 2007
- “Application of CCNY LIDAR and ceilometers to the study of aerosol transport and PM2.5 monitoring”, Leona A. Charles, Shuki Chaw, Viviana Vladutescu, Yonghua Wu, Fred Moshary, Barry Gross, Stanley D. Gedzelman, Sam Ahmed, The 87th AMS Annual Meeting, Third Symposium on Lidar Atmospheric Applications, San Antonio, TX, USA, January 13-18, 2007
- “Raman lidar calibration techniques based on daytime-nighttime measurements” Daniela Viviana Vladutescu, Yonghua Wu, Leona Charles, Barry Gross, Fred Moshary, Samir Ahmed, 2007 CUNY Conference in Science and Engineering, New York, NY, USA, February 23-24, 2007
- “Application of CCNY LIDAR to the study of aerosol transport”, Leona Charles, Shuki Chaw, Viviana Vladutescu, Yonghua Wu, Fred Moshary, Barry Gross, and Samir Ahmed, ESS/GEO Session, 2007 Joint Annual Conference of the National Society of Black Physicists and the National Society of Hispanic Physicists, Boston, MA, February 21-25, 2007
- “Lower troposphere water vapor measurements using a Raman lidar, GPS and radiosondes data fusion ” Daniela Viviana Vladutescu, , Barry Gross, Yonghua Wu, Fred Moshary, Samir Ahmed PRISM/PCCM/MIRTHE University –Industry Research Symposium, Princeton, NJ, USA, March 19-20, 2007

- “Examination of hygroscopic properties of aerosols using a combined multiwavelength Elastic –Raman lidar” Daniela Viviana Vladutescu, Yonghua Wu, Leona Charles, Barry Gross, Fred Moshary, Samir Ahmed IGARSS, Barcelona, Spain, July 23-27, 2007
- “Properties of aerosol hygroscopicity using a combined elastic-Raman lidar, GPS and nephelometer” Daniela Viviana Vladutescu, Yonghua Wu, Leona Charles, Barry Gross, Fred Moshary, Samir Ahmed SPIE Optics and Photonics, San Diego, CA, USA, August 26-30, 2007
- “Assessment of a QCL Laser approach for the simultaneous measurement of ambient ammonia and ozone.” Barry Gross, Viviana Vladutescu, Fred Moshary, Sam Ahmed., Infrared, Mid-IR, and THz Technologies for Health and the Environment II, SPIE Optics East, Boston, MA, USA, Sept 2007
- “Sensitivity of optical scattering coefficients to the hygroscopic properties of aerosols” Daniela Viviana Vladutescu, Yonghua Wu, Leona Charles, Barry Gross, Fred Moshary, Samir Ahmed in preparation for, IEEE Transactions on Geoscience and Remote Sensing
- “Raman-Mie lidar measurements of low and optically thin cloud” Yonghua Wu, Chaw Shuki, Barry Gross, Viviana Vladutescu, Charles Leona, Cao Nianwen, Fred Moshary, Samir Ahmed, SPIE Optics and Photonics, San Diego, CA, USA, August 26-30, 2007
- “Aerosol layer properties and their effect on the optical depth relation to PM<sub>2.5</sub> concentrations” Viviana Vladutescu, Barry Gross, Fred Moshary, Samir Ahmed, IGARSS, Boston, MA, USA, July 6-11, 2008

## **FUTURE WORK**

### **Research**

- Develop a research center for remote sensing
- Build and operate remote sensing technology such as Quantum Cascade Lasers(QCL) systems for ozone and ammonia in the atmosphere based on Differential Optical Absorption Spectroscopy (DOAS) technique
- Develop optical sensors designs and components
- Simulation Applications
- Operating Software of different space and land based instruments

### **Teaching**

- Establish an optics laboratory class with applications in fiber optics, spectroscopy, holography and optical systems design
- Create an environmental science program
- Assign student projects in optics and remote sensing

- Build up an optics laboratory
- Recruiting students to join NOAA, MIRTHE and NASA programs

### **SKILLS**

- **Leadership:** Innovative and creative in research. A very good team player as well as a team leader.
- **Optics:** very good understanding and conducting experiments involving various optical components and instruments
- **Programming Languages:** MATLAB, Labview, Pascal, Maple
- **Operating Programs,** HYDRA, ArcGIS, Zemax, Autoquant, GRAMS AI, SPSS, Yesdas,
- **Data Acquisition** using Parallel and Serial Interfaces - HP IB, GB IB and RS232, Labview cards
- **Languages:** Romanian (native), English (fluent)

### **INTERESTES AND ACTIVIES**

- Member, Institute of Electrical and Electronics Engineers(IEEE)
- Member, Society of Photo-Optical Instrumentation Engineers(SPIE)
- Member, New York Academy of Sciences(NYAS)

### **REFERENCES**

- Available upon request